Structural and Spectroscopic Studies of Metal Ions and Metal Clusters with Small Molecules

Philip Aidan James Pearcy

University College

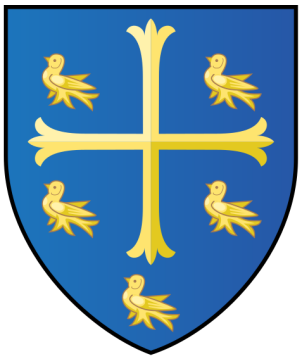

University of Oxford

A thesis presented for the degree of

Doctor of Philosophy

Michaelmas Term 2025

I dedicate this to Mum and Dad.

"The more we know, the more we feel our ignorance; the more we feel how much remains unknown"

— Humphry Davy (1778-1829)

Abstract

Gas-phase metal clusters and metal ion–ligand complexes exhibit a diverse array of structural motifs and size-dependent properties. These systems serve as valuable model platforms for exploring fundamental chemical bonding and reactivity at the molecular level. Detailed studies of such isolated clusters provide bottom-up insights into processes relevant to heterogeneous catalysis and materials chemistry, including but not limited to molecular activation at metal centres. This thesis presents experimental and computational studies on the structure and physical properties of different cluster systems of interest, as well as development work that has been completed to produce gas-phase metal clusters.

Following a general introduction to the field and methods section which details the techniques that have been used to complete the studies, the experimental sections are presented in three parts. Part A presents infrared photodissociation (IRPD) studies on metal ion-ligand complexes; with Chapter 3 presenting work on cationic nitrosyl complexes, $[M(NO)_n]^+$, of Group 9 elements (Co, Rh, Ir), and Chapter 4 focusing on platinum and platinum oxide nitrosyl complexes, $[PtO_x(NO)_n]^+$ $(x = 0, 1)$. In Chapter 3, spectroscopic and computational evidence suggested that $(NO)_2$ dimer moieties form when nitric oxide (NO) molecules bind non-covalently with other molecules that are bound directly to the metal cation centre. These dimer moieties only form following the first coordination shell for these complexes being filled with nitric oxide molecules, with the number of molecules in the first shell being dependent on the metal. In Chapter 4, it was shown that up to six ligands could bind to the platinum centre in the first coordination shell before dimer moieties form. With the oxygen-rich platinum complexes, evidence of the formation of an

N_2O_3 moiety, formed from an NO and an NO_2 molecule, is presented; this is illustrated by the appearance of intense spectral features between $1900 - 2000$ cm^{-1} in the IRPD spectra which are consistent with previous studies on $[NO_2(NO)_n]^+$ clusters.

Part B describes infrared studies on metal clusters using free-electron laser (FEL) light. Chapter 5 describes photoionisation studies of neutral tantalum and tantalum oxide clusters, Ta_nO_x, performed using the FELICE free-electron laser at the HFML-FELIX facility in Nijmegen, The Netherlands. Preliminary calculations on cationic Ta clusters, and their reactions with nitrogen oxides (NO/N_2O) are shown; with dissociative binding being predicted for all cluster sizes. In the experiment, size-dependent thermionic emission was observed with the neutral clusters, with odd-even alternations in signal intensity being caused by the clusters swapping between having open- and closed-shell electronic configurations. Ta-O stretches in the range $650 - 750$ cm^{-1} are also observed and are in close agreement with previous studies on cationic tantalum oxide clusters. The structures of the tantalum oxide clusters that contribute towards the experimental spectra are determined using quantum chemical calculations; with the dioxide clusters shown to contain two distinct oxygen atoms, rather than molecularly bound O_2 molecules.

Part C focuses on in-house development work that has been completed to build and test a new cluster source. Chapter 6 presents designs, simulations, and experimental studies on an experimental setup used to characterise a new bimetallic laser ablation cluster source. Photoionisation of nitric oxide was used to determine the shape of the gas pulse generated by the new source when different configurations and conditions were used; the shape of the pulse was then compared with predictions made using a simple kinetic theory model. Subsequently, neutral and cationic gold clusters, $Au_n^{0/+}$, were generated and studied using the custom built time-of-flight mass spectrometer. The source will be used in the future on existing experiments within the Mackenzie Group to investigate the role of cluster size and composition on reactivity with small molecules.

Acknowledgments

I have many people to thank for helping me during my time at the University of Oxford. Without them, I would not have been able to complete the work presented in this thesis, nor would I have enjoyed myself as much as I did.

Firstly, I would like to thank my supervisor, Prof. Stuart Mackenzie, for all the help and guidance he has provided over the years. Without his offer of a summer placement in 2019 to work with his group, I would never have discovered the research that inspired me to apply for a D.Phil at Oxford. He has continually encouraged me to push forward with my work, to think more deeply about the science, and to develop as a researcher. I am deeply grateful for all the time and effort he has devoted to helping me become a better scientist.

My thanks also extend to the post-doctoral researchers I have worked with in the Mackenzie Group: Dr. Alice Green, Dr. Peter Watson, and Dr. Christian Haakansson. They have each provided invaluable assistance and support throughout my D.Phil. Without them, I would not have been in a position to complete any of this work. Beyond the day-to-day discussions on science, they have also brought humour and good company, which made my time in the group so much more enjoyable. I especially thank Peter and Chris for helping to keep spirits high through their double act when things were not working in the laboratory.

I would also like to thank Dr. Edward Brewer, for his assistance both in and out of the lab and for his encyclopedic knowledge of all things aircraft-related; Dr. Gabriele

Meizyte, for all her help when I first joined the group; Peter Rubli, for bringing some much-needed sophistication; and Ellen Jones, for adding some much-needed quirkiness. My time in the group was made even more enjoyable by each of the Part II students who worked with me — Olga Duda, Matthew Doll, Lauren Wyatt, Jonty Mason, Ruby Spratt, and David Vesty. My thanks also go to all other members of the Mackenzie–Timmel team, who have brought so much enjoyment during my time here, and to Dr. Patrick Robertson for providing assistance in and out of the lab.

I must also thank others outside the group who made this work possible. I am grateful to Kevin Valentine and the electrical engineering team, Andrew Green, Johan Pretorius, and the entire mechanical engineering team, as well as Ron Tarry, Billy Fox, and Paul Mitchell who have spent countless hours making and fixing components for the experiments in Oxford. Without them, I would have got nowhere. I also wish to thank Dr. Joost Bakker for his assistance before, during, and after the group's trip to the HFML-FELIX facility in Nijmegen, The Netherlands to use the infrared free-electron laser. His expertise helped to answer many of my questions about the work we completed there.

My thanks also go to University College and the Department of Chemistry for funding my D.Phil studies *via* the Bob Thomas Scholarship, and to all involved in the EPSRC New Directions in Molecular Scattering (NDMS) project, which provided funding to build the new bimetallic cluster experiment.

I want to thank the friends I have made in Oxford. To my friends from Magpie Lane — Samuele Coen, Lisa Spiering, and Thomas Tendron — you have all provided so much support, as well as endless nights of fun and laughter, which mean a great deal to me. I also thank Nyan San Lwin and Jorin Riexinger; our first evening out together in Oxford set the blueprint for how we would enjoy our time there.

Finally, I want to thank Mum, Dad, Isabel, Lynne, Sajjad, Taff, and Frankie. Each of them, in their own way, has provided support for which I am eternally grateful.

List of Publications

1. G. Meizyte, P. A. J. Pearcy, P. D. Watson, E. I. Brewer, A. E. Green, M. Doll, O. A. Duda, and S. R. Mackenzie, "An Infrared Study of Gas-Phase Metal Nitrosyl Ion–Molecule Complexes", *J. Phys. Chem. A*, **2022**, *126*(50), 9414–9422.

2. E. I. Brewer, A. E. Green, A. S. Gentleman, P. W. Beardsmore, P. A. J. Pearcy, G. Meizyte, J. Pickering, and S. R. Mackenzie, "An Infrared Study of CO_2 Activation by Holmium Ions, Ho^+ and HoO^+", *Phys. Chem. Chem. Phys.*, **2022**, *24*, 22716-22723.

3. P. D. Watson, G. Meizyte, P. A. J. Pearcy, E. I. Brewer, A. E. Green, C. Robertson, M. J. Paterson, and S. R. Mackenzie, "Infrared Spectra and Fragmentation Dynamics of Isotopologue-Selective Mixed-Ligand Complexes", *Phys. Chem. Chem. Phys.*, **2024**, *26*, 16589-16596.

4. P. T. Rubli, C. T. Haakansson, P. A. J. Pearcy, R. G. Spratt, J. M. Bakker, P. D. Watson, and S. R. Mackenzie, "An Infrared Spectroscopic Investigation of Nitric Oxide Binding on Isolated Cobalt Cluster Cations", *J. Phys. Chem. A*, **2025**, *129*(26), 5810–5819.

5. P. D. Watson, G. Meizyte, P. A. J. Pearcy, E. I. Brewer, A. E. Green, A. J. Stace, and S. R. Mackenzie, "Infrared Photodissociation Spectroscopy of Cationic Nitric Oxide Clusters, $[(NO)_n]^+$, and $[NO_2(NO)_n]^+$", *J. Phys. Chem. A*, **2025**, *129*(17), 3867–3875.

6. P. A. J. Pearcy, E. I. Brewer, G. Meizyte, S. Harrington, M. Doll, P. D. Watson, C. T. Haakansson, and S. R. Mackenzie, "Structure, Spectra, and Intracluster

Chemistry of Gas-Phase Platinum Nitrosyl Ion-Molecule Complexes", *Phys. Chem. Chem. Phys.*, **2025**, *Submitted*.

7. P. D. Watson, R. G. Spratt, P. A. J. Pearcy, P. T. Rubli, C. T. Haakansson, J. M. Bakker, and S. R. Mackenzie, "Infrared Photoionisation of Neutral Ta_n and Ta_nO_m Clusters", *Mol. Phys.*, **2025**, *Submitted*.

8. C. T. Haakansson, E. I. Brewer, J. Mason, P. A. J. Pearcy, P. D. Watson, L. Wyatt, and S. R. Mackenzie, "Infrared Spectroscopy of $Ho(OCS)_n^+$, $HoO(OCS)_n^+$, and $HoS(OCS)_n^+$ Complexes", *In Preparation*.

Contents

Chapter 1

Introduction

Gas-phase metal clusters can be used as tractable systems to model the intrinsic catalytic behaviour of bulk metallic surfaces.[1] Figure 1.1 shows a cartoon metallic surface, with segments of the metallic surface broken down into smaller fragments, involving clusters containing a small number of atoms. Each of these fragments can be studied in isolation to better understand their role in the chemical and catalytic behaviour of a surface. The work covered in this thesis has been completed to gain a greater understanding of the structural and physical properties of specific gas-phase metal clusters and gas-phase metal ion-ligand complexes using catalytically relevant metals. In addition, studies have been completed to optimise the production of gas-phase clusters. This chapter will provide an overarching view of the motivations behind the systems that have been studied. In addition, key principles of both the experimental and theoretical techniques that have been used in later chapters will be described.

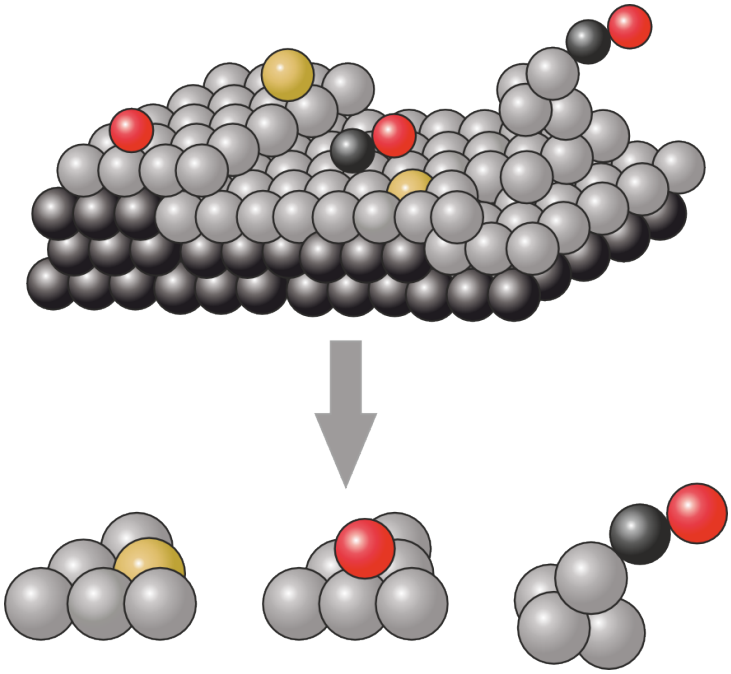

Figure 1.1: A cartoon illustration of a metal surface (silver spheres represent metal atoms) on a support material (black spheres). There are a number of additional atoms on the surface representing adsorbate atoms / molecules. Different sections of the surface can be described using metal clusters, as shown.

1.1 Motivation

1.1.1 Chemical Reactions and Utilising Catalysts

The progression of any chemical reaction can be represented using an appropriate potential energy surface (PES) that connects the reactants with the products.[2] An example potential energy surface is illustrated in Figure 1.2 **a)**. As can be seen on the cartoon surface, there are many local minima which are separated by local maxima that represent the transition states in the reaction. Depending on where they appear on the PES, these minima can be described as either an entrance channel, which represents species before they undergo the chemical reaction, or an exit channel, which describes new product-like species. The species contained within these minima can be investigated by using experimental and computational techniques, such as using infrared spectroscopy to monitor changes in the vibrational frequencies as the species move along the reaction coordinate, or by performing calculations to predict the heights of the barriers between these minima.

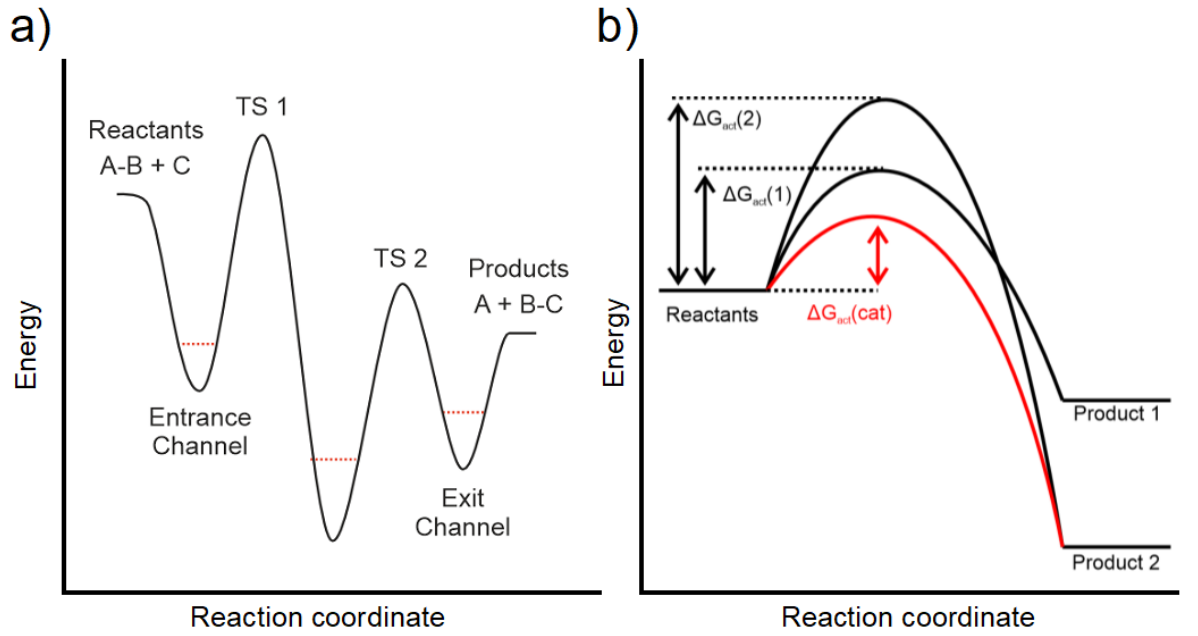

Figure 1.2: **a)**: Reaction coordinate diagram of the general reaction A-B + C progressing to A + B-C. The key features of the surface are captioned, such as the different minima and the transition states (TS). **b)**: The effect of a catalyst on the barrier heights between the reactants and products. Without the catalyst, the pathway with the smallest barrier generated the kinetic product (Product 1). With the catalyst, the activation energy, ΔG_{act}, is lower than the other pathways, leading to the production of the thermodynamic product (Product 2).

The rate of the reaction, and which species will be produced, is determined by the heights of the barriers, the temperature at which the reaction is performed, and by the pathways the reactions can follow. These can be influenced by the use of a catalyst; a material that can increase the reaction rate without being consumed itself.[1] Catalysts increase the reaction rate by providing alternative pathways with lower activation energies, as illustrated in Figure 1.2 **b)**. In the figure, a catalyst provides a lower energy reaction pathway to the thermodynamic product (Product 2), due to the activation energy, ΔG_{act}, for this pathway being lower than for the other products (Product 1). This often occurs by forming intermediates with the reactants that lead to new products that would only be formed under harsher conditions, such as increasing the temperature to allow the reactant species to have enough energy to overcome the larger barrier and form the lower energy product.[3]

Chemical production contributes approximately 7% of global anthropogenic greenhouse emissions, due to the energy required to support the chemical industry.[4] By providing lower energy pathways through which chemical reactions can proceed, catalysts can reduce industrial energy costs and the amount of CO_2 released into the atmosphere. Given the importance of catalytic materials within the chemical industries, the size of the catalyst industry was predicted to be $34.1 billion by 2025.[5] Researching how catalytic materials work and finding new materials that can improve energy efficiency and chemical selectivity is therefore of great importance.

When it comes to describing the type of materials that are catalytic, it is useful to distinguish between homogeneous (where the phase of the catalytic material and reactants are the same) and heterogeneous (where the phases are different) catalysis. Heterogeneous catalysts are typically solid-state materials that are metallic (*i.e.* metallic meshes) or contain metal atoms within them.[6–8] This can include materials such as single atom catalysts that involve embedding atoms within a zeolite or 2D-material.[9–11] Reactant molecules in either the gas- or liquid-phase pass over the catalytic material and react at the fluid-solid interface. Some key examples include the use of iron (Fe) catalysts in the Haber-Bosch process to produce ammonia from molecular hydrogen and nitrogen:[12, 13]

$$\mathrm{N_2 + 3H_2} \xrightarrow[\text{Fe cat.}]{\text{High T, High P}} \mathrm{2NH_3}, \tag{1.1}$$

as well as the use of cobalt (Co) catalysts in the Fischer-Tropsch process to generate hydrocarbons from hydrogen gas and carbon monoxide:[14, 15]

$$(2n+1)\,\mathrm{H_2} + n\,\mathrm{CO} \xrightarrow[\text{Co cat.}]{\text{High T, High P}} \mathrm{C}_n\mathrm{H}_{2n+2} + n\,\mathrm{H_2O}. \tag{1.2}$$

These materials are beneficial to industry because of how robust they are, but they can contain rare elements that have to be extracted using an energy-intensive and polluting process, which can make them costly to produce and replace; increasing overall running costs. In terms of homogeneous catalysts, beyond enzymes (biological catalysts)[16] and organocatalysts (small organic species acting as catalysts),[17] many homogeneous catalysts take the form of metal ion-ligand complexes, otherwise known as organometallic complexes. These involve ligands binding to a single metal centre, and they are ubiquitous in organic chemistry; for example, Grignards reagents, R-Mg-X, have an alkyl, aryl, or

alkenyl group (R) and a halide group attached to a magnesium centre, as well as organolithium complexes, Li-R, which are more reactive than Grignard reagents on account of the more polar Li-C bond.[18] Metal-ligand complexes can also be used as catalysts, such as Wilkinson's catalyst, $[RhCl(PPh_3)_3]$, used to enable alkene hydrogenation:[19]

$$RCH{=}CHR' + H_2 \xrightarrow{\text{Wilkinson's catalyst}} RCH_2 - CH_2R', \tag{1.3}$$

and the Monsanto process catalyst, $[RhI(CO)(PPh_3)_2]$, which is used in the carbonylation of methanol:[20]

$$CH_3OH + CO \xrightarrow{\text{Monsanto's complex}} CH_3COOH. \tag{1.4}$$

These catalysts are highly specific and can improve efficiencies, but can carry greater operational costs than heterogeneous materials and often have a lower turnover rate before they are deactivated.[21]

As shown in Figure 1.1, the surfaces of heterogeneous catalysts are not pristine and are typically made up of defect sites, terrace edges and steps, atomic clustering and additional atoms (such as oxygen).[22] Chemical reactions take place more readily at the active sites of catalysts. There are more active sites on the surface's defects and edges, as the atoms that make up the surface will have fewer direct neighbours, causing the local surface energy to increase and being more likely to interact with reactants.[23] This can make understanding of the processes that occur on heterogeneous catalysts more difficult, as additional studies are required to investigate the role of these defect sites on the rate of reaction, in addition to the role the catalyst support material plays in the overall reaction. There are also difficulties in determining all of the individual steps that arise in a catalytic process. For example, the Haber-Bosch process was shown to involve multiple steps to dissociatively adsorb nitrogen and hydrogen to form ammonia.[3]

Complications also occur in the computational simulations of molecules reacting on surfaces, and theoretical and practical limitations to them will occur. The surface chemistry can be described with a more detailed quantum picture, but will be very expensive computationally. Alternatively, the calculation can be inexpensive, but suffer from inaccuracies.[24] Some of these issues can also arise with homogeneous catalysts, as it can be difficult to understand how a single metal atom interacts with small molecules if

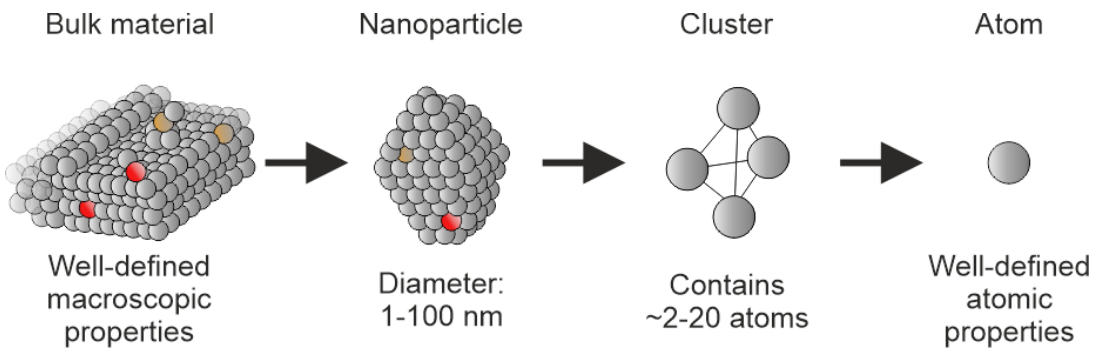

Figure 1.3: The progression from the bulk material down to the single atom, *via* the formation of nanoparticles and atomic clusters. Add-atoms in the bulk material and the nanoparticle are illustrated with different coloured spheres.

---

there is a solvent effect at play as well. The ability to study these catalytic materials in isolation is desirable, and a tractable model can be used to describe these systems.

1.1.2 Properties and Studies of Metal Clusters

One way of modelling active sites on the surface of a heterogeneous catalyst and the ion-molecule complexes that are present in a homogeneous catalyst is to use gas-phase metal clusters and ions.[1, 22, 25, 26] The size of a cluster can vary, but for the purpose of this thesis, it is defined as a structure that contains between 2-20 atoms. These aggregates act as an intermediate structure between the bulk material, with its well-defined macroscopic properties, and the single atom, as illustrated in Figure 1.3. Nanoparticles can also be considered to be in this mesoscopic regime but are not within the scope of this thesis. Atomic clusters are helpful for understanding catalytic processes because gas-phase molecules can bind to them and undergo chemical reactions. However, clusters can possess their own interesting chemistry depending on their size, structure, spin state, and composition.[27–29] For example, in this regime, changing the size of the cluster by adding or removing a single atom can dramatically affect its properties and how it interacts with small molecules. As the size of the metal species decreases from the bulk material to clusters, the electronic configuration changes from conductive and valence bands to discrete HOMO-LUMO orbitals. Metal ion-ligand complexes themselves can possess some unique size-dependent behaviour, since new structural moieties can emerge as more ligands coalesce around the metal centre.

Many studies have been performed to investigate the physical properties of gas-phase metal clusters and metal ion-cluster complexes using a range of experimental techniques, one of them being mass spectrometry.[30–34] Mobility studies have been performed to investigate how long it takes for clusters to travel through a medium to gain information about the structural and charge properties of the clusters.[35, 36] Furthermore, reactivity studies have been completed to investigate the products that form when clusters collide with small molecules across a range of collision energies. Armentrout and co-workers have performed collisional studies using transition metal clusters and atmospherically relevant molecules, such as H_2, N_2, and CH_4, to investigate the reaction energies and the internal energy of the products.[26, 37, 38] From this the reaction cross-sections and thermodynamic parameters can be deduced, which is particularly useful for studying the activation of small molecules by metal clusters. These experiments require a source that can generate the clusters and a collision cell that contains the reactant gas of interest, ion optics to control the kinetic energies of the clusters, and a mass spectrometer to detect the resulting products.

Mass spectrometry is a common analytical technique in such studies because of its high detection efficiency and resolving power. It can be used to profile the distribution of the sizes of metal-containing species clusters that are generated under different clustering conditions, as well as the emergence of new features that correspond to molecular groups attached to the clusters. In addition, it can be used to monitor fluctuations in signal intensity caused by varying physical properties. For example, specific cluster sizes may be less reactive than others, possibly due to their electronic configuration and structural properties. The reduction in product signal in the mass spectrum can be used as a way to measure the rate of reaction of the metal cluster with the reactant gas molecules.[39]

Studies have been conducted to investigate the products that form when metal clusters and metal ion-ligand complexes are irradiated with light. For example, Parry *et al.* studied the effect of blackbody infrared radiation on the dissociation products of $[Rh_n(N_2O)]^+$ clusters and the size of the activation barriers for the entrance channel products. There was a size-dependent effect on which products were produced, with $[Rh_5(N_2O)]^+$ mainly forming Rh_5^+ and $[Rh_5O]^+$ following irradition, whereas $[Rh_6(N_2O)]^+$ produced $[Rh_6O]^+$

only.[40] Photoionisation efficiency studies have also been completed on a range of metal clusters,[41–45] including on Fe and Co neutral clusters using a tunable UV radiation source ($4.8 - 6.3$ eV) combined with a mass spectrometer. The ionisation potential was observed to decrease rapidly but non-monotonically for both Fe_n and Co_n up to $n \approx 20$, beyond which IPs evolve more slowly and smoothly.[46] As well as investigating the cluster size, studies have also been performed to investigate the effect of doping clusters with different atoms, both metallic and non-metallic.[47–55] By altering the composition of a cluster, the structural and reactive properties of it can be finely tuned to promote specific processes that would be desired in a catalytic processes, such as molecular dissociation. This in turn could aid in the development of new nanoalloy materials that could improve upon the abilities of single metal materials and go beyond the limitations of single elements.

1.2 Generating Metal Clusters

In order to generate metal clusters and metal ion-ligand complexes, a source of some description is required. Studies performed on clusters in the gas-phase require the elements under investigation to be vaporised. This can be achieved *via* a number of different methods.[56] Thermally heated ovens can be used to boil off metal atoms before they escape through effusive flow.[57–64] Atoms and ions can be sputtered off a surface by using rare gas ions (*i.e.* these can be generated using the Cold Reflex Discharge Ion Source (CORDIS) to produce Ar^+, Xe^+, *etc.*),[65–72] or by using magnetic fields (*i.e.* magnetron sputtering sources).[73–77] Furthermore, clusters can be produced from solution samples using the electrospray ionisation source.[78–82] This technique enables the formation of gas-phase water clusters[83, 84] as well as salt clusters.[85] The clusters studied in this thesis were all generated using laser vaporisation,[45, 86–92] so this will be discussed in detail.

1.2.1 Laser Ablation of Materials

This process proceeds by a target containing the element(s) of interest being ablated using a highly focused laser pulse. The wavelength of the laser light can vary from source to source, with excimer lasers being used in some cases, but 532 nm is typically used

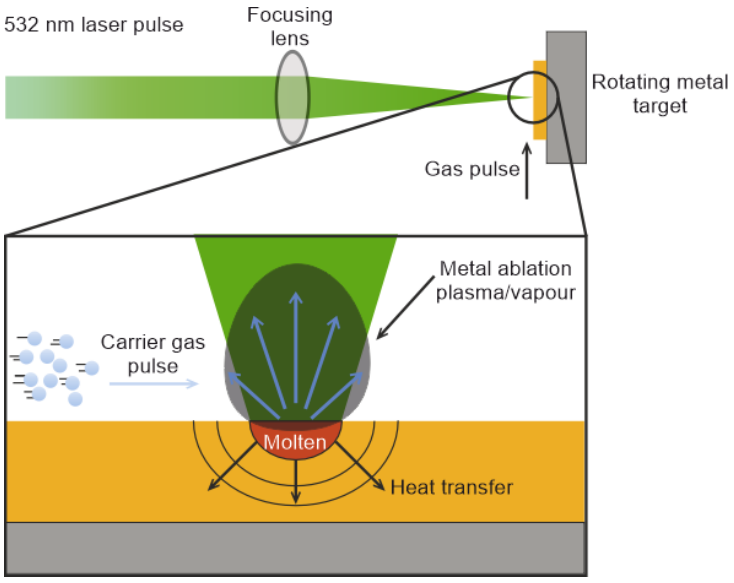

Figure 1.4: Diagram illustrating the laser vaporisation / ablation process. Following irradiation with a highly focused 532 nm laser beam on a metal surface, a metal plasma is ejected. Ablation takes place within the gas pulse to entrain the liberated ions within it.

---

given that it corresponds to the second harmonic of a Nd:YAG laser (see Section 1.6). The energy imparted into the material excites internal degrees of freedom (translational, rotational, vibrational, and electronic).[93, 94] By rapidly heating the material at or near the focal point of the laser, highly energetic neutral atoms, ions, and electrons can be ejected from the surface in the form of a vapour or a plasma.[95] This process is illustrated in Figure 1.4. The target used is typically a rod or a disc, which is coated with a thin wafer of the element under investigation. The target is rotated to provide a fresh surface that the laser pulse can ablate, ensuring there is a continuous production of atoms and ions. The atoms and ions that are liberated from the target surfaces are very energetic and expand out from the surface in all directions before being picked up by a carrier gas pulse (see the zoomed section in Figure 1.4).

The amount of energy that is required to ablate the target, which can be controlled by adjusting the laser power, depends on its reflectivity and thermal conductivity.[92, 96, 97] The laser beam width at the target's surface can be adjusted by altering the focussing lens' position in the beam line to change the focal point. This can have a significant effect on the clustering efficiency. For example, Lievens and co-workers showed that in order

to produce Au_n^+ clusters, laser fluences in the range of 2.0-3.2 mJ/mm^2 were required. Below this, little signal was observed, and above this the only signal that was detected was for Au_{1-3}^+.[98–100] Ablation sources can also be used to generate clusters with different charge states; some of the first experiments that produced gas-phase metal clusters using pulsed laser were able to study neutral species.[86] Furthermore, laser vaporisation can also produce species in even higher charge states ($\geq 2+$) by using much higher pulse energies.[101]

1.2.2 Clustering Pathways

In order for the atoms to aggregate to form clusters, as well as complexes with reactant species/ligands, they need to be cooled down to remove the excess energy they possess. Smalley and co-workers,[45, 86] as well as Bondybey *et al.*,[90] developed cluster sources that utilised supersonic expansions to generate a molecular beam.[102, 103] The first step in producing clusters and complexes is based on three-body collisions, as illustrated in Figure 1.5 **a)**. In order for a metal dimer to form, a carrier gas (CG) atom (typically a noble gas, *i.e.* He or Ar) must collide with the two metal atoms to reduce the total internal energy so that the dimer is then bound. Further collisions cool it to lower vibrational states. The energy is removed in the form of an increase in the kinetic energy of the carrier gas atom.[2, 104]

Once the initial dimer is formed, this unit can go on to cluster with other atoms to form larger structures. This can result in larger clusters with more internal energy that needs to be released in order for them to last long enough to be studied or used as catalysts. Additional pathways are available to remove excess energy, such as evaporative cooling (loss of an atom from a cluster), collisional cooling (where a carrier gas atom removes excess energy by colliding with the cluster) and radiative cooling (where the excess energy is released as a photon).[102, 103] These are illustrated in Figures 1.5 **b)**, **c)** and **d)**, respectively. However, radiative decay is unlikely to occur on the time scale of the experiment (tens of microseconds).[105] To maximise collisional cooling, it is important that the ablation takes place in the middle of the gas pulse where the number density of carrier gas atoms is at its highest. The number density of carrier gas atoms is in large excess compared to the number of atoms liberated from the target's surface, meaning

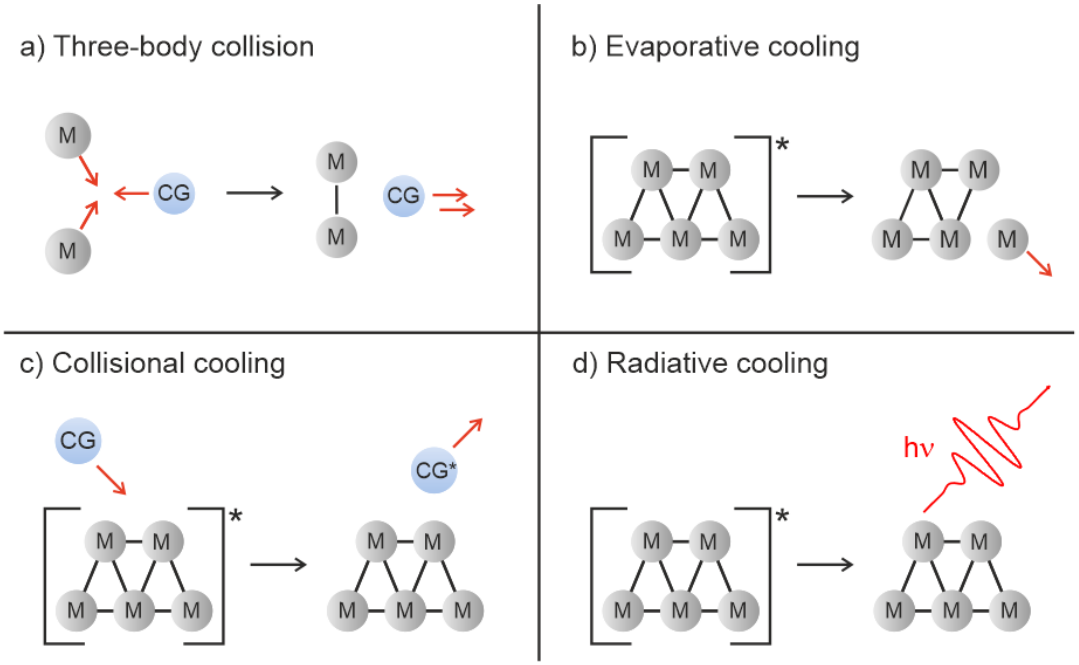

Figure 1.5: Illustration of the different clustering and cooling processes. **a)** Cluster growth *via* three-body collisions. The excess energy from metal-metal bond formation is removed in the form of an increase in the kinetic energy of the carrier gas (CG) atom. **b)** Evaporative cooling, where cooling takes place *via* the loss of a metal atom. c) Collisional cooling, where the excess energy in a cluster is removed *via* collision with a carrier gas atom. d) Radiative cooling, where the excess energy is released as a photon.

multiple collisions can take place to remove the excess energy. Larger clusters have a greater amount of total internal energy, as there are more bonds to store vibrational energy.

1.2.3 Supersonic Expansions

The use of supersonic expansions under vacuum conditions also assists in cooling the clusters and complexes that are formed after the laser ablation. The idea was developed by Kantrowitz and Grey as a way to produce a molecular beam.[106] It relies on an isentropic expansion from a high pressure region (P_1, typically within a gas reservoir at $\approx$ 0.5 - 10.0 bar) into a low pressure region (P_2, under ultra-low vacuum conditions). This causes the temperature of the molecular beam to decrease from room temperature to only a few Kelvin.[107–109] Furthermore, the translational energy within the gas is converted to direct the gas in one specific direction.[110, 111]

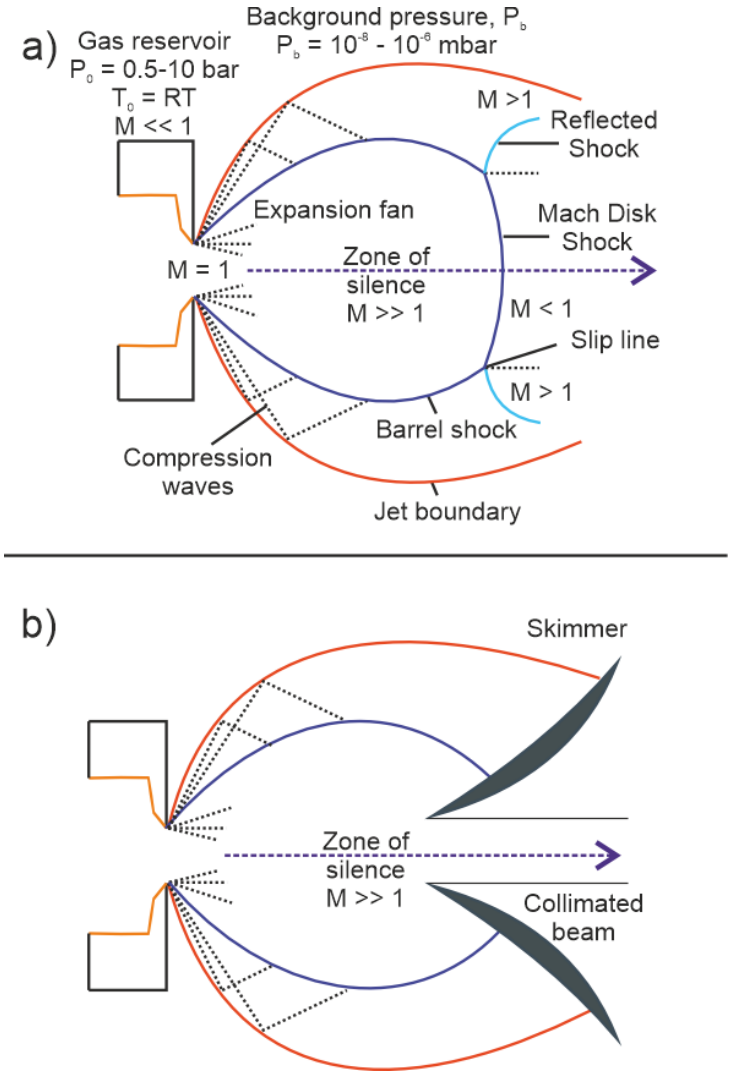

Figure 1.6: **a)** Illustration of the supersonic expansion from a nozzle, with the shock waves also shown. **b)**: The addition of a skimmer to the illustration provided in **a)** within the zone of silence leads to a collimated molecular beam forming. Adapted from Ref [112].

Figure 1.6 illustrates the shape of the wave that is produced from the supersonic expansion. The expansion is only supersonic right after the nozzle if the difference in the high- and low-pressure regions ($\frac{P_1}{P_2}$) meets the criteria set by the equation:

$$\frac{P_1}{P_2} > \left(\frac{\gamma+1}{2}\right)^{\frac{\gamma}{\gamma-1}}, \tag{1.5}$$

where γ is the heat capacity ratio, C_p/C_v, of the carrier gas used.[109, 110, 113] The mean free path of the gas, λ, must be smaller than the diameter of the orifice, Φ. These

can be related to the Knudsen number (K_n):

$$K_n = \frac{\lambda}{\Phi}, \tag{1.6}$$

and this must be less than one for a supersonic expansion to form.[114] Due to the molecular mean free path being markedly shorter than the orifice diameter, molecules passing through the orifice (as well as in the region immediately after) can undergo many collisions. Those collisions that impart momentum along the same axis as the orifice are ultimately more successful in passing through the orifice. Part of the expansion is called the zone of silence and will contain the clusters and complexes that have been cooled more effectively. At the leading edge of this region is a shock wave that can disturb the beam downstream if it continued to propagate. To avoid this, a skimmer is installed to generate a collimated molecular beam, as illustrated in Figure 1.6 **b)**. This molecular beam will contain species that have been cooled more effectively.

The supersonic expansion can be modelled as an ideal gas. With this assumption, a beam velocity (*i.e.* the speed at which the gas within the molecular beam travels) can be calculated using the following equation:

$$v_0 \approx \left(\frac{2k_BT_0}{m}\frac{\gamma}{\gamma-1}\right)^{\frac{1}{2}}, \tag{1.7}$$

where k_B is the Boltzmann constant, T_0 is the temperature within the gas reservoir behind the nozzle, m is the mass of the carrier gas, and γ is C_p/C_v (C_p/C_v equals 5/3 for ideal monatomic gases, 7/5 for ideal diatomic gases).[114] The beam velocity for He and Ar at 300 K are calculated to be $\approx 1766\,\mathrm{ms}^{-1}$ and $\approx 558\,\mathrm{ms}^{-1}$, respectively.[110, 115] Other types of expansion include effusive flow, which involves the mean free path being much greater than the orifice hole size and produces species which travel with random thermal motion. The distribution of a supersonic expansion is much tighter than that of an effusive flow as molecules collide with fast molecules behind and slow molecules in front and eventually travel at the beam velocity.[110] The distribution of the effusive flow velocity follows a Boltzmann distribution and has a mean thermal speed $\bar{\nu}$, expressed as:

$$\bar{\nu} = \sqrt{\frac{8k_BT}{\pi m}}. \tag{1.8}$$

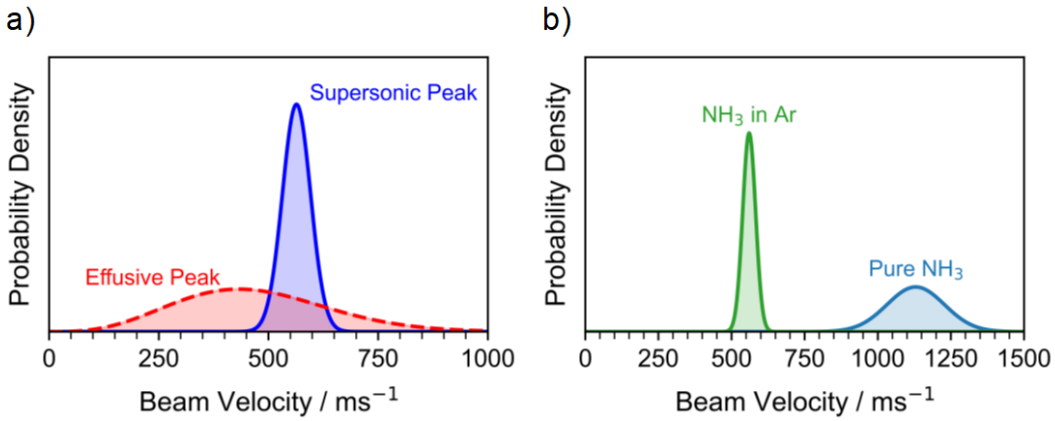

Figure 1.7: a) Illustration of the beam velocity distribution for an effusive beam (red) and a supersonic beam (blue) for Ar gas. **b)** Illustration of the beam velocity distribution for a pure reactant (ammonia, NH_3), and a narrower velocity distribution for NH_3 seeded in Ar.

The difference in the distributions is illustrated in Figure 1.7 **a)**, with the effusive flow distribution spread over a wider range of velocities compared to the supersonic flow.[114]

Often, carrier gases are seeded with a reactant gas of interest to form metal ion-ligand complexes. By seeding the carrier gases, the internal energy within the reactant gases is removed through collisional cooling, allowing the molecules to reside in their ground state. As a result, the distribution of velocities of a carrier gas seeded with a reactant gas (such as ammonia, NH_3) is much tighter than a pure reactant molecular beam, making it more useful when controlling beam velocity. It also minimises reactions within the beam until the interaction region (*i.e.* laser ionisation, extraction, *etc.*). This is shown in Figure 1.7 **b)**. It should also be noted that despite the reactant gas being seeded in a carrier gas, there are still orders of magnitude more gas molecules per unit volume than clusters from the ablation of the target.

1.2.4 Cluster Source Types

Depending on what type of species the experiment is designed to study, the configuration of the cluster source can be varied to produce metal ion-ligand complexes, $[M(L)_n]^{+/0/-}$, or metal clusters coated with ligands, $[M_nL]^{+/0/-}$.[43, 92, 116–118] Figure 1.8 illustrates

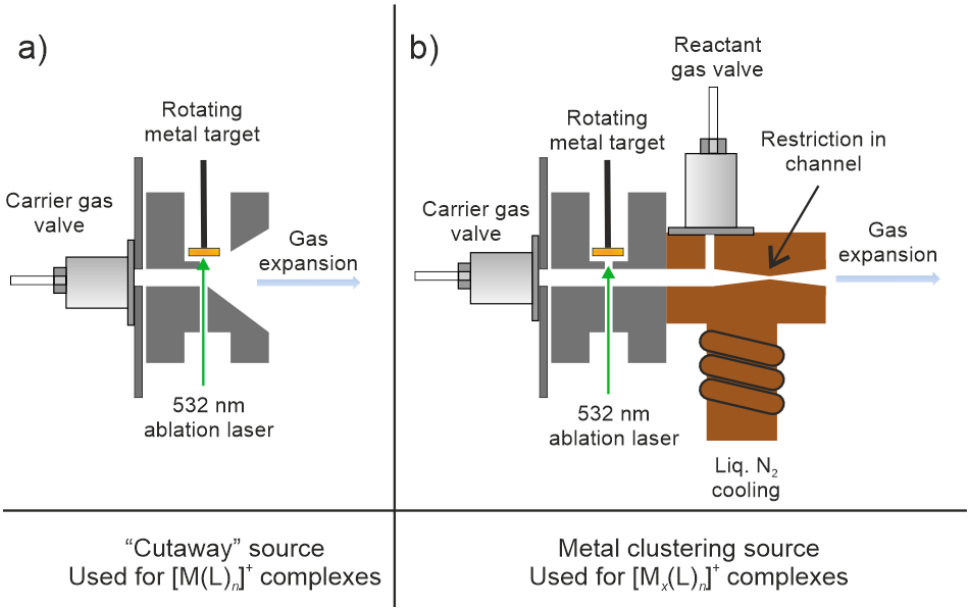

Figure 1.8: **a)** A schematic diagram of the "cutaway" source block used to generate ions *via* laser ablation. This is used to primarily form $[M(L)_n]^{+/0/-}$ metal ion-ligand complexes. **b)** A cartoon diagram of the channel source block used to generate metal clusters *via* laser ablation. This also incorporates other features such as a restriction in the channel, and liquid nitrogen cooling, to promote the formation of larger clusters.

---

two types of cluster source, with panel **a)** showing a "cutaway" source that is designed to produce metal ion-ligand complexes and panel **b)** showing a cluster channel designed to form metal clusters. The "cutaway" source, perfected by Duncan,[92] reduces cluster aggregation, and the time the gas travels before it expands is also reduced. This makes the supersonic expansion even colder, which is useful for attaching reactant gas ligands to the metal ion given that these ligands are bound relatively weakly. The clustering channel shown in Figure 1.8 **b)** is used to promote the formation of larger clusters. The pressure inside the channel, P_1, increases when the gas from the nozzle fills it, promoting the aggregation of the atoms. The maximum pressure that the source can achieve is defined by the rate at which gas flows in and gas flows out, which is determined by the dimensions of the channel.

The plasma can also be cooled down and is thermalised to the temperature of the channel's walls. Further adjustments can be made to the cluster source by adding a restriction within the channel to promote a supersonic expansion at the end of it. Using a narrow

nozzle ensures that the local pressure remains high inside the source, keeping collisional conditions favourable for clustering. A smaller orifice also accelerates the gas more efficiently, producing a colder jet overall. Furthermore, cooling the channel with liquid nitrogen (LN_2) allows larger clusters to be generated. The final gas jet temperature scales with the initial reservoir temperature, so starting at a colder temperature (*e.g.* 77 K instead of 300 K) means the expansion reaches much lower translational, rotational, and vibrational temperatures, favouring condensation of clusters. Other nozzles can be added downstream on the cluster source to attach reactant ligands onto clusters that have formed and thermalised. Cluster sources can also be floated (*i.e.* have a potential applied to it) in order to accelerate ionic species out of the ablation region and towards the interaction region.

Other cluster sources have also been produced that allow two rod targets to be ablated using two different lasers. These have been developed to generate mixed metal clusters which can behave as nanoalloys.[47, 98, 100, 119] These have allowed others to conduct studies to study the effect of doping metal clusters on the chemical and physical properties of the clusters. Chapter 6 will outline the work that has been done to build a bimetallic cluster source that can be used within the Mackenzie Group.

1.3 Mass Spectrometry

The work presented here relies heavily on mass spectrometry to monitor the distribution of charged species produced from the cluster sources. It was used for detection, such as monitoring changes caused by infrared irradiation, as well as mass filtration. This section describes the principles behind this analytical technique.

1.3.1 Time-Of-Flight Mass Spectrometry

Time-of-fight (ToF) mass spectrometry is commonly used to monitor the production and distribution of charged species produced from the cluster sources. It relies on measuring how long it takes for a charged species to travel between two points depending on its mass and charge, given a fixed or narrow distribution of kinetic energies. An ion of mass m and charge q accelerated through a potential difference of ΔV will acquire the kinetic

energy E_k defined by:

$$E_k = \Delta V q = \frac{1}{2} m v^2, \tag{1.9}$$

where v is the velocity.[120, 121] If a collection of charged species with a mass distribution accelerate through an electric field from the same starting point, each ion will be imparted with identical kinetic energy. If this were possible, the ions would spread in space and time as they continue to move over an arbitrary distance, D. This would allow the different ion masses to be recorded as a function of their time-of-flight from their starting point to a detector located after distance D from the ion optics. However, it is not possible for all the ions to start in exactly one spot, which means that they would not have identical kinetic energies. As a result, this can make it more difficult to determine the exact time-of-flight.

The Wiley-McLaren (WM) ion optics, developed in 1955, were able to overcome this issue. Consisting of three electrodes (repeller, extractor, and ground), the WM arrangement accelerated ion packets in two stages between the repeller and extractor, and then between the extractor and the ground.[122] This is illustrated in Figure 1.9. By controlling the ratios of potential applied to the electrodes, the kinetic energy imparted to all ions that are spatially distributed between the first two electrodes causes them to be spatially and temporally focused at the position D downstream of the electrode system. By strongly focussing on temporal resolution, the energy resolution must reduce, because the system no longer perfectly distinguishes small differences in kinetic energy as it compresses them into the same arrival time. The total kinetic energy (U_{total}) of the ion imparted by the Wiley-McLaren optics is given by the relationship:

$$U_{\text{total}} = U_0 + q s_0 E_s + q d E_d, \tag{1.10}$$

where U_0 is the initial kinetic energy of the ion, E_s is the electric field within the repeller-extractor region, d is the separation of the extractor ground plate, and E_d is the electric field within the extraction-ground region. Typically, the distribution of the ions will be centred at a distance s_0 from the repeller plate ($s_{\max} = s_0 + \frac{1}{2}\delta s, s_{\min} = s_0 - \frac{1}{2}\delta s$). This distance is also shown in Figure 1.9. The ion optics are often arranged to ensure s_0 is midway between the first two plates ($s_0 = \frac{s}{2}$), where s is the distance between the repeller and extractor. With equal changes in kinetic energy, ions of differing mass-to-charge ra-

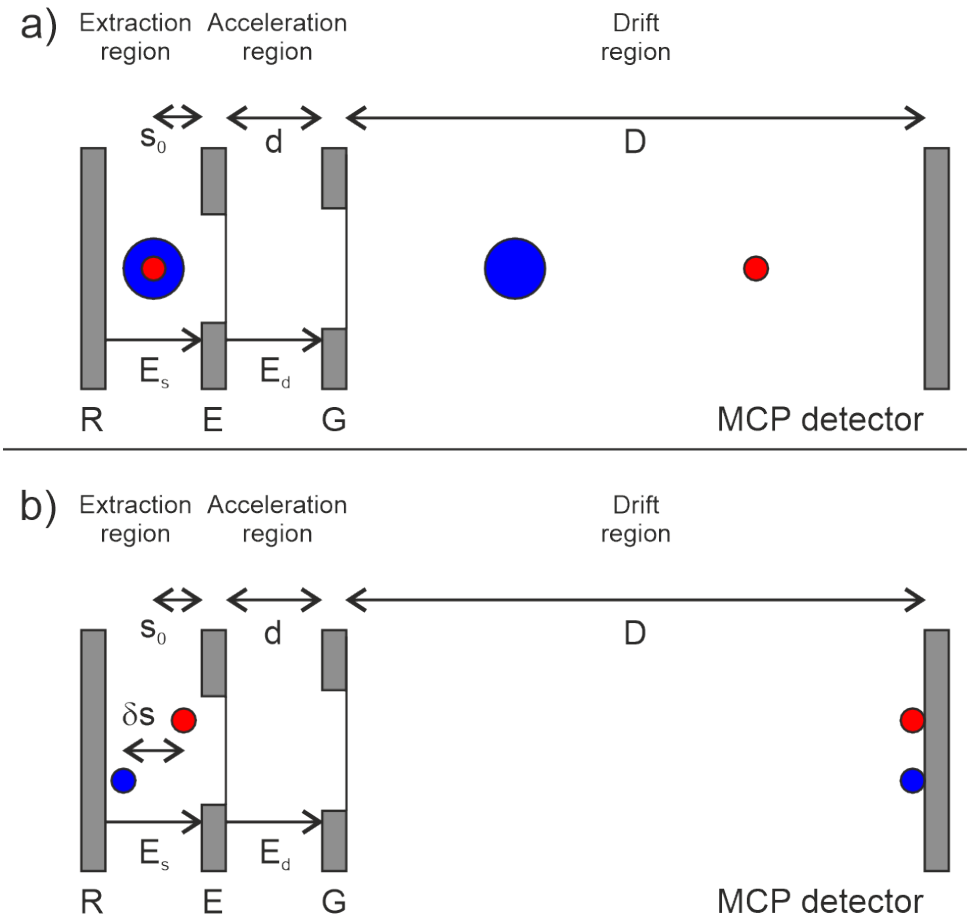

Figure 1.9: Illustration of a simple time-of-flight mass spectrometer. The Wiley-McLaren (WM) lens arrangement used to accelerate ions is shown. The lens consists of three electrodes: the repeller (R), the extractor (E) and the ground electrode (G). There is an electric field generated between R and E, referred to as E_s, and another field generated between E and G, referred to as E_d. Ions are detected at the end of the flight using the MCP detector. **a)** The red and blue circles, indicating ions of different masses, are separating in the mass spectrometer flight. **b)** Two ions of identical mass start at different points in the extraction region (between R and E). They arrive at the detector at the same time due to the spatial focusing achieved using the WM ion optics.

tios (mass of the blue dot is greater than the mass of the red dot) are separated by their velocities and consequently the time at which they reach the detector, as demonstrated in Figure 1.9 **a)**. Only singly charged ions were studied for the work presented in this thesis, so the mass-to-charge ratio is often referred to as mass in atomic mass units, u, throughout.

The total time-of-flight, $t(U_0, s)$, can be broken down into the time-of-flight in each region:

$$t(U_0, s) = t_s + t_d + t_D. \tag{1.11}$$

Assuming the ions start in the middle of the plates (*i.e.* $s = s_0$), this can be expanded to involve all the components highlighted in Equation 1.10, as well as the mass, and is expressed as:[121]

$$t(U_0, s_0) = \frac{(2m)^{\frac{1}{2}}}{E_s q}\left((U_0 + E_s q s_0)^{\frac{1}{2}} - U_0^{\frac{1}{2}}\right) + \frac{(2m)^{\frac{1}{2}}}{E_d q}\left(U_{\text{total}}^{\frac{1}{2}} - (U_0 + E_s q s_0)^{\frac{1}{2}}\right) + (2m)^{\frac{1}{2}}\frac{D}{2U_{\text{total}}^{\frac{1}{2}}}. \tag{1.12}$$

If an ion starts closer to the repeller plate, it has to travel further, but it will have gained more kinetic energy within the electric field. All of the ions will be further accelerated by the same amount within the extractor-ground region. The ion that has travelled further will eventually catch up with the ion that started closer to the extractor plate. The ions will coalesce at distance D away from the WM optics as they catch up with each other, as shown in Figure 1.9 **b)**. Determining where D exists depends on calculating the derivative of the ToF with respect to the distance between the repeller and extractor, s, being zero. This leads to the equation:[122]

$$D = 2s_0 k_0^{\frac{3}{2}}\left(1 - \frac{d}{s_0\left(k_0 + k_0^{\frac{1}{2}}\right)}\right), \quad \text{where} \quad k_0 = \frac{s_0 E_s + d E_d}{s_0 E_s}. \tag{1.13}$$

As shown in Figure 1.4 **b)**, s_0 is the distance halfway between the repeller and the extractor plates and also corresponds to the average position of the two ions shown as red and blue dots. It is possible to adjust the spacing between the electrodes (s_0 or d) as well as the ratio of the electric fields (E_s or E_d) to temporally focus the ions onto an microchannel plate (MCP) detector that is at position D. Given that most detectors and ion optic arrangements have fixed geometries and distances, tuning the electric field ratio (E_s/E_d) (*i.e.* the ratio of voltages applied to the repeller and extractor plates) is the only way of temporally focussing the ions.

Given that the greatest proportion of the flight time of the ion is in the field-free drift

region, $T(U_0, s_0)$ can be approximated as:

$$T(U_0, s_0) = T_D = (2m)^{\frac{1}{2}} \frac{D}{2(U_0 + qs_0E_s + qdE_d)^{\frac{1}{2}}}. \tag{1.14}$$

Assuming the initial kinetic energy, U_0, is zero, this allows the total time-of-flight to be simplified to the linear relationship:

$$T(0, s_0) \approx \alpha \left(\frac{m}{q}\right)^{\frac{1}{2}} + \beta, \quad \text{where} \quad \alpha = \frac{D}{2^{\frac{1}{2}}(s_0E_s + dE_d)^{\frac{1}{2}}}. \tag{1.15}$$

Here, β is an additional factor that accounts for the small delays caused by the electronics used to record the mass spectrum (*i.e.* the time it takes the ion to hit the detector and register as a signal).[123] The values of α and β are experimentally determined by assigning known peaks from the time-of-flight spectrum with a corresponding mass-to-charge ratio. A calibration curve connecting the time and the masses is produced, and allows spectra to be plotted using the mass-to-charge ratio (in almost all cases here, only singly charged ions are detected).

1.4 Spectroscopy of Molecules

One way to determine the structural properties of metal-ligand complexes and metal clusters is to measure their vibrational frequencies, as these provide information about bonds within a complex. The transitions between vibrational energy levels of molecules occur at frequencies that fall within the infrared (IR) region of the electromagnetic (EM) spectrum.[124] To understand the behaviour of these vibrations, a simple model is required to explain it.

1.4.1 Simple Harmonic Oscillator Model

Vibrational motion within a molecule can to a first approximation be described as a harmonic oscillator that obeys Hooke's Law.[125] Namely, an atom will experience a restorative force, $\overrightarrow{F}$, that is proportional to the displacement from the equilibrium position, x:

$$\overrightarrow{F} = -k_F \overrightarrow{x}, \tag{1.16}$$

resulting in it experiencing a harmonic potential:

$$V(x) = \frac{1}{2} k_F x^2. \tag{1.17}$$

Here, k_F is the force constant. In the case of molecules, the value of x can be replaced by $R - R_e$, where R is the displacement and R_e is the equilibrium position. By applying Newton's Second Law to a diatomic molecule with a reduced mass, μ, ($\mu = \frac{m_a m_b}{m_a + m_b}$), the force equation can be written as:[125]

$$\mu \frac{\mathrm{d}^2 x}{\mathrm{d}t^2} = -k_F x. \tag{1.18}$$

One solution to this second-order differential equation can be expressed as a periodic function:

$$x(t) = A \cos\left(\sqrt{\frac{k_F}{\mu}} t + \phi\right), \tag{1.19}$$

where A is the oscillation's amplitude and ϕ is the phase shift of the oscillation.[126] The component $\sqrt{\frac{k_F}{\mu}}$ is used to describe the vibrational frequency. If the molecular bond was to be weakened, this would result in a smaller force constant and a reduction in the vibrational frequency. Additionally, a reduction in the reduced mass would cause an increase in the vibrational frequency.

In order to fully describe a molecular vibration, a quantum description is required which involves solving the time-independent Schrödinger equation.[127] A Hamiltonian can be written that incorporates the harmonic oscillator's potential to describe the system:

$$\left[-\frac{\hbar^2}{2\mu}\frac{\partial^2}{\partial r^2} + \frac{1}{2} k_F x^2\right] \psi_\nu = E \psi_\nu, \tag{1.20}$$

where x is the displacement, ψ_ν is the vibrational wavefunction, and E is the energy of the system. The wavefunctions are described in the form of Gaussian functions and Hermite polynomials ($H_n(\beta x)$)[128, 129] that take the form:

$$\psi_n(x) = N_n \exp\left(\frac{-\beta^2 x^2}{2}\right) H_n(\beta x), \tag{1.21}$$

where $\beta = \sqrt{\frac{m\omega}{\hbar}}$ and the Hermite polynomial of degree n is described as:

$$H_n(x) = (-1)^n \exp\left(x^2\right) \frac{\mathrm{d}^n}{\mathrm{d}x^n} \exp\left(-x^2\right), \tag{1.22}$$

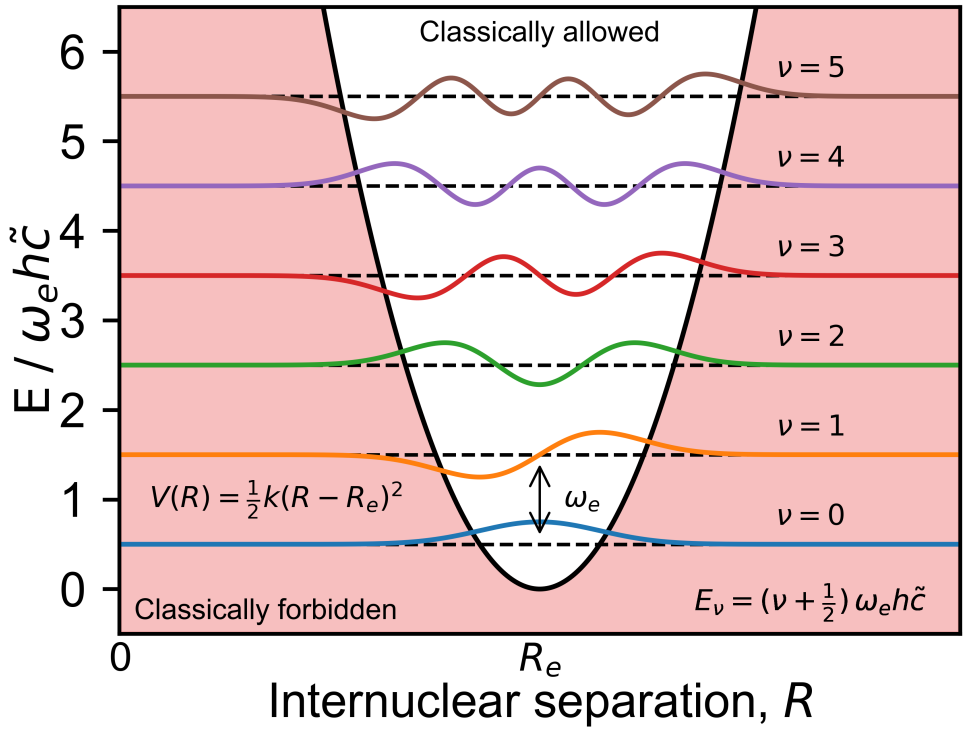

Figure 1.10: Harmonic oscillator potential energy diagram of a vibrational mode in a diatomic molecule. The oscillation is about the equilibrium distance, R_e. The vibrational levels and their associated wavefunctions are also displayed. Adapted from thesis of E. I. Brewer.[130]

Using the boundary conditions ($\psi_\nu = 0$ when $x = \pm\infty$), the values of the vibrational term, $\tilde{G}_\nu$, are equal to:

$$\tilde{G}_\nu = (\nu + \frac{1}{2})\,\omega_e \quad (\nu = 0, 1, 2, ...) \quad \text{where} \quad \omega_e = \frac{1}{2\pi\tilde{c}}\sqrt{\frac{k}{\mu}}, \tag{1.23}$$

where ν is the vibrational quantum number, ω_e is the vibrational constant in cm^{-1} (as shown in Figure 1.10),[130] and $\tilde{c}$ the speed of light in cms^{-1}.[131] Rather than adopting any energy that lies on the parabola that describes the harmonic motion in the classical model, the molecule's energy is quantised into vibrational levels in the quantum model. Molecules may be excited from lower vibrational levels into higher levels through absorbing photons that are resonant with the energy difference between the levels. Using the harmonic approximation, the gap between two adjacent vibrational energy levels is given by the equation:[131]

$$E = \omega_e h\tilde{c}. \tag{1.24}$$

The vibrational energy levels and their associated wavefunctions are provided in Figure 1.10.[130]

Not all molecular vibrations will be infrared (IR) active. In order for a transition between two vibrational levels, *i.e.* a lower state ν and an upper state ν', to be IR active, the gross selection rule states that the dipole moment must change during the vibration. The specific selection rule for harmonic oscillators states that transitions can occur only between adjacent energy levels ($\Delta\nu \pm 1$).[132] The transition dipole moment, $R_{\nu'\nu}$, is a vector property that encodes the selection rules.[133] $R_{\nu'\nu}$ is described as:

$$R_{\nu'\nu} = \int_{-\infty}^{\infty} \psi^*_{\nu'} \hat{\mu} \psi_\nu dq, \tag{1.25}$$

where $\hat{\mu}$ is the dipole moment operator (equal to $\sum_i -q_i \hat{r}_i$).[132] The transition's strength between two levels is proportional to the rate of absorption, which from the time dependent perturbation to the Schrödinger equation is proportional to $|R_{\nu'\nu}|^2$, and it is also dependent on the number of photons. A transition between two levels is forbidden when $R_{\nu'\nu} = 0$.

1.4.2 Accounting for Anharmonicity

The harmonic approximation is a good starting point to understand the behaviour of molecule vibrations, but it does not provide a realistic physical description of the system. Most importantly, when two atoms are pulled apart, the energy will not continue to increase as there will be a point where the molecule breaks apart (*i.e.* there will be a dissociation limit).[134] Accounting for this anharmonicity is therefore important when considering the energy levels of molecules.

One way of representing a more accurate potential energy surface is by using the Morse potential:[134]

$$V(x) = D_e(1 - \exp(-\alpha x))^2. \tag{1.26}$$

Here, D_e is the dissociation energy and α is a constant that represents the width of the well. x can be rewritten as $R - R_e$ to represent vibration about an equilibrium position R_e. The anharmonic potential is presented in Figure 1.11.

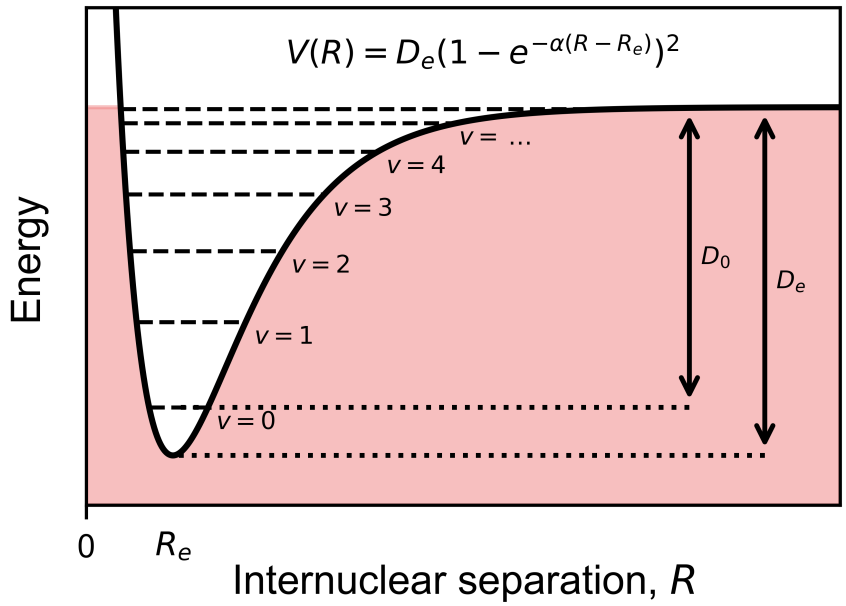

Figure 1.11: Anharmonic oscillator potential energy diagram of a vibrational mode in a diatomic molecule, modelled using the Morse potential. The oscillation is about the equilibrium distance, R_e. The vibrational levels are also displayed, which are converging towards the dissociation limit: D_0 relative to $\nu = 0$, or D_e relative to the bottom of the potential well. Adapted from thesis of E. I. Brewer.[130]

The energy levels within a quantum-mechanical Morse potential are described by:

$$\tilde{G}_\nu = \left(\nu + \frac{1}{2}\right)\omega_e - \left(\nu + \frac{1}{2}\right)^2 \omega_e x_e, \quad \text{where} \quad x_e = \frac{\omega_e}{4D_e}. \tag{1.27}$$

Here, ν is the vibrational quantum number, ω_e is the vibrational frequency seen previously. x_e is often referred to as the anharmonicity constant and is related to the dissociation energy. The energy levels are quantised, meaning that the energy required to dissociate the molecule can be recorded relative to the vibrational level $\nu = 0$ (D_0), or from the bottom of the potential (D_e). With the addition of the anharmonic term, which varies with the square of the vibrational quantum number, the spacing between the vibrational bands begins to decrease as the vibrational number increases until the dissociation limit is reached. In addition to the decreasing spacing between the levels, the anharmonicity causes a relaxation in the selection rules that were established from the harmonic oscillator (*i.e.* $\Delta\nu = \pm 1$ (± 2, 3, ... more weakly)).

Additional complexity can also be added to the transition between different vibrational

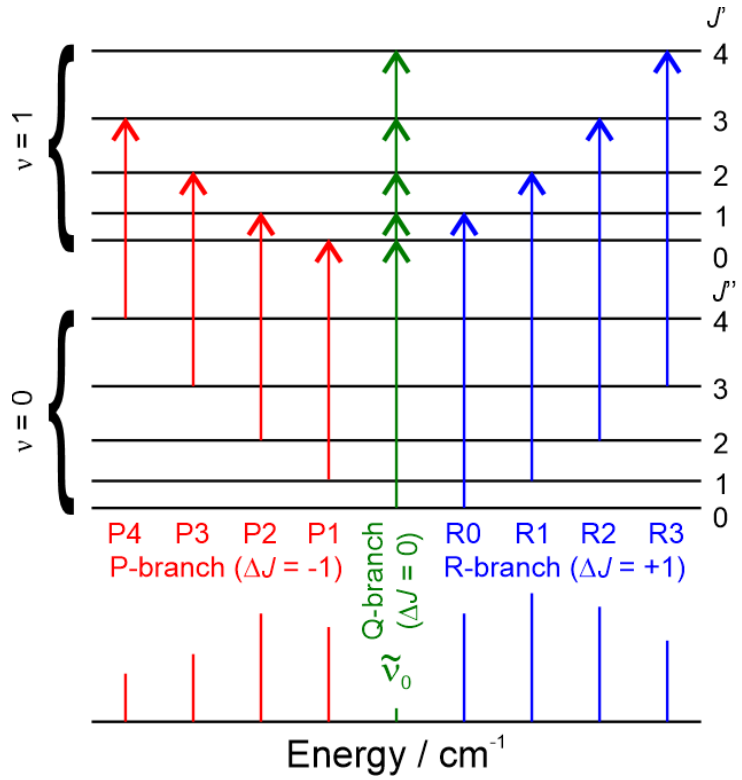

Figure 1.12: Diagram illustrating the energy levels that contribute towards the formation of rotational fine structure for the vibrational transition $\nu = 1 \leftarrow 0$. Red lines are for the P-branch ($\Delta J = -1$), and blue lines are for the R-branch ($\Delta J = +1$). The spacing between adjacent rotational levels for both vibrational level increases with increasing J. A Q-branch ($\Delta J = 0$) is shown in green, and is only allowed if the molecule has additional electronic and/or vibrational angular momentum about its axis.

---

levels by incorporating rotational levels. The rotational fine structure arises from changing the rotational quantum number, J, during a transition whilst conserving the angular momentum.[135] The eigenvalues, $\tilde{S}$, are the sum of the eigenvalues for the vibrational ($\tilde{G}_\nu$) and rotational ($\tilde{F}_J$) terms:

$$\begin{aligned}\tilde{S} &= \tilde{G}_\nu + \tilde{F}_J \\ &= \left(\nu + \frac{1}{2}\right)\omega_e - \left(\nu + \frac{1}{2}\right)^2 \omega_e x_e + \cdots + \tilde{B}_\nu J(J+1) - \tilde{D}_\nu J^2(J+1)^2,\end{aligned} \tag{1.28}$$

where $\tilde{B}_\nu$ and $\tilde{D}_\nu$ are the rotational and centrifugal constants, respectively. They both vary as a function of ν. Transitions are restricted to the same selection rules ($\Delta\nu = \pm 1, \Delta J = \pm 1$). If a molecule also has angular momentum about its axis, then transitions where $\Delta J = 0$ are also allowed (this can result in a very sharp feature at the vibrational

frequency, $\tilde{\nu}_0$, and is referred to as the Q-branch). As the rotational quantum number increases, the spacing between adjacent rotational levels increases. Therefore, the gap for $\Delta J = -1$ decreases (referred to as the P-branch) and $\Delta J = +1$ increases (referred to as the R-branch). Although the spectral features in the experimental spectra provided in this thesis do not possess fine structure, this technique of surveying all the rovibrational transitions in a molecule can be a useful calibration tool when calibrating the frequency of the light from the IR source (see Chapter 2).

1.4.3 Polyatomic Molecules

Diatomic molecules can be described using the simple model, with one vibrational frequency which is determined by the reduced mass and force constant. Larger molecules can be described using normal modes. A vibrational normal mode is a specific vibrational motion of a molecule in which every atom moves sinusoidally at a well-defined frequency (the normal mode frequency). The atoms move such that the centre of mass does not translate and there is zero net rotation. A molecule or complex will possess $3N$-6 (or $3N$-5 if linear) vibrational modes, where N is the number of atoms in the molecule or cluster.

Polyatomic molecules also have to obey the selection rules set out earlier. However, the transition dipole moment can change in any (or a combination) of the three axes: x, y, and z.[132] One of the following equations must be true:

$$R_{\nu'\nu(x)} = \int_{-\infty}^{\infty} \psi^*_{\nu'} \hat{\mu}_x \psi_\nu dx \neq 0, \tag{1.29}$$

$$R_{\nu'\nu(y)} = \int_{-\infty}^{\infty} \psi^*_{\nu'} \hat{\mu}_y \psi_\nu dy \neq 0, \tag{1.30}$$

$$R_{\nu'\nu(z)} = \int_{-\infty}^{\infty} \psi^*_{\nu'} \hat{\mu}_z \psi_\nu dz \neq 0. \tag{1.31}$$

The dipole moment operator ($\hat{\mu}_{xyz}$) in one axis is defined by:

$$\hat{\mu}_{xyz} = \Gamma_{\nu'} \otimes \Gamma_{\hat{\mu}_{xyz}} \otimes \Gamma_\nu, \tag{1.32}$$

where $\Gamma_{\nu'}$ is the symmetry of the vibrational excited state wavefunction ($\psi_{\nu'}$), $\Gamma_{\hat{\mu}_{xyz}}$ is the symmetry of the dipole moment operator, and Γ_ν is the symmetry of the vibrational

ground-state wavefunction (ψ_ν). The vibrational ground state ($\nu = 0$) always transforms as the totally symmetric irreducible representation (TSIR), meaning Γ_ν is the identity representation in the transition dipole moment expression.[126] The first vibrational excited state wavefunction ($\psi_{\nu'=1}$) always transforms as the same symmetry associated with the normal mode.[126]

1.4.4 Spectral Widths

The lower limit of the spectral line width is inherently set by the instrumentation (*i.e.* the line width of the light source that is used). Additional factors can then cause the peaks to broaden further. These include pressure broadening (spectral lines are broadened due to collisions between atoms or molecules in a gas),[136] power broadening (spectral line width of a transition increases with the intensity of the driving electromagnetic field),[137] and Doppler broadening (where a Doppler effect is induced by the thermal motion of atoms or molecules).[138] Furthermore, lifetime broadening plays an important role. This relates to the lifetime of the excited state involved in a transition. The Heisenberg uncertainty principle states that:

$$\Delta E \Delta t \geq \frac{\hbar}{2}, \tag{1.33}$$

where ΔE is the change in energy and Δt is the change in time. In other words, if the lifetime of the states involved is short, this will result in a larger uncertainty in the energy, or in this case the vibrational frequency, which is manifested as a broader spectral feature.[133, 139, 140]

1.5 Experimental Spectroscopic Techniques

This section will cover how conventional IR spectroscopy is conducted and how it utilises the principles outlined in the previous section. It will cover how a spectrum is recorded and why the limitations of this technique require alternative methods to be applied when studying species in the gas phase, such as metal clusters and metal ion-ligand complexes.

1.5.1 Absorbance Infrared Spectroscopy

IR spectroscopy for species in the solid and liquid phases is typically conducted by measuring how much IR light is transmitted through a sample at a specific frequency $\tilde{\nu}$.

This is quantified by the intensity of light before ($I_0(\tilde{\nu})$) and after ($I(\tilde{\nu})$) a sample. The absorbance A is calculated from the two intensity values using the Beer-Lambert law:

$$A = \log_{10}\left[\frac{I_0(\tilde{\nu})}{I(\tilde{\nu})}\right] = \epsilon c l. \tag{1.34}$$

Here, ϵ is the molar extinction coefficient (measured in $\mathrm{dm^3\,mol^{-1}\,cm^{-1}}$), c is the concentration (measured in $\mathrm{mol\,dm^{-3}}$), and l is the pathlength (measured in cm).[141] In order for this method of recording IR spectra to be effective though, a high number density of molecules is required.[142, 143] In the gas phase, this can prove to be difficult without the use of either very long pathlengths (order of kilometres), or cavity enhanced techniques where light is passed through a sample multiple times.[144–146] Additionally, clustering sources do not produce a large enough number of metal-ligand/metal cluster species to allow the change in intensity to be measured directly. Instead, rather than directly measuring the change in absorption, indirect techniques can be used to monitor the effect of incoming light on gaseous species, in a method known as action spectroscopy.[147–149]

1.5.2 Action Spectroscopy

Action spectroscopy covers a range of different techniques, such as infrared-ultraviolet (IR-UV) two-colour ionisation,[42] resonance enhanced multiphoton ionisation (REMPI),[150] infrared photodissociation (IRPD),[151] and infrared multiphoton dissociation (IR-MPD) spectroscopy.[152] Each of these techniques utilise the sensitivity of mass-spectrometry, which in theory and practice can detect a single ion, in order to perform spectroscopy. An additional benefit of using mass spectrometry is that, unlike direct absorption, which can be complicated by multiple species all absorbing light at a specific wavelength, the changes in an individual feature in the mass spectrum can be monitored and isolated. It can also be compared with the other spectral features to monitor how one peak changes relative to the others.

The work presented in this thesis was completed using IRPD and IR-MPD. The principle of these techniques relies on monitoring the loss of ligands from a metal ion/ metal cluster-ligand complex as a function of incoming IR frequency. The principle of IRPD is illustrated in Figure 1.13. A mass spectrum containing the complexes of interest is produced, with no IR radiation interacting with the species. Depending on whether

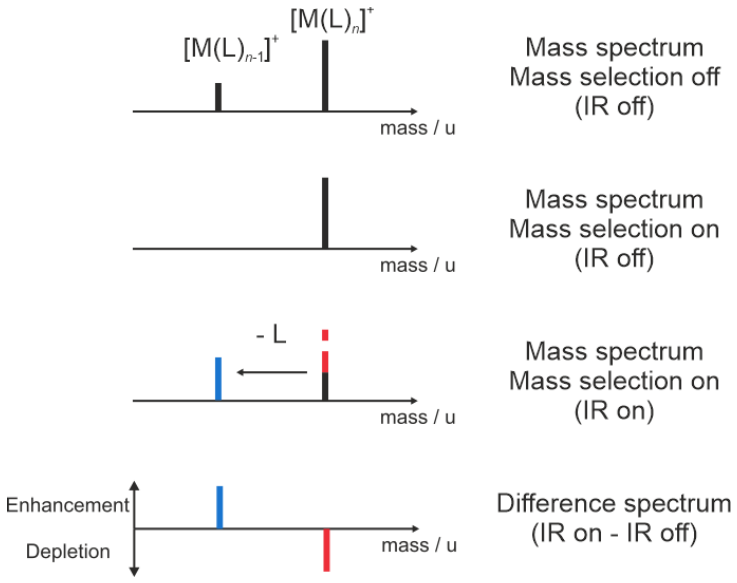

Figure 1.13: Illustration of the principle of infrared photodissociation (IRPD) action spectroscopy. A mass spectrum contain multiple species is produced with no IR light. After mass selecting, the gas-phase samples are irradiated with IR light which causes a parent species to fragment, producing a daughter species. A difference spectrum is recorded, and the change in the peak intensities can be monitored as a function of IR frequency.

---

mass-selectivity is available, a specific peak of interest, referred to as the parent ion, can be selected so that it is the only peak in the spectrum. This produces the IR off spectrum. A pulse of IR radiation then interacts with the molecular beam and can induce photodissociation. This will cause the intensity of the parent ion to decrease, with new peaks appearing at lower masses that correspond to the daughter species that form following the photodissociation. This new spectrum is the IR on spectrum. A difference spectrum can be produced by subtracting the IR off spectrum from the IR on spectrum, and it will show which peaks are enhancing (positive features) and which are depleting (negative features). The change in either the enhancement or depletion can be monitored as a function of IR wavelength, producing an IR action spectrum for the species of interest. Monitoring the enhancement of the daughter species is especially useful when mass selectivity is applied, as the measurement will be against a zero-signal background; providing a greater signal-to-noise ratio (S/N).

The infrared action spectrum will indicate the frequencies that the chromophores (*i.e.*

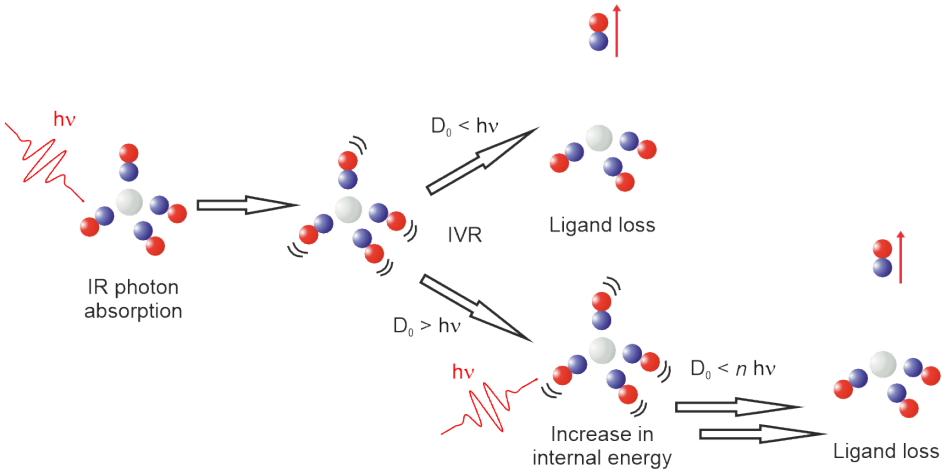

Figure 1.14: Illustration of IR-(M)PD. A complex of $[M(NO)_4]^+$ absorbs a photon of energy hν, leading to intramolecular vibrational energy redistribution. If the photon energy, hν, is great enough to overcome the M-NO bond dissociation energy, D_0, an NO ligand will be lost. If the energy is not great enough ($D_0 >$ hν), the complexes internal energy increases. The chromophores within the complex can then absorb another photon. Once the energy of all the absorbed photons, n hν, is greater than D_0, the ligand can dissociated from the complex.

---

the normal vibrational modes of the cluster/ligands) within the complex absorb. The energy absorbed by the chromophore has to be transferred to the metal-ligand dissociation mode. This is achieved by intramolecular vibrational energy redistribution (IVR). The process is illustrated by the top pathway in Figure 1.14. The types of system that are studied using IRPD usually have weakly-bound ligands attached to the complex (*i.e.* an Ar atom). This means that only a single photon is required to induce photodissociation because the energy required to dissociate the ligand is less than the photon energy. It is important as well that the photon energy is tunable in order to observe the fragment when the IR photon frequency is resonant with the mode that leads to dissociation. Systems that involve a single metal ion solvated with multiple ligands (*i.e.* $[M(L)_n]^+$) are studied using IRPD. For systems that have ligands that are more tightly bound, IR-MPD needs to be applied. This requires other light sources to provide a high enough photon flux, such as an IR free-electron laser (FEL). This will be discussed in the methods chapter (Chapter 2).

When multiple photons are required to dissociate the metal-ligand bond, the energy from the $\nu = 1$ level must be redistributed *via* IVR to other modes before another photon can be absorbed; this is because of the anharmonic bottleneck.[149] As a result of the spacing between vibrational energy levels decreasing when anharmonicity is incorporated into molecular vibration, photons resonant with the $\nu = 0$ to $\nu = 1$ transition cannot simultaneously drive the $\nu = 1$ to $\nu = 2$ transition. This can be applied to any other transition within the chromophore, such that anharmonicity causes the wavelength of a single photon to be resonant with only very few transitions. In order to overcome this, energy is redistributed around the other modes within the complex through IVR. This means that the chromophore relaxes back to the $\nu = 0$ vibrational level and can absorb a second photon. This can be repeated until the additional energy from the multiple photons is enough to overcome the dissociation threshold, as illustrated by the bottom pathway in Figure 1.14. Additionally, increasing the size of a metal cluster or metal ion-ligand complex also increases the number of vibrational modes, making it easier to transfer energy *via* IVR, as it increases the vibrational density of states and the number of near-resonant couplings, providing more pathways for energy flow. This in part can explain why larger complexes are able to dissociate ligands more easily, along with the fact that, in larger complexes, the ligands tend to be less tightly bound. With regard to metal clusters, the cluster acts as a heat bath due to the large number of internal vibrational modes, and the chromophore can absorb multiple photons.

Furthermore, absorption of multiple photons can cause broadening of spectral features by applying the lifetime broadening principle specified in Equation 1.33. When the complex absorbs multiple photons through multiple cycles of absorption and IVR, the internal energy is increased and more bath vibrational background states, within a so-called quasi-continuum, are accessible.[147, 153] With more levels available, IVR can occur more rapidly to remove the population from the excited state into these states. In this region, absorptions that are resonant with the fundamental transition can occur and can lead to dissociation. By applying the uncertainty principle, the shortening of the vibrational lifetimes can result in a broadening of the absorption lines.

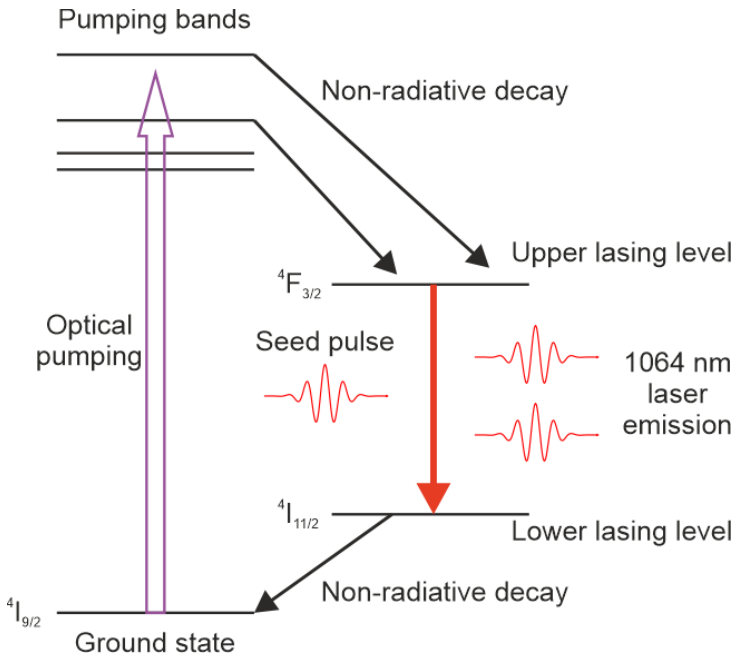

Figure 1.15: Schematic of a four-level laser system which utilises the energy levels of the Nd atoms in a Nd:YAG rod. Lasing occurs following stimulated emission from a 1064 nm seed pulse. Optical pumping is initiated using a UV-Vis flashlamp.

1.6 Light Sources

1.6.1 Lasers

In order to ablate the metal targets, as well as perform high resolution spectroscopy, lasers are required. First demonstrated in 1960,[154] the light that is produced from a laser has a number of desirable properties such as being coherent, monochromatic, and highly directional.[155] All lasers rely on the principle of stimulated emission of radiation; this occurs when an excited state species relaxes back down to the ground state following the interaction of a photon. This also results in the formation of a second photon which possesses the same properties as the first, as shown by the equation:

$$\mathrm{A}^* + h\nu \rightarrow \mathrm{A} + 2h\nu. \tag{1.35}$$

Figure 1.15 provides an illustration of a four-level system, such as that used in a Nd:YAG laser.[156] The ground level is pumped using broadband light from a flashlamp, or in some cases a secondary laser, before fast relaxation *via* non-radiative decay into the upper lasing band occurs; providing the necessary population inversion ($N_{\mathrm{upper}} > N_{\mathrm{lower}}$).[157]

Once in this lasing level, a photon interacts with the electrons and induces stimulated emission. For Nd:YAG, the spacing between the upper and lower lasing levels produces light with an emission wavelength of 1064 nm. The rate of the non-radiative decay must be faster than the rate of stimulated emission in order to produce the required population inversion necessary for lasing to occur.[155, 157] The initial photon needed to induce lasing can come from spontaneous emission or from a seed photon from another laser. In order to increase the photon density, the lasing material is positioned inside of a cavity with two high reflective mirrors at either end. This creates a positive feedback loop, where photons previously produced from stimulated emission can then be used to induce further lasing.

The Nd:YAG lasers used in this thesis operate at either 10 or 20 Hz, and produce light pulses which have nanosecond (ns) time duration. Pulsed light can be produced from a laser by Q-switching; the procedure of changing the reflectivity of one of the mirrors in the cavity using a Kerr cell.[158] By making the exit mirror unreflective (*i.e.* it is able to transmit light), the light produced from the stimulated emission can escape the cavity. This allows the population inversion caused by the flashlamps to build. When the Q-switch is activated, the mirror becomes reflective again and the cavity is restored. This allows for a sudden increase in the amount of stimulated emission and the production of a temporally short laser pulse.

1.6.2 Generating Different Frequencies Using Non-Linear Optics

Often, the wavelength of the light that is produced from a laser system needs to be tuned, depending on the application. Nd:YAG lasers can be used to pump adjustable laser systems such as optical parametric oscillator/ optical parametric amplifiers (OPO/OPA).[159] These systems rely on the use of non-linear optics in order to generate different (IR) frequencies *via* non-linear three wave mixing processes known as optical parametric generation (OPG) and difference-frequency generation (DFG).[160, 161] Before understanding these processes, it is important to understand how a photon can interact with a crystalline material.[161] When a photon, referred to as the pump (p), passes through a crystalline lattice and is not absorbed, it can induce oscillations in the valence electrons. This gen-

erates a moving dipole within the crystal that can be modelled by a time-dependent polarisation density $\overrightarrow{P}(t)$. This can be expressed using the Taylor expansion:

$$\overrightarrow{P}(t) = \epsilon_0(\chi^{(1)}\overrightarrow{E}(t) + \chi^{(2)}\overrightarrow{E}^2(t) + \chi^{(3)}\overrightarrow{E}^3(t) + ...), \tag{1.36}$$

where ϵ_0 is the permittivity of free space, $\overrightarrow{E}^n$ is the incident electric field, and χ^n is the electric susceptibility of nth-order of the crystal. The polarisation density generates an electric field, defined as:

$$\nabla^2\overrightarrow{E} - \frac{n^2}{c^2}\frac{\partial^2}{\partial t^2}\overrightarrow{E} = \frac{1}{\epsilon_0 c^2}\frac{\partial^2}{\partial t^2}\overrightarrow{P}, \tag{1.37}$$

where n is the order of the electric field, c is the speed of light, and t is time.[162] The second-order differential equation implies that only the accelerating polarisation density generates the electric field, meaning the Taylor expansion can be truncated at the χ^2 term and approximated as:

$$\overrightarrow{P}^{(2)}(t) = \epsilon_0\chi^{(2)}\overrightarrow{E}^2(t). \tag{1.38}$$

The pump frequency can be related to two other frequencies that correspond to waves that arise from the non-linear polarisation. These are known as the signal (s) and the idler (i), and are related to the pump using the law of energy conservation:

$$\omega_p = \omega_s + \omega_i, \tag{1.39}$$

$$\text{and} \quad \omega_p > \omega_s > \omega_i. \tag{1.40}$$

We assume that the electric field can be described using two frequency components:

$$\overrightarrow{E}(t) = E_s\cos(\omega_s t) + E_i\cos(\omega_i t), \tag{1.41}$$

this will lead to the second-order term $\overrightarrow{P}^{(2)}$ taking the form:

$$\overrightarrow{P}^{(2)} \propto (E_s\cos(\omega_s t) + E_i\cos(\omega_i t))^2. \tag{1.42}$$

By expanding the expression and applying trigonometric identities, $\overrightarrow{P}^{(2)}$ can be expressed as:

$$\overrightarrow{P}^{(2)}(t) = \varepsilon_0\chi^{(2)}\left[\frac{E_s^2}{2} + \frac{E_i^2}{2} + \frac{E_s^2}{2}\cos(2\omega_s t) + \frac{E_i^2}{2}\cos(2\omega_i t) + E_s E_i\cos((\omega_s + \omega_i)t) + E_1 E_2\cos((\omega_s - \omega_i)t)\right]. \tag{1.43}$$

This expression can show the different non-linear processes that occur: second harmonic generation (SHG, 2ω, shown in blue), sum frequency generation (SFG, $\omega_s + \omega_i$, shown in green) and difference frequency generation (DFG, $\omega_s - \omega_i$, shown in orange).[159, 161] There is also an additional term in red which is the optical rectification. This does not possess a frequency component, as it originates from second-order nonlinear polarisation $\overrightarrow{P}^{(2)}$ where the difference-frequency contribution produces a quasi-static (DC-like) polarisation rather than an oscillatory response.[161, 163] Depending on the process required, different types of nonlinear optic (*i.e.* different crystalline materials) should be used.

The wavelength of the signal and the idler are determined by changing the incident angle of the light with the non-linear crystal. This is typically done by rotating the crystals with respect to the polarisation of the incident pulse using motors. This is done to satisfy phase matching requirements, based on both energy (angular frequency, ω) and momentum (or wavevector, k) conservation:

$$n_p \frac{\omega_p}{c} = n_s \frac{\omega_s}{c} + n_i \frac{\omega_i}{c}, \tag{1.44}$$

$$k_p = k_s + k_i. \tag{1.45}$$

The types of crystal used in non-linear generation of light are birefringent, meaning that changing the angle of incident light changes the refractive index n, experienced by the light polarised in that plane.

Frequency doubling is required to convert 1064 nm light from a Nd:YAG laser system to 532 nm light. This light can be used for laser ablation, and it can also be used as a pump in other non-linear processes. Additionally, these processes are important in optical parametric generation, where a pump beam is used to generate two new photons, a signal and an idler, that have the desired frequencies. This can be applied to optical parametric oscillators, where one of the frequencies is produced and resonates within a cavity, as well as optical parametric amplifiers, where two photons, a weak signal and a strong pump, interact within a non-linear crystal to amplify the signal wave by generating a matching idler frequency. Specific details about the OPO/OPA system used in the work presented are provided in Chapter 2.

1.7 Computational Methods

The assignment of spectral features to the experimental IR spectra can be helped by using computational techniques. These can deduce the vibrational frequencies of energetically low-lying structures that may be present within the molecular beam. This requires methods that can calculate energies, find low-energy structures, and produce vibrational frequencies based upon the force constants of the molecules within the complexes.

1.7.1 Solving the Schrödinger Equation

In order to calculate ground state structures of molecules and complexes, quantum mechanical approaches are required; namely, solutions to the time-independent Schrödinger equation:

$$\hat{H}\Psi(\mathbf{r}) = E\Psi(\mathbf{r}), \tag{1.46}$$

where $\Psi(r)$ is the wavefunction that describes the state of the system (in this case, its spatial distribution), $\hat{H}$ is the Hamiltonian operator and E is the energy of the system.[24] The Hamiltonian operator is equal to:

$$-\frac{\hbar^2}{2m}\nabla^2 + V(\mathbf{r}), \tag{1.47}$$

and contains the total kinetic ($-\frac{\hbar^2}{2m}\nabla^2$, also expressed as T) and potential energies ($V(\mathbf{r})$) of the particles within the quantum system. These terms can be broken down further and expressed as follows:

$$\hat{H} = \hat{T}_e + \hat{T}_n + \hat{V}_{ee} + \hat{V}_{en} + \hat{V}_{nn}, \tag{1.48}$$

where:

- $\hat{T}_e$ is the electron kinetic energy,
- $\hat{T}_n$ is the nuclei kinetic energy,
- $\hat{V}_{ee}$ is the electron-electron repulsion energy,
- $\hat{V}_{en}$ is the electron-nuclei attraction energy, also known as the external potential, and,

- $\hat{V}_{nn}$ is the nuclei-nuclei repulsion energy.

Apart from a number of very simple cases, solving the Schrödinger equation analytically is not possible.[164] As a result of this, approximations are required to solve the equation. Among them is the Born-Oppenheimer approximation, which allows separation of the nuclear and electronic degrees of freedom.[165] This allows the nuclei-nuclei repulsive force, $\hat{V}_{nn}$, to be calculated once based on their clamped positions and reduces $\hat{T}_n$ to zero since the nuclei are not moving. The other terms involving electrons can be compiled into an electronic Hamiltonian operator, $\hat{H}_e$, which needs to be solved separately.

1.7.2 Hartree-Fock Theory

One method of approximating the solution to the electronic Schrödinger equation for atoms and molecules is the Hartree-Fock theory.[24, 165–168] This relies on calculating the multi-electron wavefunction, $\Psi(\mathbf{r}_1, \mathbf{r}_2, ..., \mathbf{r}_N)$, as the product of N one-electron wavefunctions:

$$\Psi(\mathbf{r}_1, \mathbf{r}_2, ..., \mathbf{r}_N) = \psi_1(\mathbf{r}_1)\psi_2(\mathbf{r}_2)...\psi_N(\mathbf{r}_N). \tag{1.49}$$

However, this simple Hartree product is not a good representation of the electrons because it does not account for the electron's spin. The simple product does not obey the Pauli principle (the wavefunction must be antisymmetric with respect to interchange of a pair of electrons) nor the Pauli exclusion principle (two electrons of the same spin cannot exist in the same orbital).[165, 169] Therefore, in order to calculate the many-electron wavefunction, a Slater determinant is built from one-electron spin orbitals:

$$\Psi(\mathbf{r}_1, \mathbf{r}_2, ..., \mathbf{r}_N) = \frac{1}{\sqrt{N!}} \begin{vmatrix} \psi_1(\mathbf{r}_1) & \cdots & \psi_N(\mathbf{r}_1) \\ \vdots & \ddots & \vdots \\ \psi_1(\mathbf{r}_N) & \cdots & \psi_N(\mathbf{r}_N) \end{vmatrix}. \tag{1.50}$$

This obeys the Pauli exclusion principle, as the written wavefunction is antisymmetric under exchange of electrons, and ensures that no two electrons have the same set of quantum numbers.[170, 171]

The energy of each one-electron spin orbital is calculated using the Hartree-Fock equation:

$$\hat{f}_i\psi_i = \epsilon_i\psi_i, \tag{1.51}$$

where the one-electron Fock operator, $\hat{f}_1$ is equal to:

$$\hat{f}_1 = \hat{h}_1 + \sum_{j}^{occ} \left[\hat{J}_j(1) - \hat{K}_j(1) \right], \tag{1.52}$$

where $\hat{h}_1$ is the one-electron Hamiltonian operator for kinetic and nuclear attraction, $\hat{J}_j$ is the Coulomb operator which describes the average repulsion of electron 1 from electron j, and $\hat{K}_j$ is the exchange operator, which accounts for the quantum mechanical exchange interaction arising from the antisymmetry of the wavefunction, contributing only between same-spin electrons.[165] This calculation is only performed over orbitals that are occupied (occ).

In order to determine the best spin-orbitals to construct the full Slater determinant, an optimisation procedure, known as the self-consistent field (SCF) method, is performed.[168, 169, 172] First, a basis set containing basis functions, χ_k, is chosen. Basis functions are atom-centred mathematical functions that represent atomic orbitals. These functions are typically Gaussian fucnctions because they make the calculations (evaluating integrals) tractable and efficient, while still being flexible enough to approximate true atomic orbitals.[173] The basis sets can vary in how they describe the orbitals, such as with additional descriptors that account for polarisation and diffuseness.[174] These can help to make the described electron density more accurate.

Generally, a large basis set will provide a chemically more accurate result but will be more computationally expensive.[165, 175] In the cases where the core electrons are not involved in bonding (say, for atoms with larger atomic numbers), these electrons can be approximated using an effective core potential (ECP).[176] The use of an ECP reduces the computational cost as the interactions of these electrons do not need to be explicitly incorporated into the calculations. Other basis sets can incorporate other functions that can describe other features, such as relativity.[177]

In addition to the basis set, an overlap matrix, S_{ij}, is calculated where:

$$S_{ij} = \langle \chi_i | \chi_j \rangle = \int \chi_i^*(\mathbf{r}) \chi_j(\mathbf{r}) d^3\mathbf{r}. \tag{1.53}$$

Then, initial guesses are made for the expansion coefficients, c_{kj}, which are used with the basis functions to create linear combinations of atomic orbitals (LCAO):[105, 127]

$$\psi_i = \sum_{k=1}^{m} c_{kj}\chi_k. \tag{1.54}$$

A Fock matrix, $\mathbf{F}$, is built, with each element being the Fock operator for electrons i and j. The Fock matrix is used to solve the equation:

$$\mathbf{Fc} = \mathbf{Sc}\epsilon, \tag{1.55}$$

in order to generate new coefficients, $\mathbf{c}$, and eigenvalues, ϵ. These are used to calculate new spin-orbitals. This procedure of producing the Fock matrix and solving the equations is repeated until the energies of the spin-orbitals have converged within user defined parameters. These orbitals are then used to produce the Slater determinant, from which an energy for the entire multi-body wavefunction can be determined.

Hartree-Fock theory obeys the variational principle, namely:

$$E = \frac{\langle\psi|\,\hat{H}\,|\psi\rangle}{\langle\psi|\psi\rangle} \geq E_0, \tag{1.56}$$

where E is the energy of a "trial" wavefunction, and E_0 is the energy of the true ground state.[105, 165] This states that the wavefunctions that are used to describe the system will produce an energy that will be either greater than or equal to the true energy (*i.e.* as the wavefunction describing the system becomes more accurate, the system energy will converge towards the true value from above).

This method of solving the electronic Schrödinger equation produces solutions that are close to the true electronic energy. However, whilst the calculations account for electron exchange (interaction of electrons with the same spin), the Hartree-Fock method is a mean-field approach, where the method solves equations for each electron moving in the mean-field of all other electrons. The correlation energy is defined as:

$$E_C = E_{\text{exact}} - E_{HF}. \tag{1.57}$$

This means Hartree-Fock does not fully describe the electron correlation; the interaction of an electron with other electrons. As a result of Hartree–Fock intrinsically not incorporating this component, it cannot provide greater chemical accuracy and an alternative

way of calculating the correlation energy in order to produce values that are closer to the true value is required, with common approaches including perturbative expansions such as Møller–Plesset (MP) theory,[178] variational treatments like Configuration Interaction (CI),[179] or more sophisticated coupled cluster and multireference methods, such as Complete Active Space Self Consistent Field (CASSCF).[180]

1.7.3 Density Functional Theory

Instead of using *ab initio* methods such as Hartree-Fock which require an explicit wavefunction, semi-empirical approaches can be utilised. One such method is density functional theory (DFT) which relies on using the total electron density, $\rho(\mathbf{r})$, of a system.[181, 182] It is based on the Fermi-Thomas model which showed that atomic energies can be provided in terms of $\rho(\mathbf{r})$.[183, 184] This approach has advantages over *ab initio* methods as the electron density is a function of three coordinates (x, y, z), rather than $3n$ coordinates for n electrons, making it much easier to calculate. The theory was developed with the addition of the Hohenberg-Kohn Theorems which proves that there is a one-to-one invertible mapping between the external potential, V_{ext}, with $\rho(\mathbf{r})$.[172, 185] This means that the energy of the system can be formulated as an electron density functional, the ground-state electron density $\rho(\mathbf{r})$ determines all ground-state properties, and that, by using the variational principle, there exists a universal energy functional, $E[\rho(\mathbf{r})]$, which reaches its minimum at the true ground-state density.

This was developed further by the Kohn-Sham equations, which showed that the electron density can be connected to two different external potentials.[186] By calculating a ground-state density of non-interacting electrons in an effective potential, ν_{eff}, which is computationally manageable, this density can be used to calculate the energy of the system by the true external potential, ν_{ext}, as illustrated in Figure 1.16. The kinetic energy functional of the system is unknown, so it is calculated using the one-electron Kohn-Sham equation:

$$\left[-\frac{1}{2}\nabla^2 + \nu_{eff}\right]\psi_i(\mathbf{r}) = \epsilon_i\psi_i(\mathbf{r}), \tag{1.58}$$

with an effective potential ν_{eff} that incorporates the electron-electron potential, ν_{ee}, the external potential, ν_{ext}, and the exchange-correlation potential, ν_{xc}.[186] The values for ν_{eff} depend on ψ_i, so they need to be solved independently in a way similar to what was

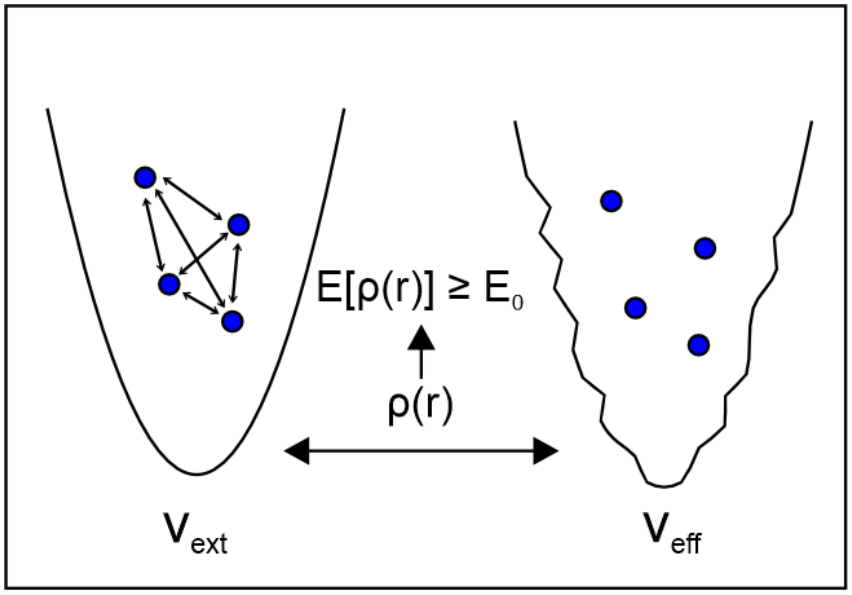

Figure 1.16: Illustration of how the Kohn-Sham equations can be used to generate an effective potential, ν_{eff}, with non-interacting electrons which has the same electron density, $\rho(\mathbf{r})$, as the true external potential, ν_{ext}.

---

described for Hartree-Fock theory. The initial guesses for the Kohn-Sham orbitals are generated from a linear combination of basis functions and coefficients, before iteratively being improved through the Kohn-Sham equation until their energies converge. These Kohn-Sham orbitals are then used to calculate the energy of the system in the effective potential.

The exact ground-state energy of the Kohn-Sham system, E_{KS}, of an n-electron system can be written as the sum of multiple energies that all depend on the electron density, $\rho(\mathbf{r})$:

$$E_{KS}[\rho(\mathbf{r})] = T[\rho(\mathbf{r})] + E_{\text{ext}}[\rho(\mathbf{r})] + E_{ee}[\rho(\mathbf{r})] + E_{xc}[\rho(\mathbf{r})], \tag{1.59}$$

where:

- $T[\rho(\mathbf{r})]$ is the kinetic energy of the non-interacting electrons,
- $E_{ext}[\rho(\mathbf{r})]$ is energy due to the external potential,
- $E_{ee}[\rho(\mathbf{r})]$ is the Coulomb self interaction of electron density (*i.e.* electron-electron repulsion), and,

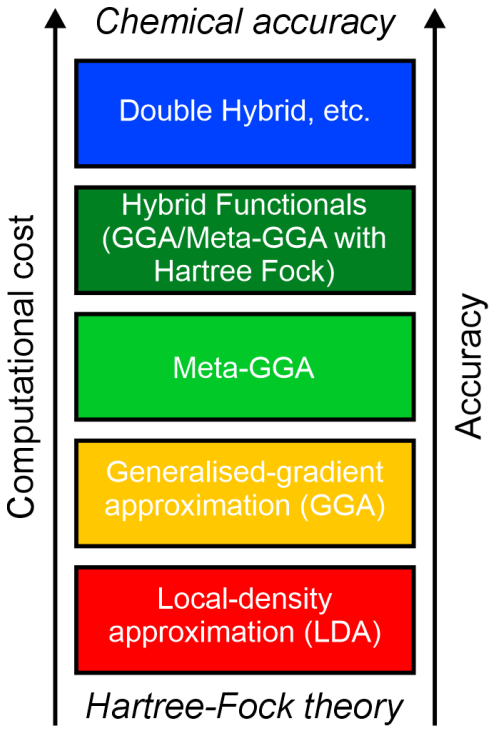

Figure 1.17: The Jacob's ladder illustration of exchange-correlation functionals, with the simplest local density approximation (LDA) at the bottom, and the double hybrid functional at the top. As the rungs of the ladder get higher, the accuracy of the calculation increases, but with greater computational cost. Adapted from Perdew *et al.*.[189]

- $E_{xc}[\rho(\mathbf{r})]$ is the exchange-correlation energy.

Unlike Hartree-Fock, DFT can account for electron correlation with the addition of the exchange-correlation energy, $E_{xc}[\rho(\mathbf{r})]$.[186, 187] However, it, as well as the exchange-correlation potential, $\nu_{xc} = \frac{\partial E_{xc}[\rho]}{\partial \rho}$, is unknown and needs to be approximated. In order to do this, an exchange-correlation functional must be used.[188]

There are many different exchange-correlation functionals that vary in the way in which they approximate the behaviour of the electron density. They can be categorised and ordered in a Jacob's ladder model, as shown in Figure 1.17.[189] The greater the complexity of the functional, the closer the calculation will get to chemical accuracy, but this will also increase the computational cost. The simplest functionals rely on local density approximation (LDA, *i.e.* the energy only depends on the electron density value at one point), and treat the electron density as a uniform electron gas.[174, 190] They can work well for metals, but do not provide accurate predictions for other systems because of the

exchange being underestimated and the correlation being overestimated. Generalised-gradient approximation (GGA) and meta-GGA functionals improve accuracy by adding how the local and longer-range electron density gradients vary.[187, 189, 190] Meta-GGAs also incorporate second order differentials and orbital angular momentum. Beyond that, hybrid and double-hybrid functionals incorporate some Hartree-Fock theory to provide a better description of the exchange energy, whilst still using DFT to calculate the correlation energy.[175, 187, 188, 191]

1.7.4 Using DFT to Predict Physical Properties

The energies of computed structures that reside on a potential energy surface can be calculated using density functional theory. In order to survey the minima or transition states of these potential energy surfaces, geometry optimisation algorithms need to be applied to adjust the structures by taking a number of steps along the surface until their energies are minimised.[24] The Taylor-expanded PES around a local minimum, $\mathbf{r}_0$ is defined as:

$$V(\mathbf{r}) = V(\mathbf{r}_0) + \sum_k \left.\frac{\partial V}{\partial x_k}\right|_{\mathbf{r}_0} (x_k - x_k^0) + \frac{1}{2}\sum_j \sum_k (x_j - x_j^0) \left.\frac{\partial^2 V}{\partial x_j \partial x_k}\right|_{\mathbf{r}_0} (x_k - x_k^0) + \dots \quad (1.60)$$

The component $\frac{\partial^2 V}{\partial x_j \partial x_k}$ is called the Hessian matrix, H'_{jk},[192] and provides information about stationary points. Some optimisation algorithms rely on line searches using the potential energy surface, such as the steepest gradient method.[24] This first-order approximation method involves calculating the PES gradient following the displacement of some of the atoms in the complex. This will be followed by a step in the opposite direction to the increasing gradient, which will lead to convergence at the minima where the gradient $\frac{\mathrm{d}V}{\mathrm{d}\mathbf{r}}$ is zero.[193] Other methods, such as the Newton-Rhapson method, utilise the second derivative of the Taylor expansion of the PES which confirms whether the stationary point on which the algorithm converged is a minimum ($\frac{\mathrm{d}^2 V}{\mathrm{d}\mathbf{r}^2} < 0$). This method is able to converge on the minimum structure more quickly than the steepest gradient method.[24] Figure 1.18 illustrates an optimisation procedure, with each step shown by a blue dot.

In addition to calculating the minima along the potential energy surface, calculations are also performed to find the turning points that correspond to transition states. Here,

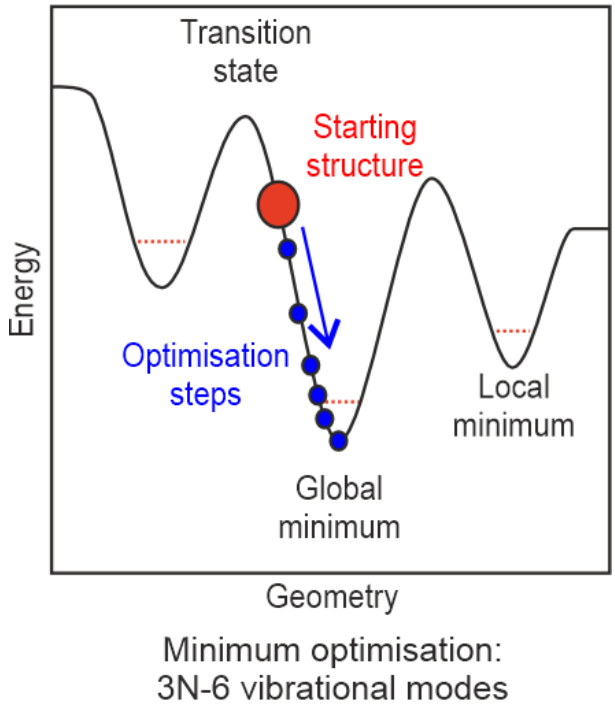

Figure 1.18: The process of minimum geometry optimisations.The blue circles indicate the steps taken from the starting structure (red circle). In this case, the arrow is pointing in the direction that the structure will move on the potential energy surface as the energy is minimised. The figure follows the change in geometry along one vibrational mode, with the gradient being minimised for all modes. The energy is also minimised for all vibrational modes. For transition state optimisations, one (reactive) mode will remain.

---

the idea is to find a stationary point that is a maximum ($\frac{\mathrm{d}^2V}{\mathrm{d}\mathbf{r}^2} > 0$) for one of the vibrational modes. The displacement of this mode will be along the reaction coordinate in order to transfer between the local minima on either side of the transition state. In order to properly survey the maxima of the PES, the starting structures often have to be close to the transition states. This minimises the risk of the species collapsing into a minimum, and it also minimises the chance of locating a higher order transition state. The connections between the transition states and the minima can be confirmed by intrinsic reaction coordinate (IRC) calculations, but this has not been performed in the work completed for this thesis.

1.7.5 Computational Software and Techniques

The computational calculations presented in this thesis were performed using the Gaussian16 software package.[194, 195] In Gaussian16, the Berny algorithm is applied to minimise the energies of the starting structures.[196] This method uses internal coordinates such as bond lengths, bond angles, and dihedral angles which are more chemically intuitive and more efficient as molecular motion often occurs more naturally along the internal coordinates. It works in addition with the GEDIIS optimiser, which constructs a new geometry guess based on a linear combination of several previous geometries and gradients to extrapolate a better estimate.[197] These estimates should be closer to the energy minimum or saddle point, and also converge faster than standard quasi-Newton steps.

Whilst programmes like Gaussian16 can aid in the convergence of specific minimum, multiple starting structures are required to fully survey the entire potential energy surface because the starting structure will determine which minimum the structure converges to. This can be of great importance, as the structure that provides the best agreement with experimental results may not be from the global minimum. The starting structures can be built up using chemical intuition (*i.e.* using prior knowledge to provide an educated guess of what the structure may be). Alternatively, randomly generated structures can be produced by placing components of the complexes (*i.e.* atoms, ligands, *etc.*) as is done using the *Kick*[3] algorithm.[198, 199] Developed by Addicoat *et al.*, it allows a greater proportion of the PES to be sampled. This algorithm proved to be very useful in producing multiple starting structures for the systems under investigation in Chapters 3-5, before they were optimised using Gaussian16.

In order to produce simulated IR spectra, normal mode frequency calculations are performed at the same level of theory as the optimisation. Using the Taylor expansion defined previously, this can be truncated to:

$$V(\mathbf{r}) \approx V(\mathbf{r}_0) + \frac{1}{2}\sum_{j,k}(x_j - x_j^0)\left.\frac{\partial^2 V}{\partial x_j \partial x_k}\right|_{\mathbf{r}_0}(x_k - x_k^0), \tag{1.61}$$

providing a local harmonic expansion of the PES for the minimum energy structures.[24] Using this approximation, the Hessian matrix can be used to calculate the force constants and nuclear displacements with the complex based on Hooke's Law:

$$k = -\frac{\mathrm{d}F}{\mathrm{d}\mathbf{r}} = \frac{\partial^2 V}{\partial x_j \partial x_k}. \tag{1.62}$$

The vibrations that correspond to the calculated force constants will all be positive if the stationary point that has been examined is a true minimum. Alternatively, if the structure is instead a local maximum (*i.e.* a transition state), this will produce one eigenvalue which is imaginary. Given that these calculations are performed under a harmonic approximation, a scaling factor is applied to account for systematic errors due to anharmonicity in the experimental species, as well as intrinsic deficiencies in the methods to optimise the structures.[192, 193]

The intensities of these vibrations are predicted by calculating how the electronic dipole changes with respect to motion along a normal mode ($\mu = (\mu_x, \mu_y, \mu_z)$) - *i.e.* the derivative of μ with respect to the nuclear motion. The IR transition dipole moment, presented in Equations 1.29, 1.30, and 1.31 can be calculated through the dot product of the dipole moment gradient and the Cartesian normal modes.[24] The IR intensities for each normal modes are then obtained by taking the square of the calculated transition dipole moment. This value is then expressed and plotted as the molar coefficient, ϵ (units: $\mathrm{dm^3\,mol^{-1}\,cm^{-1}} = 1000\,\mathrm{cm^2\,mol^{-1}}$), that arises from the linear absorption described previously in the Beer-Lambert law (Equation 1.34).

Population analysis can also be performed to partition the electron density over atoms, for example, as charges.[200–202] Charge distributions arise from the minimum energy structures and their subsequent orbitals generated from the Gaussian16 software optimisation algorithm.[194] There are several different methods of partitioning the charge, which are based on the wavefunction, the electron density, or fitted to an electrostatic potential. The simplest way is to calculate Mulliken charges, which splits the electron density shared between atoms 50:50.[200, 201] Alternatively, Hirshfeld population analysis can be performed, which requires density matrices for both the molecule and isolated atoms.[202] The charge on an atom, q_A, is related to the total electron density of the

molecule at point $\mathbf{r}$, $\rho(\mathbf{r})$, and the spherically averaged electron density of the isolated atom A at point $\mathbf{r}$, $\rho_A^0(\mathbf{r})$ by:

$$q_A = Z_A - \int \frac{\rho_A^0(\mathbf{r})}{\sum_B \rho_B^0(\mathbf{r})} \rho(\mathbf{r}) \mathbf{dr}, \tag{1.63}$$

where Z_A is the nuclear charge on A, and $\sum_B \rho_B^0(\mathbf{r})$ is the sum of the atomic densities of all atoms as if they were non-interacting. Hirshfeld charges are less sensitive to the choice of basis set than Mulliken charges, making them more consistent across different quantum chemical calculations.

1.8 Thesis Overview

This thesis adopts an integrated form, and the results sections include a mix of a published paper along with unpublished work. This chapter has provided a background of the key principles that were applied to collect, analyse, and understand the results of the work that was completed; both experimental and theoretical. Following on from this, the thesis is presented in the following way:

Chapter 2 will outline the specific methods, both experimental and computational, that were used to study metal ion-ligand complexes and metal clusters. With regard to explaining the details of the experimental setups, this includes:

- The in-house IRPD experiment that the Mackenzie Group uses at the University of Oxford (data presented in Chapters 3 and 4), and
- The IR-MPD experiment was carried out at the HFML-FELIX facility based in Nijmegen, The Netherlands (data presented in Chapter 5).

Details of the specific calculations performed for all the results chapters are also presented in Chapter 2.

Chapter 3 presents a published article that describes the IRPD study performed for ion-molecule complexes formed from Group 9 metals (Co, Rh, Ir) with nitric oxide (NO), $[M(NO)_n]^+$. This paper is included to allow comparisons to be made with other nitrosyl complexes presented in later chapters.

Chapter 4 describes the IRPD study performed on platinum-containing ion-molecule complexes $[PtO_x(NO)_n]^+$. Building upon the work presented in Chapter 3, this demonstrates the differences between Group 9 and Group 10 elements, as well as illustrating the effect an additional oxygen atom can have on the IRPD action spectra.

Chapter 5 covers the work done to investigate the properties of tantalum (Ta) clusters, both neutral and cationic, using a free-electron laser (FEL) at the HFML-FELIX facility, and the computational analysis performed to investigate how nitric oxide molecules bind to cationic Ta clusters.

Chapter 6 outlines the development work that has been completed to produce a new bimetallic cluster source that can be used in-house at the University of Oxford. This includes the development of prototypes, the simulation of the ion optics used to direct the cationic species, characterisation work, and the first mass spectra demonstrating the formation of metal clusters.

The conclusions, future work, and proposed improvements to the experiments are presented in Chapter 7.

Chapter 2

Experimental and Computational Methods

This chapter outlines the experimental setups that were used to collect the data presented in this thesis. Section 2.1 describes the instrumentation used at the University of Oxford to collect infrared photodissociation spectra of cationic gas-phase metal-ion nitrosyl complexes, $[M(NO)_n]^+$. In addition, the free-electron laser experiment in the HFML-FELIX facility that was used to study neutral tantalum clusters is described in Section 2.2. Details of the DFT calculations used to produce possible low-lying isomers for the species studied in Chapters 3−5 are also provided in Section 2.3. The work related to the development of the bimetallic cluster source is contained entirely in Chapter 6.

2.1 Infrared Photodissociation Experiment - University of Oxford

Figure 2.1 provides a simple schematic of the IRPD setup that has been used to study the systems described in Chapters 3 and 4, as well as other systems highlighted in the List of

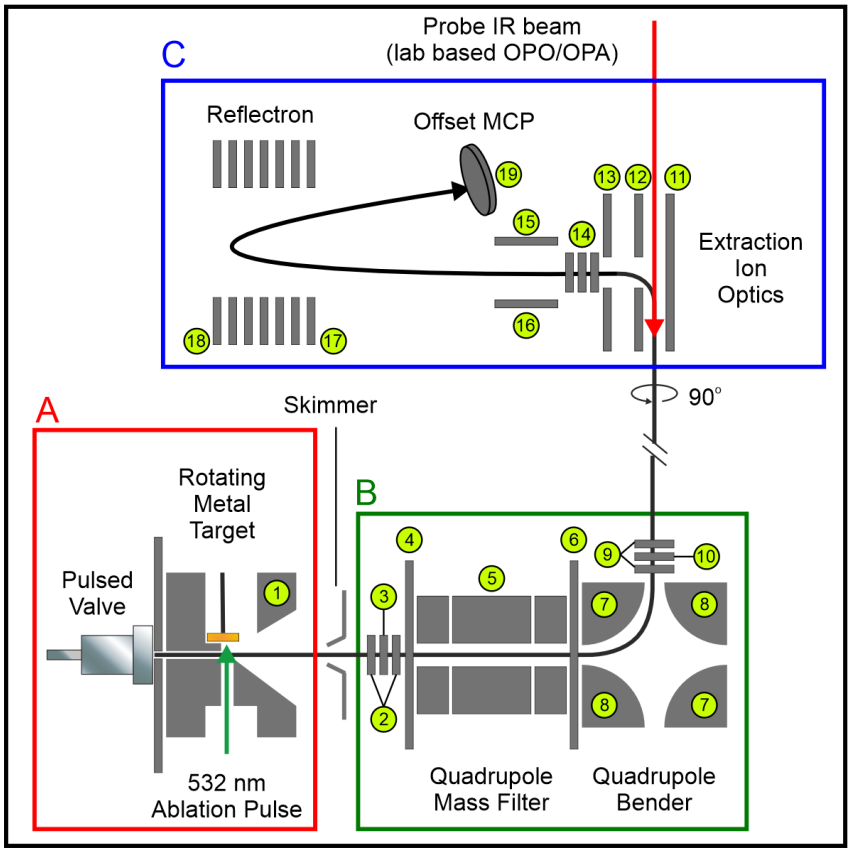

Figure 2.1: IRPD experimental setup at the University of Oxford (not to scale). The experiment has been broken up into three distinct sections: A, the cluster source, B, the quadrupole mass filter and quadrupole bender, and C, the extraction optics and reflectron time-of-flight (ReToF) mass spectrometer. The black arrow indicates the path of the cluster beam. The green and red arrows represent the ablation and IR laser beams, respectively. The extraction optics as well as the reflectron form a commercial ToF spectrometer made by R.M. Jordan Co.. The numbers relate to the specific components to which potentials are applied, as detailed in Table 2.1.

Publications, such as $[HoO_x(CO_2)_n]^+$, $[(NO_2)NO)_n]^+$, and $\left[Au(^{12/13}CO)_m(N_2O)_n\right]^+$.[203–205] As is shown in the figure, the experiment is broken down into three main sections: A; the laser ablation cluster source which is used to generate the metal ion-ligand complexes, B; the quadrupole mass filter (QMF) and quadrupole bender (QB) that can mass-select and direct the species of interest towards the extraction region, and C; the Wiley-McLaren ion extraction optics[122] and reflectron time-of-flight (ReTOF) mass spectrometer used to detect the ions for the purpose of spectroscopy.

Each component illustrated in Figure 2.1 is contained within differentially pumped vacuum chambers under ultrahigh vacuum conditions (*ca.* 1×10^{-7} mbar). The source chamber (section A) is pumped to high vacuum by a Leybold Turbovac MAG600 iP (pumping speed: 550 L/s) is backed by a Leybold EcoDry 40 Roots vacuum pump. The QMF-QB chamber (section B) is pumped using a MAG400 (pumping speed: 365 L/s) and the ToF chamber (section C) is pumped using a Turbovac 151 (145 L/s), both of which are backed by a Leybold EcoDry 25. During experimental operation, the pressure in section A can increase to $\sim 1 \times 10^{-4}$ mbar following the opening of the carrier gas pulsed valve and $\sim 8 \times 10^{-6}$ mbar in sections B and C.

2.1.1 Cluster Source

To generate the metal ion-ligand complexes in section A, a pulsed solenoid valve (Parker-Hannifin Series 9 General Valve) opens to deliver a pulse of carrier gas, typically helium or argon, seeded with the reactant gas (ligand) under investigation. This gas mixture is pre-made in a cylinder and typically contains between $0.5 - 5\%$ of the reactant gas in the carrier gas. The backing pressure (*i.e.* the pressure of gas behind the valve's orifice) is controlled using a regulator and can be increased up to the pressure in the mixing cylinder, typically 10 bar. The usual backing pressures used during the experimental runs range between $4 - 6$ bar. The time the valve is open for is controlled using a Parker Iota One pulse driver, and is typically set between $250 - 450$ µs. Following the valve firing, a laser pulse of the second harmonic output of a Nd:YAG laser (532 nm, $2 - 5$ mJ) ablates a rotating metal disc target (disc diameter; 12 mm, disc thickness; ~ 1 mm).[206] The ablation laser used for the experiments was either a Continuum Minilite II (pulse repetition rate: 10 Hz, pulse width: $6 - 8$ ns) or a Quantel Ultra (pulse repetition rate: 20 Hz, pulse width: 6 ns). The ablated metal atoms and ions are entrained within the carrier gas released by the valve. A "cutaway" source, as described in Section 1.2.4, is used to minimise metal-metal aggregation and maximise $[M(L)_n]^+$ complexes.[92] The metal containing complexes produced will exist in single charge states ($[M(L)_n]^{+/0/-}$), but only cationic species were studied for the work performed on this instrument in this thesis. The polarity of the ion optics can in principle be reversed in order to study anionic species, but the experimental setup as it is constructed at the moment cannot be used to study neutrals as the charged species would have to be separated from the molecular

beam, before additional ionisation of the neutrals takes place to direct the species towards the extraction region.

The carrier gas carries the charged ion-molecule complexes away from the ablation region. This can also be assisted by the application of a DC float potential applied to the source block which will repel the cationic species away from the ablation region (described by the circular label 1 in Figure 2.1, float potential $\sim$ 20 –60 V). The beam is skimmed (using a Beam Dynamics Model 2 Ni molecular beam skimmer, orifice diameter; 1.0 or 2.0 mm) before entering the second vacuum chamber containing the quadrupole mass filter and quadrupole mass bender (Fig 2.1 section B).

2.1.2 Quadrupole Mass Filter and Quadrupole Bender

The mass filter allows ions of a specific m/z ratio to be screened out of all species that are generated from the cluster source; allowing spectroscopy to be carried out on single masses. The quadrupole arrangement involves four parallel rods; two in the x-z plane and two in the y-z plane, with z being the direction of travel of the ions. The rods are arranged so that the rods inscribe a circle, with a radius r_0.[207] Opposite rods (*i.e.* those that reside in the same plane) have the same voltage applied to them, which is composed of a mix of DC voltages and radio-frequency (RF) AC voltages.[208, 209] The rods in the specific planes are applied with voltages that obey the following equations:

$$\Phi_x = U + V_0 \cos(\omega t), \tag{2.1}$$

$$\Phi_y = -U - V_0 \cos(\omega t), \tag{2.2}$$

where Φ_x is the voltage applied to the ions in the x-z plane, Φ_y is the voltage applied to the ions in the y-z plane, U is the DC potential and $V_0 \cos(\omega t)$ is the RF potential.[210, 211] As can be seen from Equations 2.1 and 2.2, Φ_x and Φ_y will always be 180° out-of-phase with each other. The combination of these potentials creates an oscillating electric quadrupole field inside the circle inscribed by the parallel rods. At any given instant, one set of opposite rods is RF focussing whilst the other is RF de-focussing. The DC voltage adds a constant bias to one set of rods (making it a little more de-focussing) and the opposite to the other (a little more focussing). When an ion enters along the principal axis of the rods (in the z-direction), the stability of its trajectory within this field will depend on its

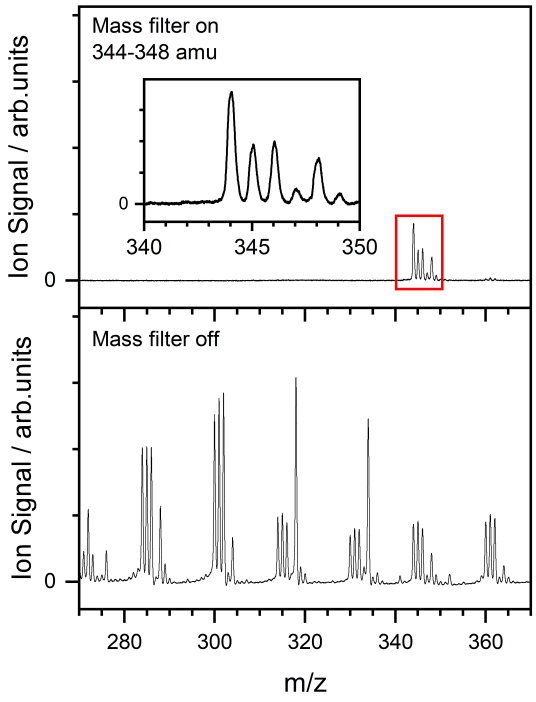

Figure 2.2: Example mass spectra of $[PtO_x(NO)_n]^+$ with the quadrupole mass filter turned on (top panel) and off (bottom panel). In the top panel, a mass filter between 344–348 amu, corresponding to $[Pt(NO)_5]^+$, is applied. The inset shows the individual isotopologues of the mass-selected species. The data in the top and bottom panels were recorded on different days.

---

mass and the frequency and voltages that are applied to the rods. For a given DC/RF potential ratio, only ions with the right m/z ratio will be able to pass all the way through the ion beam rather than hit the rods and be lost from the ion beam. This means that the voltages can be altered to change the masses that pass through and allows specific ions to be gated.

Figure 2.2 demonstrates the effect the mass filter can have in picking out specific peaks in the mass spectrum. Here, a full mass distribution for platinum nitrosyl species, $[PtO_x(NO)_n]^+$, is presented in the bottom panel. Using the commercial quadrupole mass filter-quadrupole bender (Extrel QMS 150) with its associated software (Merlin Automation), specific masses can be selected, as shown in the top panel where masses 344–348 amu were selected, which corresponds to the $[Pt(NO)_5]^+$ species. In this example, there are multiple isotopologues because Pt has multiple stable isotopes,[212] so the mass filter

has been set to incorporate all of these species. The mass filter can be narrowed further to select out single peaks from this distribution, which can be useful when looking for daughter species against a zero background, as the daughter fragments could only be formed from the mass-selected peak. However, this can result in large transmission losses, which makes experiments more difficult to do on account of the low ion signal. Once the desired ions are mass-selected, the voltages that control the ion optics within the experimental setup can be altered to maximise the ion intensity, as well as to minimise the peak widths, before the ions are irradiated with the IR light.

The quadrupole bender that follows the quadrupole mass filter is used to deflect the mass-selected ions by 90° towards the ion extraction optics used in the ToF mass spectrometer. The QB consists of four diagonally opposite quadrants that are vertically orientated, as shown in Figure 2.1. Two different DC potentials are applied to pairs of opposite quadrants, with the inner poles (circular label 7 in Figure 2.1) negatively charged to attract the cationic complexes, and the outer poles (circular label 8 in Figure 2.1) positively charged to repel them. The magnitude of the inner and outer pole voltages can be altered to control the output trajectory of the ions. This assists in overlapping the ion beam with the counterpropagating IR beam in order to maximise the parent complex fragmentation (*i.e.* daughter fragment production). Additionally, the bender also ensures that only the mass-selected ions are irradiated with the IR beam.[213]

2.1.3 Time-Of-Flight Mass Spectrometer

The ion beam exits the QB and proceed towards the commercial reflectron time-of-flight (ReToF) mass spectrometer (R.M. Jordan Co.), as shown in section C of Figure 2.1. The complexes within the ion beam are orthogonally extracted by applying pulsed voltages to the repeller and extractor plates simultaneously in the Wiley-McLaren ion lens stack, before being accelerated into the time-of-flight chamber. The trajectories of the complexes that are accelerated using the WM ion optics can be altered by using a pair of deflector plates directly above after the ground plate. A DC potential can be applied to each plate to push the complexes in or against the direction of travel of the ion beam. This can assist in directing specific masses towards the detector, and improve its signal in the time-of-flight mass spectrum. Furthermore, an einzel lens is positioned between

the Wiley-McLaren lens and the deflector plates to focus the ion beam onto the detector.

Figure 2.3 illustrates the structure of a time-of-flight mass spectrometer that uses a reflector.[121, 214] The reflectron acts as an ion mirror and can cause ions to reverse their direction, before they are detected using an offset MCP detector. It consists of multiple electrostatic plates stacked on top of each other, with a potential applied to the front (bottom of the reflectron stack) and back (top of the reflectron stack). The plates are connected *via* a series of resistors that linearly step the voltage between the front and back of the reflectron, which assists in slowing the ions down. The potentials that are applied have to be great enough to make the potential gradient the ions have to climb up steep enough that they lose the kinetic energy gained from the WM optics and are directed towards the detector. Typical reflectron voltages that are applied to the reflectron and WM plates are provided in Figure 2.3. The plate at the very front of the reflectron is grounded, and has an electroformed mesh spanning the hole in the plate that the ions pass through, in order to minimise the electric field from the reflectron permeating into the field-free time-of-flight region. Stray fields can cause the ions to be deflected away from the detector, which will reduce the ion signal, and they can affect the time-of-flight of the ions, thus making it more difficult to determine which species are reaching the detector.

The ion mirror not only increases mass resolution by increasing the distance the ions have to travel, but also by refocusing ions of the same mass that acquired different kinetic energies depending on where they were accelerated within the WM repeller and extractor plates, as described in Equation 1.13. As shown in Figure 2.3, two coloured dots are used to represent ions with the same mass but different starting positions. For the potentials applied in the figure, the average potential between the repeller and the extractor is 2400 V. The red ion will experience a slightly greater potential and therefore a greater acceleration than the blue ion. As a result, the red ion will penetrate deeper into the potential well generated by the reflectron than the blue ion. The red ion will spend a greater amount of time in the reflectron potential well, meaning that it will eventually reach the offset MCP detector at the same time as the blue ion, which has travelled a shorter distance after it has been reflected lower down in the reflectron. By

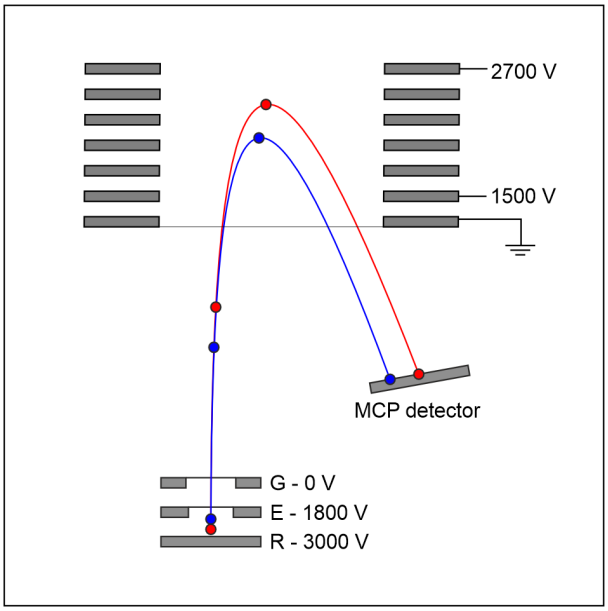

Figure 2.3: The configuration of the reflectron time-of-flight (ReToF) mass spectrometer, along with trajectories of ions. The coloured circles have the same mass, but different starting positions within the extraction region, leading to the red circle gaining more vertical kinetic energy. In the extraction region, R, E and G label the repeller, extractor and ground plates. The voltages provided are typical of an optimised ReToF system.

---

making the two ions arrive at the MCP detector at the same time, the resolution of the ToF spectrum is improved. An estimate for the resolving power, RP, of the spectrometer can be calculated as:

$$RP = \frac{m}{\Delta m}, \tag{2.3}$$

where m is the mass-to-charge ratio of the ion being measured, and Δm is the smallest difference in mass that the instrument can resolve at that mass.[120] The value for Δm can be approximated at full width at half maximum (FWHM) of the peak in the mass spectrum. Using the peak at m/z = 361 amu in Figure 2.2, the RP is calculated to be 702 (FWHM: 0.514 amu).

In order for the time-of-flight mass spectrum to be recorded, the ions have to hit a dual microchannel plate (MCP) detector that is mounted on an offset flange. The collision of the ion causes electrons to cascade from the charged plates onto an anode. The time it takes for ions to travel from the WM plates to the MCP detector is recorded, with the time-of-flight being referenced to the time that the WM ion optics were pulsed, *i.e.* t_0

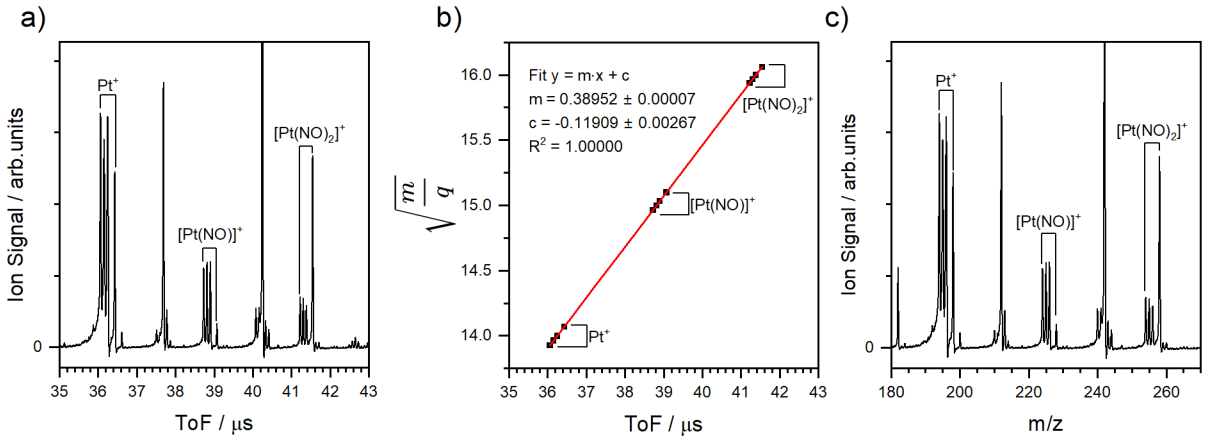

Figure 2.4: Converting a ToF spectrum into a m/z spectrum. **a)** An example time-of-flight spectrum for $[PtO_x(NO)_n]^+$, with the peaks for $[Pt(NO)_n]^+$ $(n = 0 - 2)$ being labelled, with the distinctive pattern of the stable Pt isotopes being observed.[212] **b)** The calibration curve used to extract the fitting constants that are required to convert between the time and m/z domains. **c)** The final m/z spectrum, with the corresponding peaks used in the calibration curve being labelled again.

$= t_{TOF} = 0\,\mu s$, is defined as the time that the potentials are applied to the repeller and extractor plates. The current from this anode and the time that the ions took to hit the detector can be captured on an oscilloscope (LeCroy Wavesurfer 64X: 600 MHz, Up to 2.5 GS/s, 8 bits resolution, or National Instruments 5160: 500 MHz, Up to 2.5 GS/s, 10 bits resolution), before the spectrum is recorded through communication between the oscilloscope and a PC using a custom-made LabVIEW programme.

As was shown by Equation 1.15 in Chapter 1, the time-of-flight of an ion is linearly related to the square root of its mass-to-charge ratio. This means that a time-of-flight spectrum can be converted to a mass spectrum by determining the values of α and β by using a calibration curve. Figure 2.4 illustrates the process of generating the calibration curve and then forming the mass spectrum. Here, panel **a)** shows a time-of-flight spectrum for $[PtO_x(NO)_n]^+$ species (spanning the time-of-flight for the lightest species, $n = 0 - 2$). The peak centres of selected spectral lines in the time-of-flight spectrum are assigned to specific masses (more specifically, the m/z ratio). The assigning procedure can be assisted by using the QMF to mass-select specific features to minimise the risk of mis-assigning them. Additionally, when elements have multiple isotopes, this can be used

to assign species based on the element's isotopic distribution. The selected time-of-flight values should span as much of the spectrum as possible to provide a good fit throughout the region. The square root of the m/z ratio is plotted as a function of the time-of-flight to produce a calibration curve (the y-axis uses $\sqrt{\frac{m}{q}}$ to be consistent with Equation 1.15, but will be presented as m/z from now on), before applying a linear fit $y = mx + c$ to the points, as shown in panel **b)** of Figure 2.4. The fit must have an R^2 value of 1 that is accurate to six significant figures to provide confidence that the calibration is accurate. The gradient and intercept of this calibration curve are then used to convert the time domain to the mass domain, as shown in panel **c)** of Figure 2.4.

2.1.4 IR Light Source - LaserVision OPO/OPA System

In order to irradiate the complexes in the ion beam and induce photodissociation, a tunable IR laser source is required. This is achieved using a commercial OPO/OPA system from LaserVision[215] pumped with 1064 nm light produced from an Nd:YAG laser (Continuum Powerlite II, 10 Hz repetition rate, $6 - 8$ ns pulse duration); the layout of which is presented in Figure 2.5. The Powerlite II can generate up to 1.1 J per laser pulse, but this is reduced to $\sim 600 - 650$ mJ by controlling the trigger delay between the flashlamp and the Q-switch of the laser in order to prevent damaging the non-linear optics used to generate the IR light. This section will provide the practical and specific details of the LaserVision OPO/OPA arrangement, and how it is used to generate light in the desired frequency range.

In brief, the incoming 1064 nm from the Powerlite is split into two beams using a beam-splitter to direct the light towards the OPO and OPA stages, with 1/3 of the energy going to the OPO and 2/3 going to the OPA. The polarisation of the beams is controlled using half-waveplates (labelled in Figure 2.5 **a)** as $\lambda/2$ waveplate) to ensure they match with the phase-matching conditions that are required of the non-linear crystals. Before entering the OPO stage, the 1064 nm light is frequency doubled to 532 nm using a potassium titanyl phosphate (K[TiO]PO_4, abbreviated KTP) crystal, which is then used as the pump beam to drive optical parametric down-conversion.

The OPO consists of two KTP crystals that are held in place using motorised mounting

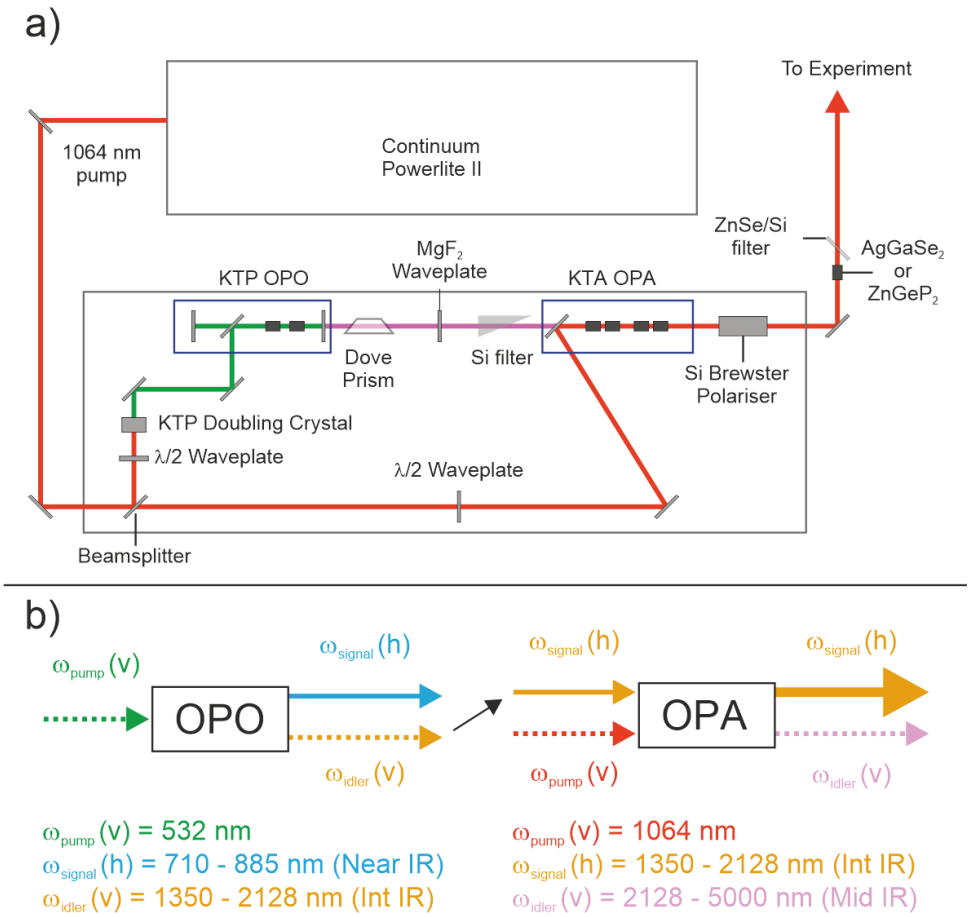

Figure 2.5: The layout of the LaserVision OPO/OPA setup. **a)** The main optics for the operation of the IR OPO/OPA system generating tunable infrared light, as well as the seventh crystal positioned after the OPO/OPA setup. **b)** The principle processes of optical parametric oscillation (OPO) and optical parametric amplification (OPA), with the arrows being used to illustrate the different electromagnetic waves passing through the non-linear crystals. The polarisation is illustrated, with dashed lines for vertical (v), and solid lines for horizontal (h). The black arrow indicates that the output idler beam from the OPO becomes the input signal beam for the OPA. For space reasons, the pump beams are not shown leaving the crystals.

---

plates. There are two KTP crystals within the OPO to account for beam walkoff within the crystal.[216–219] The 532 nm pump beam generates the signal and idler which are in the near IR region ($710 - 885$ nm) and intermediate IR region ($1350 - 2128$ nm), respectively. Two mirrors are used to form the oscillator optical cavity in order to increase the output power of the signal and idler by allowing multiple passes through the crystals. By using the motorised mounts, the frequencies are tuned by counter-propagating the

crystals, as this will change the effective refractive index. The rotation of the crystals is controlled using a motor control programme provided by LaserVision. Using the birefringence of the crystals to phase match the three waves propagating through, the change in the effective refractive index will manifest itself in a change in the frequency of the waves; meaning that the energy and phase matching requirements specified in Equations 1.44 and 1.45 are satisfied. The KTP crystals are Type II phase-matched for parametric oscillation, meaning that the signal and idler waves have orthogonal polarisations. This is illustrated in Figure 2.5 **b)** using solid and dotted arrows, with solid arrows indicating horizontal polarisation (h) and dotted arrows indicating vertical polarisation (v). After the beams are formed, the output idler is allowed to pass through a Si filter and becomes the signal beam in the OPA stage, as illustrated by the black arrow in Figure 2.5 **b)**. Before passing through the OPA stage, the polarisation of the output idler is rotated by 90° using a half-waveplate to change it from vertical to horizontal.

The other 1064 nm beam generated from the beamsplitter is also passed into the OPA, and acts as the pump. The OPA stage is made up of two pairs of potassium titanyl arsenate ($K[TiO]AsO_4$, abbreviated KTA) crystals. These, like the KTP crystals in the OPO, are Type II phase-matched but are used to drive difference frequency generation (DFG). The pump and signal waves are mixed together and can generate a new idler beam with vertical polarisation that resides in the mid-IR (2128–5000 nm), with the signal wave being amplified, as symbolised by the larger arrow after the OPA stage in Figure 2.5 b). Again, the KTA crystals are mounted on motorised stages, which allows each pair of them to be counter-rotated to vary the frequency of IR light that is produced. The 1064 nm pump light that leaves the OPA is removed using a dichroic mirror, thus allowing the signal and idler to propagate further. Either of these beams can be used to perform spectroscopy, but this requires that one of them be filtered out. This can be achieved using a Si Brewster polariser positioned at the very end of the LaserVision system. By rotating the Si filter, the beam that is allowed through will change due to the different polarisations of the signal and idler beams. The two beams can also be distinguished by measuring the power after the OPA stage and rotating the polariser, as the pulse energy for the signal beam will be greater after the optical parametric amplification.

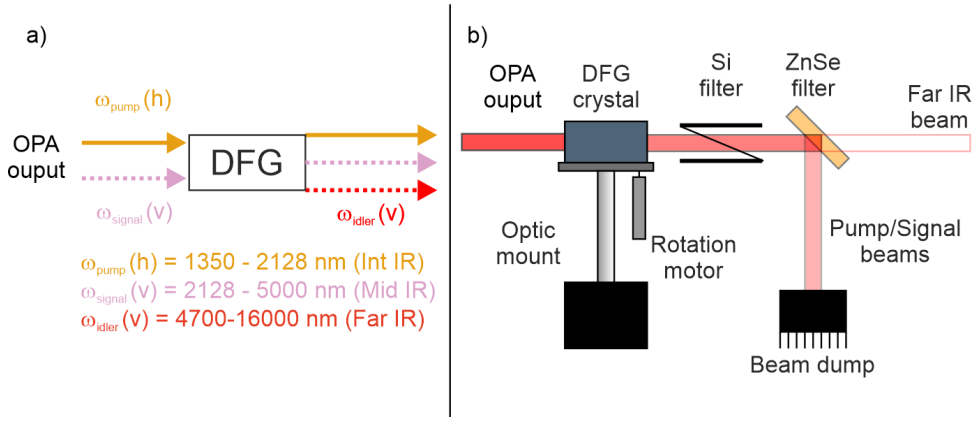

Figure 2.6: The generation of far-IR light using the seventh crystal *via* difference frequency generation (DFG). **a)** The principle of DFG being applied to the frequencies that are generated from the OPO/OPA system. With this arrangement, the output idler wave will have a wavelength of $4.7 - 16$ µm ($2128 - 625$ cm^{-1}). **b)** The optics arrangement for the seventh crystal. The DFG crystal is mounted on a motorised stage that can either rotate horizontally or vertically, based on the crystal in use. The output light is filtered out using the Si and ZnSe filters to select out the far-IR beam.

2.1.5 Generation of Far-IR Light

The species studied on the IRPD instrument in this thesis all contained nitric oxide (NO) ligands. The fundamental vibrational frequency of the NO molecule is 1875.84 cm^{-1}; lower than the output frequencies that are produced by the OPA.[215] To produce light with longer wavelengths, an additional round of DFG can be performed using the signal and idler generated from the OPA with a seventh non-linear crystal. This requires the Si Brewster polariser to be removed to allow both beams to exit the box that contains the OPO/OPA setup. Figure 2.6 **a)** provides an illustration of the non-linear processes occurring within the seventh crystal that can generate light in the far-IR ($4700 - 16000$ nm). Two materials have been used as the seventh crystal to produce far-IR light in this work: silver gallium selenide ($AgGaSe_2$) and zinc germanium phosphide ($ZnGeP_2$, abbreviated ZGP).[220–224] Both work by utilising the same principle of DFG, but differ in how effectively they can generate the output idler and also in how the crystal is mounted.

Both the $AgGaSe_2$ and $ZnGeP_2$ crystals are birefringent, which means that the output frequency they generate after DFG can be altered by rotating them using the motorised

stage. They differ in their birefringence, in that $AgGaSe_2$ has a negative birefringence, whilst $ZnGeP_2$ has a positive birefringence. The crystals also have different types of phase-matching, with $AgGaSe_2$ being phase-matched of Type II and $ZnGeP_2$ being phase-matched of Type I. This means that the way the $ZnGeP_2$ crystal has to be mounted to the rotation stage in a different orientation to the $AgGaSe_2$ crystal; namely, the ZGP crystal and mount rotate by 90° compared to the mount used for the other crystal so it rotates vertically (*i.e.* the top of the crystal rotates into the beam) rather than rotating in the horizontal plane. The two materials also differ in their transmission ranges, with the $AgGaSe_2$ crystal able to transmit light within the wavelength range $0.7 - 18.0$ µm, compared to $ZnGeP_2$ which has a much narrower range ($0.75 - 12.0$ µm). Finally, the damage thresholds of the two materials differ ($AgGaSe_2$: $10 - 20$ MW/cm^2, $ZnGeP_2$: 60 MW/cm^2).[221, 224] This means that $ZnGeP_2$ can be positioned closer to the outlet of the OPO/OPA box compared to $AgGaSe_2$ (~ 0.25 m compared to ~ 2 m, respectively). The input photon flux into the $ZnGeP_2$ can be greater, and in turn the output photon flux will be greater. The increase in the photon flux produces higher energies-per-shot, making it more likely that metal ion-ligand complexes will dissociate.

To begin with, $AgGaSe_2$ was the only seventh crystal available to perform the studies detailed in this thesis. It was able to generate far-IR light that spanned the frequency range of interest for the metal nitrosyl complexes ($\sim 1500 - 2100$ cm^{-1}). Around 1500 cm^{-1}, the recorded pulse energies were on the order of tens of µJ (this is approximately equal to the minimum power meter trigger threshold, 40 µJ). As the photon frequency increased, the pulse energy gradually increased to ~ 0.4 mJ at ~ 2100 cm^{-1}, before the pulse energy rapidly decreased when the edge of the frequency range was reached (2200 cm^{-1}). The pulse energies were great enough to induce photodissociation in the metal nitrosyl complexes, among other systems, in a sufficient number of complexes to produce an appreciable ion signal on the oscilloscope. The crystal can also produce pulse energies of $\sim 1.0 - 1.5$ mJ between $625 - 800$ cm^{-1}, which means that lower frequency vibrations (*i.e.* molecular bends, C-C, C-N stretches, *etc.*) could be investigated. However, this has not been completed for this thesis. In 2022, a ZGP crystal was obtained that could produce greater pulse energies in the region $1300 - 2100$ cm^{-1} compared to the $AgGaSe_2$ crystal. This led to the crystals being swapped to improve the photon flux that interacts

with the ion beam in the experiment. However, as stated earlier, the transmission range of the ZGP crystal is narrower compared to the $AgGaSe_2$ crystal, so it cannot be used to investigate the low-energy molecular vibrations described above. Following the production of the far-IR idler beam using either crystal, it is selected from the pump and signal beams by passing through a ZnSe filter set at $\sim 45^{\circ}$, as shown in Figure 2.6 **b)**. The pump and signal beams are reflected into a beam dump, allowing the far-IR to continue along towards the IRPD instrument. When using the ZGP crystal, an additional Si filter is also installed before the ZnSe filter. In the case of the data presented in this thesis, $AgGaSe_2$ was used to record the IRPD data for the Group 9 nitrosyl complexes in Chapter 3, and $ZnGeP_2$ was used for the platinum nitrosyl complexes described in Chapter 4.

Before using the laser light to irradiate the complexes, the system needs to be calibrated correctly to ensure that it produces light at the same wavelength as is specified in the crystal motor control software. This is done by recording the rovibrational spectrum of a gas by utilising the photoacoustic (PA) effect and comparing the peak positions and spacings with known literature values.[225, 226] The IR beam is passed through a cell containing $\sim 0.2 - 1.0$ bar of the survey molecule in a carrier gas ($\sim 1 - 5\%$ in He or Ar). The frequencies of light that cause the molecules to vibrate are recorded using a microphone, with the amplitude of the detected sound being proportional to the optical absorption of the sample at that frequency. Figure 2.7 shows typical rovibrational spectra produced from PA scans for three different regions of the IR spectrum, corresponding to the fundamental vibrations of the nitric oxide and carbon monoxide molecules in panels **a)** and **b)**, respectively, and the ν_3 vibration of methane in panel **c)**. The nitric oxide PA scan was recorded after the seventh crystal using the far-IR, whereas the carbon monoxide and methane spectra were recorded using the mid-IR output of the OPA. The spectra all show the P and R rovibrational branches for these molecules, as discussed in section 1.4.2, with the methane spectrum also possessing rotational fine structure. The central frequency between these peaks, which aligns with the position of the Q-branch for NO and CH_4, is used to check the laser calibration compared to the line width of the laser (3.7 cm^{-1}).[215] In each of the spectra presented, the laser frequency is within 1 cm^{-1} of the fundamental frequency as stated in the literature (1876 cm^{-1} for NO, 2143 cm^{-1} for CO, 3019 cm^{-1}).[227, 228]

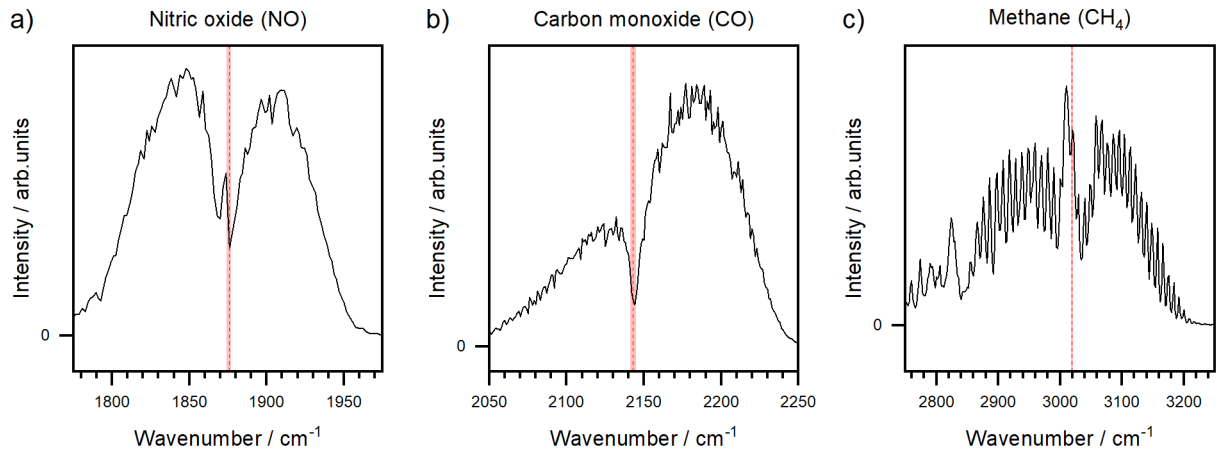

Figure 2.7: Example rovibrational spectra recorded from the photoacoustic (PA) scans recorded using the OPO/OPA setup with dilute mixtures of **a)** nitric oxide, **b)** carbon monoxide, and **c)** methane in a carrier gas ($\sim$ 1-5% in He or Ar). Panel **a)** was recorded after the $AgGaSe_2$ crystal, whereas panels **b)** and **c)** are recorded directly after the OPA to calibrate using the mid-IR light. The fundamental vibrational frequencies of the molecules (ν_3 mode for methane) are illustrated with red lines in each panel, with the width of these lines equalling the OPO/OPA linewidth (3.7 cm^{-1}).

2.1.6 Producing IRPD Spectra

Following its production from the LaserVision setup, the IR light is directed into the vacuum chamber through a window, and counterpropagates against the ion beam once it has passed through the quadrupole bender. Mass spectra are recorded with the IR light on and off; this is done differently depending on which ablation laser was used. Initially, when using the Minilite which ran at the same repetition rate as the Powerlite (10 Hz), a shutter would be used to control when the IR light entered the chamber. It would open for three shots of the IR laser before closing for three further shots before opening again. The mass spectra would be extracted from the oscilloscope using a custom built LabVIEW programme. Each spectrum would be binned and averaged in different arrays, IR off or IR on, depending on whether the shutter was closed or open until a user defined number of shots has been reached (*e.g.* 300 shots would have 150 traces in either bin). Following the installation of the 20 Hz Ultra ablation laser and the National Instruments 5160 oscilloscope, the LabVIEW programme was altered so that the IR laser would fire on every other shot of the ablation laser, given the Ultra laser's repetition rate is twice

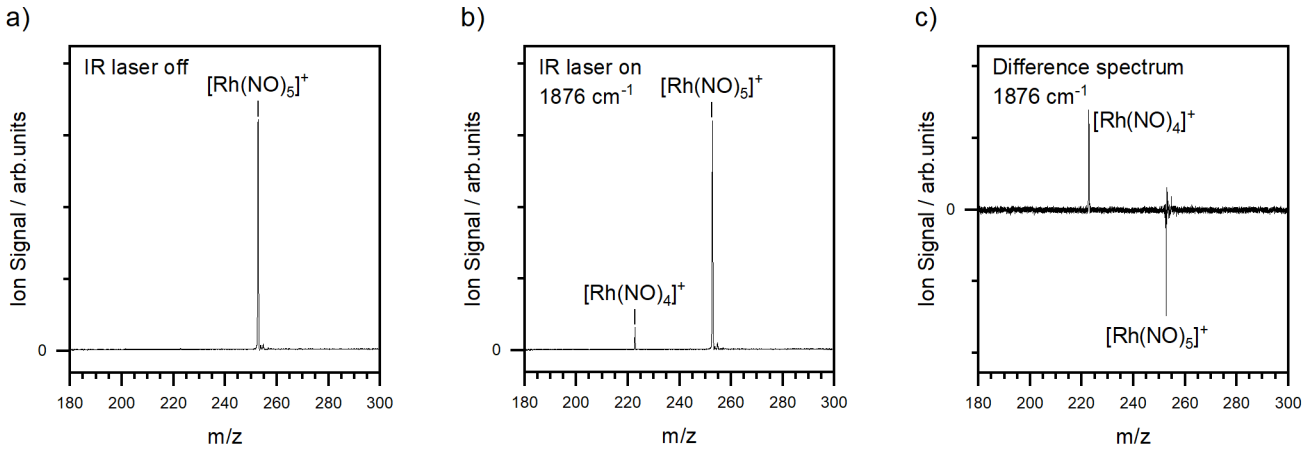

Figure 2.8: The production of difference spectra. **a)** A mass-selected spectrum of $[Rh(NO)_5]$ produced when no IR light interacts with the ion beam. **b)** The mass spectrum produced when $[Rh(NO)_5]^+$ was irradiated with IR light at 1876 cm^{-1}. **c)** The difference spectrum produced by subtracting panel **a)** from panel **b)** (IR on - IR off).

that of the Powerlite (20 Hz compared to 10 Hz). Sequential mass spectra are binned into IR off and IR on arrays directly. The installation of the Ultra laser thus doubled the acquisition rate and removed the need for the shutter.

Figure 2.8 **a)** shows a mass-selected mass spectrum of $[Rh(NO)_5]^+$ before it has been irradiated with the IR laser (IR off spectrum). At 1876 cm^{-1}, there is some depletion of the parent peak, with a new daughter species of $[Rh(NO)_4]^+$ forming, as shown in panel **b)** (IR on spectrum). These spectra are used to produce the subsequent difference spectrum (IR on - IR off) which is provided in panel **c)**. For one specific scan over a set frequency range, a difference spectrum is produced for each IR frequency through which the laser system is scanned, and these data can be extracted using a separate custom-made LabView analysis programme. Figure 2.9 shows an example difference spectrum for the parent ion $[Rh(NO)_5]^+$ and the daughter ion $[Rh(NO)_4]^+$ being converted, as indicated by the black arrow, into an IRPD spectrum using the enhancement of the daughter ion. In order to increase the signal-to-noise ratio (S/N) of the IRPD spectrum, multiple scans can be performed over specific regions to average the noise from the experiment. Furthermore, recording action spectra in the enhancement channel improves the S/N by eliminating large background signals, thereby reducing noise contributions and maximising contrast. The IRPD scans are repeated until the spectral features are clear enough

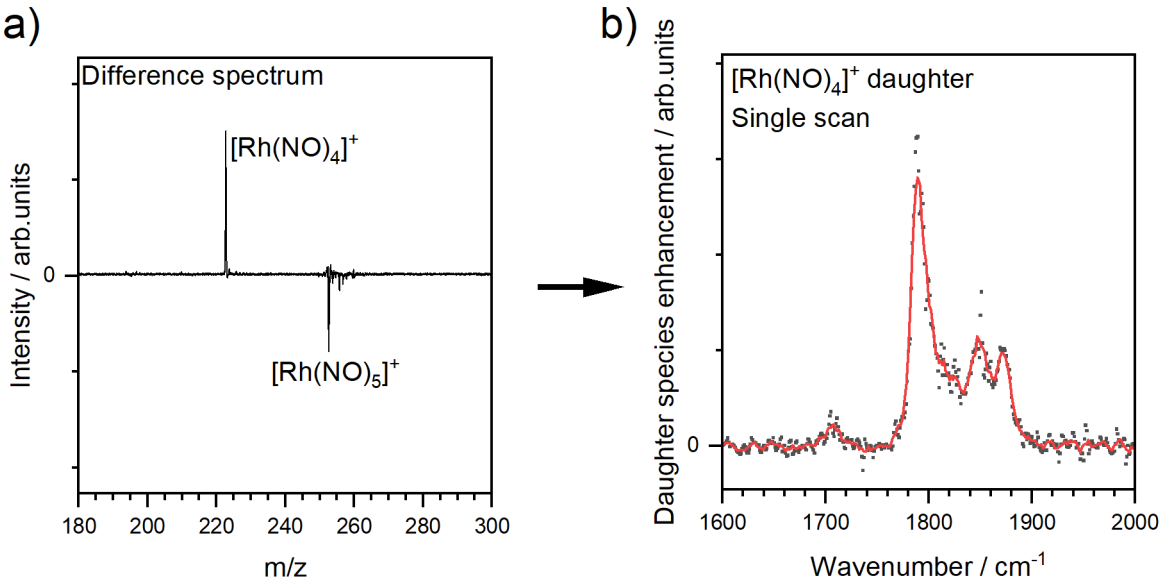

Figure 2.9: Converting the difference spectrum (panel a)) to an enhancement spectrum (panel b)). An example difference spectrum for $[Rh(NO)_n]^+$ $(n = 4, 5)$ is provided. The enhancement of the $[Rh(NO)_4]^+$ peak is recorded as a function of IR laser frequency, ν, and is plotted to show the enhancement of the daughter species. This data is from one scan, between $1600 - 2000$ cm^{-1}. The raw data points are plotted as black dots, with a four-point adjacent average also plotted as a red line.

---

to be assigned, and they can then be assigned to structural features of the complexes.

The IRPD spectrum presented so far in Figure 2.9 does not account for OPO/OPA conversion efficiency across the frequency range that has been scanned which has an effect on the pulse energy and subsequently the photon flux. Fluctuations in the photon flux as a function of frequency need to be accounted for to properly describe the IR spectrum and minimise the risk of generating artefacts in the data. A better way to describe the IRPD spectrum is to use the absorption cross section of the species $\sigma(\nu)$. This can be described using the following equation:

$$\sigma(\nu) = -\frac{1}{\Phi(\nu)} \ln\left(1 - \frac{N_f(\nu)}{\alpha N_0(\nu)}\right), \tag{2.4}$$

where Φ is the photon flux, N_f is the intensity of the daughter species after depletion, N_0 is the intensity of the parent species before depletion, and α is the proportion of the molecular beam that overlaps with the IR beam (this is assumed to be 1 for simplicity).

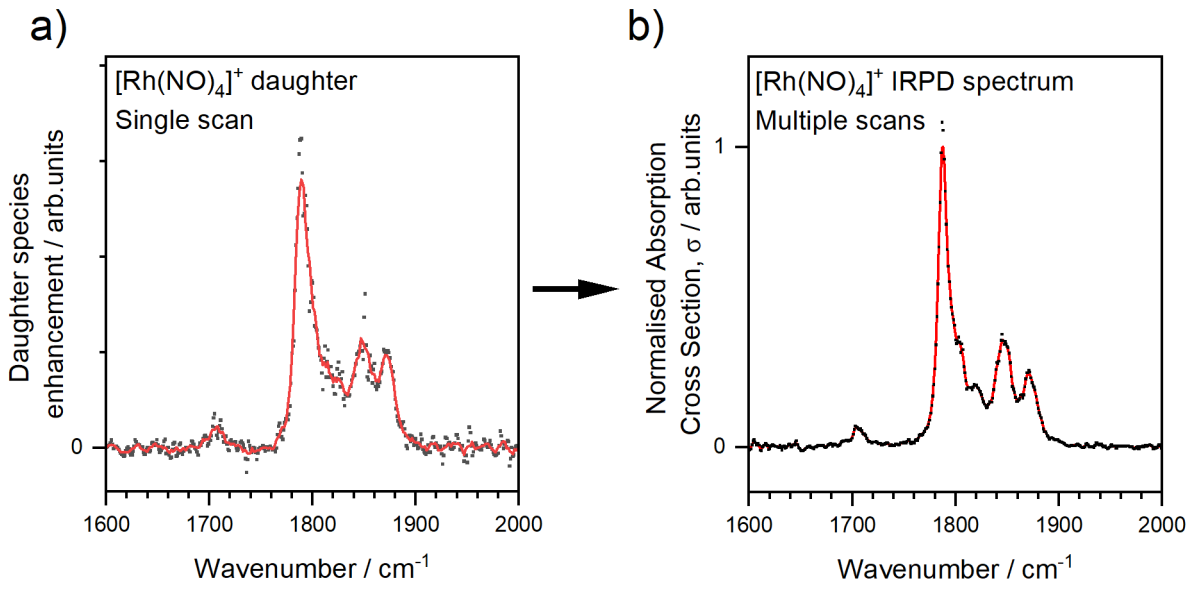

Figure 2.10: Conversion of the raw enhancement data into a normalised absorption cross section. The data plotted in the left panel is used as N_0 in Equation 2.4 in order to produce the normalised absorption cross section, as shown in the right panel. The right panel is formed from multiple sets of scan data, hence the improved signal-to-noise ratio.

In addition to α, all these variables depend on the frequency of the IR light, ν. The photon flux describes how many photons pass through an area per unit time. This is described using Equation 2.5 :

$$\Phi = \frac{n_{\text{photon}}}{At} = \frac{E_{\text{shot}}}{E_{\text{photon}}At} = \frac{E_{\text{shot}}}{h\nu At}, \tag{2.5}$$

where n_{photon} is the number of photons, A is the laser beam area, t is the pulse duration, E_{shot} is the pulse energy of the IR laser, E_{photon} is the photon energy and ν is the photon frequency.

The values for N_0 and N_f are determined from the mass spectra, whereas the value of E_{shot} is recorded using a power meter at the far-end of the IRPD experiment after the IR pulse enters, passes through, and exits the vacuum chamber, ignoring losses at the windows. Using Equation 2.5, the photon flux for each IR photon frequency can be calculated before it is used to calculate the absorption cross section using Equation 2.4. The absorption cross section can then be normalised by dividing each point by the maximum value of the smoothed curve. Figure 2.10 shows the conversion of a single IRPD

Table 2.1: The different voltages that are applied to the ion optics and components within the IRPD instrument, broken up by the sections and number highlighted in Figure 2.1. The typical values for these components, and whether they are pulsed, is also presented. For the reflectron, the front voltage represents the first electrode following the meshed ground plate.

Section	Number	Voltage control	Pulsed?	Typical values / V
A	1	Float	No	20 – 60
B	2	Einzel lens A 1/3	No	-80 – -130
	3	Einzel lens A 2	No	-220 – -300
	4	Entrance lens	No	-50 – -30
	5	Pole bias	No	-5.5 – -8.0
	6	Exit lens	No	-260 – -320
	7	Inner poles	No	-200 – -280
	8	Outer poles	No	0 – 10
	9	Einzel lens B 1/3	No	-200 – -280
	10	Einzel lens B 2	No	-260 – -320
C	11	Repeller	Yes	3000
	12	Extractor	Yes	1750 – 1800
	13	Ground	No	0
	14	Focus	No	-80 – -120
	15	Deflection 1	No	-40 – -100
	16	Deflection 2	No	-80 – -150
	17	Reflectron Front	No	1500 – 1550
	18	Reflectron Back	No	2700 – 2750
	19	MCP	No	4200 – 4900

spectrum using only the raw daughter enhancement data (left panel) into a spectrum that is described using the normalised absorption cross section (right panel). The right panel was formed using multiple scans in order to improve the S/N ratio, hence the reduction in the fluctuation of the raw data points. Unless otherwise stated, all the IRPD spectra presented in Chapters 3 – 4 are plotted as normalised absorption cross sections.

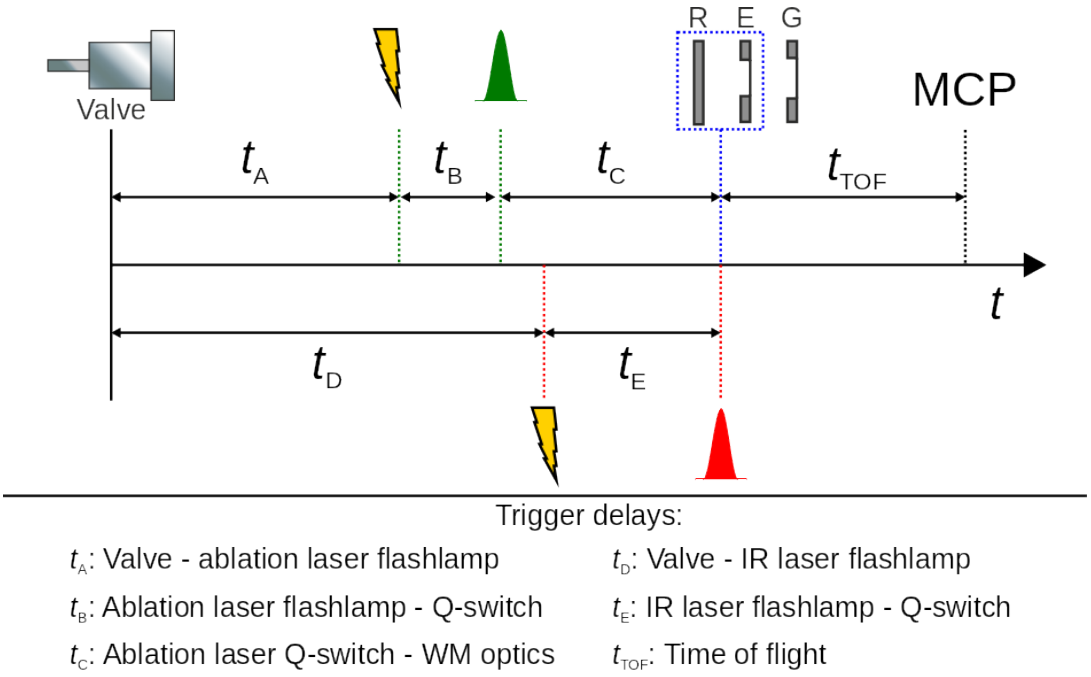

Figure 2.11: Simplified timing diagram for the trigger pulses applied within the IRPD experiment. The timing labels are described at the bottom of the figure.

The ion signal strength and quality can be improved by fine tuning the voltages applied to the electrodes contained within the instrument. Table 2.1 presents the voltages that are applied to the components, whether the voltages applied to the electrodes are pulsed, and also their typical values. The timing of the WM plates firing has to be synchronised with the other components pulsed within the instrument; namely the gas valve, the two lasers used, and the oscilloscope trigger.

Figure 2.11 provides a very simple timing diagram that details each trigger pulse used in the IRPD experiment. The first trigger signal is for the solenoid valve to open, which is followed by the trigger for the ablation laser flashlamp (depicted using a lightning bolt) which follows after delay time t_A ($\sim$ 250 – 500 µs). The Q-switch of the ablation laser is triggered time t_B after the flashlamps have fired to initiate lasing and release the ns-wide laser pulse (t_B is fixed at 150 µs for optimum beam stability). The complexes produced by the ablation laser pulse are then extracted using WM optics by pulsing these plates after time t_C ($\sim$ 180 – 300 µs). To ensure that the ion beam and the IR laser overlap with each other in time, the delay time between the triggers of the Powerlite's flashlamps

and the gas valve, t_D, is calculated as:

$$t_D = t_A + t_B + t_C - t_E - \text{const.}, \tag{2.6}$$

where t_E is the delay between the triggers for the Powerlite's flashlamps and the Q-switch ($\sim$ 280 – 310 µs, depending on which timing is capable of producing $\sim$ 600 – 650 mJ of energy from the Powerlite to pump the LaserVision OPO/OPA). An additional constant is included to fine tune the overlap of the ion beam and IR beam to maximise the photodissociation (typically, this is on the order of 5 – 15 µs). The triggering of the WM plates is then used as the time-zero (t_0) for the ToF spectrum. Pulse widths, triggers, and delays are controlled using a pulse generator (Berkeley Nucleonics Corporation Model 565).

2.2 Free-Electron Laser Experiment - HFML-FELIX Facility, Nijmegen

In addition to the studies performed on the IRPD instrument at the University of Oxford, Chapter 5 details the work that was performed using the infrared free-electron laser (IR-FEL) at the HFML-FELIX facility in Nijmegen, The Netherlands [229]. This work had originally planned to study the cationic tantalum clusters $[Ta_n]^+$, and how they interact with nitrogen oxides (NO_x, namely nitric oxide and nitrous oxide).

2.2.1 Nijmegen Experimental Setup

Figure 2.12 provides a simple illustration of the experimental layout used to study gas-phase metal clusters using the free-electron laser beamline, FELICE (Free-Electron Laser for Intra-Cavity Experiments, up to $100 - 2000$ cm^{-1}).[230–232] As was the case for the IRPD instrument at the University of Oxford, it relies on a setup that produces metal-containing species in a source before they are irradiated with light from an IR source and then analysed using mass spectrometry. The experiment is carried out at a background pressure of $\sim 10^{-6}$ mbar through the use of a 1200 L/s turbomolecular pump. Unlike the IRPD experiment, the experimental instrument utilises a Smalley-type ablation cluster source rather than a "cutaway" source in order to produce a molecular beam that contains metal clusters rather than metal ion-ligand complexes. The source chamber also

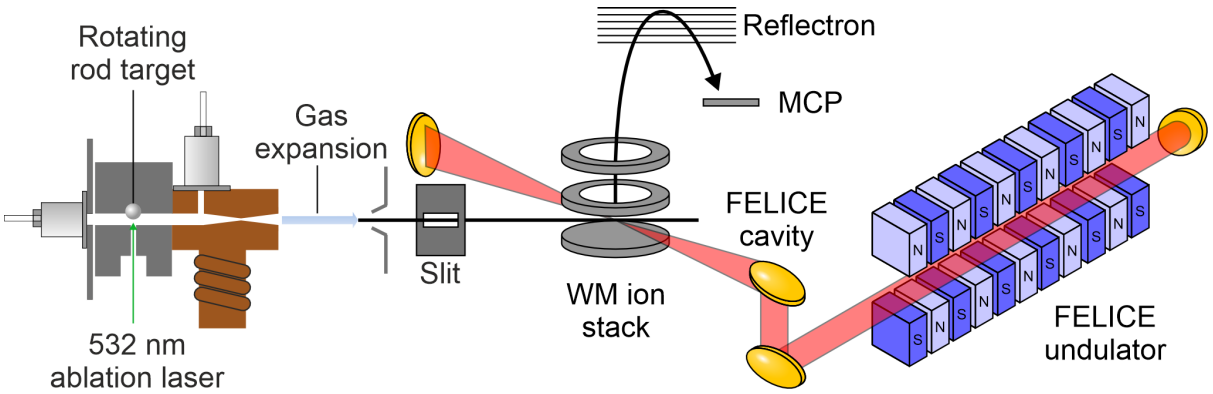

Figure 2.12: The layout of the experimental setup at the HFML-FELIX facility, Nijmegen, The Netherlands (not to scale). The clusters are produced from the cluster source (left side), before being extracted into the ReToF mass spectrometer (centre). A counter-propagating IR beam from the FELICE beam line (right side) is directed between the repeller and extractor plates of the WM ion optics. The ions pass through the FELICE cavity in order to experience very high laser powers.

---

possesses a clustering channel (3 mm diameter, 60 mm length) to maximise the number of collisions between metal atoms and the carrier gas following the laser ablation in order to produce metal clusters. The gas pulse used to entrain the clusters was produced using a Parker Series 9 General Valve using an Ar in He gas mixture (between $10-15\%$). Rather than using a disc target pressed against the source block, a metal rod ($\sim$ 5 mm in diameter, $\sim$ 20 cm long) is inserted into the clustering channel, thus ensuring that all of the ablated material is contained within the channel. The rod is rotated whilst being translated in or out of the channel, before being ablated using the second harmonic of a 20 Hz pulsed Nd:YAG laser (532 nm, 8 ns pulse width). The focal point of the ablation laser is finely controlled using a translating focussing lens positioned within the beamline, and its pulse energy can be controlled from the power supply (laser pulse energy: $\sim 10-15$ mJ).

Attached to the end of the main source block is a short copper reaction channel (3 mm diameter, 45 mm length). Here, an additional pulsed solenoid valve is attached to the reaction channel block, which is used to add reactant gas, such as nitric oxide, after the production of the clusters earlier in the source block. The backing pressure and opening duration can be fine tuned to control how much reactant is added in the channel, so that clusters will have one ligand adsorbed to them. Reactant gases such as NO or O_2 can

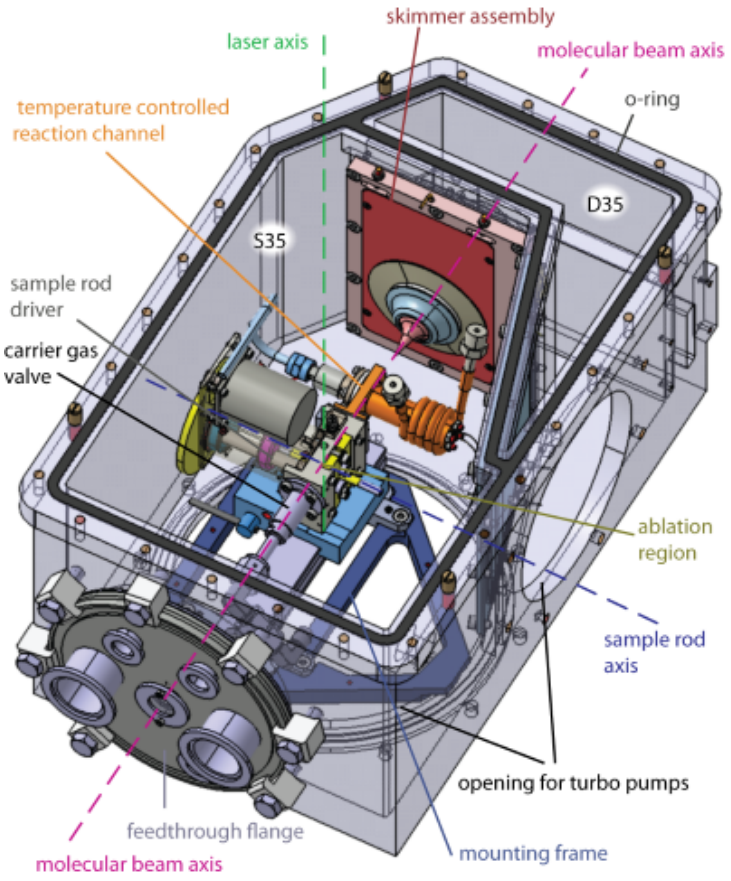

Figure 2.13: A CAD diagram of the cluster source used at HFML-FELIX, along with the details of its internal components. Reproduced with permission from the thesis of O.Lushchikova.[232]

---

be added *via* this secondary valve to form tantalum oxide clusters. The reaction channel can also be cooled down to 77 K using liquid nitrogen, or the cooling can be regulated by using a heating tape to set the temperature of the nozzle between 77 K and room temperature. The carrier gas collides with the cluster source's walls, where some of its kinetic energy is imparted, before it then goes on to collide with the clusters and cools them down further. By having additional control over the temperature of the cluster source, it can allow the cluster distribution to be altered; meaning that more clusters of a specific size, or with a specific number of ligands, can be produced. Mass spectra were recorded over a range of temperatures when conditions were optimised for specific cluster sizes. Additional nozzle attachments were added to the clustering channel to increase the source channel pressure, which increased the likelihood that the ligands were attached to the clusters, but also reduced the overall ion signal. The clusters within the

clustering channel expand into vacuum to produce a cold supersonic molecular beam that propagates along the experimental axis (see Figure 2.12). A detailed CAD diagram of the cluster source used in the experiment is provided in Figure 2.13.

A skimmer is used to collimate the beam before it is then reshaped by a small rectangular aperture (either 2 mm or 0.45 mm in height) to select which part of the ions meet the laser, and in turn improve the contrast when the IR light is turned on and off. The cluster beam travels towards the WM ion optics to extract the species into the reflectron time-of-flight mass spectrometer. There is no quadrupole mass filter in this setup, meaning no mass selection is possible, and the mass spectrum will contain all species that are produced and detected by the MCP plates. The experiment operates at 20 Hz, and the main IR source (FELICE) operates at 10 Hz. The IR-MPD spectra can then be expressed as an absorption cross section $\sigma(\nu)$, using an adapted version of Equation 2.4:

$$\sigma(\nu) = -\frac{1}{\Phi(\nu)} \ln\left(\frac{I_{\text{on}}(\nu)}{I_{\text{off}}(\nu)}\right), \tag{2.7}$$

where $\Phi(\nu)$ is the intra-cavity FELICE energy, and I_{on} and I_{off} are the FEL-on and FEL-off ion signals, respectively.

2.2.2 Infrared Light Source - FELICE

The clusters in the Nijmegen instrument are intercepted at a 35° angle by the FELICE IR beam. There are some notable differences between the two experimental setups; mainly how the IR light is generated, and the fact that the Nijmegen experiment is an intracavity experiment. The light source is a free-electron laser; a high fluence, tunable light source that produces intense beams of electromagnetic radiation. FELs have been developed that allow them to produce radiation ranging from microwaves to hard X-rays.[233–236] Unlike conventional lasers, which rely on bound electrons in atoms or molecules to generate light at fixed wavelengths, a FEL uses relativistic free electrons (not bound to atoms) moving through an oscillatory magnetic structure. Figure 2.14 provides an illustration of how light is produced within a FEL. An electron gun is used to generate a beam of free electrons before they are accelerated to relativistic speeds using a linear accelerator (Linac). The beam is then guided into an array of alternating magnets known as an undulator. The two rows of alternating magnets cause the electrons to move in a

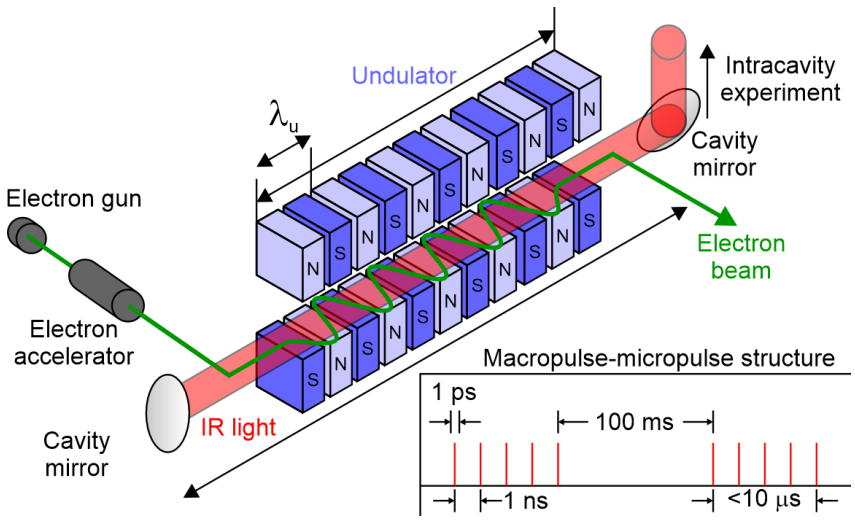

Figure 2.14: The production of infrared light in the free-electron laser at HFML-FELIX. The light and dark blue blocks represent north and south poled magnets, respectively, in the undulator. The light generated in the undulator is then directed towards the extraction optics. Unlike the other beamlines at HFML-FELIX, the light is not outcoupled as the extraction optics are placed within the optical cavity. In the bottom right corner, the structure of the beam is presented; comprising a train of micropulses within a macropulse (not to scale).

---

sinusoidal fashion due to the Lorentz force acting up the electrons as they pass through the oscillating field. The resultant acceleration of the charges causes monochromatic light to be emitted. The wavelength of the light emitted, λ_0, is given by the equation:

$$\lambda_0 = \frac{\lambda_u}{2\gamma^2}\left(1 + \left(\frac{\gamma\lambda_u}{2\pi\rho}\right)^2\right), \tag{2.8}$$

where λ_u is the undulator period (as shown in Figure 2.14), and ρ is the radius of the electron curvature, which depends on the magnetic field. γ is the Lorentz factor and is defined as:

$$\gamma = \frac{1}{\sqrt{1 - \frac{v^2}{c^2}}}, \tag{2.9}$$

where v is the speed of the electrons and c is the speed of light. The light that is generated by the electron acceleration can then be reflected by mirrors at either end of the cavity that the undulator is placed within. This causes the radiation to interact multiple times with the electron beam, enhancing the interaction through stimulated emission. The feedback loop amplifies light at certain resonant wavelengths that match the cavity

length and electron beam parameters.

Changing the frequency of light depends on the undulator period, λ_u, the electron beam's speed (energy), and the magentic field strength in the undulator. Practically, λ_u cannot be changed once the undulator is being used in an experiment, and the electron beam speed will be set for an experimental run as realignment and reoptimisation of the laser cavity can be a time-consuming procedure; especially in a time-limited beamtime run. This means that the wavelength is changed by adjusting the magnetic field strength, which is done by varying the distance between the two rows of magnets in the undulator using actuators. The pulses of light produced from the FEL adopt a micropulse/macropulse model. As shown in the bottom left corner of Figure 2.14, within each macropulse (10 µs width, up to 5000 mJ pulse energy) there is a train of intense micropulses ($0.2 - 10$ ps width, 1 ns spacing between micropulses, up to 1000 µJ pulse energy). On the time scales of IVR, multiple photons can be absorbed and lead to the photodissociation of tightly bound ligands in metal cluster-ligand complexes, $[M_nL]^+$; something that would not be possible with other IR light sources.

The FELICE beamline at Nijmegen is able to scan between *ca.* $100 - 2000$ cm^{-1}. When used for the work presented in this thesis, the IR laser was scanned from $\sim 640{-}2100$ cm^{-1} to investigate the ligand vibrations, before the electron beam energy was re-optimised to go to longer wavelengths ($\sim 260 - 800$ cm^{-1}). Furthermore, the cluster beam generated in the source intersects the FELICE beam in the cavity in which the undulator is placed. Rather than having an outcoupling hole where a set amount of the light from the FEL is released, as is the case for the other beamlines at HFML-FELIX and also at the Fritz Haber Institute (FHI) in Berlin,[237] this allows ions within the cavity to experience very high laser powers. This in turn can assist in dissociating, or in some cases ionising, more species which can be observed by changes in the mass spectrum.

Table 2.2: Calculated vibrational frequencies for the ligands under investigation in this thesis, calculated at B3P86/def2TZVP level of theory, along with the experimental frequencies and subsequent scaling factor.

Molecule	Calc. ν / cm^{-1}	Exp. ν / cm^{-1}	Scaling factor
Nitric oxide (NO)	2006.79	1875.84	0.9347
Nitrous oxide (N_2O) (N=N stretch)	2384.98	2223.5	0.9323
Nitrogen dioxide (NO_2) (asymmetric stretch)	1752.83	1616.85	0.9224

2.3 DFT Calculations for Metal Complexes / Metal Clusters

In Chapters 3 – 5, DFT calculations were performed to assist in the assignment of experimental spectra. All calculations were performed using Gaussian16 with the B3P86/def2TZVP functional/basis set combination.[188, 238–240] This hybrid functional has been chosen given its previous successful use within the Mackenzie Group that reproduces the experimental spectral features. The def2TZVP basis set is a second-generation "def" (default) basis set from the Karlsruhe group, with triple-zeta valence with polarisation (TZVP). This means that the valence orbitals are described by three basis functions (zeta = number of functions per orbital), which gives flexibility for chemical bonding, and the polarisation functions are added to better describe angular distortions in electron density. It has also been used by the group previously, as the basis set incorporates effective core potentials for the larger atoms (*i.e.* transition metals). This means that the core electrons for these elements that are not involved in chemical bonding can be described by an effective potential, rather than treating them explicitly, making the calculations less computationally expensive.

As described in Chapter 1, the starting structures can be generated either by using chemical intuition (*i.e.* placing ligands or atoms in positions that one would expect them to reside) or by using the *Kick*[3] algorithm.[198] These structures must be optimised (*i.e.*

their energies must be minimised) before their harmonic vibrational frequencies are calculated. In addition, the vibrational frequencies were scaled to account for the effect of anharmonicity. For the ligands of interest in this thesis, nitric oxide (NO), nitrous oxide (N_2O) and nitrogen dioxide (NO_2), their vibrational frequencies were calculated using the B3P86/def2TZVP combination. The scaling factor is then determined as the reciprocal of the ratio of the calculated value compared to the known experimental vibrational frequency for specific vibrations (*e.g.*, the N=N stretch within the N_2O molecule). The scaling factors are shown in Table 2.2.

Part A: Infrared Studies on Metal Ion–Ligand Complexes

Chapter 3

An Infrared Study of Gas-Phase Metal Nitrosyl Ion-Molecule Complexes, $[M(NO)_n]^+$ (M = Co, Rh, Ir, n = 3-7)

This chapter contains a published article detailing an infrared photodissociation (IR-PD) study of cationic gas-phase Group 9 metal nitrosyls complexes, $[M(NO)_n]^+$ (M = Co, Rh, Ir, $n = 3-7$). The complexes were formed by ablating the metal targets in a beam of Ar seeded with NO. IRPD spectra were recorded in the NO stretch region ($1600-2000\,cm^{-1}$), with supporting DFT calculations being used to aid in assigning the spectral bands by generating predicted structures with their corresponding simulated IR spectrum.

The NO ligands within the $[M(NO)_n]^+$ complexes have been observed to bind linearly and nonlinearly to the metal centre, with clear evidence that the Co and Ir complexes can accommodate up to four ligands within their first coordination shells. The $[Rh(NO)_n]^+$ IRPD spectra differ from the other two metals because there is a pronounced redshift in the spectral features as the complex size increases; suggesting that the ligands within the

complex are interacting in a different way than with the other metals. This idea is further supported by the emergence of low-lying calculated structures that can accommodate five ligands. In all of the complexes, spectral evidence of NO dimer moieties, $(NO)_2$, appears once the first coordination shell of the complexes has been filled. Additional evidence of the dimer moiety is provided by spectral differences recorded in the dissociation channels for the loss of one and two ligands.

The results of this chapter were collected in the Mackenzie Group laboratory in Oxford. The Group 9 nitrosyl work, both computationally and experimentally, was completed jointly by myself, Dr. Gabriele Meizyte, Dr. Edward Brewer, Dr. Peter Watson, Dr. Alice Green, Olga Duda, and Matthew Doll. The Statement of Authorship form detailing the contributions to this paper is attached at the end of this chapter. As this chapter comprises the article published in The Journal of Physical Chemistry A, the numbering and labelling of the figures, equations, and references will be specific and will not relate to the styles used in the rest of the thesis.

The page numbers displayed at the bottom are for the journal in which the paper was published. For the reader, this chapter runs from page 81 to 95 of the thesis.

THE JOURNAL OF PHYSICAL CHEMISTRY A
A JOURNAL OF THE AMERICAN CHEMICAL SOCIETY

pubs.acs.org/JPCA

Article

An Infrared Study of Gas-Phase Metal Nitrosyl Ion−Molecule Complexes

Published as part of The Journal of Physical Chemistry virtual special issue "Marsha I. Lester Festschrift".

Gabriele Meizyte, Philip A. J. Pearcy, Peter D. Watson, Edward I. Brewer, Alice E. Green, Matthew Doll, Olga A. Duda, and Stuart R. Mackenzie*

Cite This: *J. Phys. Chem. A* 2022, 126, 9414−9422

Read Online

ACCESS | Metrics & More | Article Recommendations | Supporting Information

ABSTRACT: We present a combined experimental and quantum chemical study of gas-phase group 9 metal nitrosyl complexes, $M(NO)_n^+$ (M = Co, Rh, Ir). Experimental infrared photodissociation spectra of mass-selected ion-molecule complexes are presented in the region 1600 cm^{-1} to 2000 cm^{-1} which includes the NO stretch. These are interpreted by comparison with the simulated spectra of energetically low-lying structures calculated using density functional theory. A mix of linear and nonlinear ligand binding is observed, often within the same complex, and clear evidence of coordination shell closing is observed at n = 4 for $Co(NO)_n^+$ and $Ir(NO)_n^+$. Calculations of $Rh(NO)_n^+$ complexes suggest additional low-lying five-coordinate structures. In all cases, once a second coordination shell is occupied, new spectral features appear which are assigned to $(NO)_2$ dimer moieties. Further evidence of such motifs comes from differences in the spectra recorded in the dissociation channels corresponding to single and double ligand loss.

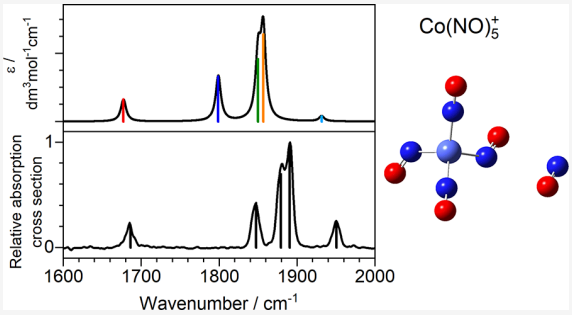

1. INTRODUCTION

Nitrogen oxides (NO_x) are well-known for their detrimental effects on the environment and as a major source of air pollution harmful to human health.[1,2] Although formed naturally, e.g., in lightning and/or forest fires, anthropogenic sources represent a significant fraction of NO_x production. Both NO_2 and NO are generated by the internal combustion engine, and this has led to the introduction of stringent emission controls.[3,4] Current mitigation strategies include the widespread use of automobile catalytic converters which harness surface catalytic chemistry of finely dispersed transition metals.[5,6] In turn, this has stimulated extensive research aimed at developing a better understanding of this chemistry including that of nitric oxide, NO, the subject of this work. For its role in both the environment and in biology, NO was named *Science* magazine's molecule of year for 1992[7] and a whole edition of *Chemical Reviews* was dedicated to NO chemistry.[8]

Atomic ions and small gas-phase metal clusters can represent tractable model systems, providing molecular level insight into fundamental metal−ligand interactions, including those important in catalytic chemistry, free of complications arising from substrates, solvation, or aggregation.[9] The thermal reactivity of NO with a wide range of gas-phase metal cations has been studied by Bohme and co-workers by inductively coupled plasma/selected-ion flow tube (ICP/SIFT) tandem mass spectrometry.[10] This revealed extensive and varied chemistry involving electron donation and both atom acceptor and donor reactions. Relevant to the metal centers studied here, a mix of molecular and dissociative NO binding on Co_n^+ clusters has been observed under different conditions.[11−14] $Rh_n^±$ reactions with NO have been studied extensively under single[15−17] and multiple collision conditions, and the chemistry has been reviewed recently.[18] There have also been spectroscopic studies of NO binding to Au_n^+ and Ir_n^+ clusters.[19,20]

NO is an intriguing ligand in coordination chemistry. A kinetically inert, stable radical, it exhibits a range of different binding motifs, coordinating formally via one- or three-electron donation, and nitrosyl complexes often exhibit very different chemistry to their carbonyl analogues.[21] The open-shell nature of nitric oxide presents particular challenges for quantum chemical calculations. Blanchet et al. employed density functional theory (DFT) to study first row transition metal atom-NO molecules. They established nonlinear binding

Received: October 14, 2022
Revised: November 21, 2022
Published: December 8, 2022

https://doi.org/10.1021/acs.jpca.2c07228
J. Phys. Chem. A 2022, 126, 9414−9422

through the N atom in CoNO arising from the Co 3d and 4s orbitals with the highest occupied 5σ orbital in NO with a triplet ground state favored due to symmetry breaking.[22] Bauschlicher and Hall applied DFT and coupled cluster calculations to the equivalent cationic species and, for $CoNO^+$, found a linear geometry preferred.[23]

This work presents an infrared photodissociation (IR-PD) study of NO binding to group 9 cations $Co(NO)_n^+$, $Rh(NO)_n^+$, and $Ir(NO)_n^+$ (n = 3−7) with interpretation aided by comparison with simulated spectra of low-energy structures calculated by DFT. The present work follows detailed IR-PD studies of $M(NO)_n^+$ (M = Fe, Cu, Ag, and Au) complexes by Zhou and co-workers which showed marked differences in the structures adopted for different metal ions.[24−26] $Fe(NO)_n^+$ structures exhibit linear (three-electron) binding until closure of the first coordination shell is achieved at 4, with the messenger Ar tag atoms leading to strong distortions.[24] $Cu(NO)_n^+$ complexes are characterized by bent (one-electron) binding and significant ligand−ligand interactions with clear evidence of bidentate dimer $(NO)_2$ ligand.[25] Nonlinear ligand binding and dimer structures were also observed in $Ag(NO)_n^+$ and $Au(NO)_n^+$ complexes albeit with first coordination shells of 4 and 2, respectively.[26]

2. EXPERIMENTAL AND COMPUTATIONAL METHODS

The experimental setup has been described in detail previously[27,28] and modified recently to include the mass selection of ions via a quadrupole mass filter.[29] Briefly, a rotating disc target of the required metal (Co, Rh, or Ir) is ablated at 532 nm by a pulsed Nd:YAG laser (10 Hz, ca. 2−10 mJ as necessary). Ablated species are entrained in a gas pulse of Ar seeded with 1−5% NO which expands into the vacuum forming a molecular beam with the higher NO mole fractions required for efficient generation of $Ir(NO)_n^+$. The beam is skimmed before passing through a quadrupole mass filter−quadrupole bender assembly and then entering the extraction region of a reflectron time-of-flight (ToF) mass spectrometer.

To record IR-PD spectra, the cluster beam is subjected to tunable pulsed infrared radiation from a tabletop optical parametric oscillator/optical parametric amplifier (OPO/OPA, Laservision) system, operating in the 1600−2000 cm^{-1} range. Following mass-selection of the parent ion−molecule complex, spectra are recorded as a function of wavenumber in the daughter fragment channels against a zero background.

To account for variations in the infrared pulse energy across the wavenumber region scanned, spectra are reported here in terms of a normalized cross-section in a given fragment channel using a modified Beer−Lambert law:[30]

$$\sigma = -\frac{\log\left(1 - \frac{N_f}{\alpha N_0}\right)}{\Phi} \quad (1)$$

in which σ is the absorption cross-section, N_f and N_0 correspond to the intensity of the fragment and parent signals, respectively, and Φ is the photon flux. The factor α describes the overlap between the ion beam, and the infrared beam and is assumed to be 1. Spectra are normalized to the strongest peak in the spectrum.

To aid assignment, experimental $M(NO)_n^+$ IR-PD spectra are compared with simulated spectra of energetically low-lying structures determined from DFT using the Gaussian 16 software package[31] with novel potential structures generated by a modified KICK algorithm.[32] It is worth noting that open-shell ligands such as NO pose particular difficulties for DFT, as complexes often give rise to multiple low-lying electronic states as well as large numbers of isomeric forms.[33] The B3P86[34,35]/def2TZVP[36,37] functional/basis set combination was used throughout, having proven reliable in similar studies by our group.[38,39] To provide a better match with experimental data, computed harmonic vibrational frequencies were scaled by a factor of 0.9347, determined by calculating the vibrational frequency of the free NO stretch which is found experimentally at 1876 cm^{-1}.[40] Calculated spectral lines are convoluted with Lorentzian line shapes with full width half-maximum (fwhm) = 8 cm^{-1} to aid comparison with spectra. All energies reported here include zero-point energy corrections. Only molecularly bound ligands have been considered, as these are the only structures expected to exhibit spectra in our experimental region. Dissociatively bound complexes lie substantially lower in energy, but access to these minima is kinetically hindered by large activation barriers.

3. RESULTS AND DISCUSSION

A. Time-of-Flight Mass Spectra. A typical time-of-flight mass spectrum produced by laser ablation of a Co target in the presence of NO seeded in Ar is given in Figure 1. The mass

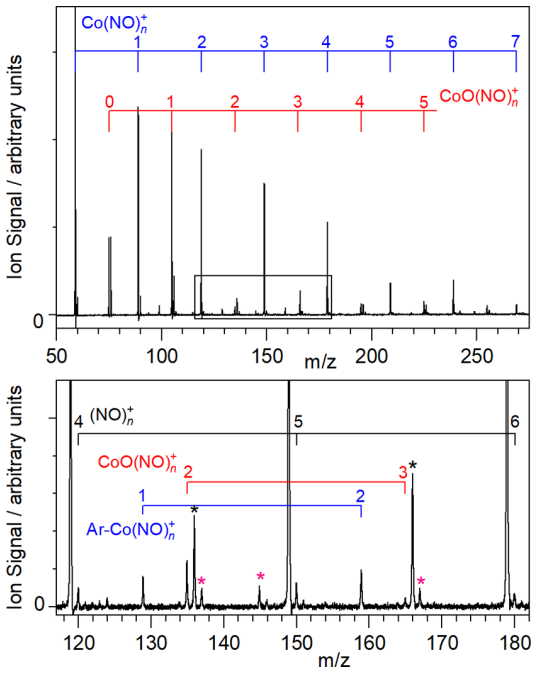

Figure 1. Time-of-flight mass spectrum produced upon ablating the Co metal target in the presence of NO in Ar gas mix (1.5%). The lower panel shows an expanded region indicated in the top panel. Other species observed include $[O(NO)_n]^+$ complexes (black asterisks), Ar-tagged peaks and water-containing species (red asterisks).

spectrum is dominated by the $Co(NO)_n^+$ peaks. Smaller mass species are favored under expansion conditions used here, with a marked drop in signal intensity for n > 4 which is suggestive of a first coordination sphere of four ligands. Consistent with the reactivity study of Bohme and co-workers, CoO^+ and $CoONO^+$ are also formed in significant number densities[10] along with several Ar-tagged species.

https://doi.org/10.1021/acs.jpca.2c07228
J. Phys. Chem. A 2022, 126, 9414−9422

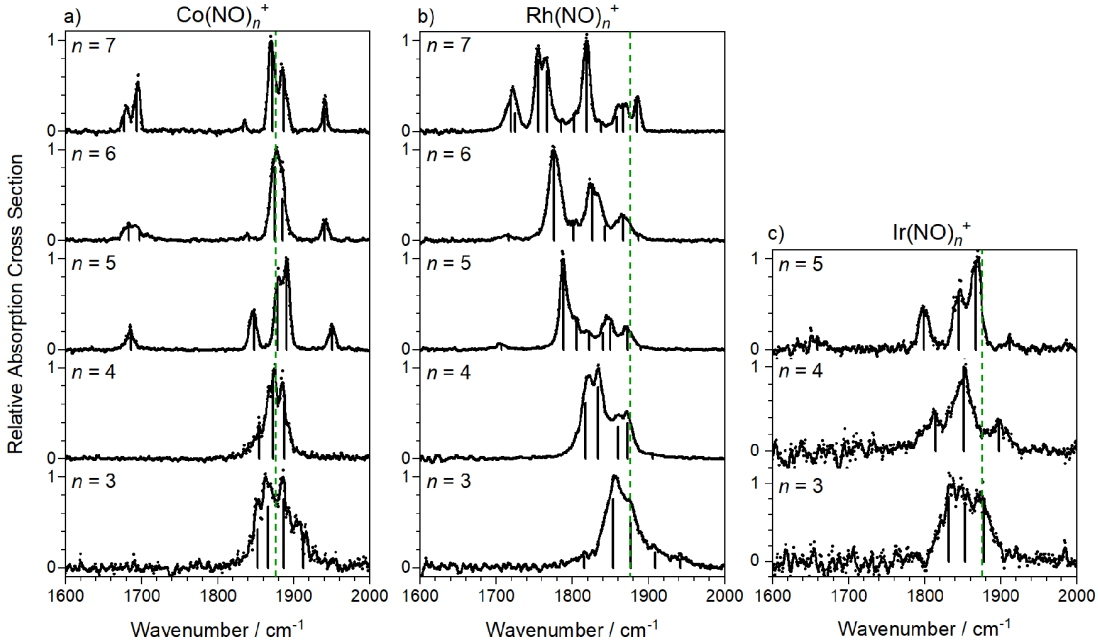

Figure 2. Infrared photodissociation spectra of (a) Co(NO)$_n^+$, (b) Rh(NO)$_n^+$, and (c) Ir(NO)$_n^+$ complexes, recorded in the enhancement of the M(NO)$_{n-1}^+$ daughter channel and shown as normalized relative absorption cross-sections for each complex size. Vertical lines arise from fitting of the spectrum to Gaussian functions. Green dashed lines indicate the wavenumber of the free NO stretch at 1876 cm^{-1}.[41]

Mass spectra obtained following Rh and Ir ablation can be found in Supporting Information. The rhodium mass spectrum is cleaner than that for cobalt and is dominated by the progression of Rh(NO)$_n^+$ (n = 0−7) peaks whose intensity decrease monotonically with n with little obvious sign of clear coordination shells. Of the oxides, only [RhO(NO)$^+$] is formed in significant number density. Iridium has two stable isotopes of 191 u and 193 u, and this complicates the mass spectrum. Even so, the mass spectrum is markedly richer than the cobalt and rhodium. Below m/z = 300 the mass spectrum is dominated by strong Ir(NO)$_n^+$ and IrO(NO)$_n^+$ signals, the latter reflecting the O atom transfer reactivity of Ir$^+$ toward nitric oxide.[10] Perhaps as a result of this reactivity it proved impossible to generate Ir(NO)$_n^+$ (n > 5) in sufficient number density to record infrared spectra with acceptable signal-to-noise ratio.

In all mass spectra there is evidence for naked (NO)$_n^+$ and NO$_2$(NO)$_n^+$ clusters. These are produced within the ablation plasma, and their infrared action spectra will be the subject of a future study.

B. Infrared Spectra of M(NO)$_n^+$ Ion−Molecule Complexes. An overview of the infrared action spectra of M(NO)$_n^+$ (M = Co, Rh, Ir) complexes is shown in Figure 2. In all cases the dominant fragmentation observed following photoexcitation is NO loss, and the spectra shown are recorded against a zero background in enhancement in the daughter M(NO)$^+_{n-1}$ (i.e., simple NO loss) mass channel. Vertical lines shown under each spectrum represent the centers of Gaussian functions used to fit to the spectra from which trends in band positions can be extracted as well as providing an estimate of the number of bands contributing. For each spectrum, the full width at half-maximum was fixed to that of the most highly resolved band and the number of bands was guided by the number of infrared active modes in simulated spectra.

Negligible fragmentation was observed for the very smallest, n = 1, 2 complexes. This is common in IR-PD and reflects the fact that the first few ligands typically bind strongly to a metal center and that many photons are required to dissociate the complex. In the present case, the binding energies of each of the first two nitrosyl ligands is ≥1.4 eV (see Supporting Information), while the photon energy in this spectral region is ca. 0.20−0.25 eV (of course, the complexes have significant internal energy of their own). For similar reasons, the spectra of the n = 3, 4 complexes exhibit comparatively poor signal-to-noise ratios, reflecting their own weak fragmentation efficiency. Their broad, partially resolved appearance suggests that in these cases, too, multiple photons are needed to drive NO loss. By contrast, the infrared spectra of the larger M(NO)$_n^+$ (M= Co, Rh, Ir, n ≥ 5) complexes are both significantly better resolved and exhibit higher signal-to-noise ratios. This is consistent with the binding energy of the fifth (and higher) NO ligand being comparable with the IR photon energy (see Supporting Information).

The evolution of the Co(NO)$_n^+$ and Ir(NO)$_n^+$ spectra with cluster size is similar with most intensity observed close to the free NO stretch at 1876 cm^{-1} and new features appearing for larger complexes. In these regards the spectra are very similar to those reported previously for Fe(NO)$_n^+$.[24] The Rh(NO)$_n^+$ spectra, by contrast, are qualitatively different, and although there is a persistent band around the free NO stretch, a noticeable overall red shift in the IR spectrum is observed with increasing n and any satellite bands are much less prominent.

In the spectra of Co(NO)$_n^+$ complexes, a new pair of bands appears for larger (n ≥ 5) complexes with one band around 1680 cm^{-1} and another near 1950 cm^{-1}. Similar pairs of bands are visible in the Ir(NO)$_5^+$ spectrum and, to a lesser extent, the Rh(NO)$_n^+$ (n > 4) spectra. Zhou and co-workers have also reported very similar bands in the spectra of M(NO)$_n^+$ (M = Au, Ag, Cu, Fe). These bands have been attributed to the formation of a dimer, (NO)$_2$, motif forming following closure

https://doi.org/10.1021/acs.jpca.2c07228
J. Phys. Chem. A 2022, 126, 9414−9422

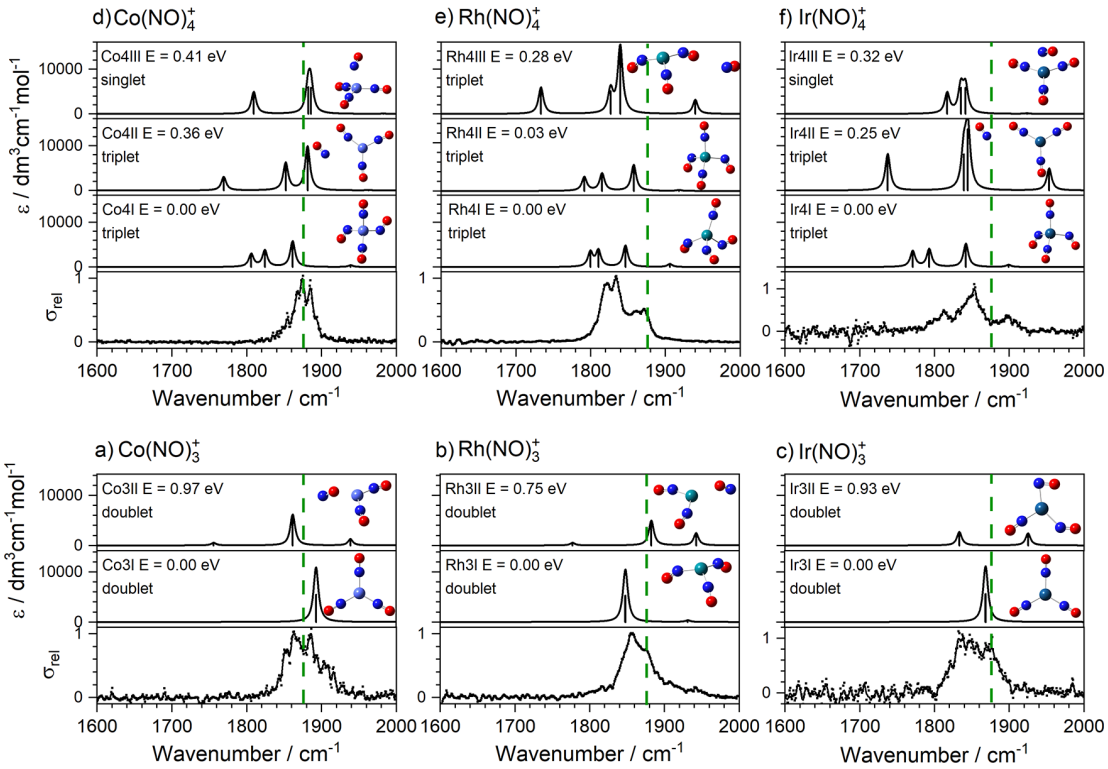

Figure 3. Comparison of experimental and simulated spectra for $M(NO)_n^+$ (M = Co, Rh, Ir; n = 3 (a–c), 4 (d–f)) complexes showing the lowest energy calculated structures only. Green dashed lines indicate the wavenumber of the free NO stretch at 1876 cm^{-1}.[40]

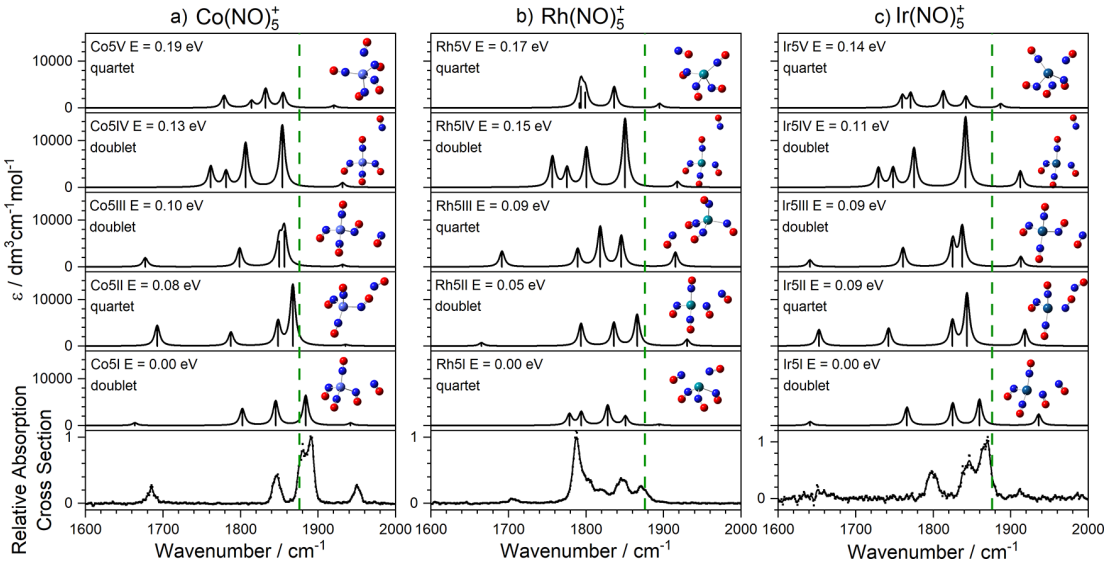

Figure 4. Comparison of experimental and simulated spectra of low-lying isomers for (a) $Co(NO)_5^+$, (b) $Rh(NO)_5^+$, and (c) $Ir(NO)_5^+$. In most cases the fifth ligand binds more weakly in a second coordination shell giving rise to new spectral features. Green dashed lines indicate the wavenumber of the free NO stretch at 1876 cm^{-1}.[40]

of the inner coordination shell.[24−26] The appearance of these bands is thus consistent with an inner coordination shell of four with the fifth ligand forced to start a new coordination shell and binding preferentially to one of the inner-shell ligands.

C. Comparison of Experimental and Simulated Spectra. The binding of the NO radical at charged metal centers is a complex balance of many contributing factors. The dominant electrostatic interaction is the charge−dipole attraction which favors N-binding with the proximity of the metal cation strongly polarizing the NO bond. In addition, there are multiple components of incipient chemical bonding arising from (i) NO lone-pair σ donation, (ii) π donation from the unpaired NO π^* electron, and (iii) π-back bonding from the occupied d orbitals on the metal center into the NO π^* orbitals. The relative contributions of these factors lead to subtle structural differences which are reflected in the infrared spectra. For example, σ-donation, in which NO acts formally as

https://doi.org/10.1021/acs.jpca.2c07228
J. Phys. Chem. A 2022, 126, 9414−9422

a three-electron donor, leads to near linear $M^+-N{=}O$ binding. By contrast, one-electron π^*-donation leads to nonlinear coordination.[42] The latter was found to dominate the structures of the coinage-metal nitrosyl complexes[25,26] while a mix of the two was invoked to interpret the spectra of $Fe(NO)_n^+$.[24]

Figure 3 shows a comparison of experimental and simulated spectra for the $M(NO)_n^+$ (M = Co, Rh, Ir, n = 3, 4) complexes. Extended versions of this figure with additional (higher-lying) calculated structures and electronic states are provided in Supporting Information. Notwithstanding the broad, unresolved nature of the experimental spectra, a few clear conclusions can be drawn. For n = 3 complexes, all low energy structures (within the lowest 1 eV) have doublet multiplicity. A clear lowest energy isomer is identified, labeled M3I (M = Co, Rh, Ir), whose simulated spectrum accounts well for that observed. Co3I and Ir3I are planar D_{3h} structures with rigidly linear ligand binding indicating the dominance of (three-electron) σ-donation. By contrast, the bent C_{3v} Rh3I reflects π-donation. There is negligible evidence of ligand activation in either the wavenumber of the spectral bands or the calculated NO bond lengths. In all cases ligands bind via the nitrogen atom with, at most, weak evidence for the presence of energetically higher-lying O-bound structures.

The lowest energy $M(NO)_4^+$ structures are all triplet multiplicity, tetrahedral-based, N-bound structures. We calculate low-lying excited electronic states for each species (see Supporting Information) as well as multiple isomeric structures on the ground-state surface, some of which include a second coordination shell (e.g., Co4II, Rh4III, and Ir4II). There is, however, little evidence for these structures in the experimental spectra. In both $Co(NO)_4^+$ and $Ir(NO)_4^+$ the lowest energy structures identified (Co4I and Ir4I) have two linear and two nonlinear bound ligands. Again, though, the effect on the bond lengths is negligible. The equivalent $Rh(NO)_4^+$ structure (Rh4II) lies just 0.03 eV higher than the lowest energy Rh4I structure, with three of its ligands bound nonlinearly. There is little in the experimental spectrum to distinguish between them, and it is possible that both are present.

With the addition of a fifth ligand, our calculations show the opening of a second coordination shell and binding in dimer motif to one of the inner ligands (Figure 4). The exception is the lowest energy calculated structure for $Rh(NO)_5^+$ (structure Rh5I) which shows a five-coordinate structure. The weaker binding in the second shell gives rise to a richer distribution of both low-lying electronic states (doublet and quartet states) and structural isomers predicted as shown in Figure 4. In all cases, the signature of the $(NO)_2$ motif is provided by the new vibrational bands, most prominent in the spectrum of $Co(NO)_5^+$ at 1680 and 1950 cm^{-1} but also visible in the other two complexes.

In the case of $Co(NO)_5^+$ and $Ir(NO)_5^+$ there is convincing agreement between the experimental spectrum and that of the energetically low-lying structures. Figure 5 shows one such comparison for the $Co(NO)_5^+$ spectrum with the simulated spectrum of structure Co5III (E = 0.1 eV above the lowest energy calculated structure). This structure exhibits an NO-dimer in trans form though the isomerism of the dimer has very minor effect on the spectrum. Figure 5 also depicts the ligand vibrations responsible for the five high frequency infrared active bands in this region (labeled A–E). The A mode at ca. 1680 cm^{-1} is highly localized and arises from the antisymmetric motion of the two ligands comprising the dimer

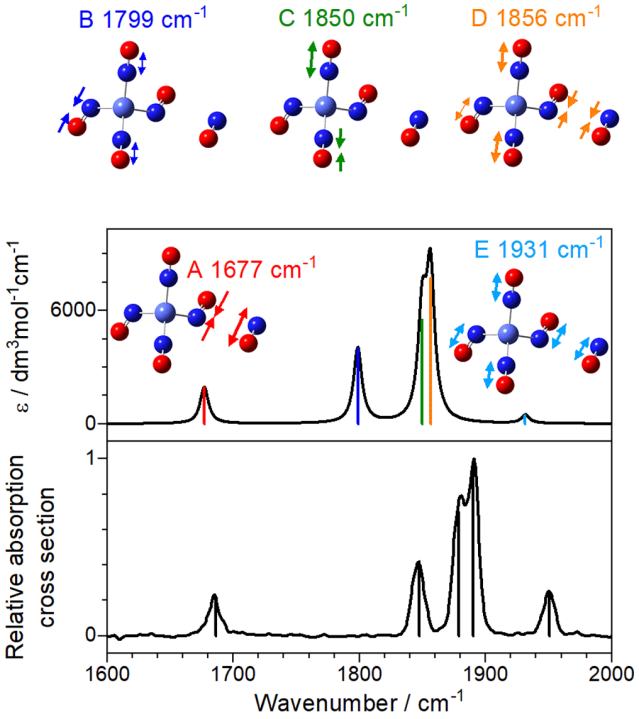

Figure 5. A comparison of the experimental and computational spectrum (Co5III) for $Co(NO)_5^+$ with color-coded mode vectors.

moiety. The red-shift in this band reflects weak activation of the inner of the two dimer ligands whose bond length (1.146 Å) is slightly longer than that of its partner (1.119 Å). The B mode comprises out-of-phase vibrations of the three nondimer ligands, mainly that opposite the dimer. The C mode (calculated at 1850 cm^{-1}, observed at 1880 cm^{-1}) involves out-of-phase motion of the two near linear bound ligands. Finally, the two highest frequency modes, D and E, comprise concerted motion of all ligands with the symmetric vibration in the dimer either in-phase (mode E) or out-of-phase (D) with the other ligands. A mode analogous to the symmetric "breathing" mode E appears in the simulated spectra of all tetrahedral n = 4 complexes, but in this case it gains oscillator strength from the lower symmetry arising from the fifth ligand.

The lowest energy calculated structures (and, thus, spectra) of $Ir(NO)_n^+$ are very similar to those of the $Co(NO)_n^+$ complexes (Figure 4). The agreement between simulated and experimental spectra is not quite as good for the $Rh(NO)_n^+$ complexes, but the dimer motif is almost certainly signified by the band around 1700 cm^{-1}. No single isomer provides as convincing a fit as that for the $Co(NO)_5^+$ complex in Figure 5. In particular, the most intense feature at 1790 cm^{-1} is missing from most simulated spectra. However, even a small frequency shift in a single band (for example, in the spectra of structures Rh5I or Rh5 V) would recover it.

The spectra of the $Co(NO)_n^+$ complexes do not change markedly as sixth and seventh ligands bind, with the exception of the dimer band around 1680 cm^{-1} which splits into (at least) two bands as more dimer moieties form. Figures 6 and 7 contain the comparison of experimental and simulated spectra for energetically low-lying structures of n = 6, 7 complexes, respectively. The spectra of the $Rh(NO)_n^+$ complexes continue more significant evolution with additional ligands. The trend for the overall spectrum to shift further red of the free NO

https://doi.org/10.1021/acs.jpca.2c07228
J. Phys. Chem. A 2022, 126, 9414–9422

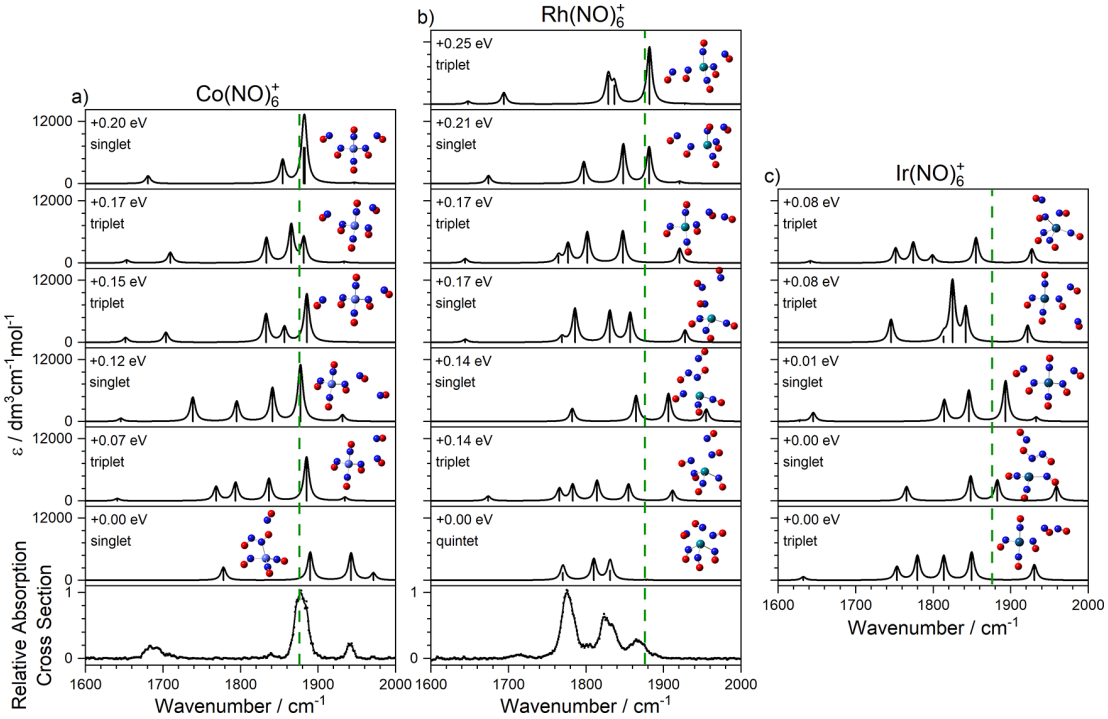

Figure 6. Comparison of experimental and simulated spectra of low-lying isomers for (a) $Co(NO)_6^+$, (b) $Rh(NO)_6^+$, and (c) $Ir(NO)_6^+$. Green dashed lines indicate the wavenumber of the free NO stretch at 1876 cm^{-1}.[40]

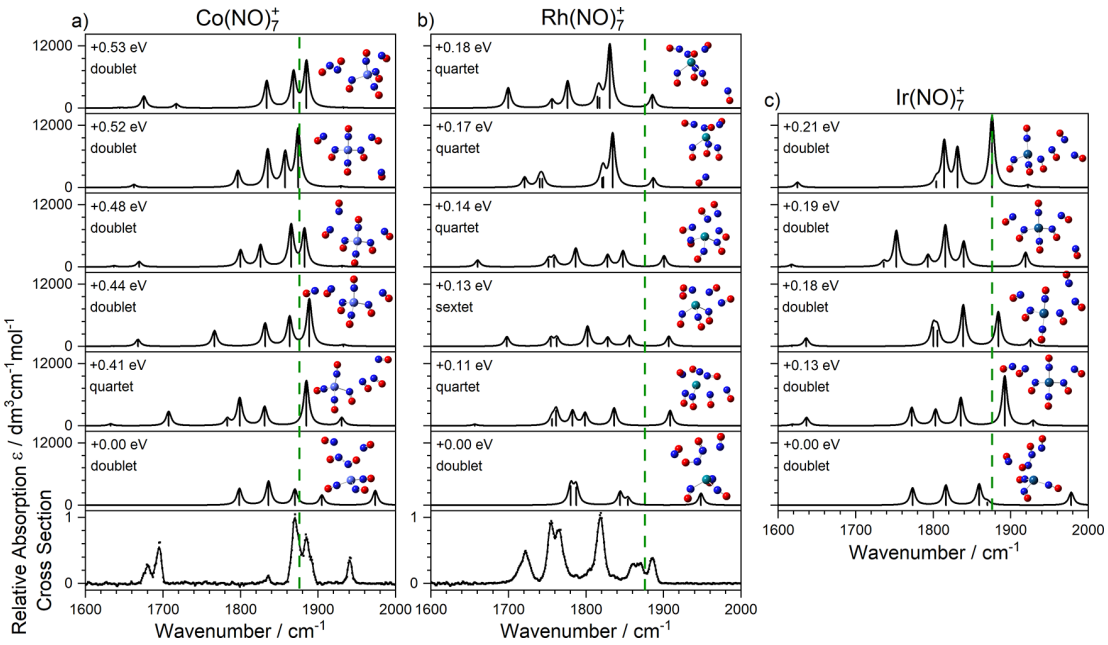

Figure 7. Comparison of experimental and simulated spectra of low-lying isomers for (a) $Co(NO)_7^+$, (b) $Rh(NO)_7^+$, and (c) $Ir(NO)_7^+$. Green dashed lines indicate the wavenumber of the free NO stretch at 1876 cm^{-1}.[40]

stretch continues, and more low-lying electronic states are predicted than for Co^+ or Ir^+ complexes. The origin of the increased red-shift observed in the spectra of $Rh(NO)_n^+$ complexes may lie in the increased propensity for nonlinear (one-electron) binding with Rh^+. As a result, the addition of more ligands leads to more effective back-bonding into the NO π^* system. This is consistent with the smaller spectral shifts and reduced intensity of the dimer bands in the $Rh(NO)_n^+$ complexes. Despite the apparent simplicity of the spectra observed, however, it is difficult to make unambiguous assignments beyond the presence of dimer structures, and it seems likely that more than one isomer and/or electronic state is present.

D. Different Dissociation Channels. The spectra shown above in Figures 2−7 were all recorded in the daughter fragment channel corresponding to the loss of a single NO ligand. In some cases, especially for larger complexes, weaker additional fragment channels were observed which provide

https://doi.org/10.1021/acs.jpca.2c07228
J. Phys. Chem. A 2022, 126, 9414−9422

additional information on the structure of the complex. At a basic level, the degree of fragmentation observed provides additional information on coordination shells with the $Co(NO)_n^+$ ($n > 6$) showing loss of two ligands consistent with a first coordination shell of 4 (see Supporting Information).

Further structural information is provided by the spectra recorded in the −2(NO) (*i.e.*, double ligand loss) fragmentation channels for $Co(NO)_n^+$ ($n = 6, 7$) and $Rh(NO)_n^+$ ($n = 6, 7$) as shown in Figure 8. In the $Co(NO)_n^+$ spectra at least

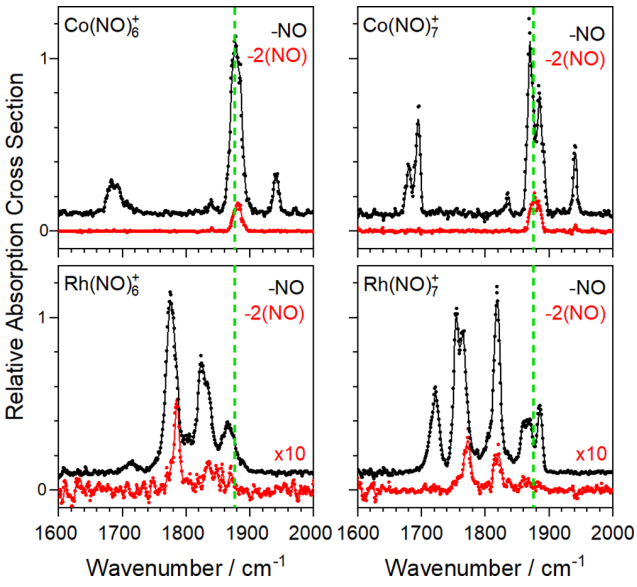

Figure 8. IR-PD spectra of $Co(NO)_n^+$ ($n = 6–7$) (upper panels) and $Rh(NO)_n^+$ ($n = 6–7$) (lower panels) species, recorded in different fragmentation channels: −NO (black line), −2(NO) (red line). Spectra are given in terms of normalized absorption cross-sections for the −NO channel (black line), and the other channel is scaled accordingly as shown. The NO loss channel spectrum data is shown offset vertically for clarity. Green dashed lines indicate the wavenumber of the free NO stretch at 1876 cm^{-1}.[40]

some components of the strong bands in the central (1750–1900 cm^{-1}) spectral region appear in both the single, −(NO), and the double, −2(NO), loss channel. The same is true in the $Rh(NO)_n^+$ spectra though some of the bands are noticeably narrower and slightly blue-shifted in the −2(NO) channel. It is possible that only one spectral component in a blended band is observed in the double-loss channel. In all cases, however, the peripheral bands, while clear in the −NO loss channel, are essentially absent in the −2(NO) spectra. We interpret this as further confirmation that the outer spectral bands in the spectrum (especially the low frequency band) arise from the dimer moiety (see Figure 5). In these bands, once a first photon is absorbed, a ligand from the outer coordination shell is lost and, with it, crucially the chromophore itself. As a result, no subsequent photon can be absorbed at the same wavenumber to remove a second ligand. These results strongly suggest that the dimer $(NO)_2$ moiety itself is not lost as an intact entity but rather the −2(NO) channel comprises two sequential single loss processes. This is consistent with the strength of binding direct to the metal center exceeding the one-photon energy. By contrast, the more central IR modes, which do not involve motion of the dimer (See Figure 5), can absorb more than one photon, leading to the loss of two ligands. In this way, differences in the spectra recorded in different fragment mass channels provide exquisite detail on the nature of the vibrational mode excited.

4. CONCLUSIONS

A comparison of infrared action spectra with simulated spectra of calculated low energy isomers has revealed the structures of $M(NO)_n^+$ (M = Co, Rh, Ir) ion−molecule complexes. Notwithstanding the difficulties of applying DFT to multiple open-shell ligands, some clear structural features are observed, including evidence of complete coordination shells. A mix of linear and nonlinear ligand binding motifs is also observed, often within the same complex, and a range of energetically low-lying isomers and/or electronic states is found for all complexes with $n \geq 4$. The $Co(NO)_n^+$ and $Ir(NO)_n^+$ complexes exhibit similar spectra/structures throughout the size range studied. The spectra of the $Rh(NO)_n^+$ complexes appear qualitatively different which may result from an increased propensity for nonlinear (one-electron) ligand binding.

In common with previous studies of gas-phase metal nitrosyl complexes, there is clear evidence for the formation of NO dimers once binding in a second coordination shell occurs at $n \geq 5$. New spectral features appear that are not present in the spectra of smaller complexes, including a strongly red-shifted band (≤1700 cm^{-1}). Further evidence for some of the vibrational mode assignments comes from the difference in the action spectra observed in different fragmentation channels, illustrating the benefits of parent ion mass-selection.

■ ASSOCIATED CONTENT

Supporting Information

The Supporting Information is available free of charge at https://pubs.acs.org/doi/10.1021/acs.jpca.2c07228.

Additional time-of-flight spectra, computational structure details, comparison of experimental and simulated spectra for additional complex sizes, photofragment time-of-flight spectra, relative energy of electronic states (PDF)

■ AUTHOR INFORMATION

Corresponding Author

Stuart R. Mackenzie − *Department of Chemistry, University of Oxford, Physical and Theoretical Chemistry Laboratory, Oxford, United Kingdom OX1 3QZ*; orcid.org/0000-0002-3166-8631; Email: stuart.mackenzie@chem.ox.ac.uk

Authors

Gabriele Meizyte − *Department of Chemistry, University of Oxford, Physical and Theoretical Chemistry Laboratory, Oxford, United Kingdom OX1 3QZ*

Philip A. J. Pearcy − *Department of Chemistry, University of Oxford, Physical and Theoretical Chemistry Laboratory, Oxford, United Kingdom OX1 3QZ*

Peter D. Watson − *Department of Chemistry, University of Oxford, Physical and Theoretical Chemistry Laboratory, Oxford, United Kingdom OX1 3QZ*; orcid.org/0000-0002-8195-1232

Edward I. Brewer − *Department of Chemistry, University of Oxford, Physical and Theoretical Chemistry Laboratory, Oxford, United Kingdom OX1 3QZ*

Alice E. Green − *Department of Chemistry, University of Oxford, Physical and Theoretical Chemistry Laboratory, Oxford, United Kingdom OX1 3QZ*
Matthew Doll − *Department of Chemistry, University of Oxford, Physical and Theoretical Chemistry Laboratory, Oxford, United Kingdom OX1 3QZ*
Olga A. Duda − *Department of Chemistry, University of Oxford, Physical and Theoretical Chemistry Laboratory, Oxford, United Kingdom OX1 3QZ*

Complete contact information is available at: https://pubs.acs.org/10.1021/acs.jpca.2c07228

Author Contributions

All authors were responsible for recording data, data analysis, and interpretation of the computational work. The manuscript was written through contributions of all authors. All authors have given approval to the final version of the manuscript.

Funding

This work was funded by EPSRC Programme Grant EP/T021675 held jointly between the University of Oxford and Heriot Watt University.

Notes

The authors declare no competing financial interest.

■ ACKNOWLEDGMENTS

G.M., P.A.J.P., and E.I.B. are grateful to Worcester College, University College, and Somerville College, Oxford, respectively for financial support.

■ REFERENCES

(1) Mannucci, P. M.; Harari, S.; Martinelli, I.; Franchini, M. Effects on health of air pollution: a narrative review. *Internal and Emergency Medicine* **2015**, *10* (6), 657−662.
(2) Boningari, T.; Smirniotis, P. G. Impact of nitrogen oxides on the environment and human health: Mn-based materials for the NOx abatement. *Curr. Opin. Chem. Engin.* **2016**, *13*, 133−141.
(3) *Nitrogen oxides (NOx): why and how they are controlled*; Office of Air Quality Planning and Standards, U.S. Environmental Protection Agency: Research Triangle Park, NC, 1999.
(4) Lenner, M. Nitrogen dioxide in exhaust emissions from motor vehicles. *Atmos. Environ.* **1987**, *21* (1), 37−43.
(5) Shelef, M. Nitric Oxide: Surface Reactions and Removal from Auto Exhaust. *Catalysis Reviews* **1975**, *11* (1), 1−40.
(6) Kašpar, J.; Fornasiero, P.; Hickey, N. Automotive catalytic converters: current status and some perspectives. *Catal. Today* **2003**, *77* (4), 419−449.
(7) Koshland, D. E. The Molecule of the Year. *Science* **1992**, *258* (5090), 1861−1861.
(8) Richter-Addo, G. B.; Legzdins, P.; Burstyn, J. Introduction: Nitric Oxide Chemistry. *Chem. Rev.* **2002**, *102* (4), 857−860.
(9) Böhme, D. K.; Schwarz, H. Gas-Phase Catalysis by Atomic and Cluster Metal Ions: The Ultimate Single-Site Catalysts. *Angew. Chem., Int. Ed.* **2005**, *44* (16), 2336−2354.
(10) Blagojevic, V.; Flaim, E.; Jarvis, M. J. Y.; Koyanagi, G. K.; Bohme, D. K. Nitric Oxide as an Electron Donor, an Atom Donor, an Atom Acceptor, and a Ligand in Reactions with Atomic Transition-Metal and Main-Group Cations in the Gas Phase. *J. Phys. Chem. A* **2005**, *109* (49), 11224−11235.
(11) Klaassen, J. J.; Jacobson, D. B. Dissociative versus molecular chemisorption of nitric oxide on small bare cationic cobalt clusters in the gas phase. *J. Am. Chem. Soc.* **1988**, *110* (3), 974−976.
(12) Hanmura, T.; Ichihashi, M.; Okawa, R.; Kondow, T. Size-dependent reactivity of cobalt cluster ions with nitrogen monoxide: Competition between chemisorption and decomposition of NO. *Int. J. Mass Spectrom.* **2009**, *280* (1), 184−189.
(13) Hanmura, T.; Ichihashi, M.; Watanabe, Y.; Isomura, N.; Kondow, T. Reactions of nitrogen monoxide on cobalt cluster ions: Reaction enhancement by introduction of hydrogen. *J. Phys. Chem. A* **2007**, *111* (3), 422−428.
(14) Koyama, K.; Kudoh, S.; Miyajima, K.; Mafuné, F. Thermal Desorption Spectroscopy Study of the Adsorption and Reduction of NO by Cobalt Cluster Ions under Thermal Equilibrium Conditions at 300 K. *J. Phys. Chem. A* **2015**, *119* (37), 9573−9580.
(15) Anderson, M. L.; Ford, M. S.; Derrick, P. J.; Drewello, T.; Woodruff, D. P.; Mackenzie, S. R. Nitric oxide decomposition on small rhodium clusters, $Rh_n^{\pm}$. *J. Phys. Chem. A* **2006**, *110* (38), 10992−11000.
(16) Ford, M. S.; Anderson, M. L.; Barrow, M. P.; Woodruff, D. P.; Drewello, T.; Derrick, P. J.; Mackenzie, S. R. Reactions of nitric oxide on Rh_6^+ clusters: abundant chemistry and evidence of structural isomers. *Phys. Chem. Chem. Phys.* **2005**, *7* (5), 975−980.
(17) Harding, D.; Mackenzie, S. R.; Walsh, T. R. Structural isomers and reactivity for Rh_6 and Rh_6^+. *J. Phys. Chem. B* **2006**, *110* (37), 18272−18277.
(18) Bakker, J. M.; Mafuné, F. Zooming in on the initial steps of catalytic NO reduction using metal clusters. *Phys. Chem. Chem. Phys.* **2022**, *24* (13), 7595−7610.
(19) Yamaguchi, M.; Zhang, Y.; Lushchikova, O. V.; Bakker, J. M.; Mafuné, F. NO Bond Cleavage on Gas-Phase Ir_n^+ Clusters Investigated by Infrared Multiple Photon Dissociation Spectroscopy. *J. Phys. Chem. A* **2022**, *126* (38), 6668−6677.
(20) Fielicke, A.; von Helden, G.; Meijer, G.; Simard, B.; Rayner, D. M. Direct observation of size dependent activation of NO on gold clusters. *Phys. Chem. Chem. Phys.* **2005**, *7* (23), 3906−3909.
(21) Hayton, T. W.; Legzdins, P.; Sharp, W. B. Coordination and Organometallic Chemistry of Metal−NO Complexes. *Chem. Rev.* **2002**, *102* (4), 935−992.
(22) Blanchet, C.; Duarte, H. A.; Salahub, D. R. Density functional study of mononitrosyls of first-row transition-metal atoms. *J. Chem. Phys.* **1997**, *106* (21), 8778−8787.
(23) Thomas; Bauschlicher, C. W.; Hall, M. B. Binding of Nitric Oxide to First-Transition-Row Metal Cations: An ab Initio Study. *J. Phys. Chem. A* **1997**, *101* (45), 8530−8539.
(24) Wang, L.; Wang, G.; Qu, H.; Wang, C.; Zhou, M. Infrared Photodissociation Spectroscopy of Iron Nitrosyl Cation Complexes: $Fe(NO)_n^+$ (n = 1−5). *J. Phys. Chem. A* **2014**, *118* (10), 1841−1849.
(25) Wang, L.; Wang, G.; Qu, H.; Li, Z. H.; Zhou, M. Flexible bonding between copper and nitric oxide: infrared photodissociation spectroscopy of copper nitrosyl cation complexes: $[Cu(NO)_n]^+$ (n = 1−5). *Phys. Chem. Chem. Phys.* **2014**, *16* (22), 10788−10798.
(26) Li, Y.; Wang, L.; Qu, H.; Wang, G.; Zhou, M. Infrared photodissociation spectroscopy of mass-selected silver and gold nitrosyl cation complexes. *J. Phys. Chem. A* **2015**, *119* (15), 3577−86.
(27) Iskra, A.; Gentleman, A. S.; Kartouzian, A.; Kent, M. J.; Sharp, A. P.; Mackenzie, S. R. Infrared Spectroscopy of Gas-Phase $M^+(CO_2)_n$ (M = Co, Rh, Ir) Ion−Molecule Complexes. *J. Phys. Chem. A* **2017**, *121* (1), 133−140.
(28) Brewer, E. I.; Green, A. E.; Gentleman, A. S.; Beardsmore, P. W.; Pearcy, P.; Meizyte, G.; Pickering, J.; Mackenzie, S. R. An infrared study of CO_2 activation by holmium ions, Ho^+ and HoO^+. *Phys. Chem. Chem. Phys.* **2022**, *24*, 22716.
(29) Green, A. E.; Brown, R. H.; Meizyte, G.; Mackenzie, S. R. Spectroscopy and Infrared Photofragmentation Dynamics of Mixed Ligand Ion−Molecule Complexes: $Au(CO)_x(N_2O)_y^+$. *J. Phys. Chem. A* **2021**, *125* (33), 7266−7277.
(30) Walther, C.; Becker, S.; Dietrich, G.; Kluge, H. J.; Lindinger, M.; Lützenkirchen, K.; Schweikhard, L.; Ziegler, J. Photo fragmentation of metal clusters stored in a penning trap. *Zeitschrift für Physik D Atoms, Molecules and Clusters* **1996**, *38* (1), 51−58.
(31) Frisch, M. J.; Trucks, G. W.; Schlegel, H. B.; Scuseria, G. E.; Robb, M. A.; Cheeseman, J. R.; Scalmani, G.; Barone, V.; Petersson, G. A.; Nakatsuji, H.et al.. *Gaussian 16 Revision C.01*; Gaussian, Inc.: Wallingford, CT, 2016.

(32) Addicoat, M. A.; Metha, G. F. Kick: constraining a stochastic search procedure with molecular fragments. *J. Comput. Chem.* **2009**, *30*, 57−64.
(33) Gräfenstein, J.; Cremer, D. Can density functional theory describe multi-reference systems? Investigation of carbenes and organic biradicals. *Phys. Chem. Chem. Phys.* **2000**, *2* (10), 2091−2103.
(34) Perdew, J. P. Density-functional approximation for the correlation energy of the inhomogeneous electron gas. *Phys. Rev. B* **1986**, *33* (12), 8822−8824.
(35) Becke, A. D. Density-functional thermochemistry. III. The role of exact exchange. *J. Chem. Phys.* **1993**, *98* (7), 5648−5652.
(36) Weigend, F. Accurate Coulomb-fitting basis sets for H to Rn. *Phys. Chem. Chem. Phys.* **2006**, *8*, 1057−65.
(37) Weigend, F.; Ahlrichs, R. Balanced basis sets of split valence, triple zeta valence and quadruple zeta valence quality for H to Rn: Design and assessment of accuracy. *Phys. Chem. Chem. Phys.* **2005**, *7* (18), 3297−3305.
(38) Cunningham, E. M.; Gentleman, A. S.; Beardsmore, P. W.; Iskra, A.; Mackenzie, S. R. Infrared Signature of Structural Isomers of Gas-Phase $M^+(N_2O)_n$ (M = Cu, Ag, Au) Ion−Molecule Complexes. *J. Phys. Chem. A* **2017**, *121* (40), 7565−7571.
(39) Cunningham, E. M.; Gentleman, A. S.; Beardsmore, P. W.; Mackenzie, S. R. Structural isomers and low-lying electronic states of gas-phase $M^+(N_2O)_n$ (M = Co, Rh, Ir) ion−molecule complexes. *Phys. Chem. Chem. Phys.* **2019**, *21* (26), 13959−13967.
(40) Herzberg, G.*Molecular Spectra and Molecular Structure: II Infrared and Raman Spectra of Polyatomic Molecules*; Krieger: Malabar, FL, 1991.
(41) Dinerman, C. E.; Ewing, G. E. Infrared spectrum, structure, and heat of formation of gaseous $(NO)_2$ I. *J. Chem. Phys.* **1970**, *53* (2), 626−631.
(42) McCleverty, J. A. Chemistry of Nitric Oxide Relevant to Biology. *Chem. Rev.* **2004**, *104* (2), 403−418.

https://doi.org/10.1021/acs.jpca.2c07228
J. Phys. Chem. A 2022, 126, 9414−9422

Statement of Authorship for joint/multi-authored papers for PGR thesis

To appear at the end of each thesis chapter submitted as an article/paper

The statement shall describe the candidate's and co-authors' independent research contributions in the thesis publications. For each publication there should exist a complete statement that is to be filled out and signed by the candidate and supervisor **(only required where there isn't already a statement of contribution within the paper itself).**

Title of Paper	An Infrared Study of Gas-Phase Metal Nitrosyl Ion-Molecule Complexes
Publication Status	□**Published** □ Accepted for Publication □Submitted for Publication □Unpublished and unsubmitted work written in a manuscript style
Publication Details	Meizyte, G., **Pearcy, P.A.J.**, Watson, P.D., Brewer, E.I., Green, A.E., Doll, M., Duda, O., Mackenzie, S.R. (2022). An Infrared Study of Gas-Phase Metal Nitrosyl Ion-Molecule Complexes. Journal of Physical Chemistry A, 126(50), 9414-9422., DOI: 10.1021/acs.jpca.2c07228

Student Confirmation

Student Name:	Philip Aidan James Pearcy		
Contribution to the Paper	My contribution was to collect the experimental data for each of the systems (for Co, Rh, and Ir) along with G. Meizyte, and analyse it to determine which structural motifs were present within the complexes. Additionally, I lead the calculations to examine the different structures present within the $[Rh(NO)_n]^+$ complexes. I produced figures that ended up in the paper, and helped in editing the manuscript whilst G.Meizyte took the lead in writing it.		
Signature: 		Date	04/08/2025

Supervisor Confirmation

By signing the Statement of Authorship, you are certifying that the candidate made a substantial contribution to the publication, and that the description described above is accurate.

Supervisor name and title: Prof. Stuart Mackenzie		
Supervisor comments As outline above this was collaborative work performed jointly within the group with Gabi Meizyte focusing on the Co and Ir complexes and Philip taking the lead on the rhodium. The joint publication facilitated the comparisons between all data.		
Signature 	Date	26/08/2025

This completed form should be included in the thesis, at the end of the relevant chapter.

Chapter 4

Structure, Spectra, and Intracluster Chemistry of Gas-Phase Platinum Nitrosyl Ion-Molecule Complexes

This chapter details a spectroscopic study of gas-phase $[Pt/PtO(NO)_n]^+$ complexes (n = 3-7 for $[Pt(NO)_n]^+$, n = 4-7 for $[PtO(NO)_n]^+$). The complexes were formed by ablating Pt in a beam of either He or Ar seeded with NO. IRPD spectra were recorded in the NO stretch region ($1500 - 2000$ cm^{-1}), with supporting DFT calculations used to aid in assigning bands through predicted structures.

For the $[Pt(NO)_n]^+$ system, an inner core of Pt with up to 6 NO molecules has been observed, with $[Pt(NO)_6]^+$ best described with a pseudo-octahedral structure. There is evidence of a NO dimer moiety for n = 7, with the emergence of new satellite bands illustrating the localised $(NO)_2$ mode seen in other IRPD studies of gas-phase metal nitrosyl complexes, as well as a band that implies the breaking of the octahedral symmetry through the addition of NO in a secondary solvation shell. For the $[PtO(NO)_n]^+$ com-

plexes, evidence of the formation of NO_2 in the form of an N_2O_3 moiety is apparent. Again, evidence of up to six ligands binding in the first cooridation shell in an octahedral structure is present for these oxygen-rich complexes.

The results in this chapter were collected in the Mackenzie Group laboratory in Oxford. The $[Pt(NO)_n]^+$ work was led by myself with the help of Part II student Matthew Doll, as well as Dr. Edward Brewer and Dr. Peter Watson. The $[PtO(NO)_n]^+$ studies were completed jointly by me along with Peter Rubli, Dr. Peter Watson, and Dr. Christian Haakansson. Computational studies were conducted by many members of the group, with the final structure compilation and analysis completed by myself.

4.1 Introduction

Nitrogen oxides (NO_x) are molecules of interest given their known effects on human health, both beneficial and malevolent, as well as their role within environmental processes. [241–244] The simplest of these molecules is the stable radical nitric oxide (NO, X $^2\Pi$), which plays a role in many physiological processes within mammalian bodies as a messenger molecule.[245] However, it is also a well-known pollutant gas produced by both anthropogenic sources such as fuel combustion and agriculture,[246] as well as from natural sources such as plasma produced from lightning strikes, causing reactions between N_2 and O_2 to form NO_x.[247] One mitigation strategy to reduce anthropogenic NO_x levels involves passing pollutant gases over solid-state materials (e.g., γ-Al_2O_3, TiO_2) which contain finely dispersed transition metal atoms such as rhodium (Rh) and palladium (Pd).[248, 249] These materials utilise the catalytic behaviour of transition metals interacting with small molecules to form less environmentally harmful products.[8]

An element ubiquitous with catalytic materials is platinum (Pt). It is a dense, silvery-white precious metal known for its exceptional resistance to corrosion and high melting point. The element itself has four stable isotopes; the mass and abundance of each are presented in Table 4.1.[212] Pt is used in heterogeneous and homogeneous catalysis. Industrial applications of Pt catalysts include it being used in both NO oxidation reactions, forming NO_2 in diesel exhaust after-treatment systems, and in nitric acid

Table 4.1: The atomic masses and natural abundances of the four naturally occuring isotopes of Pt, presented to 2 decimal places.[212]

Nuclide	Atomic Mass / Da	Natural Abundance / %
^{194}Pt	193.96	32.86
^{195}Pt	194.96	33.78
^{196}Pt	195.96	25.21
^{194}Pt	197.97	7.34

production.[11, 250–254] Additionally, Pt is used in NO reduction reactions, often in electrochemical cells,[255] which leads to the formation of other nitrogen containing molecules (N_2, N_2O, NH_3, *etc.*).[256–259] During use, oxide evolution can lead to the formation of platinum oxide (PtO) on the catalyst surface,[251] potentially leading to a reduction in catalytic activity. Ribeiro and co-workers have also shown that the size of Pt particles on the support material affected the rate of nitric oxide oxidation, with larger particles being shown to produce a higher turnover rate than smaller ones. [260] Therefore, understanding how NO interacts with platinum-containing active sites, whether it is pure platinum or platinum oxides, is of interest. This in turn can assist in the development of new catalytic materials that better utilise NO in the catalytic process.

One way of studying the interactions of metal centres with atmospherically relevant molecules is through the use of gas-phase metal atoms and ions, as well as ionic metal clusters. As discussed previously, the ion-molecule complexes formed from these small metal centres (1-20 atoms) can act as tractable model systems for catalytic active sites[30, 261] that allow the intrinsic behaviour of molecules with the metal centre to be examined. As well as structural information, ion-molecule complexes can be studied to examine whether intracluster chemistry takes place (*i.e.* whether chemistry occurs within the complex to form new structures/molecules).[262–264] Reactivity and spectroscopic studies of NO with isolated metal centres, whether they are cationic, anionic, or neutral, have been completed with first row transition metal elements (*i.e.* Co[70, 265–270] and Ni[271–273]), as well as precious metals (Rh,[274–277] Ag,[278] Ir,[279] and Au[280]). Given the wide-ranging uses of Pt in many catalytic processes, much work has been done

to understand the properties of Pt clusters and complexes, both as neutral and ionic species. The structures of $Pt_n^{+/0/-}$ and $Pt_nO_x^{+/0/-}$ clusters have been studied both experimentally and computationally[281, 282] along with how these species interact with other atmospherically relevant molecules,[38, 283–295] including nitric oxide.[296] For example, Böhme *et al.* explored the many reactions the NO molecule can undergo with metal cations at room temperature, with different reaction products formed (metal oxide cations, metal atoms, metal-ligand complexes, *etc.*).[297] For Pt^+, it was observed that the main reaction products were neutral PtNO (90%), as well as cationic $PtNO^+$ (10%). It has also been shown that, unlike CO binding to metal centres (binding linearly (angle of M-C=O $\approx 180°$) and acting as a two-electron donor when molecularly bound), NO can molecularly bind either nonlinearly or linearly depending on whether it acts as a one- or three-electron donor, respectively. This also affects the bond order of the NO molecule, with non-linear binding leading to a NO double bond, and linear binding leading to a NO triple bond.[298] This is reflected in the change in vibrational frequencies. In turn, this means that a large number of structural isomers may need to be considered in investigating the binding of NO molecules to metal centres.[299] Additionally, the open-shell nature of NO can present challenges for quantum chemical calculations, such as density functional theory (DFT) calculations,[300] leading to a more complex potential energy surface where many energetically low-lying isomers may reside.

Infrared photodissociation (IRPD) studies of transition metal nitrosyl cation-ligand complexes, $[M(NO)_n]^+$, have been performed by Zhou and co-workers, providing evidence of the different ways NO can bind to metal cationic centres (Fe,[301] Cu,[302] Ag and Au[303]), with NO dimers forming after the closure of the first solvation shell. The formation of NO dimers was illustrated by the emergence of new satellite bands in the infrared action spectrum. The number of NO molecules in the first coordination shell varies, with the most favourable coordination numbers shown to be 4, 4, 5 and 2 for the metals detailed earlier. In addition, gas-phase nitrosyl complexes of metals of Group 9 have been studied, as presented in Chapter 3.[304] Co^+ and Ir^+ showed a pattern similar to that of the metals studied by Zhou, with an inner shell of 4 NO molecules bound to the metal centre. Evidence of NO dimer formation was illustrated by the emergence of new satellite bands in the spectra for $n \geq 5$. The IRPD of Rh^+ nitrosyl complexes exhibited a

different behaviour, with a redshift observed in spectral features with increasing complex size, as well as satellite bands appearing, suggesting a more complex aggregation around the metal centre. Combined with DFT calculations, it suggested that NO molecules had a greater propensity to bind non-linearly to Rh^+ compared to Co^+ and Ir^+, and it was less clear how many NO molecules were bound in the inner shell.

This work presents IRPD studies of NO binding to the Pt^+ and PtO^+ centres, forming gas-phase complexes of $[Pt(NO)_n]^+$ and $[PtO(NO)_n]^+$ ($n = 3-7$ for Pt^+, $n = 4-7$ for PtO^+), along with complementary DFT calculations that helped to interpret the experimental spectra. The square bracket nomenclature (*i.e.* $[PtO_x(NO)_n]^+$) is used to highlight that the species are assigned putatively based on their mass and does not provide information on their structure (*i.e.* PtO(NO) will have the same mass as $Pt(NO_2)$).

4.2 Experimental and Computational Methods

The experiments are performed on an experimental setup that has been previously detailed in Chapter 2, and in previous articles.[205, 305, 306] In brief, a rotating Pt disc target is ablated within a "cutaway" source[92] using a focused 532 nm pulse from a Nd:YAG laser (either a Continuum Minilite (10 Hz repetition rate) or a Quantel Ultra (20 Hz repetition rate), 8 ns pulse, ca. 2-10 mJ/pulse as necessary). The target is ablated in the presence of a pulsed supersonic expansion of NO in a carrier gas (NO in Ar v/v: ~2% for $[Pt(NO)_n]^+$, NO in He v/v: ~5% for $[PtO(NO)_n]^+$). The resulting molecular beam is skimmed before passing through a quadrupole mass filter (QMF), allowing for mass selectivity, followed by a quadrupole bender (QB). Subsequently, the cationic species are extracted into a reflectron time-of-flight (ReToF) mass spectrometer.

IRPD spectra are recorded by intersecting the cluster beam with a counter-propagating tunable infrared pulse produced from a tabletop optical parametric oscillator/optical parametric amplifier (OPO/OPA, Laservision), operating in the range 1500-2000 cm^{-1} for $[Pt(NO)_n]^+$, and 1500-2100 cm^{-1} for $[PtO(NO)_n]^+$. The parent ions are mass-selected using the QMF, and the spectra are recorded as a function of the wavenumber in the daughter fragment channels against a zero background. IRPD spectra are then reported

as absorption cross sections σ. This is calculated using a modified Beer-Lambert law:

$$\sigma = -\frac{1}{\Phi} \ln \left(1 - \frac{N_f}{\alpha N_0} \right), \tag{4.1}$$

where Φ is the photon flux and N_f and N_0 are the intensities of the fragment and parent ion signals, respectively.[307] α is a scaling factor used to describe the overlap between the molecular beam and the infrared beam, and it is assumed that it is equal to 1. The ion signal for the complexes containing the most abundant Pt isotopes (^{194}Pt, ^{195}Pt, ^{196}Pt) are used given the poor ion signal for the species containing the ^{198}Pt isotope.[212] Due to the masses of nitrogen and oxygen isotopes being approximately even numbers (14.0031 u for ^{14}N, 15.9949 u for ^{16}O, 17.9992 for ^{18}O), complexes using combinations of these atoms will provide approximately even masses. As a result, there is a risk of mass degeneracies caused by the complexes that contain Pt isotopes with even masses and the nitric oxide complexes, $[O_x(NO)_n]^+$. For example, ^{196}Pt has the same mass as $[O(NO)_6]^+$. The spectra of each isotopologue is compared with those of the ^{195}Pt isotopologue before being included in the averaging.[204] Using the spectral features associated with the Pt isotope with an odd mass as a reference will minimise the risk of contamination of $[O_x(NO)_n]^+$ complexes. The mean cross section is produced from the calculated cross section from each scan, and these data are smoothed using a 10-point adjacent average. The smoothed data are then normalised to produce the normalised absorption cross section.

The assignment of features in the experimental spectra is assisted through the simulated spectra of energetically low-lying structures computed using DFT. The calculated structures are produced using the Gaussian 16 software package[194] with multiple starting structures generated using a modified *Kick*^{3} algorithm.[198] These structures were generated from sequential addition of NO to a cationic core of Pt or PtO, producing optimised $[Pt(NO)_n]^+$ and $[PtO(NO)_n]^+$ ($n = 0 - 7$). The open-shell nature of NO and the large number of electrons associated with transition metals raises particular difficulties for DFT, and can lead to multiple low-lying electronic states and isomeric forms.[300] The B3P86/def2TZVP[188, 238–240] level of theory is used for these calculations, as it has shown good agreement with experimental results when used in previous studies.[203, 308] In order to better match the experimental and simulated spectra, a scaling factor of 0.9347 is applied to the computed harmonic vibrational frequencies of the platinum nitrosyl com-

plexes derived from comparison between the calculated frequency of the 'free' NO stretch, and literature (1875.84 cm^{-1}).[227] Final energies reported here are zero-point corrected. Calculated line spectra are convoluted with Lorentzian line shapes with a full width at half maximum (FWHM) of 8 cm^{-1} to better aid in comparison with experimental data. Based on previous work on gas-phase nitrosyl complexes,[204] additional calculations for $[PtO(NO)_n]^+$ are performed to include both $[PtO(NO)_n]^+$ and $[Pt(NO_2)(NO)_{n-1}]^+$ structures. The nomenclature of the isomers in the figures describes the number of NO molecules attached, denoted by a number, whether they contain an oxygen (apostrophe means a nominal structure $[PtO(NO)_n]^+$) and the ordering relative to the putative ground state, denoted using letters in alphabetical order (*i.e.* Isomer 3'a is the lowest energy structure of $[PtO(NO)_3]^+$). Isomeric forms contain both an N_2O and an NO_2 ligand, $[PtO_x(N_2O)(NO_2)(NO)_{n-3}]^+$, have not been calculated as there is no experimental evidence from this study and previous studies by Meizyte *et al.* showing N_2O or NO_2 loss as a fragmentation pathway.[304] In order to determine how strongly the NO molecules are bound in the complexes, a bond dissociation energy (BDE) is calculated using the zero-pointed corrected energies for the parent and fragment species, and the free NO molecule, using the following equation:

$$BDE = E([PtO_x(NO)_{n-1}]^+) + E(NO) - E([PtO_x(NO)_n]^+) \quad (4.2)$$

The parent and fragment species are chosen on the basis of whether they are the lowest energy structures, mainly for the smaller complexes that do not have experimental data, or whether the calculated structures produce a simulated IR spectrum, which is in good agreement with the experimental data. In some instances, a daughter fragment is produced by removing an NO molecule from the parent structure that best fits the experimental data, before the zero-point corrected electronic energy for the new daughter fragment is calculated.

4.3 Results and Discussion

4.3.1 Time-Of-Flight Spectra and Cluster Distributions

Figure 4.1 shows a representative mass spectrum recorded using a 2% NO in an Ar gas mixture to show all the complexes that are produced. The mass spectrum is dominated by

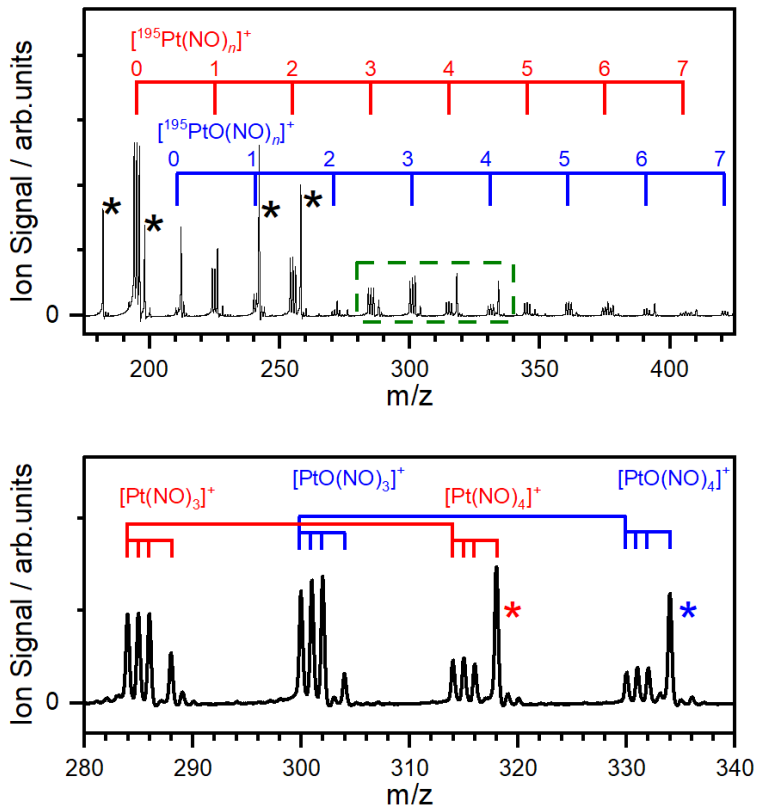

Figure 4.1: Top panel: Time-of-flight mass spectrum of species produced upon ablation of a Pt target in the presence of a 2% NO in Ar (6 bar backing pressure). **Bottom panel**: Expanded $280 \leq m/z \leq 340$ region of the mass spectrum in which the four most abundant Pt isotopes are clearly resolved. Asterisks indicate blended peaks contaminated by pure N, O complexes, specifically $[(NO)_3(N_2O_3)_3]^+$ (red) and $[(NO)(N_2O_3)_4]^+$ (blue).

$[Pt(NO)_n]^+$ and $[PtO(NO)_n]^+$ peaks which are identifiable by the distinctive Pt isotope distribution. The intensities of the $[Pt(NO)_n]^+$ species appear to follow a simple Poisson distribution that peaked at $n = 2$. The ion signals for the $[PtO(NO)_n]^+$ ($n = 1, 2$) appear anomalously weak and the $[PtO(NO)_3]^+$ pronounced.

The origin of the $[PtO(NO)_n]^+$ species is uncertain. Importantly, they do not arise from NO binding to PtO^+ as no oxide peaks are observed when the Pt target is ablated in pure Ar, as shown in Figure 4.2. It has been shown in reactivity studies by Böhme and co-workers that the dominant product from Pt^+ reacting with NO was NO^+ and $[Pt(NO)_{1-3}]^+$, with no $[PtO(NO)_n]^+$ produced.[297] Additionally, Armentrout and co-

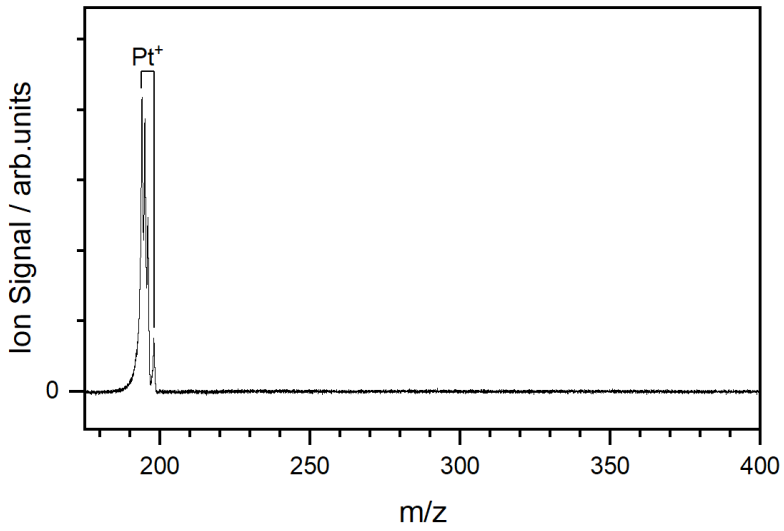

Figure 4.2: Time-of-flight (ToF) mass spectrum produced upon ablating a Pt target in the presence of Ar carrier gas at a backing pressure of 5 bar. The only species observed are the isotopes of Pt^+. There is no evidence of $PtO_x{}^+$ production.

---

workers have shown that when PtO^+ collides with NO *via* a two-body collision, the main products are Pt^+, which suggests dissociation of the PtO^+ unit, $[Pt(NO)]^+$, and NO^+, with charge transfer between PtO^+ and NO to form NO^+ being the most efficient process at low collision energies.[309] In order to produce $[PtO(NO)_n]^+$ complexes, it may be that NO molecules within $[Pt(NO)_n]^+$ undergo intracluster reactions. Some of the possible reaction pathways are as follows:

$$[Pt(NO)_n]^+ + NO \rightarrow [PtO(NO)_{n-1}(N_2O)]^+ \rightarrow [PtO(NO)_{n-1}]^+ + N_2O \qquad (4.3)$$

$$\text{or } [Pt(NO)_n]^+ + NO \rightarrow [Pt(NO_2)(NO)_{n-2}(N_2O)]^+ \rightarrow [Pt(NO_2)(NO)_{n-2}]^+ + N_2O \qquad (4.4)$$

Based solely on the mass spectrum, it is not possible to deduce whether the species containing the excess oxygen atom follow the reactions detailed in Equations 4.3 or 4.4, and requires IR spectroscopy to identify which products are being formed. However, the possibility that the ablation laser is involved in a photochemical step cannot be ruled out. We have previously reported spectroscopic evidence for analogous reactions that occur in pure gas-phase $[(NO)_n]^+$ clusters.[204]

It should also be noted that there are intense features within the mass spectrum separated by 76 amu, suggesting the formation of $[(NO)_{1,3}(N_2O_3)_n]^+$ complexes. These peaks are much more intense than those of the platinum complexes, given their relative stability and the amount of NO present in the molecular beam. $[(NO)_{1,3}(N_2O_3)_n]^+$ complexes have been observed in the literature,[310] and arise from NO molecules being ionised; whether that be from charge transfer reactions with Pt/PtO cations, or in the laser ablation process. The N_2O_3 arises from NO and NO_2 radicals interacting; causing a spin pairing that produces a stable singlet species that can cluster around an NO^+ or $(NO)_3{}^+$ trimer core. These complexes are isobaric with certain complexes of $[^{198}PtO_x(NO)_n]^+$, as shown in Figure 4.1.

4.3.2 IRPD Spectra of $[Pt(NO)_n]^+$ $(n = 3 - 7)$

The IRPD spectra recorded for $[Pt(NO)_n]^+$ $(n = 3-7)$ are shown in Figure 4.3. The only fragmentation pathway observed is the loss of NO, and the spectra shown are recorded in enhancement of the daughter $[Pt(NO)_{n-1}]^+$. Figure 4.4 shows how the fitted peak positions change as a function of complex size, n.

For $[Pt(NO)_n]^+$, no dissociation was observed for $n = 1, 2$. As has been observed in other IRPD studies of metal ion–ligand complexes, the initial ligands bind especially tightly to the metal centre.[302, 304] The calculated bond dissociation energies (BDE) for $n = 1, 2$ using the lowest energy calculated DFT structures are 4.63 and 2.00 eV, respectively. A plot of the BDE for the Pt nitrosyl complexes discussed, which is provided in a later section of this chapter (Subsection 4.3.5, Figure 4.13, panel **a)**), shows the values for the $[Pt(NO)_n]^+$ complexes (Figure 4.13, panel **b)** provides the bond dissociation energies for the $[PtO(NO)_n]^+$ complexes). Given that the photon energies in the scanned region ranged between $\sim 0.19 - 0.25$ eV (shown in Figure 4.13 by a red band), it is highly unlikely that the complexes would be able to absorb a sufficient number of photons to induce dissociation, even if the complexes themselves possessed a large amount of internal energy.

The first complex that was observed to fragment was $[Pt(NO)_3]^+$. The relatively poor signal-to-noise (S/N) ratio, and the broad peaks shown in the spectrum, are indicative that the process of removing an NO requires multiple photons. The S/N ratio of the

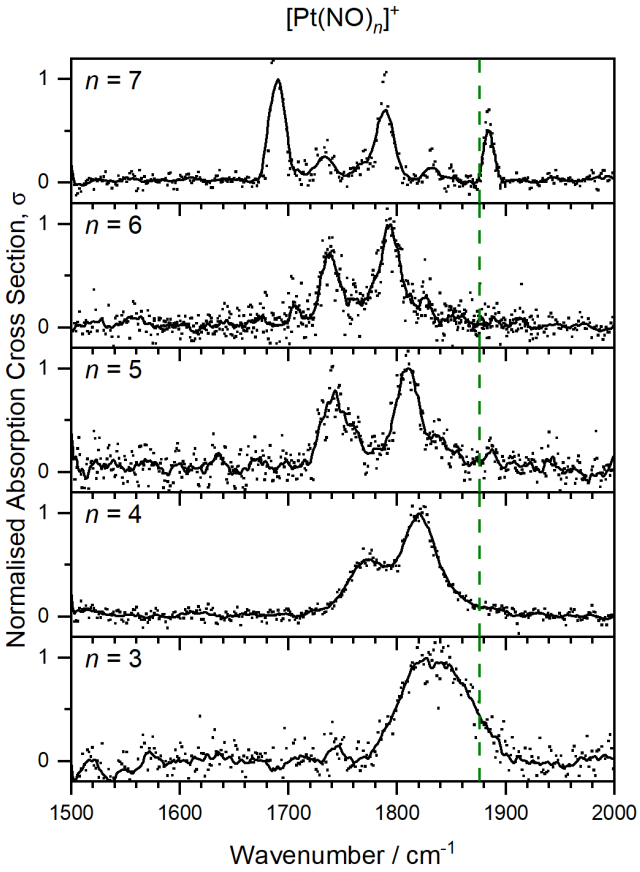

Figure 4.3: IRPD spectra of the $[Pt(NO)_n]^+$ complexes ($n = 3-7$), measured in the enhancement of the $[Pt(NO)_{n-1}]^+$ daughter fragment channel, and presented as normalised absorption cross sections for each value of n. The green dashed line indicates the free NO stretch at 1875.84 cm^{-1}.[227]

IR action spectrum for $[Pt(NO)_4]^+$ is improved compared to $[Pt(NO)_3]^+$, indicating that fewer photons are required to remove an NO molecule. Furthermore, the width of the peaks decreases as n increases from 3 to 4, with it being possible to discern two distinct bands in the IRPD spectrum for $n = 4$ which can be deconvoluted using Gaussian functions. The results of the deconvolution are shown in Figure 4.4.

The main trend observed within the $[Pt(NO)_n]^+$ data from $n = 3$ to $n = 6$ is a red-shift of the peaks away from the free NO stretch at 1875.84 cm^{-1}. Additionally, the separation of the broad feature that is first observed for $n = 4$ continues with increasing complex size up to $n = 6$. These observations are consistent with what was observed for $[Rh(NO)_n]^+$.[304] There appear to be some very weak satellite peaks that emerge

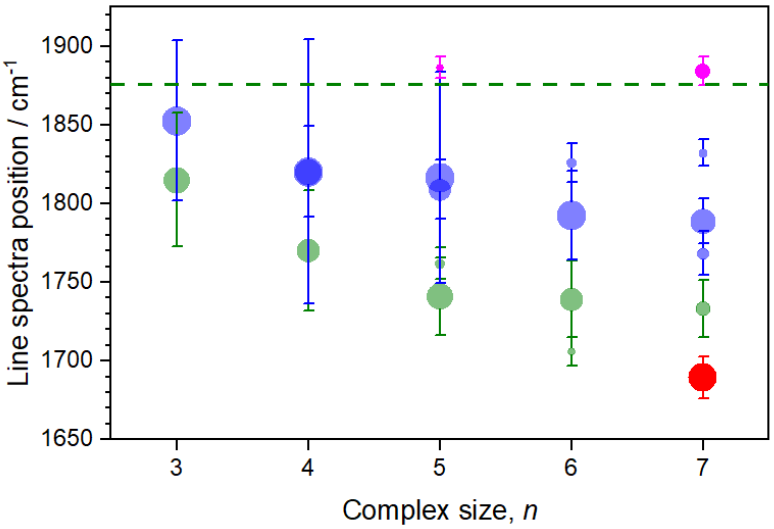

Figure 4.4: Experimental peak positions plotted as a function of cluster size, n, in $Pt(NO)_n^+$ complexes. The uncertainties in peak positions correspond to the FWHM of the Gaussian curves used for peak deconvolution. The area of the spots for each complex size is scaled internally to the normalised amplitude of the largest Gaussian used in the deconvolution. The green dashed line indicates the position of the free NO vibrational frequency at 1875.84 cm^{-1}.[227] The localised stretch of the $(NO)_2$ dimer moiety is highlighted in red, with the symmetric in-phase stretch highlighted in magenta.

---

in the range of 1700-1875 cm^{-1} from $n = 5$ onwards, but they are difficult to discern from the baseline and are not as pronounced as observed satellite bands that have arisen from NO dimer moieties in other $[M(NO)_n]^+$ studies.[303, 304] Additionally, by looking at Figure 4.3, there does not immediately appear to be a peak in the region of the free NO stretch, shown by the green dashed line. This band is associated with the symmetric in-phase "breathing" motion of all NO molecules with the complex that arises from an NO molecule being attached in a secondary solvation shell. As shown in Figure 4.4, in the case of $n = 5$, the Gaussian de-convolution fits a peak at ~1880 cm^{-1}, but it is very weak compared to the main bands shown in the IRPD spectrum, and it is very difficult to distinguish it from the noise level of the spectrum. For $n = 6$, there is no discernible peak, illustrated in Figure 4.4 by the lack of a magenta spot in the range of $1870 - 1900$ cm^{-1}. It should be noted that the S/N ratio has not improved for $n = 5$. This is typically the size where an NO dimer moiety is formed by an NO molecule bound in a secondary

solvation shell. Collectively, the redshift continues until $n = 6$, together with the decreasing S/N ratio and the lack of much more pronounced satellite bands further to both the red and blue of the main peaks suggest that the fifth and sixth NO molecules are binding differently in the Pt complex compared to other cationic metal nitrosyl complexes.

For $n = 7$, the peaks within the spectrum are better resolved and the S/N ratio is much improved. The two main spectral features observed for the smaller species appear to remain in the same position, with two additional intense satellite bands appearing at 1691 cm^{-1} and 1885 cm^{-1}, respectively. On the basis of previous studies, this could arise from the seventh NO molecule coordinating with the complex in a different fashion, mainly in a secondary solvation shell. This implicitly and notably suggests that the Pt cation can accommodate up to six NO molecules in the first coordination shell; this is a marked difference from what has been observed in the literature.

With respect to NO binding to metal centres, the dominant mode of interaction is charge-dipole attraction, with the NO bond polarised in the process. Alternatively, the NO molecule can bind through a) NO lone pair σ donation, b) π donation from the unpaired NO π^* electron, and c) occupied d-orbitals from the metal centre π-backbonding with the NO π^* orbital (expected to be negligible when it bonds to a metal cation). Hence, NO can act as a (π^*) one-electron donor; leading to nonlinear coordination with a weakened N=O bond, or as a three-electron donor which leads to linear M^+–N≡O coordination and a strengthened N≡O bond.[242, 311]

4.3.3 Comparison with Calculations for $[Pt(NO)_n]^+$ ($n = 3, 4$)

Figure 4.5 shows the simulated structures and IR spectra with the experimental data for $[Pt(NO)_3]^+$ (panel **a)**) and $[Pt(NO)_4]^+$ (panel **b)**). For $n = 3$, whilst it is difficult to resolve the broad feature in the experimental spectrum, the simulated spectrum for Isomer 3a is in the closest agreement. This structure is the lowest energy structure calculated and has triplet spin multiplicity. It is also a planar complex, with two NO molecules binding linearly (acting as three-electron donors) and the third one binding nonlinearly (acting as a one-electron donor). Using electron counting techniques on a Pt^+ ion ($[Xe]4f^{14}5d^9$) would result in a 16-electron system, which is known to be a stable electron configuration

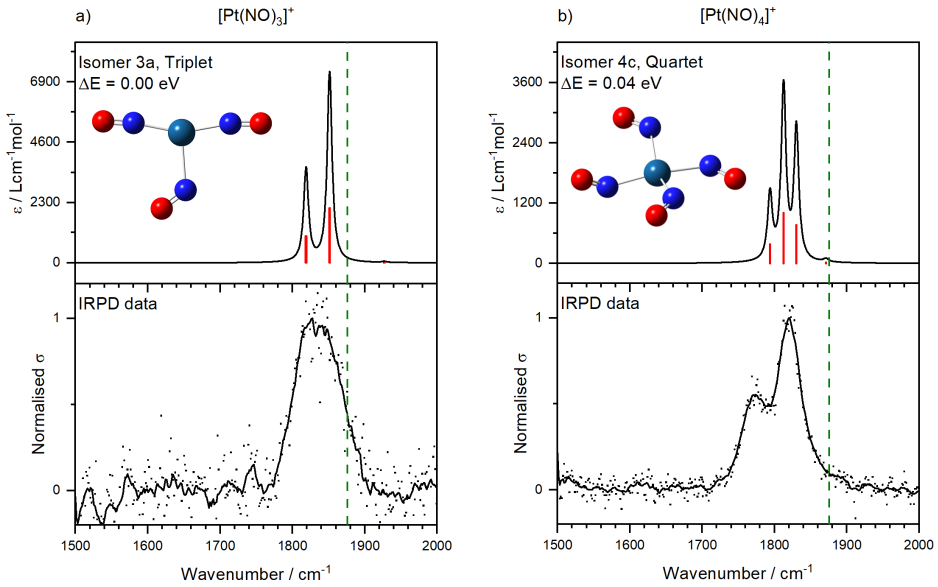

Figure 4.5: Experimental IRPD spectra (bottom panels), along with the simulated IR spectra and structures (top panel) for the best-fit low-lying isomers for **a)** $[Pt(NO)_3]^+$, and **b)** $[Pt(NO)_4]^+$. The green dashed line indicates the free NO stretch at 1875.84 cm^{-1}.[227]

in inorganic transition metal complexes.[312] The two main features of the simulated spectrum at 1818 cm^{-1} and 1850 cm^{-1} arise from normal modes involving all three NO molecules. The mode at 1818 cm^{-1} involves a larger contribution from the bent NO molecule, with the mode at 1850 cm^{-1} corresponding to the out-of-phase vibration of the two linearly bound NO ligands. There is also a very weak mode at 1926 cm^{-1}, which corresponds to the symmetric in-phase "breathing" motion of all NO ligands. Additional structures involving dimer moieties, singlet multiplicities, or O-bound NO molecules were not considered likely structures, given their poor comparison with the experimental data and the fact that they were at least 0.3 eV higher in energy than the putative ground state.

For $[Pt(NO)_4]^+$, the structure that best replicates the experimental data is Isomer 4c, a near-square-planar structure that is 0.04 eV higher than the putative ground state structure. Isomer 4c has four NO ligands bound to the Pt core nonlinearly, implying that they act as one-electron donors. As shown in Figure 4.5**b)**, the main bands seen in the experimental data can be described by three distinct modes, as shown from the simulated IR spectrum for Isomer 4c, which are not fully resolved in the experimental spectrum. Ad-

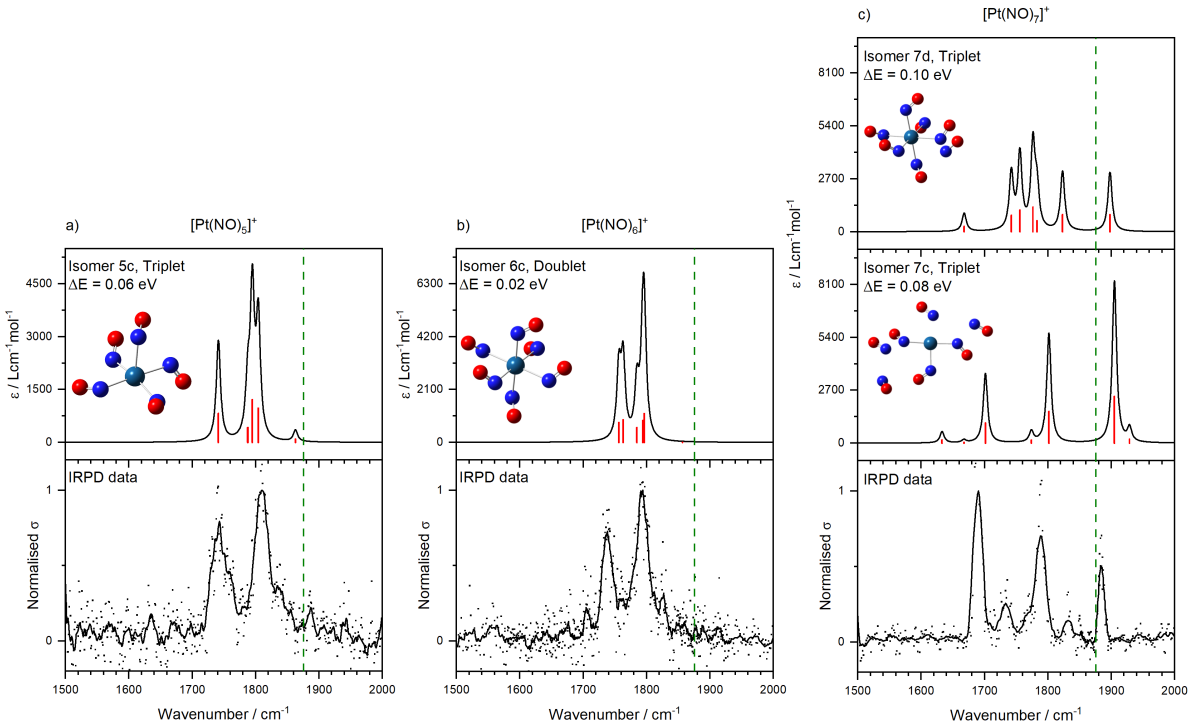

Figure 4.6: Experimental IRPD spectra (bottom panels) along with the simulated IR spectra and structures (top panels) for the best-fit low-lying isomers for **a)** $[Pt(NO)_5]^+$, **b)** $[Pt(NO)_6]^+$, and **c)** $[Pt(NO)_7]^+$. The green dashed line indicates the free NO stretch at 1875.84 cm^{-1}.[227]

ditionally, a very weak vibration at 1871 cm^{-1} in the simulated spectrum corresponding to the "breathing" motion is not discernible in the experimental spectrum. These modes are also redshifted compared to what was observed for $n = 3$, suggesting that with the NO coordination switching from linear to nonlinear, the vibrational frequency decreases. This is comparable to what was observed for $[Rh(NO)_n]^+$, where the IR peaks shifted further to the red as more NO molecules were added to the complexes in a nonlinear fashion. For Rh, the broad feature for $n = 3$ spanned the region ∼1830-1950 cm^{-1}, the maximum appearing at ∼1860 cm^{-1}. For $[Rh(NO)_4]^+$, the main peaks span the region ∼ 1800-1900 cm^{-1}, with two distinct features centred at ∼ 1800 cm^{-1} and 1860 cm^{-1}.

4.3.4 Comparison with Calculations for $[Pt(NO)_n]^+$ $(n = 5 - 7)$

The calculated structures and IR spectra compared to the IRPD data for $n = 5 - 7$ are presented in Figure 4.6. As seen in panels **a)** and **b)**, rather than forming NO dimers, as has been observed in previous studies for other metals with the same number of molecules,

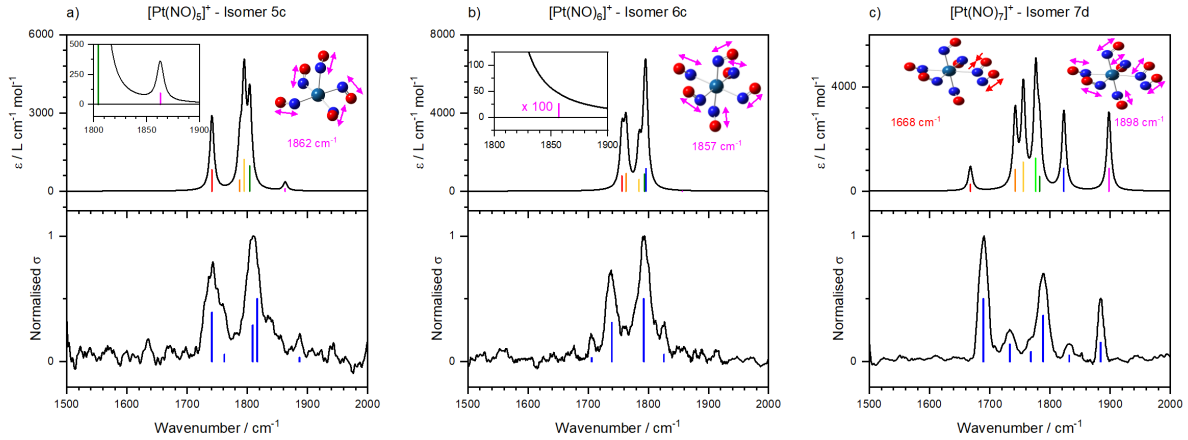

Figure 4.7: Experimental IRPD spectra (bottom panel), along with the simulated IR spectra and structures (top panel), for the lowest-lying isomers for **a)** Isomer 5c, **b)** Isomer 6c, and **c)** Isomer 7d for $[Pt(NO)_5]^+$, $[Pt(NO)_6]^+$, and $[Pt(NO)_7]^+$, respectively. Within **a)** and **b)**, there is an inset for the range 1800-1900 cm^{-1} to highlight the symmetric in-phase "breathing" motion. The blue line spectra in the bottom panels related the positions of the Gaussian peak centres used in the curve deconvolution. The colour-coded mode vectors on top of the structures highlight the key motions for these $[Pt(NO)_n]^+$ complexes.

the complexes that best fits the experimental data adopt a square-pyramidal structure for $n = 5$, and an octahedral structure for $n = 6$. Isomer 5c (triplet multiplicity, 0.06 eV above the putative ground state) builds on the structure of Isomer 4c by having a base with four NO molecules that are nonlinearly bound to the Pt centre, with a fifth NO molecule adding to the top site, also in a nonlinear fashion. The experimental and simulated spectra agree well, with two main bands centred at 1743 cm^{-1} and 1810 cm^{-1} being reproduced. In the simulated spectrum, the band at 1810 cm^{-1} is composed of multiple modes; all different combinations of NO molecules vibrating in or out-of-phase. Additionally, a small feature is attributed to the "breathing" motion at 1863 cm^{-1} in the simulated spectrum and at 1887 cm^{-1} in the IRPD spectrum; further supporting the square-pyramidal structural assignment.

The "breathing" vibrational mode is illustrated with arrows in Figure 4.7, and the other individual calculated modes are highlighted in colour-coded line spectra below the simulated IR spectra. However, given the relatively poor S/N ratio, it is difficult to discern

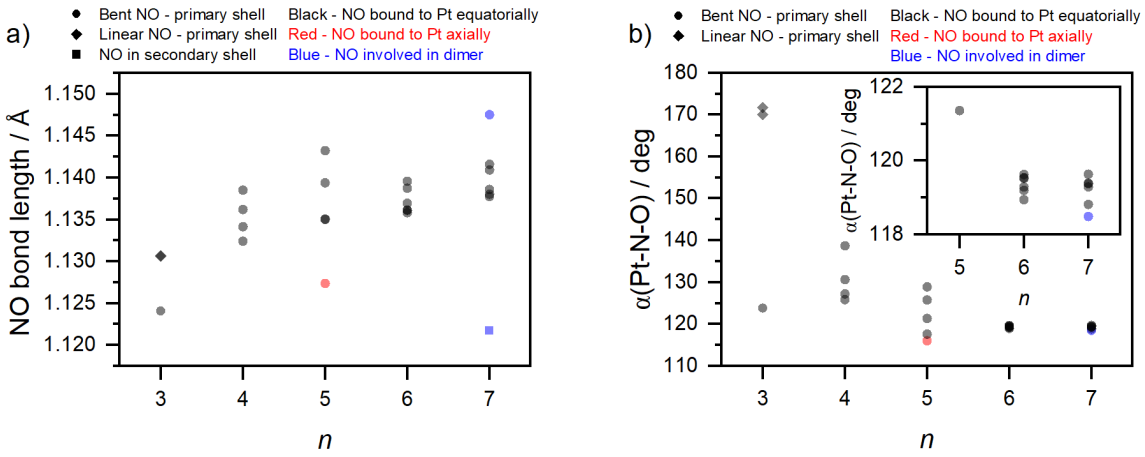

Figure 4.8: **a)** NO bond length vs cluster size, n, for the calculated structures which best fit the experiment IRPD spectra for $[Pt(NO)_n]^+$. **b)** Pt-N-O bond angle, α, versus cluster size, n, for the calculated structures which best fit the experiment IRPD spectra for $[Pt(NO)_n]^+$. The different types of NO molecule are highlighted using the different symbols and colours. The symbols illustrate whether the NO is in the primary or secondary shell, and whether it is bound in a linear or bent fashion, and the colours illustrate where the NO is in the complex. For $n = 7$, the data is from Isomer 7d (octahedral core).

this feature in the experimental spectrum. Using Isomer 5c as a basis led to the formation of the octahedral structure for $[Pt(NO)_6]^+$, Isomer 6c (doublet, 0.02 eV above the putative ground state), with all six NO molecules bound in a nonlinear fashion. The NO molecules and the way they bind to the metal centre are indistinguishable from each other. This is demonstrated in the NO bond lengths and bond angles within the complex being very similar for $n = 6$, as shown in Figure 4.8.

As shown in Figure 4.6 **b)**, there is again very good agreement between the experimental and simulated spectra for $n = 6$, with two main bands in both spectra. The bands in the experimental spectrum at 1739 cm^{-1} and 1793 cm^{-1} are only slightly to the red of the bands observed for $n = 5$. The simulated spectrum again shows that the main bands are composed of multiple modes that are combinations of NO vibrations, with no prominent satellite bands to the red and blue of the main features appearing that would arise from NO dimers. However, there is a very small feature in the simulated spectrum at 1857 cm^{-1} that arises from the "breathing" motion. Compared with $n = 5$, this transition is much weaker (see Figure 4.7 **b)**) due to the reduced transition dipole moment for this

vibration, which correlates with the reduced dipole moment caused by the imposition of the octahedral symmetry following the addition of the sixth NO molecule. Due to the weak IR intensity of this motion, it is difficult to identify this vibrational mode in both the simulated spectrum and experimental spectra. Looking at the IRPD spectrum and the simulated spectrum for $[Pt(NO)_6]^+$, the octahedral six-coordinate structure provides the best fit; something that has not been observed for other comparable metal nitrosyl ion-molecule complexes. Given this configuration, it would be predicted that the Pt core cannot accommodate any additional NO molecules in its primary core, and hence the spectrum for $n = 7$ would be significantly different from the other complex sizes.

Figure 4.6 **c)** shows the IRPD spectrum for $[Pt(NO)_7]^+$, as well as the two structures, Isomers 7c and 7d, which align more closely with the observed features. Within the experimental spectrum, there are new bands that appear at 1691 cm^{-1} and 1885 cm^{-1}, respectively. Both isomers detailed above have triplet spin multiplicities, and are 0.08 and 0.10 eV above the putative ground state, respectively. Despite being close in energy, there are notably differences between the structures of the two isomers; highlighting the complex potential energy surface that arises from the multiple energetically low-lying isomers. Isomer 7c adopts a square-planar core, with an NO dimer and also an NO trimer forming on two separate Pt-coordinated NO molecules. This has produced a simulated IR spectrum with three intense bands, along with smaller features that closely match some of the bands that appear in the IRPD spectrum. These arise from modes that contain vibrations associated with the NO dimer and trimer, with the feature at 1701 cm^{-1} also containing a large contribution of one of the Pt-bound NO molecules. Isomer 7d follows the pattern for $n = 5, 6$ by forming an octahedral structure, with the seventh NO molecule residing in a secondary coordination shell to form a dimer. The new satellite band that appears at 1668 cm^{-1} arises from the localised out-of-phase vibration of the NO dimer (see Figure 4.7 **c)**) that has been identified in many other metal nitrosyl systems. The feature at 1898 cm^{-1}, associated with the "breathing" motion, is much more intense than for the smaller clusters due to the increase in the transition dipole moment caused by the increase in the dipole moment after the addition of the seventh NO. This "breathing" mode spectral feature being observed for the square-planar isomer for $n = 5$, being lost for the octahedral structure of $n = 6$, and reappearing with the octahedral

structure with the dimer for $n = 7$ is a neat example of the effect of the imposition and removal of higher symmetries on IR spectral features.

The central spectral features seen for Isomer 7d may also explain the other peaks observed in the IRPD spectrum, as they do not appear in Isomer 7c. This would also be the structure one might expect to be produced given the degree to which the smaller complexes with octahedral structures reproduce the experimental spectra. Given they have similar energetics and the fact that the two isomers produce spectral features which are in some agreement with the experimental results, it is possible that both isomers are present within the molecular beam.

4.3.5 IRPD Spectra of $[PtO(NO)_n]^+$ $(n = 4 - 7)$

In addition to the IRPD spectra that were recorded for $Pt(NO)_n^+$ $(n = 3 - 7)$, IRPD spectra were recorded for $[PtO(NO)_n]^+$ for $n = 4 - 7$ in the range 1500-2100 cm^{-1}, as shown in Figure 4.9. These spectra were recorded by monitoring the daughter species associated with the loss of one NO molecule. No dissociation was observed for $n = 1 - 3$. The BDE using the lowest energy calculated structures is 2.48 eV, 2.70 eV, and 1.28 eV, for $n = 1, 2$, and 3, respectively. As was the case for $[Pt(NO)_n]^+$, these values are much higher than the photon energies in the region surveyed. Additionally, the value of $n = 3$ for $[PtO(NO)_n]^+$ is higher than for $[Pt(NO)_n]^+$ (0.95 eV), which might explain why no dissociation was observed. The loss of NO was the only fragmentation pathway observed from these species, and therefore the IRPD spectra are recorded in the $[PtO(NO)_{n-1}]^+$ enhancement channel. There are also noticeable differences between the spectra for the complexes with and without the additional oxygen atom; mainly a strong feature farthest to the blue in each of the panels. This follows a similar trend that was observed in our previous work on $[(NO_2)(NO)_n]^+$ complexes, with a discernible feature appearing in the region 1880-1950 cm^{-1} in the IRPD spectrum of the $[(NO_2)(NO)_n]^+$ complexes.[204] For $[(NO_2)(NO)_n]^+$, the new feature is not explicitly illustrating vibrations in the $NO_2{}^{(+)}$ moiety, but rather from NO molecules whose oscillator strength is increased due to interaction with the NO_2 moiety. In the IRPD spectra for the $[PtO(NO)_n]^+$ complexes, as the complex size increases, the peak that is farthest to the blue redshifts towards the free NO vibrational frequency. All of the peaks in the spectra also become better resolved

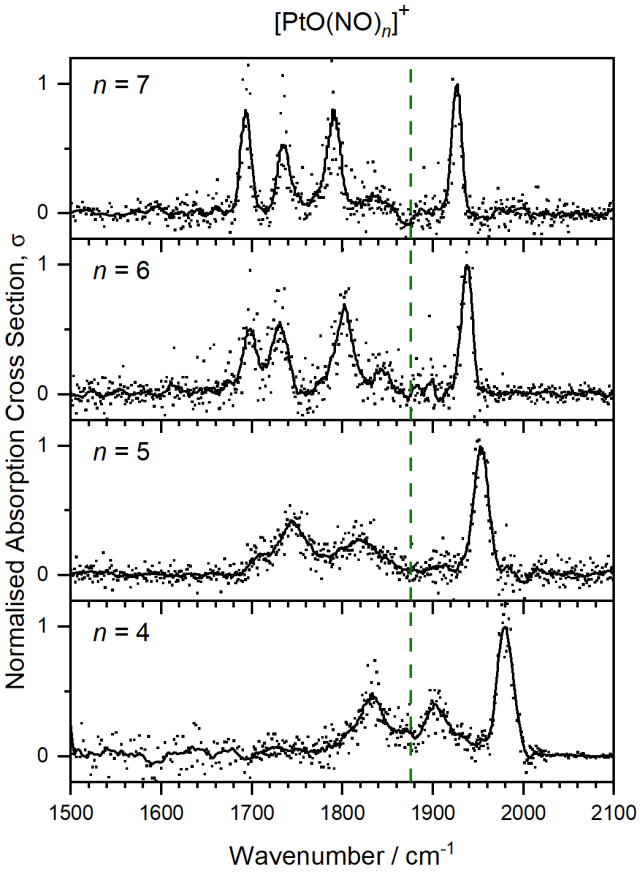

Figure 4.9: IRPD spectra of the $[PtO(NO)_n]^+$ complexes ($n = 4 - 7$), measured in the enhancement of the $[PtO(NO)_{n-1}]^+$ daughter fragment channel, and presented as normalised absorption cross sections for each value of n. The green dashed line indicates the free NO stretch at 1875.84 cm^{-1}.[227]

with increasing complex size, suggesting a decrease in the ligand binding energy. For $[PtO(NO)_4]^+$, there are also additional discernible peaks that arise to the red and the blue of the free NO stretch, at 1831 cm^{-1} and 1905 cm^{-1}, respectively, with what may be another feature in-between the other two at 1868 cm^{-1}.

With respect to $n = 5$, there are two small peaks which are to the red of the free NO stretch; at 1745 cm^{-1} and 1817 cm^{-1}, respectively. There is also a new shoulder that appears at 1706 cm^{-1}. These peaks, similar to what is seen for $[Pt(NO)_n]^+$, arise from combinations of vibrations associated with the NO and NO_2 moieties. Given that the vibrational frequency of the symmetric stretch the free NO_2 is at 1322.5 cm^{-1} and the asymmetric stretching frequency is 1616.0 cm^{-1},[228] it is more likely that the peaks in the

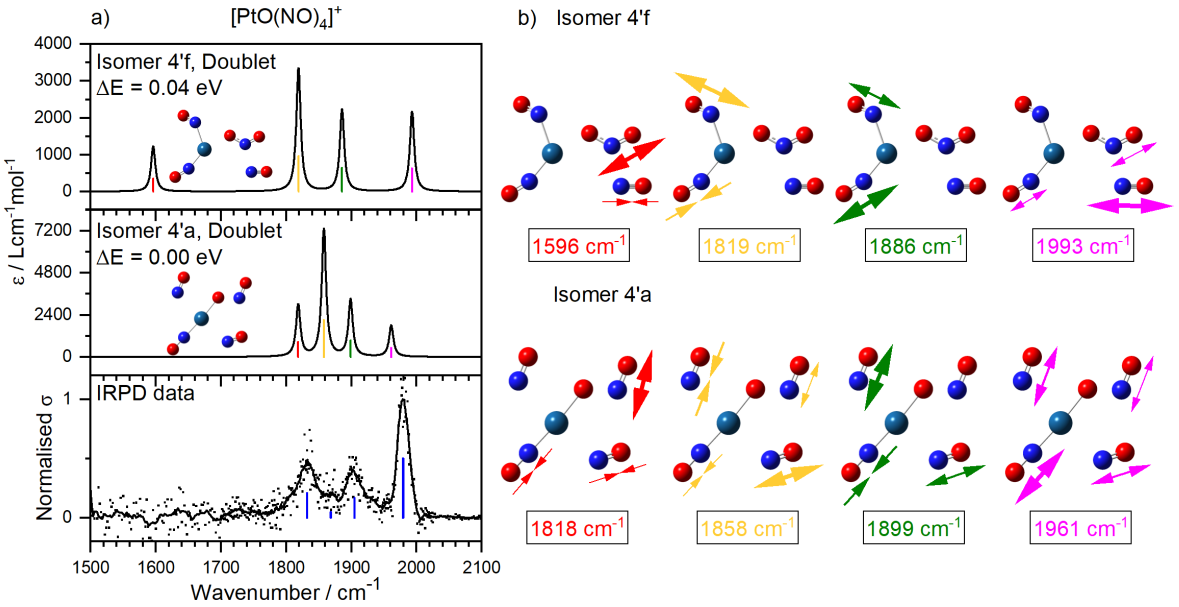

Figure 4.10: **a)** Experimental IRPD spectra (bottom panel), along with the simulated IR spectra and structures (top panels) for the two low-lying isomers that best fit the experimental spectrum of $[PtO(NO)_4]^+$. **b)** The vibrational modes for Isomers 4'a and 4'f illustrated using arrows. The colours match the line spectra that appear in **a)**. The thickness of the arrow indicates the relative amplitude of the vibration for the molecule within the specific normal mode.

region 1600-1950 cm^{-1} arise from vibration modes with more NO character. The peaks to the red of the free NO stretch continue to redshift, similar to what was observed for the $[Pt(NO)_n]^+$ complexes. This could suggest that from $n = 4$ onwards, additional NO molecules are binding directly to the Pt core. However, unlike for $n = 7$ in $[Pt(NO)_n]^+$, there does not appear to be a new set of peaks that appear, which could be caused by NO dimer moieties. This suggests differences in the way NO molecules are arranged in the two sets of complexes, and potentially the inner coordination shell is only fully filled when $n = 7$, unlike for $[Pt(NO)_n]^+$ where this occurs at $n = 6$.

4.3.6 Comparison with $[PtO(NO)_n]^+$ Calculations

Figure 4.10 **a)** shows the IRPD for $[PtO(NO)_4]^+$ along with the simulated spectra of the isomers that best replicate the observed spectral features. For $n = 4$, although there are a large number of energetically low-lying isomers, there are two calculated structures that agree relatively well with the experimental spectrum, Isomers 4'a ($\Delta E = 0.00$ eV, Dou-

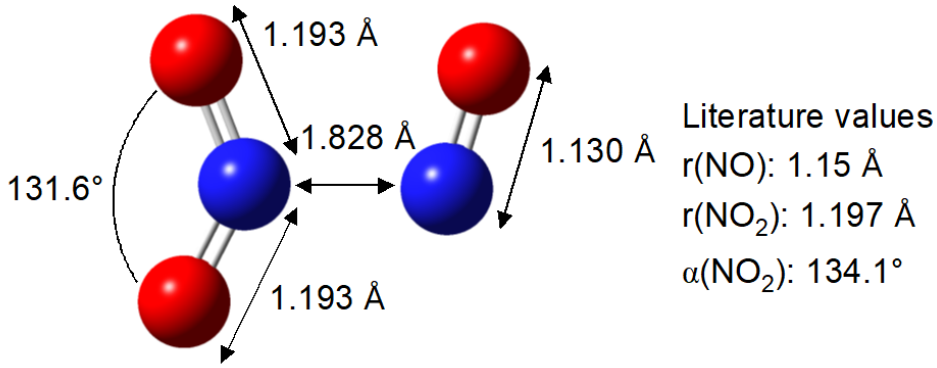

Figure 4.11: Structure and bond angles for the lone N_2O_3 moiety, calculated using B3P86/def2TZVP level of theory. The literature values for the moiety are also provided.[228]

---

blet) and 4'f (ΔE = 0.04 eV, Doublet). Isomer 4'a has three NO molecules bound directly to the Pt centre, with the fourth NO molecule in the NO_2 moiety. They are arranged in a square-planar configuration. The Pt-bound NO molecules next to the NO_2 unit adopt non-linear binding, whereas the NO molecule opposite the NO_2 is linearly bound. Compared to the experimental spectrum, the simulated spectrum produced by Isomer 4'a contains peaks that are approximately in the correct positions, even if the intensities do not match as well. The simulated peak at 1961 cm^{-1} arises from the "breathing" motion of all NO molecules, with the linearly bound NO opposite the NO_2 undergoing the greatest vibrational motion within this specific mode. The feature at 1818 cm^{-1} arises largely from the vibration of NO attached to the oxide, and the other two modes are produced from in-phase and out-of-phase vibrations from the nonlinearly bound NO molecules bound *via* the metal centre. Additionally, no peak is predicted in the region 1500-1700 cm^{-1} for Isomer 4'a.

Isomer 4'f is based on an isomer for $n = 3$ that has two NO molecules bound to the Pt centre, with the additional NO molecule interacting with the Pt-bound NO_2 unit, forming an N_2O_3 moiety. The structure of this moiety is provided in Figure 4.11. There is, unlike with Isomer 4'a, a small peak in the simulated spectrum at 1596 cm^{-1}. This feature arises from the vibration that closest resembles the asymmetric stretch of NO_2.

This mode also contains a very small out-of-phase vibrational motion of the other NO that is coupled with the NO_2 to form the N_2O_3 unit. There is no peak in the experimental spectrum below 1600 cm^{-1} which may be caused by a combination of factors; namely that the oscillator strength of the actual complex may be weaker than the simulated structures, the peaks are further to the red and outside of the spectral range recorded, or the photon energy and laser power in this region are too low to induce photodissociation. Alternatively, it could be experimentally broad due to the wide amplitude motion, making it difficult to discern from the baseline. The lack of the feature in this region makes absolute assignment of the presence of NO_2 difficult. The features at 1819 cm^{-1} and 1886 cm^{-1} are from the out-of-phase and in-phase vibrations of the Pt-bound NO molecules, with the peak farthest to the blue at 1993 cm^{-1} coming from the outermost NO in the N_2O_3 unit vibrating by itself. As mentioned above, this peak farthest to the blue is diagnostic of the outer NO in the N_2O_3 unit, as demonstrated in our studies of $[(NO_2)(NO)_n]^+$ complexes.[204] The vibrational modes for Isomers 4'a and 4'f are illustrated in Figure 4.10. Using Isomer 4'f and the second lowest energy structure calculated for $[PtO(NO)_3]^+$ (Isomer 3'b, contains an N_2O_3 moiety), the dissociation energy to remove an NO molecule that is bound directly to the Pt centre is 0.41 eV. Alternatively, removing the NO that forms the N_2O_3 unit requires 1.04 eV, presumably on account of it being unfavourable to break the stable unit into two radicals. The bond dissociation energies for these structures are presented in Figure 4.13 **b)**. This would suggest that when the larger complex fragments, the NO molecule that is lost comes from the inner coordination shell.

Figure 4.12 shows the energetically low-lying isomers that best fit the IRPD spectrum for $[PtO(NO)_{5-7}]^+$. For $n = 5$, as illustrated in panel **a)**, there are two computed structures that produce simulated spectra that are on first inspection in good agreement with the experimental spectrum, at least with regard to the peak positions. Both are shown here to illustrate that either of these structures could contribute to the experimental spectrum. As shown in the Isomer 4'f spectrum, the two isomers for $n = 5$ both contain a unit of N_2O_3, with the NO_2 molecule bound to the Pt^+ centre. The main difference between the two isomers is the spin multiplicity; Isomer 5'a ($\Delta E = 0.00$ eV) is a triplet, and Isomer 5'b ($\Delta E = 0.11$ eV) is a singlet. As was observed for $[Pt(NO)_4]^+$, Isomer 5'a adopts a square

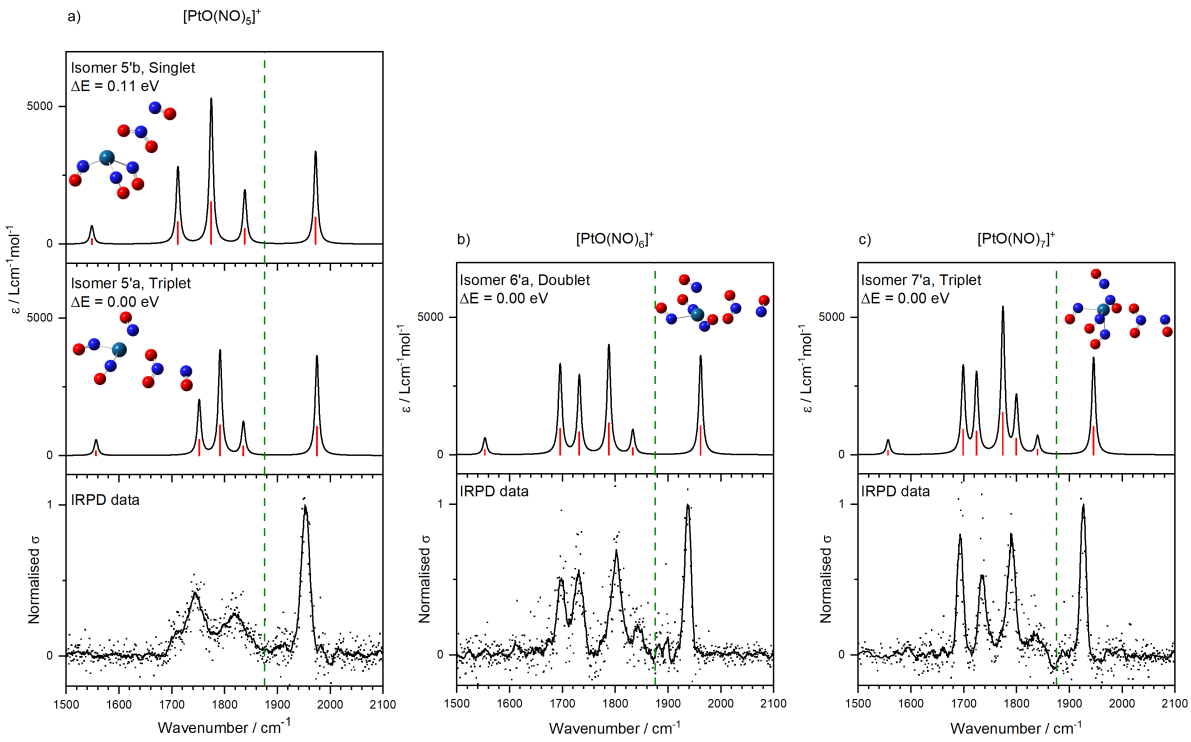

Figure 4.12: Experimental IRPD spectra (bottom panels) along with the simulated IR spectra and structures (top panels) for the best-fit low-lying isomers for **a)** $[PtO(NO)_5]^+$, **b)** $[PtO(NO)_6]^+$, and **c)** $[PtO(NO)_7]^+$. The green dashed line indicates the free NO stretch at 1875.84 cm^{-1}.[227]

planar configuration, whilst for Isomer 5'b, three NO form a pyramidal structure with Pt^+, with the N_2O_3 unit attached to the top site. The spectral features of the simulated spectra can be broken down into three distinct regions: a weak characteristic below 1600 cm^{-1} arising from the asymmetric stretch of NO_2, combinations of in- and out-of-phase NO vibrations between 1700-1875 cm^{-1}, and the characteristic vibration that is localised on the NO molecule that forms the N_2O_3 unit that arises above 1900 cm^{-1}. The lack of a discernible peak below 1600 cm^{-1} in the experimental spectrum may be caused by a combination of factors; namely that the oscillator strength of the actual complex may be weaker than the simulated structures, the peaks are further to the red and outside of the spectral range recorded, or the photon energy and laser power in this region are too low to induce photodissociation. Alternatively, it could be experimentally broad due to the wide amplitude motion, making it difficult to discern from the baseline. The lack of the feature in this region makes absolute assignment of the presence of NO_2 difficult. However, the strong features to the blue of the free NO vibration for both Isomers 5'a and 5'b

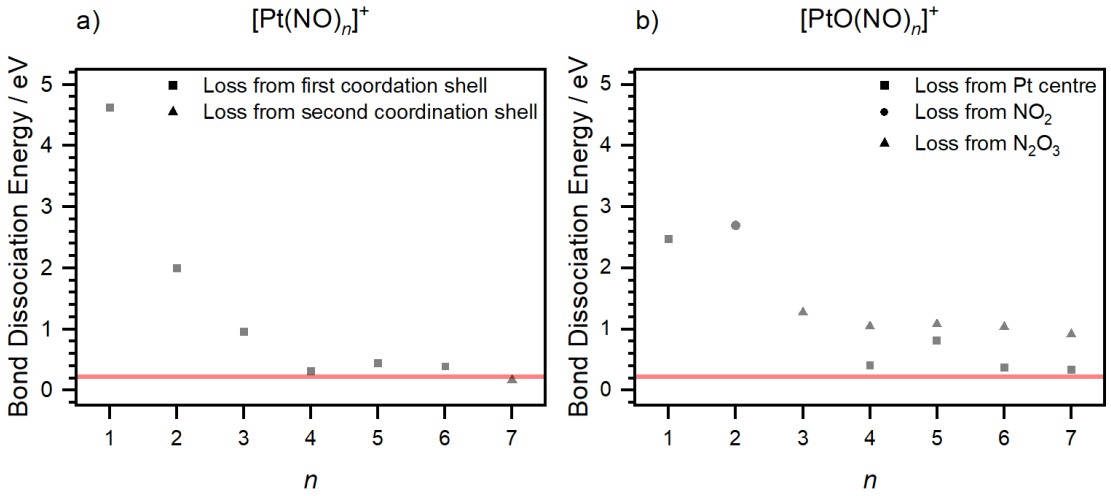

Figure 4.13: Bond dissociation energy (BDE) for the reaction $[PtO_x(NO)_n]^+ \rightarrow [PtO_x(NO)_{n-1}]^+ + NO$, for increasing cluster size, n, for **a)** $x = 0$, and **b)** $x = 1$. For $n = 1, 2$ for both Pt and PtO, the BDE is calculated using the lowest energy computed structures. In **a)**, for $n = 3 - 6$, the BDE has been calculated using the computed structures that best fit with the experimental data. For $n = 7$, the BDE is calculated by removing the NO in the second coordination shell from Isomer 7'd. In **b)**, for $n = 1 - 2$, the BDE is calculated using the lowest energy structures. For $n = 3$, the BDE is calculated for the lowest energy structure with an N_2O_3 moiety. For $n = 4 - 7$, the BDE are calculated by removing an NO from either the Pt centre (squares) or the N_2O_3 unit (triangles) from the computed structures that best fit with the experimental data. The red shaded region indicates the range of IR photon energies across the OPO/OPA scan range used to record the $[PtO_x(NO)_n]^+$ IRPD spectra (1500-2100 cm^{-1}).

provide evidence of the emergence of the N_2O_3 unit. The next lowest energy structure, Isomer 5'c ($\Delta E = 0.21$ eV), has NO molecules aggregating around the N_2O_3 unit, but there is poorer agreement between the simulated and experimental spectra, especially in the region of 1700-1875 cm^{-1}.

For $n = 6$ and $n = 7$, the putative ground state structures, Isomers 6'a and Isomer 7'a, both produce simulated spectra that agree very well with the experimental data, as shown in Figure 4.12. For both sizes, there is a difference of 0.1 eV between the lowest and second lowest energy structures. There is especially good agreement with the peaks in the region 1650-1875 cm^{-1} that arise from different combinations of NO vibrations from the

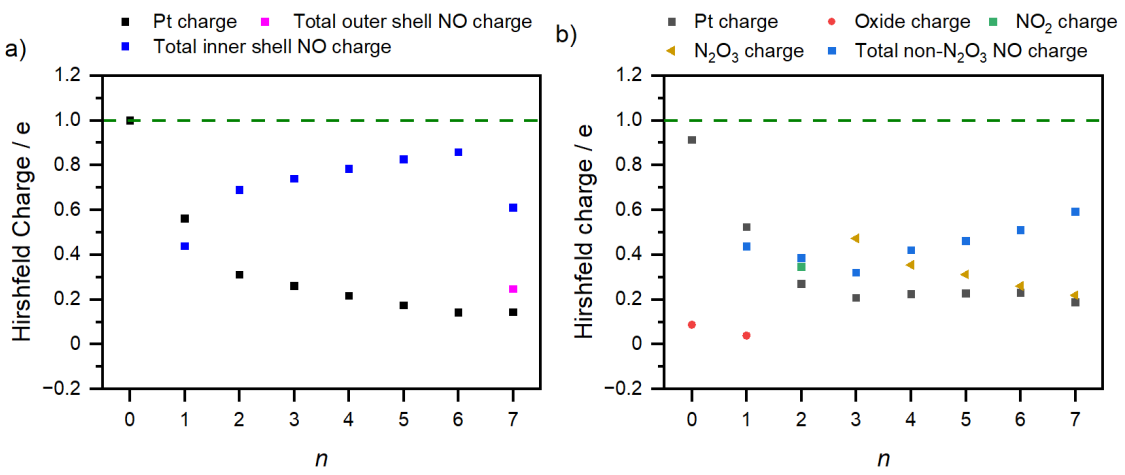

Figure 4.14: Hirshfeld charges for the different components of **a)** $[Pt(NO)_n]^+$ and **b)** $[PtO(NO)_n]^+$ as a function of n using the complexes that best fit the experimental IRPD data. The different colours representing the distinct moieties and metal cores are shown at the top of each panel. The green dashed line is used to illustrate the overall charge of the complexes (+1).

NO molecules bound directly to the metal centre. For $[PtO(NO)_6]^+$, a square-pyramidal structure arises, with the NO_2 unit residing in the equatorial plane, whereas $[PtO(NO)_7]^+$, adopts a pseudo-octahedral structure where the seventh NO molecule attaches to the Pt centre in the remaining coordination site. This reflects the structural geometric pattern that was observed for $[Pt(NO)_n]^+$, and would suggest that $[PtO(NO)_7]^+$ has a filled first coordination shell. If the pattern observed for $[Pt(NO)_n]^+$ persists for $[PtO(NO)_n]^+$, this could suggest that for $n = 8$, new bands would appear following the formation of the $(NO)_2$ dimer. However, this was not recorded because of the lack of signal in the mass spectrum. It should be noted that when the simulated spectra are compared, the spectral feature farthest to the blue arising from the NO in the N_2O_3 moiety redshifts; from 1975 cm^{-1} for $n = 5$ (Isomer 5'a), to 1961 cm^{-1} for $n = 6$, and then to 1945 cm^{-1} for $n = 7$. This reproduces the trend observed within the experimental data.

This gradual red shift is matched by the change in the Hirshfeld charge on the N_2O_3 unit which increases NO ligation, as shown in Figure 4.14 **b)**. The simulated spectra for $n = 6$ and $n = 7$ also have small features arising at 1553 cm^{-1} and 1557 cm^{-1}, respectively, which reflect the asymmetric stretch of NO_2 within the N_2O_3 unit. On

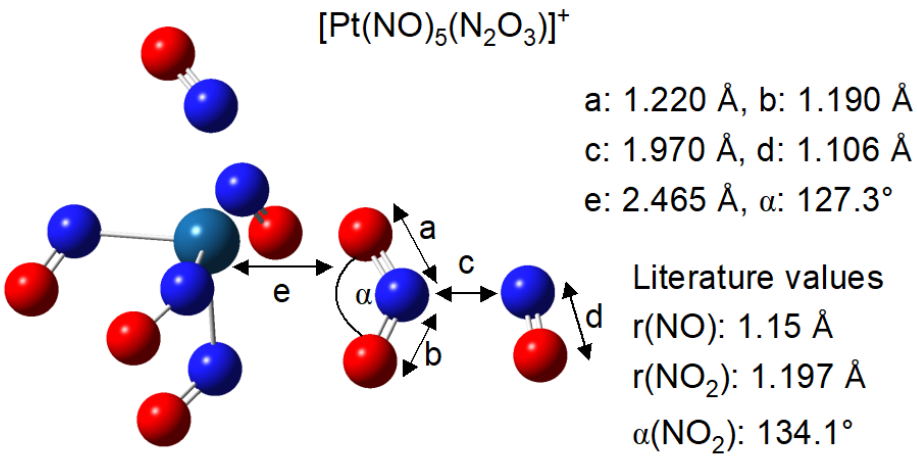

Figure 4.15: The structure of Isomer 7'a for $[PtO(NO)_7]^+$, which adopts the form $[Pt(NO)_5(N_2O_3)]^+$. The bond lengths and angles within the N_2O_3 moiety are illustrated and labeled, with literature values for the bond length of the free NO, and also for the bond length and angle for the free NO_2 being provided.[227, 228] The N_2O_3 moiety is planar, and is rotated approximately 44° out of the equatorial plane formed by the NO directly opposite it, two other NO molecules and the Pt^+ core.

---

close inspection, it could be argued that there are very weak features in the experimental spectra for both $n = 6$ and $n = 7$ around 1600 cm^{-1} that may be produced from this mode, but they are barely discernible from the baseline and this assignment is difficult to perform. As stated earlier, this may be because of linewidth broadening due to wide amplitude motion which makes it hard to observe.

It is quite apparent that NO_2 is contained within the complex, and the chemical formula should actually take the form $[Pt(NO_2)(NO)_{n-1}]^+$, or even $[Pt(N_2O_3)(NO)_{n-2}]^+$. The structure of the lone N_2O_3 is already presented in Figure 4.11 and shows that the bond lengths and angles are comparable to the known values for the individual components of the moiety, namely the NO and NO_2 molecules. Figure 4.15 provides the structural properties for $[PtO(NO)_7]^+$, which can clearly take the structural formula $[Pt(NO)_5(N_2O_3)]^+$. As was the case for $[Pt(NO)_6]^+$, the Pt centre can accommodate up to six ligands binding in the first coordination shell. The lengths and angles of the bonds within the N_2O_3 differ from what was observed for the lone moiety. For example, within the NO_2 part, the N=O bond lengths are different, with the side binding to

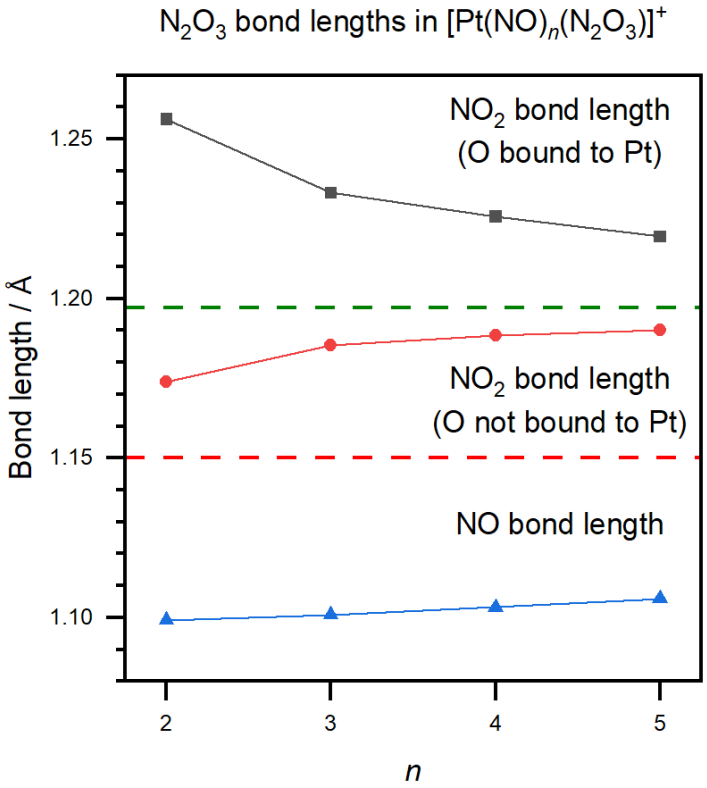

Figure 4.16: The change in the NO and NO_2 lengths within the N_2O_3 moiety in the structures $[Pt(NO)_n(N_2O_3)]^+$ as a function of n. The NO_2 bond lengths are separated to distinguish which oxygen atom is binding to the Pt^+ core in the calculated structure (in each case, the lowest energy calculated structure containing the N_2O_3 moiety). The red dashed lined illustrates the free NO bond length (1.15 Å), and the green dashed line illustrates the free NO_2 bond length (1.197 Å). As the complex size increases, the calculated bond lengths are tending towards the known values for the free molecules, as well as towards the values calculated for the isolated N_2O_3, as shown in Figure 4.11

---

the Pt^+ centre being longer. The NO_2 bond angle is also tighter than for the free moiety.

The changes in the structure of the N_2O_3 unit bound to the Pt^+ centre as a function of the size of the complex, n, are presented in Figure 4.16. The structures used were those that contained the N_2O_3 moiety and best reproduced the IRPD spectra. The NO bond length, shown using blue triangles, represents the NO molecule whose vibration contributes towards the peak farthest to the blue in the IRPD spectrum. As the size of the complex increases, the length of the bond of this molecule increases towards the

Table 4.2: Energy of formation, ΔH_f, for the reaction $[Pt(NO)_n]^+ \rightarrow [PtO(NO)_{n-2}]^+ + N_2O$ presented in eV. The energy is zero-point corrected. The isomers chosen are either the lowest energy structures, or have simualted spectra that best fit the IRPD spectra.

n	$[Pt(NO)_n]^+$ isomer	$[PtO(NO)_{n-2}]^+$ isomer	ΔH_f / eV
2	2a	PtO^+	3.52
3	3a	1'a	1.99
4	4c	2'a	-0.39
5	5c	3'b	-1.28
5	5c	3'c	-1.06
6	6c	4'a	-1.30
6	6c	4'f	-1.26
7	7c	5'a	-1.89
7	7c	5'b	-1.78
7	7d	5'a	-1.91
7	7d	5'b	-1.80

length of the free NO bond (1.15 Å). This increase in the bond length reflects a weakening of the bond, which manifests itself in the redshift observed in the IRPD spectrum towards the free NO vibration at 1875.84 cm^{-1}. The bond lengths within the NO_2 molecule also tend towards the literature values with increasing complex size. The distance between the N_2O_3 moiety and the Pt^+ centre (denoted distance **e** in Figure 4.15) increases as the size of the complex increases; from 2.13 Å for $[Pt(NO)_2(N_2O_3)]^+$ to 2.46 Å for $[Pt(NO)_5(N_2O_3)]^+$. The moiety is moving away from, and being less influenced by, the Pt centre. This may be due to steric effects that make it more difficult for the moiety to approach the metal centre as more NO molecules are bound, as well as the fact that the Pt centre and N_2O_3 become more neutral as the size of the complex increases, as shown in Figure 4.14, meaning that the charge-dipole interaction between the two species weakens and reduces the attraction between them.

The clear evidence of N_2O_3 moieties in the experimental and simulated spectra provides evidence that the oxygen-rich complexes under investigation have been produced

via intracluster chemistry. As stated above, this is further supported by the lack of platinum oxide species when no nitric oxide was added to the carrier gas, as shown in Figure 4.2. The results suggest that NO ligands within a $[Pt(NO)_n]^+$ complex have reacted to form an NO_2 molecule, with loss of an N_2O molecule. This NO_2 can then interact with an NO molecule to form a $[Pt(N_2O_3)(NO)_{n-4}]^+$ complex. This is a reaction described by Equation 4.4 earlier in the chapter. Using the isomers detailed above, the formation energy ΔH_f was calculated for the formation of $[PtO(NO)_n]^+$ from $[Pt(NO)_{n+2}]^+$ with loss of N_2O. The energies are presented in Table 4.2 using isomers that are either the lowest energy or the best fit to the IRPD spectra. The reaction becomes more exothermic with increasing cluster size, and the reaction becomes exothermic for $n \geq 3$. This is consistent with the increased presence of the $[PtO(NO)_n]^+$ complexes compared to $[Pt(NO)_n]^+$ from $n = 3$ onwards, as observed in Figure 4.1. It should also be noted that bond dissociation energies have been calculated to deduce how strongly NO in the N_2O_3 moiety is bound compared to NO molecules that attach *via* the Pt centre. For $n = 4 - 7$, breaking the N_2O_3 moiety by removing an NO molecule requires ≈ 1 eV. As seen in Figure 4.13 **b)**, the energy required to break the N_2O_3 unit is always greater than what is required to remove an NO from the first coordination shell, suggesting that one of the molecules in the first shell is removed when the parent complex fragments following IR irradiation.

4.4 Conclusions

Infrared photodissociation action spectra have been recorded for $[PtO_x(NO)_n]^+$ ($n = 3{-}7$, $x = 0, 1$), with quantum chemical calculations being performed to aid in assigning the observed spectral features. For $[Pt(NO)_n]^+$, there is evidence that the inner shell can accommodate up to six NO ligands in an octahedral structure before NO dimerisation begins. In a similar way to what was observed for $[Rh(NO)_n]^+$, this was demonstrated through a redshift in the peak positions with increasing n, from $n = 3$ to $n = 6$, before new satellite features appear to illustrate the formation of NO dimer moieties at $n = 7$. This is a greater number of ligands binding in the first coordination shell than other gas-phase metal nitrosyl complexes that have been investigated in comparable IRPD studies. From the $[PtO(NO)_n]^+$ IRPD spectra, a strong band appearing to the blue of the free NO stretching frequency implies the formation of a NO_2 molecule, in the

form of an N_2O_3 moiety; following a similar trend that was observed for $[(NO_2)(NO)_n]^+$ complexes. The spectral evidence of the NO_2 moiety implies the experiment has probed the product of intracluster chemistry, and quantum chemical calculations suggest that the formation of $[Pt(NO_2)(NO)_{n-3}]^+$ from $[Pt(NO)_n]^+$, with the loss of an N_2O molecule, is energetically viable. The spectral data also suggests that $[PtO(NO)_7]^+$ adopts a six-coordinate geometry, with a chemical formula of $[Pt(N_2O_3)(NO)_5]^+$ better describing the complex. The structural evolution with complex size follows a similar path between the two Pt systems detailed here; with and without the excess oxygen atom.

Part B: Infrared Free-Electron Laser Studies on Metal Clusters

Chapter 5

Spectroscopic and Chemical Properties of Gas-Phase Neutral and Cationic Tantalum and Tantalum Oxide Clusters, $[Ta_nO_x]^{0/+}$

This chapter presents a combined experimental and computational study of isolated neutral and cationic tantalum and tantalum oxide clusters, $[Ta_nO_{x=0-2}]^{0/+}$. Preliminary computational studies were completed to investigate the binding of nitrogen oxides (NO and N_2O) to cationic Ta clusters. Anomalous increases in the ion signal were observed when the molecular beam was irradiated by the high fluence IR beam produced by the FELICE free-electron laser, based in Nijmegen, The Netherlands. This unexpected behaviour led to photoionisation studies being completed on the neutral tantalum species using IR light from FELICE. These photoionisation studies were assisted by further DFT calculations, which were used to predict the structure of the neutral tantalum species.

An unexpected common broad feature with an onset above 600 cm^{-1} is assigned to the thermionic emission of neutral cluster species. Variations in the onset position of this band show some correlation with the ionisation potentials of the associated neutral clusters. There is generally good agreement between the experimental and simulated spectra for $Ta_nO_{x=1,2}$ using energetically low-lying calculated structures. The symmetric oxide stretching features observed from 650-750 cm^{-1} are assigned to a bridged oxygen atom bonding motif and dissociatively bound O_2 in Ta_nO_2 clusters. The Ta-O stretching frequency redshifts with increasing cluster size and decreasing Ta-O bond strength. There is also evidence that photofragmentation occurs; specifically, the parent clusters of $Ta_nO_{x=1,2}$ can decay with the loss of Ta and/or TaO, producing a daughter Ta_n.

The experimental work was completed by myself along with Dr. Peter Watson, Dr. Christian Haakansson, Ruby Spratt and Peter Rubli. Initial calculations on the cationic Ta species with nitrogen oxides were completed by myself, with the others leading the calculations for the neutral clusters. The analysis of the experimental and computational results was performed jointly.

5.1 Introduction

In previous chapters of this thesis, the importance of dealing with nitrogen oxides (NO_x) has been outlined. The three-way catalytic converter described previously uses a mixture of late transition metals (Rh, Pd, and Pt) to remove CO and NO_x from vehicle exhaust by converting them into less harmful gases.[249, 313] This fact made the study of these systems an interesting proposal, and the results could be compared with previous research completed by Zhou and co-workers on other gas-phase cationic nitrosyl complexes including late transition metals (Fe, Cu, Ag, Au).[301–303] However, as has been described in Chapter 1, gas-phase clusters are interesting models that can be used to replicate catalytic active sites.[1] Instead of varying the number of molecules bound to a single cation, studying the effect on the reactivity of a cluster by changing its size could provide useful information about how small molecules bind to catalytic active sites.[64, 69, 267, 314, 315]

Studies have been conducted on late transition metal neutral and cationic clusters,

$[M_n]^{0/+}$ (M = Co, Rh, Ag, Ir, Pt, Au), with nitric oxide (NO) and nitrous oxide (N_2O) using a range of experimental and computational spectroscopic techniques.[266, 267, 276, 280, 284, 288, 309, 316–320] IR spectroscopy has been performed on collisionally-stabilised metal cluster-ligand complexes, and have shown that N_2O preferentially binds to cationic metal clusters *via* the terminal N-atom for Rh and Au.[318, 321] Studies have also shown that N_2O molecules can bind through the terminal O-atom in Co clusters, and some evidence for specific sizes of Pt clusters.[320, 321] Reactivity studies have also been completed using metal clusters with nitrogen oxides. Oxygen transfer was shown to be the dominant reaction channel observed for late transition metal clusters reacting with N_2O in the gas-phase under single-collision conditions. Furthermore, when these metal cluster-ligand complexes were irradiated with IR radiation resonant with the N_2O modes, the fragmentation pathways include the production of the metal oxide cluster, $[M_nO]^+$, with the loss of an N_2 molecule, in addition to the pathway that involves the loss of the N_2O ligand.

A similar pattern is also observed in reactivity studies with NO, in that the high exothermicity of oxide formation causes these ligands to bind dissociatively in clusters formed from late transition metals.[69, 267, 269, 271, 272, 278, 279] Subsequent additions of NO molecules can result in the formation of more metal-oxide bonds, with small molecules such as N_2 or even N_2O boiling off.[265, 274, 277, 319, 322] NO molecules will attach non-dissociatively once a number of oxygen atoms are attached to the cluster, with the number of oxygen atoms binding to the cluster increasing as the size of the cluster increases. For $[Rh_n]^+$ and $[Ir_n]^+$ clusters, size-selective NO dissociation was predicted using DFT calculations.[276, 323] However, when the experiment was performed for $[Rh_n(NO)Ar]^+$, the IR bands were consistent with molecularly bound NO.[323] This changed however when the clusters were doped with a single Ta or Ir atom, with new oxide and nitride peaks appearing that showed that the adsorbed NO molecule had dissociated.[276, 324] For Au cationic clusters, the NO molecules were seen to bind molecularly, but the vibrational frequency of the ligand oscillates with cluster size, with the NO vibrational frequency being greater for odd cluster sizes.[280] The HOMO, which is comprised of one of the NO π^* orbitals, is singly occupied for odd-sized $[Au_n(NO)]^+$, and doubly occupied for the even sizes, *i.e.* the NO ligand behaves as an electron acceptor. As a consequence,

the formal N-O bond order oscillates between 2.5 and 2, which in turn causes the observed fluctuation in the vibrational frequencies with increasing size.

As stated earlier, each of these studies have been limited to late transition metal elements, but as was shown by the doping of the Rh cationic clusters with Ta, the use of earlier transition metal elements could be a promising avenue to promote molecular activation of nitrogen oxide. For example, inductively coupled plasma/selected-ion flow tube (ICP/SIFT) tandem mass spectrometry studies showed that early transition metals atomic cations undergo O-transfer reactions with CO_2 to form metal oxides, whereas later transition metals form ion-ligands complexes.[325] In each row of the transition metals, Ti^+, Nb^+, and W^+ represent the border of this trend, which implies there is a possibility of tunability as a function of cluster size. For the elements within Group 5 (V, Nb, Ta), studies have been performed looking at the structure of the clusters, and how these elements interact with small molecules.[147, 326–332]

Ta is of interest given the notable differences between its bulk properties and the properties of the individual atoms/metal clusters. Ta in the bulk is an inert, refractory metal with an extremely high melting point (3290 K)[333] and density (16.6 g/cm^{-3}),[333] and has a high work function (211 crystal: 4.352 ± 0.0001 eV).[334] Gas-phase Ta clusters are known to have a lower melting-like transition temperature than the bulk,[335] and the small clusters can show size-dependent magnetism due to unpaired d-electrons not fully delocalised, with the magnetic moments oscillating with cluster size.[336] In addition, studies with Ta_n clusters have highlighted their increased reactivity compared to the bulk material,[337] and have been shown to react with CH_4, O_2, and simple alcohols.[338–342] Ta_n^+ clusters have been shown to dissociate multiple N_2 molecules on its surface,[317] even at cryogenic temperatures (26 K).[343] This is of interest given the N_2 triple bond's strength and the importance of cleaving this bond in the Haber-Bosch process. This also implies that Ta clusters could be used to reduce nitrogen oxides. Apart from some DFT calculations of Ta cationic clusters interacting with NO,[344] little has been done to investigate Ta cations and cationic cluster reactivity with nitrogen oxides. Given its reactivity with N_2 and CO_2,[345] and its promising catalytic activity for CO oxidation, a size-dependent spectroscopic study of Ta_n^+ with nitrogen oxides was deemed worthwhile.

5.2 Study of Ta Cationic Clusters

5.2.1 Computational Ta Cationic Clusters with N_xO_y - Methods

Our group was granted time at the FELIX/HFML facility to perform IR-MPD studies on $[Ta_n(NO/N_2O)]^+$ complexes using the FELICE beamline.[229, 230] This had two benefits over the IRPD setup used in Oxford: 1) the beamline at HFML-FELIX used a cluster source that could generate the clusters, as described in Chapter 2, and 2) the FELICE beamline can span the entire frequency range (260-2100 cm^{-1}) required to deduce whether the NO or N_2O molecules are molecularly bound (even if they are highly activated), or if they are dissociatively bound. The structures of the Ta clusters could also be investigated using FELICE by looking at the Ta-Ta vibrational modes (frequencies on the order of hundreds of wavenumbers). However, prior to the experiments, DFT calculations were performed to determine the structures of the $[Ta_n]^+$ clusters and also to determine the vibrational frequencies the complexes possess when the ligands (NO/N_2O) are added.

As described in Chapter 2, the calculated structures are produced using the Gaussian 16 software package at the B3P86/def2TZVP level of theory [188, 238–240] with multiple starting structures generated using a modified *Kick*[3] algorithm.[198] To start with, the bare Ta_n^+ structures were calculated before they were decorated with oxygen atoms, as well as NO and N_2O molecules. These preliminary calculations were used to predict how many peaks should appear for the different isomers and where they should approximately appear. Given that the ligands may be highly activated or even bind to the clusters dissociatively, no scaling factor was applied. Additionally, the frequency of Ta-Ta vibrations would only change by a few wavenumbers if they were multiplied by the typically scaling factors ($\sim 0.92 - 0.96$), so this also led to a scaling factor not being applied for these calculations. The final energies reported here are zero-point corrected, and the calculated line spectra are convoluted with Lorentzian line shapes with a full width at half maximum (FWHM) of 8 cm^{-1}.

5.2.2 Computational Ta Cationic Clusters with N_xO_y - Results

The structures of the bare cationic Ta clusters had to be generated before they were coated with the ligands. Figure 5.1 shows the structures for the lowest energy isomers

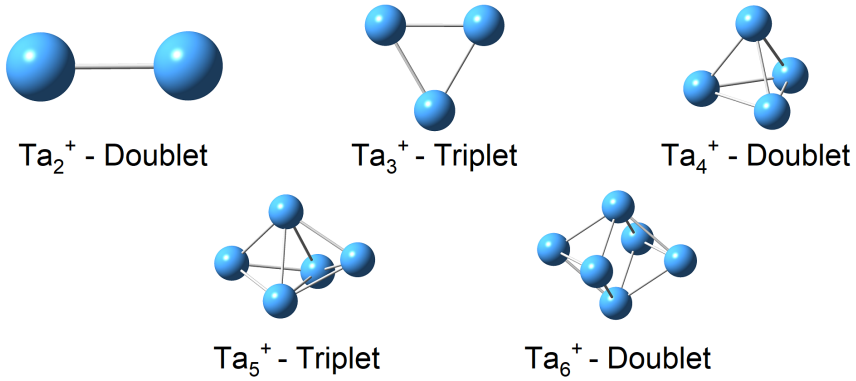

Figure 5.1: Structures and multiplicities of the lowest energy structures for bare Ta_n^+ clusters (n = 2–6).

that were calculated for the Ta_n^+ clusters ($n = 2-6$). Each cluster was built up from the previous structure (*i.e.* Ta_4^+ was formed by running the *Kick*[3] algorithm on Ta_3^+ with a Ta atom). The structures that have been adopted similar properties to the Ta clusters studied in previous experimental and theoretical studies.[327, 336, 346] For example, the Ta_2 ground state structure (doublet spin multiplicity) bond length was calculated to be 2.18 Å, and the unscaled vibration frequency was 338.39 cm^{-1}. This is compared to 2.199 Å, and 343.2 cm^{-1} calculated for Ta_2^+ (doublet spin multiplicity) which was calculated by Wu, Kawazoe, and Meng at the B3LYP/LANL2DZ level of theory.[347] Other studies have also shown that the progression of structures follows the same pattern from $n = 3$: equilateral triangle, tetrahedral, trigonal bipyramidal, octahedral.[327, 336] The lowest energy structures also adopt low-spin states (doublets for clusters with even numbers of Ta atoms, triplets for clusters with odd number of Ta atoms) which agrees with what has been noted in the literature.[336]

Using the lowest energy bare cationic Ta clusters, the NO and N_2O ligands were added using the *Kick*[3] algorithm to investigate how they bind. Figure 5.2 provides a stacked plot of the lowest energy isomers for the $[Ta_n(NO)]^+$ clusters ($n = 1-5$). The vibrational frequency of the free NO is shown with the dashed green line at 1875.84 cm^{-1}. As shown, all of these structures have dissociated the NO molecule, with the atoms adopting different binding motifs depending on how many Ta atoms are in close proximity. It should also be noted that all these motifs are relatively weak; the most intense features have

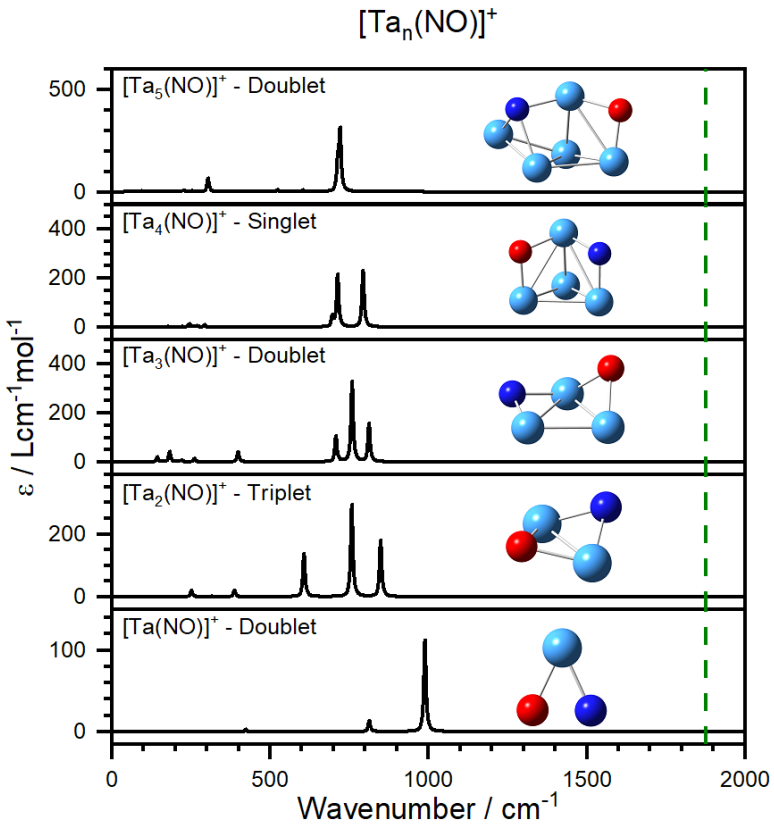

Figure 5.2: Stacked simulated spectra for the lowest energy isomers for $[Ta_n(NO)]^+$ ($n = 1 - 5$). The structures for each of the cluster sizes is also presented in each panel. The green dashed line illustrates the free NO vibrational frequency at 1875.84 cm^{-1}.[227]

intensities of $\sim$ 350-400 Lcm^{-1}mol^{-1}. For $n = 1$, NO has attached side-on (*i.e.* both N and O atoms are bound to the metal centre). This binding has weakened the NO bond (N=O bond distance in $[Ta(NO)]^+$ = 1.51 Å) and caused it to break. As a result, the two strongest bands that appear at 813.41 cm^{-1} and 989.66 cm^{-1} correspond to the N-Ta-O asymmetric and symmetric stretches, respectively. The next lowest structure for $[Ta(NO)]^+$ (ΔE = 0.41 eV) adopted a linear Ta-N=O structure, with an unscaled NO vibrational frequency of 1741.92 cm^{-1}.

From $n = 2$ onwards, the atoms from the NO molecule can attach to the edges formed within the Ta_n^+ complexes and act as bridging atoms (adopting μ_2 binding). This lowers the vibrational frequency compared to what was observed in $n = 1$ where the atoms of the NO molecule are attached to only one Ta atom as the effective reduced mass is larger due to two metal atoms moving during vibration. The vibrational frequencies of

Table 5.1: Vibrational frequencies for the tantalum oxide and tantalum nitride stretches, ν(Ta-O/Ta-N), for $[Ta_n(N)(O)]^+$ ($n = 2-5$). The binding motifs for the bridging oxygen and nitrogen atoms are also presented (μ_n denotes how many Ta atoms the additional atoms bridge, *i.e.* μ_2).

n	ν(Ta-O) / cm^{-1}	Ta-O binding	ν(Ta-N) / cm^{-1}	Ta-N binding
2	758.64	μ_2	849.59	μ_2
3	759.52	μ_2	812.89	μ_2
4	713.77	μ_2	794.04	μ_2
5	721.62	μ_2	714.24	μ_3

Ta-O and Ta-N and the binding motifs for the nitrogen and oxygen atoms that bind to $[Ta_n(N)(O)]^+$ clusters ($n \geq 2$) are presented in Table 5.1. For $[Ta_2(NO)]^+$, the ground state structure has the atoms of the NO molecule binding on either side of the Ta-Ta bond; forming a near-planar quadrilateral structure. The oxide and nitride stretching frequencies in $[Ta_2(NO)]^+$ are 758.64 cm^{-1} and 849.59 cm^{-1}, respectively. For $[Ta_3(NO)]^+$, the nitrogen and oxygen atoms attach to different edges, the nitrogen atom residing in the same plane as the three Ta atoms and the oxygen atom pointing out of the plane. The frequencies for the same modes in $[Ta_3(NO)]^+$ are 759.52 cm^{-1} and 812.89 cm^{-1}, respectively. With the nitrogen being in the plane of all the Ta atoms, the N 2p orbital can overlap with the molecular orbitals of the entire cluster, causing the electrons to be delocalised around the entire cluster.[348] This causes the metal-nitrogen bond to weaken and reduces the metal nitride vibrational frequency. For both of these cluster sizes, the other spectral peak of comparable intensity appears at 607.42 cm^{-1} for $n = 2$ and 708.24 cm^{-1} for $n = 3$. For $n = 2$, this peak arises from the symmetric N-Ta-O vibration, whereas for $n = 3$, this arises from the asymmetric N-Ta_2 vibration.

For $n = 4$, the atoms from the NO molecule are attached along one of the edges of the three-dimensional tetrahedral cluster. There are two main peaks, appearing at 713.77 cm^{-1} and 794.04 cm^{-1} that correspond to the Ta-O and Ta-N stretches, respectively. The reduction in the vibrational frequency, as shown in Table 5.1, is due to the metal-oxide bond weakening with increased electron density delocalisation as more metal-metal

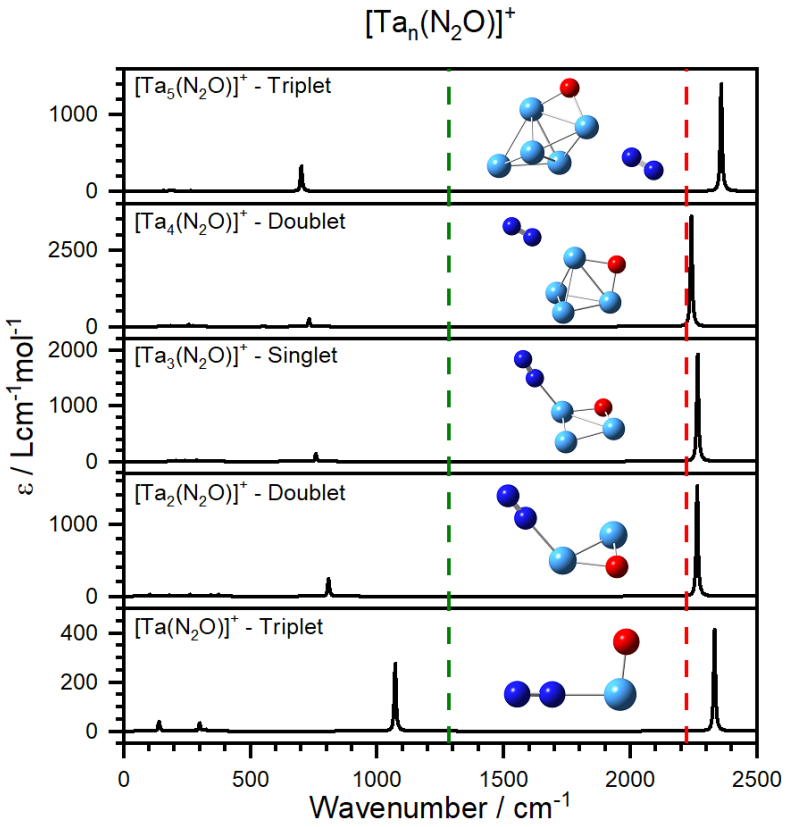

Figure 5.3: Stacked simulated spectra for the lowest energy isomers for $[Ta_n(N_2O)]^+$ (n=1–5). The structures for each of the cluster sizes is also presented in each panel. The green and red dashed line illustrates the free N_2O vibrational frequencies at 1285 cm^{-1} (N=O stretch) and 2223.5 cm^{-1} (N=N stretch), respectively.[228]

bonds are formed. There is also a shoulder appearing at 696.62 cm^{-1} that arises from the symmetric N-Ta-O vibration, but it is a weak feature. In addition to that, a corresponding feature for the asymmetric N-Ta-O appears at 536.23 cm^{-1}, but this mode has an intensity that is near zero due to the fact that there being nearly no change in the dipole moment due to the highly symmetric structure. For $n = 5$, there is a difference in that the nitrogen atom attaches to the cluster on one of the trigonal faces and it adopts μ_3 binding. As a result of this, the vibrational frequency for the Ta-N mode is reduced from 794.04 cm^{-1} for $n = 4$ to 714.24 cm^{-1} for $n = 5$. The Ta-O vibrational frequency for $n = 5$ is 721.62 cm^{-1}; greater than the Ta-N vibrational frequency as shown in Table 5.1.

The predicted lowest energy structures for $[Ta_n(N_2O)]^+$ are presented in Figure 5.3. In this stacked graph, the vibrational frequencies for the N_2O N=O and N=N stretch at

Table 5.2: Calculated energy of formation, ΔH_f, of $[Ta_nO(N_2)]^+$ from Ta_n^+ and N_2O, using the lowest energy isomers highlighted in Figures 5.1 and 5.3. The $[Ta_nO]^+$ – N_2 bond dissociation energy (BDE) is also presented.

n	$\Delta H_f([Ta_nO(N_2)]^+)$ / eV	BDE($[Ta_nO]^+$ – N_2) / eV
1	-6.63	1.05
2	-6.30	0.65
3	-6.78	0.69
4	-6.41	0.62
5	-5.51	0.38

1285 cm^{-1} and 2223.5 cm^{-1} are illustrated using the green and red dashed lines, respectively. For each of the cluster sizes shown, the N_2O molecule has dissociated to form $[Ta_nO(N_2)]^+$ complexes. This is likely driven by the energetic favourability of forming an N_2 molecule,[349] as well as the oxophilicity of Ta that drives it to form Ta-O bonds.[350] Each of the simulated spectra in Figure 5.3 has a strong characteristic that appears in the blue of the N_2O N=N stretch at 2223.5 cm^{-1} which arises from the N_2 molecule that has formed. This band is outside the range of frequencies that FELICE can reach (up to 2100 cm^{-1}). However, even if FELICE's frequency range could be extended, it was assumed that this band would not be present in an experimental spectrum as the N_2 would likely dissociate given the energy that would be released on its formation and how weakly it is bound to the cluster. Table 5.2 shows the formation energy ΔH_f, for the $[Ta_nO(N_2)]^+$ clusters, as well as the $[Ta_nO]^+$ – N_2 bond dissociation energy. This shows that the process of forming the complex is highly exothermic and that the magnitude of the energy released is greater than the energy required to remove the N_2 molecules. If these vibrational frequencies associated with the N_2 molecule were observed experimentally using IR-(M)PD, it would likely require the complex to be cryogenically cooled and Ar-tagged to reduce the probability that the N_2 molecule would be lost before being extracted on the ToF mass spectrometer. It should also be noted that there are bands with the simulated spectra which correspond to the Ta-O stretch. For $n = 1$, this peak appears at 1072.29 cm^{-1}, which is comparable to the frequency calculated by Wu, Kawazoe, and Meng for TaO^+ at 1077.3 cm^{-1} (triplet spin multiplicity).[347] Going from $n = 1$ to $n = 2$, the

oxygen atom bridges two Ta atoms, hence the redshift in the Ta-O stretching frequency. There is a gradual redshift in the Ta-O stretching frequency, owing to the increase in the effective reduced mass as more Ta atoms are added to the cluster. The intensity of the peaks for each of the clusters is weak due to the symmetry of the vibrations, which is caused in part by the high symmetry of the cluster.

Although these lowest energy calculated structure do not contain vibrational frequencies that arise from molecularly bound N_2O, it was important to determine where these bands may appear in case the experimental setup surveys an entrance channel complex that does have an N_2O molecule attached to a cluster, albeit highly activated. Figure 5.4 provides the lowest energy structures for $[Ta_4(NO)]^+$ **(a)**, bottom panel) and $[Ta_4(N_2O)]^+$ **(b)**, bottom panel), as well as the lowest energy molecularly bound complexes (top panels). The complexes that contain molecularly bound ligands are much higher in energy than the dissociated structures, with the difference being 4.74 eV for $[Ta_4(NO)]^+$ and 5.28 eV for $[Ta_4(N_2O)]^+$. For the N_2O complex, there is also a change in spin multiplicity (from doublet to quartet). The ligands in the complexes are also highly activated, as seen through the vibrational frequencies. For panel **a)**, the vibrational frequency of NO has been significantly red shifted to 1272.02 cm^{-1}. This is compared to the free NO stretch at 1875.84 cm^{-1}, as illustrated by the green dashed line in Figure 5.4 **a)**. The NO bond has also elongated to 1.29 Å, compared to the free NO bond length of 1.15 Å. For the N_2O complex, the vibrational frequencies have also redshifted significantly: to 800.35 cm^{-1} for the N=O stretch compared to 1285 cm^{-1} in the free molecule (shown as the green dashed line in Figure 5.4**b)**), and 1297.22 cm^{-1} for the N=N stretch compared to 2223.5 cm^{-1} (shown with the red dashed line). The bond lengths are significantly altered; the N=N bond length for the calculated structure is 1.25 Å compared to 1.13 Å, and the N=O bond length is 1.41 Å compared to 1.19 Å. The molecule also bends when attached to the cluster, with the N=N=O angle is equal to 122.1° instead of 180° observed in the free molecule. Given that multiple N_2 molecules have been observed to dissociatively bind to gas-phase Ta clusters,[343] it is not surprising that these nitrogen oxides break apart as the N=O bond is weaker.

From these initial calculations, it was clear that the dissociated structures were the

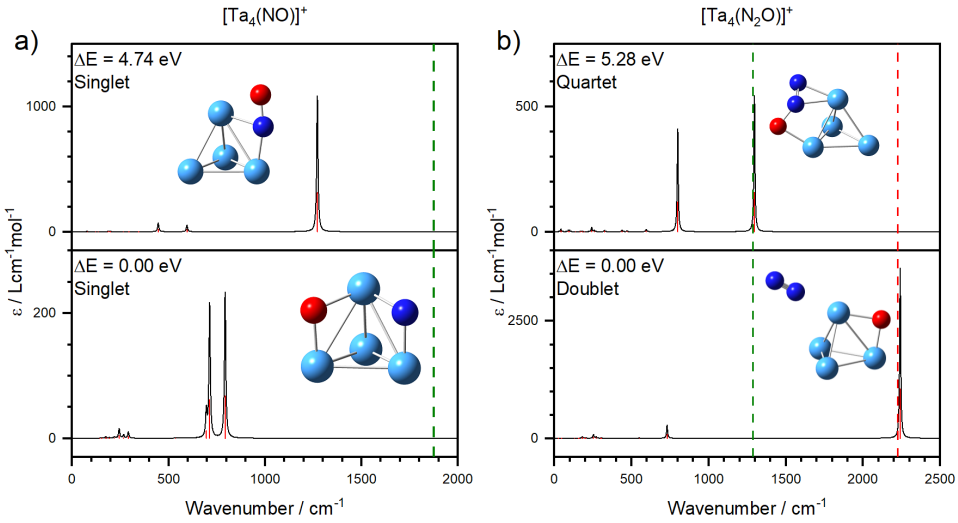

Figure 5.4: Simulated spectra for the lowest energy dissociated structures for $[Ta_4(NO)]^+$ (panel **a)**, bottom) and $[Ta_4(N_2O)]^+$ (panel **b)**, bottom), as well as the lowest energy molecularly bound structures (top panels). The structures for each of the cluster sizes is also presented in each panel. The dashed lines in panels **a)** and **b)** represent the same vibrations described in Figures 5.2 and 5.3.[227, 228]

favoured thermodynamic product. However, if the highly redshifted ligand vibrations from the molecularly bound structures were to appear, it would imply that the reaction followed a pathway that led to higher energy products, meaning additional studies would be required to determine the relative barrier heights along the different pathways. Fortunately, the FELICE setup would be able to investigate the entire frequency range required to determine how the ligands bind to the Ta cationic clusters. The next step was to perform the experiment and examine which of these structures was observed.

5.2.3 Mass Spectra of Ta Cationic Clusters

The general setup used to carry out the experiment has been described in Chapter 2. Initial mass spectrometry studies were performed to ascertain how large the Ta cationic cluster could be made, and whether it was possible to tag them with Ar atoms in order to deplete them using the messenger tag method. A carrier gas mixture of 15% Ar in He was produced and the source block was cryogenically cooled using liquid nitrogen. Several mass spectra were recorded at different temperatures to see how the distribution changes as a function of temperature. Figure 5.5 provides an example mass spectrum generated when the reactant block in the source chamber was cooled to -157 °C (116 K,

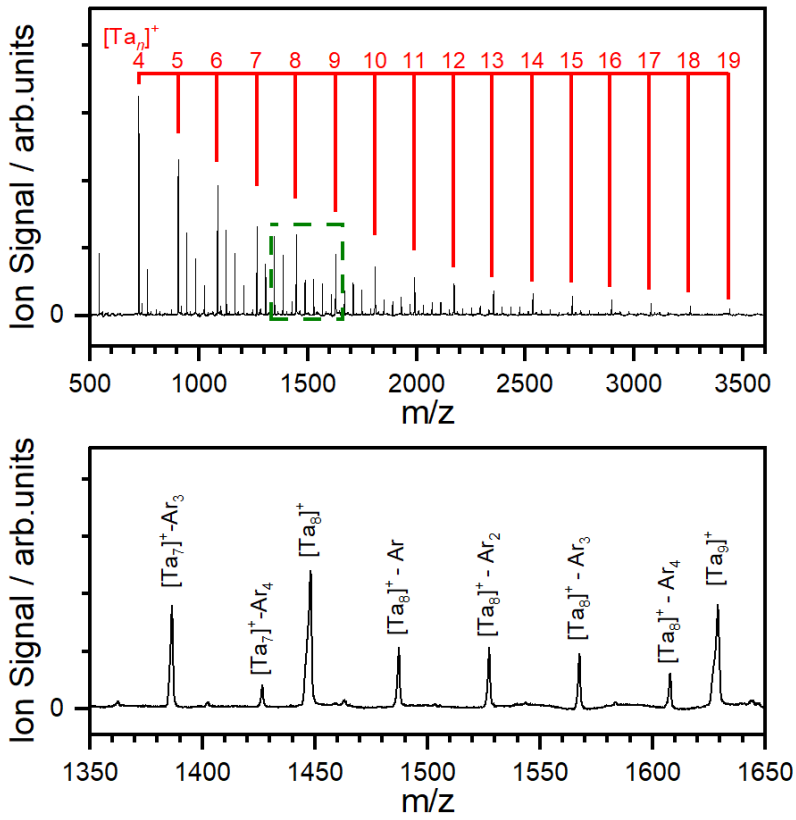

Figure 5.5: Top panel: Mass spectrum for Ta_n^+ species spanning from 500 to 3500 amu, using a 15% Ar in He gas mixture. The source was cooled to -157 °C (116 K). The red railroad diagram is used to pinpoint the bare cationic Ta clusters of size n. **Bottom panel**: Zoomed-in mass spectrum of the region highlighted by the green dashed box in the top panel (1350 to 1650 amu). Up to four Ar tags are observed on the Ta_7^+ and Ta_8^+ clusters.

---

the temperature was finely controlled by balancing cryogenic cooling and heating using the filament). As can be seen in the top panel, clusters could be generated between $n = 4 - 19$. In the bottom panel, a zoomed-in section of the spectrum above, denoted by the dashed green box, shows that up to four Ar tags can be attached to Ta_7^+ and Ta_8^+. This provided evidence that the clusters could be tagged if necessary and that large clusters can be generated if the source block is cooled to a sufficiently low temperature. The next step was to investigate whether the clusters could be coated with the reactant nitric oxide ligands and to see which species were generated.

Nitric oxide was added *via* the secondary nozzle, with a backing pressure of 1.2 bar.

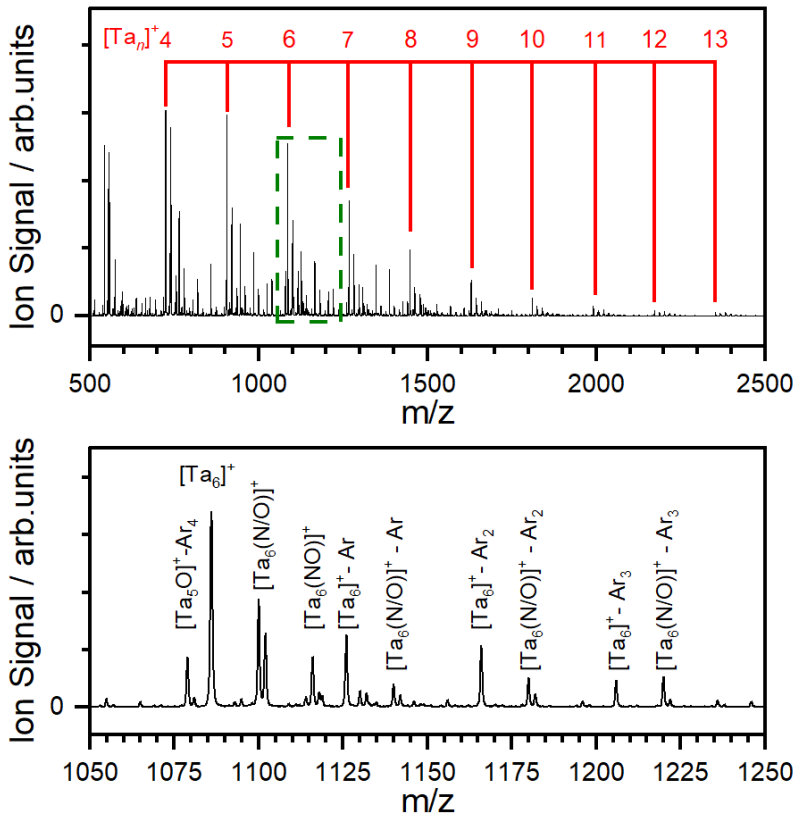

Figure 5.6: Top panel: Mass spectrum for $[Ta_n(NO)]^+$-Ar species spanning from 500 to 2500 amu, using a 10% Ar in He gas mixture as the carrier gas, and 1.2 bar backing pressure of pure NO for the reactant gas valve. The source was cooled to -45 °C. The red railroad diagram is used to pinpoint the bare cationic Ta clusters of size n. **Bottom panel**: Zoomed-in mass spectrum of the region highlighted by the green dashed box in the top panel (1050 to 1250 amu). Up to three Ar tags are observed on the Ta_6^+ clusters. The nomenclature $[Ta_n(N/O)]^+$-Ar_m is used to describe the two peaks that arise from the formation of the $[Ta_nN]^+$-Ar_m and $[Ta_nO]^+$-Ar_m species.

The carrier gas mixture was changed to a 10% mixture of Ar in He, and the temperature was increased to -50 °C to bias the distribution of the cluster towards smaller masses. 2 preamplifiers, each of which increases the signal by five times, were installed to increase the amount of ion signal displayed on the oscilloscope. Figure 5.6 shows the mass spectrum generated under these conditions. As seen in the top panel, there are clusters seen from $n = 3 - 13$. There is also much more complexity in this mass spectrum after the addition of NO gas to the reactant channel at the end of the source block. The bottom panel of Figure 5.6 shows the large number of different clusters that could be produced

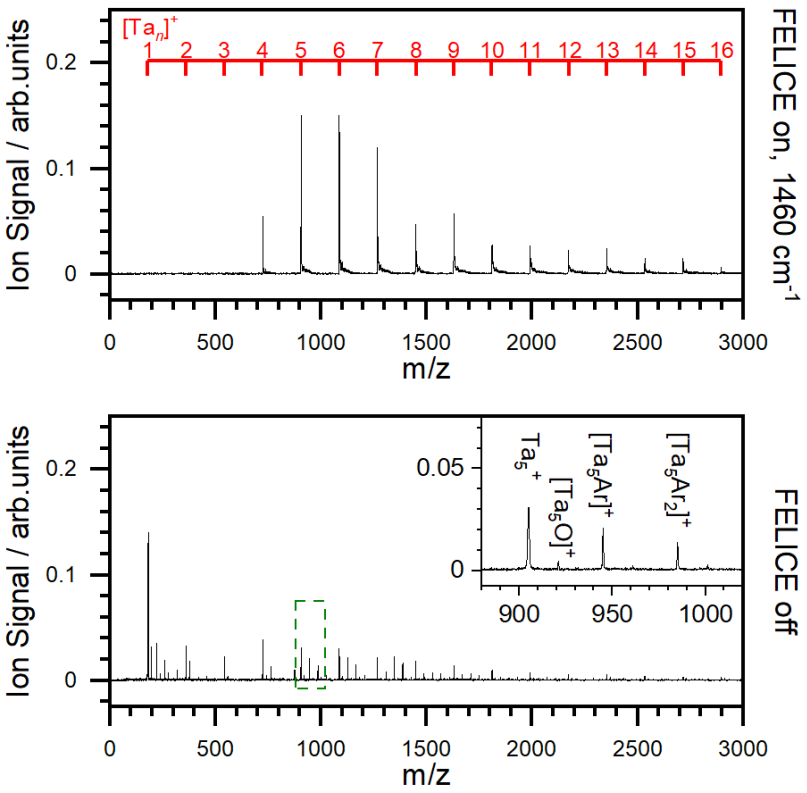

Figure 5.7: The mass spectrum of Ta_n^+ species when FELICE is off (**Bottom panel**), and when FELICE is on (**Top panel**, FEL frequency: 1460 cm^{-1}). As observed, when FELICE is turned on, the ion signal of the Ta_n^+ clusters markedly increased. The inset in the bottom panel highlights the Ta_n^+-Ar_m species being produced. The railroad diagram in the top panel shows the position of the Ta cationic clusters in both the panels.

---

with Ta_5^+ and Ta_6^+; including clusters that contained NO and the corresponding Ar-tagged species. The label $[Ta_n(N/O)]^+$-Ar_m is used to describe the two peaks that arise after the dissociation of NO to form $[Ta_nN]^+$-Ar_m and $[Ta_nO]^+$-Ar_m species. The distribution was then optimised to maximise the amount of Ar-tagged clusters before the FELICE laser light was introduced to irradiate them.

5.2.4 Effect of FELICE on Cationic Ta Mass Spectrum

A preliminary mass spectrum of the Ta_n^+ clusters was obtained, shown in the bottom panel of Figure 5.7, with the intention of being an IR off spectrum to generate the action spectrum. This distribution is dominated by the monomer cation Ta^+ at 181 amu, with the maximum signal intensity rapidly decreasing as the cluster size increases. Peaks

corresponding to Ta_n^+ species are observable up to $n = 16$. The inset in the bottom panel, corresponding to the green dashed box, illustrates the other Ta_5^+ clusters (oxides and Ar-tagged species). However, when the FELICE laser was introduced to irradiate the molecular beam, the ion signal for the bare Ta_n^+ increased markedly and unexpectedly. This growth could not be explained by the simple loss of the Ar-tags from the other clusters, so an additional physical process must have been taking place. In order to investigate this process, the skimmer used to collimate the beam being produced from the source was floated at 100 V to exclude cationic species produced and allow only the neutrals to pass through. Then a mass spectrum was collected with FELICE on, set at 1460 cm^{-1}, which is presented in the top panel of Figure 5.7.

Blocking of the cationic species produced by the source means that the signal being produced must arise from the photoionisation of neutral species, as described by Equations 5.1 to 5.3:

$$Ta_n + n\ h\nu \rightarrow Ta_n^* \tag{5.1}$$

$$Ta_n^* \rightarrow Ta_n^+ + e^-, \tag{5.2}$$

$$Ta_n^* \rightarrow Ta_{n-m}^+ + Ta_m + e^-, \tag{5.3}$$

As can be seen in the FELICE-on spectrum in Figure 5.7, strong features are seen for $n = 4 - 7$, with the most intense peaks of the mass distribution occurring for $n = 5, 6$. No features were observed for $n \leq 3$. The threshold at $n = 4$ reflects a general trend of decreasing ionisation potential (IP) with increasing cluster size.[328] As the IP increases, the number of photons of a specific energy required to reach this threshold increases. It would appear that this threshold is too high for the smallest clusters, and hence no peak is observed.

The Ta_n^+ peaks shown in the top panel exhibit a tail that extends towards higher m/z values (seen clearly for $n = 5 - 10$). These features could be attributed to the fragmentation of the parent cluster, as described in Equation 5.3, or they could also be due to thermionic emission-induced delayed ionisation, as will be discussed in the next section of this chapter. When a cluster of a heavier mass is accelerated within the WM plates,

it may be in a pre-fragmentation state. Upon fragmentation to a smaller cluster, the acceleration experienced by the fragment is increased. However, as the fragment spends less time in the WM optics, this can cause a decrease in the final velocity of the cluster which manifests itself by a delayed time-of-flight. Given that the literature IPs for the Ta_3 cluster is 5.58 ± 0.05 eV,[328] and the Ta_4 cluster is 5.78 eV,[328] the absence of Ta_3^+ and the presence of Ta_4^+ implies that the larger cluster was formed through photofragmentation (Equation 5.3) rather than ionisation.

The growth in the signal caused by the photoionisation of the neutral clusters obscures the expected depletion of peaks related to the vibrational modes of the cationic species. This unexpected issue was believed to be caused by the high photon flux of the FELICE beamline; meaning that this experimental setup could not be used to collect IRMPD of the cationic species, as had been originally planned. If one were to collect the IRMPD spectra of the cationic clusters without ionising source-generated neutrals, a different tunable IR radiation source, such as the OPO/OPA setup described in Chapter 2, would be required. Following the appearance of this anomalous effect, the decision was made to study the neutral clusters. This would require alterations to be made to the experiment set up to allow the neutrals to be studied. Quantum chemical calculations were also performed for the neutral Ta_nO_x species.

5.3 Investigating Ta_n Neutral Clusters

5.3.1 Thermionic Emission in Bulk Materials and Clusters

As was seen when FELICE was introduced to the neutral clusters, IR-driven photoionisation occurred; meaning that an electron was emitted in the process. In bulk materials, the process of heating a material, typically a metal, until electrons are emitted is called thermionic emission.[351] When the material is heated, the thermal energy supplied to the electrons increases their kinetic energy. If an electron gains enough energy to overcome the work function barrier, it can escape from the surface. This process can occur within refractory metals, such as tantalum, because they have very high melting points. This means that electrons can be imparted with enough energy to overcome the work function without causing the metal to melt, which is part of the reason why some electron guns

use Ta filaments, as the filament can be heated to temperatures that are high enough to liberate electrons while retaining structural rigidity.[334]

Thermionic emission from clusters involves photon absorption, causing vibration-electronic excitations before the energy is redistributed among the internal modes of the cluster. Once enough energy has been absorbed to overcome the electron binding energy, an electron is emitted from the 'hot' cluster. Thermionic emission is also in competition with other processes, such as radiative decay and cluster fragmentation. The relative branching ratio for these processes is dependent on the atomic and electron binding energies, with thermionic emission being dominant when the atomic binding energy is greater than the electron binding energy. When this condition is met, such as with refractory metal clusters, thermionic studies have been completed to investigate how much energy is required to remove an electron. Studies on niobium and tungsten clusters showed that these clusters could be ionised using multiple photons using a 1064 nm laser as different pulse energies (up to 85 mJ/pulse, 10 ns pulse duration), with the smaller clusters only being ionised once the photon flux is increased because of their higher IPs.[352] Additionally, higher charge states (+2, +3) were observed when the photon flux increased, and the rate of ionisation process *via* thermionic emission became faster. That means that it was not possible to distinguish between this process and direct multiphoton ionisation. Additionally, single photon induced photo-detachment has been observed for small W_n^-, as well as the equivalent single and double-photon process for small Ta_n, W_n and Nb_n clusters.[41, 328, 353] Thermionic emission has also been observed in transition metal carbide clusters.[354, 355]

5.3.2 Techniques to Ionise Neutral Clusters

In addition to thermionic emission, which is dependent on internal conversion and takes place on the order of ns-µs,[356] resonance enhanced multi-photon ionisation has also been conducted on gas-phase neutral metal clusters. This technique relies on continued resonant electronic excitation, which eventually results in the loss of an electron. The species under investigation absorbs n photons to excite it to an intermediate electronic state, before additional photons are absorbed to cause photoionisation. REMPI leads to a narrower internal energy distribution as well as a shorter time delay before an electron

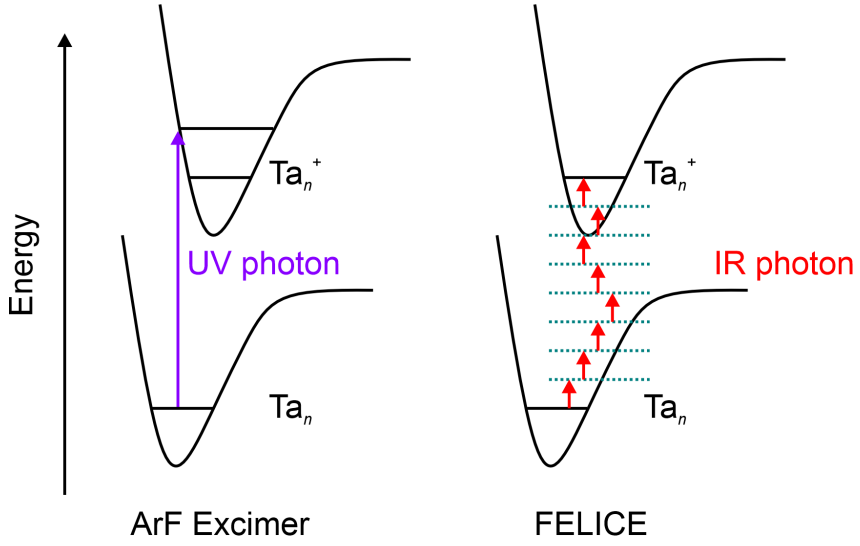

Figure 5.8: A representation of the ionisation process of a neutral Ta_n cluster when irradiated with the ArF Excimer (left side, a single UV photon process), or FELICE (right side, a multiple IR photon process).

is emitted (on the scale of fs-ps). Studies that aim to distinguish the different processes that occur within metal clusters often rely on time-dependent measurements to determine what happens when a cluster is irradiated. REMPI studies have been performed on refractory metals, such as Nb_n clusters, as well as fullerenes, by utilising the high photon fluxes provided by FELs.[357, 358]

In addition to multi-photon ionisation, studies have also been performed using single photons that have enough energy to overcome the ionisation potential.[359] This technique is commonly applied to study neutral species, as charged species can be easily detected and studied. For refractory metals, the high IPs mean that higher energy photons are required, often in the ultraviolet region of the EM spectrum. Figure 5.8 provides an illustration of how ionisation can take place for a Ta_n cluster, using either a single UV photon from an ArF laser (193 nm) or by using multiple IR photons, as can be produced using a free-electron laser. The UV photoionisation takes place on the order of a few femtoseconds, whereas the multiple photon ionisation can take longer because of there being a greater number of ways the ionisation could occur. This could be done *via* virtual states where all the photons are absorbed at once, *via* multiple photon absorption where energy is transferred to the cluster *via* IVR, or when there are essentially many

electronic excited states,[360] with corresponding vibrational states, within the neutral that electrons can reside within until there is enough energy to cause ionisation.

The single photon ionisation can therefore be used as a way of producing reference mass spectrum to capture how much of each neutral is present in the molecular beam, before the distribution changes following thermionic emission caused by absorbing multiple photons from the FEL. In the context of the experiment at HFML-FELIX, this involved installing a new 193 nm ArF ionisation laser (10 Hz repetition rate) which would intersect the molecular beam within the WM plates in order to ionise the neutrals. The laser would fire on the off shots of the FEL; allowing for mass spectra of the neutrals to be recorded before the IR beam enters and irradiates the neutrals and allowing them to be ionised through absorbing multiple photons. Figure 5.9 provides an illustration of the adaptation applied to the original experimental setup. To produce infrared spectra, the adapted Beer-Lambert expression described in Chapter 2 (Equation 2.7) is used to express the changes induced by the FELICE beam. The parent signal, N_0 comes from the ArF reference spectrum, with the fragment signal, N_f coming from the FELICE-on data. The power correction uses the intra-cavity macropulse energy of FELICE, which varies as a function of photon energy. The FELICE macropulse energy is determined by measuring the outcoupled energy, which is a fraction of the intra-cavity energy. The maximum intra-cavity power of the macropulse recorded during these experiments was 0.86 J at 1300 cm^{-1}.

5.4 Experimental Results for Ta_n Neutral Clusters

5.4.1 Mass Spectrum of Ta_n Clusters

Figure 5.10 illustrates the mass spectra of the neutrals that were recorded when the ArF laser was fired (bottom panel) and when FELICE was fired (top panel). The IR-on mass spectrum was produced when FELICE produced light at 1400 cm^{-1}. Other mass spectra were produced at different FELICE frequencies, but the one at 1400 cm^{-1} is shown here to compare it to the spectrum recorded at 1460 cm^{-1} in Figure 5.7. The reference spectrum shows Ta_n clusters ranging from $n = 3 - 21$, with small peaks also appearing that correspond to oxides and Ar-tagged species, both bare Ta clusters and Ta oxide clusters.

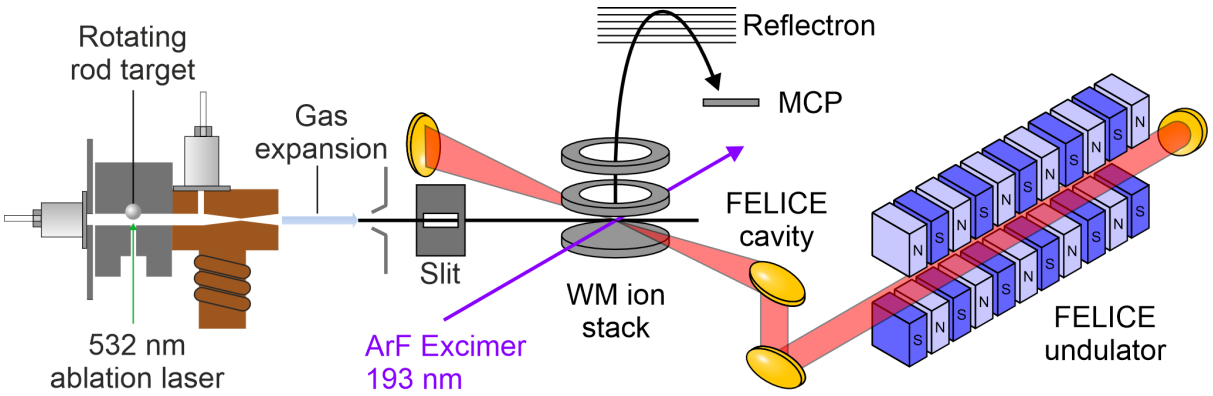

Figure 5.9: The layout of the experimental setup at the HFML-FELIX facility, as described in Figure 2.13, with an additional pulsed ArF excimer laser (193 nm) included. This is used to ionise the neutral species between the WM plates in order for them to be extracted into the ToF mass spectrometer, and provides a reference mass spectrum inbetween the shots from the FEL (FELICE off spectrum).

There are distinct differences in the mass spectra observed upon irradiation with FELICE and the ArF excimer which can be explained in terms of the ionisation potential of the cluster. The energy of a single photon from the excimer laser (6.43 eV) is greater than the IP for all but the smallest clusters. It can be assumed that if a cluster absorbs a 193 nm photon, it will be ionised. Additionally, the overlaps of the molecular beam with both the FELICE and excimer beams are assumed to be unity, despite their different beam dimensions. Therefore, the differences between the two spectra are attributed to their respective photon energies. When multiple, lower energy photons are absorbed, a small change in IP will change the number of photons required to reach the ionisation threshold, which impacts the likelihood of ionisation. This is reflected in the greater relative quantity of larger clusters in the FELICE mass spectra than in the excimer spectrum in Figure 5.10, reflecting the trend in IPs with changing n where the IP decreases.

For Ta_2, the IP is 6.828 eV, whereas for Ta_{14}, the IP is 4.644 eV. This later value is closer to the work function of Ta (4.352 eV).[334] In essence, as the clusters become much larger, they become less atom-like and become more like the bulk material, meaning the electrons are less tightly bound in bands, rather than well defined molecular orbitals.[361] There is also a clear odd-even alternation in the signal intensity for the FELICE mass spectrum, which is highlighted by the addition of the red data points to illustrate the

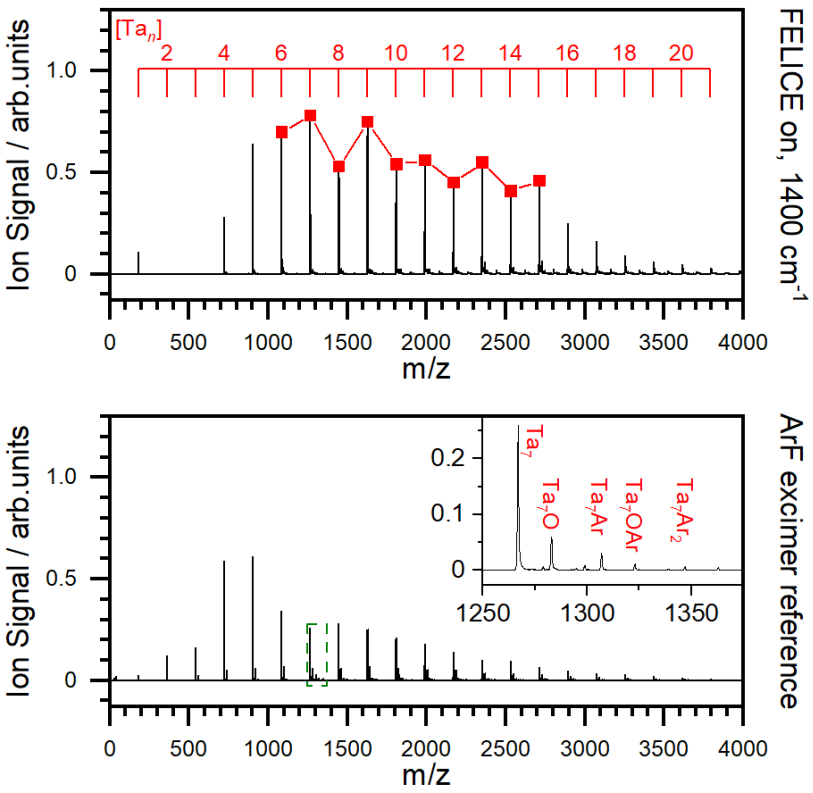

Figure 5.10: Top panel: Ta_n mass spectrum recorded using FELICE set to 1400 cm^{-1}. **Bottom panel**: Ta_n mass spectrum taken with 193 nm ArF excimer laser, as a reference for the number of neutral species being created by the source. The inset in the bottom panel shows the oxides and Ar-tagged species produced for $n = 7$. The red line in the top panel highlights the even-odd alternation in the number of species being ionized from $n = 6 - 15$.

tops of the mass spectral peaks. This can be explained by the predicted lower IPs for Ta_n clusters with odd numbers of atoms. These clusters are radicals, meaning that they will hold onto their unpaired electron less strongly relative to closed shell clusters with even numbers of atoms in them. The magnitude of the ion signal in the FELICE mass spectrum increased with increasing FELICE frequency, reflecting the greater ability of photons with more energy to ionise the neutral Ta_n clusters. There is also an increased magnitude of the Ta^+ peak with increasing photon energy, potentially due to the high IP of Ta. This further illustrates that photon energy plays an important role in the ionisation of these species.

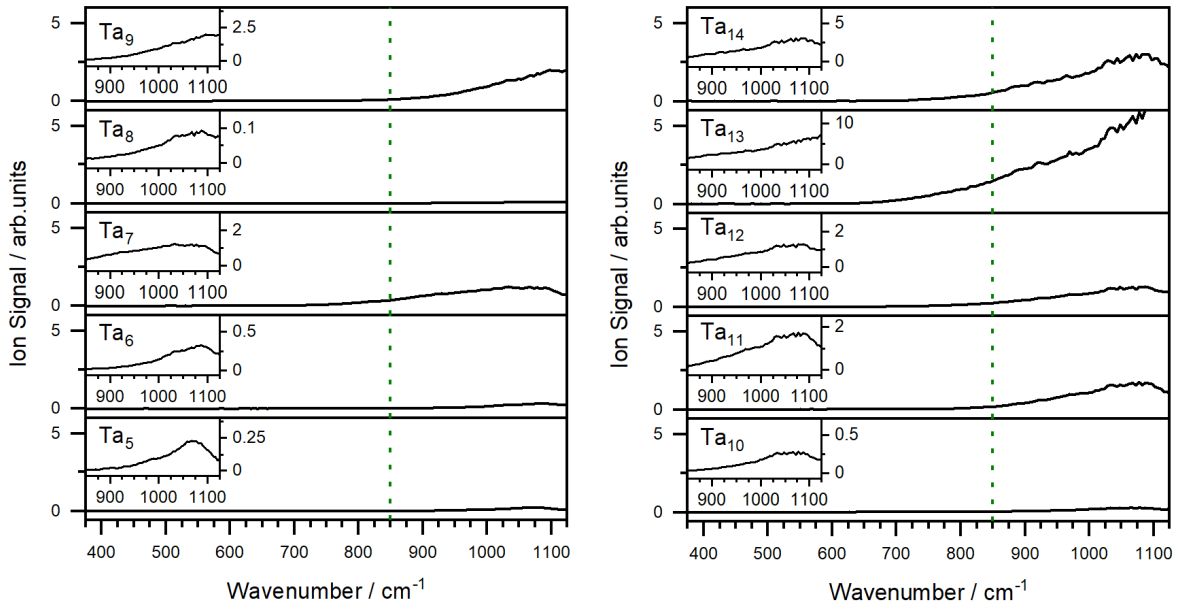

Figure 5.11: Photoionisation spectra of the Ta_n clusters ($n = 5-14$). Each spectrum is measured in the Ta_n^+ enhancement channel relative to the ion cross-section on alternate ArF ionisation pulses.

5.4.2 IR Photoionisation of Ta_n $(n = 5 - 14)$

Figure 5.11 shows the IR photoionisation spectra for Ta_{5-14}. Here, the ionisation efficiency of all clusters has been monitored as a function of the IR wavenumber. Each panel has an inset that spans from 850 cm^{-1} (marked using the green dashed line) to 1125 cm^{-1} to illustrate the thermionic emission that occurs at higher frequencies (thermionic emission begins in the region $600 - 900$ cm^{-1}). The FELICE photon energy at which thermionic emission begins will ultimately depend on the IPs for each cluster, given that the FELICE power is consistent across all species as the mass spectra capture all the species at once. Some clusters show a gradual onset ($n = 8, 12$), while others show a sharper onset ($n = 9, 11, 13$).

Each of the main panels in Figure 5.11 have also been set to the same y-scale to highlight the odd-even alternation in the intensity of the thermionic emission, especially between Ta_6 and Ta_{11}. This again reflects the differences in the open and closed shell clusters that were highlighted in the mass spectrum in Figure 5.10. The large ion signal for Ta_{13} is likely due to it being a larger cluster with an odd number of atoms, as well as the

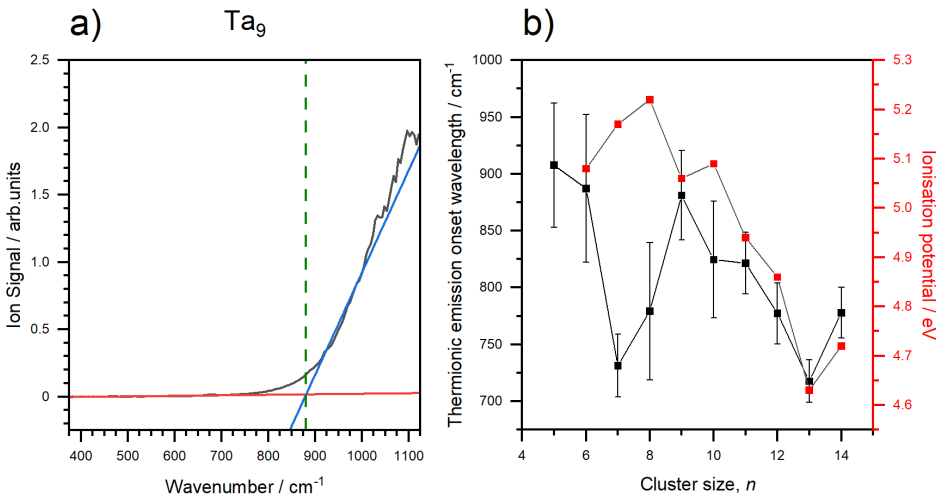

Figure 5.12: **a)** Illustration of the linear fits applied to the photoionisation spectrum of Ta_9. The linear fits are used for the baseline (red line) and the rising edge (blue line) that arises due to thermionic emission. The intercept of the two linear fits is depicted with the dashed green line and is used as an approximation for the thermionic emission onset frequency. **b)** A comparison of the thermionic emission onset position with literature IP values for each cluster size, n.

---

fact that at $n = 13$, the cluster can form a perfect icosahedron, as 13 is a 'magic number' for the stability of the cluster.[336, 362] Within the IR spectra, there are also very weak features that appear at approximately 680 cm^{-1} for Ta_8 and Ta_{10}. The calculated ground state structures of these species do not predict peaks in this region, meaning that they could arise from the fragmentation of larger oxide clusters that contain a resonant vibration around 680 cm^{-1} to give $Ta_{n=8,10}$ as products, as will be discussed in Section 5.5.

To determine where the thermionic emission onset approximately begins for each cluster size, linear fits were applied to the curve before and after the increase in the ion signal. The intersection point of these two linear fits would be used to define the start of the band. Figure 5.12 **a)** provides an example of this fitting process for the IR photoionisation spectrum for Ta_9. The fit of the baseline (red line) and the fit of the rising edge (blue line) intersect as the curve's gradient begins to increase (marked by the dashed green line). This approach was applied to each of the photoionisation spectra produced for the bare Ta clusters. Table 5.3 provides the value for the onset of the thermionic emission for each cluster size that was shown in Figure 5.11, along with its associated error which is derived

Table 5.3: Onset wavenumber for Ta_n clusters. This is defined as the intersection point between the linear fits for the baseline and rising edge, defined in Figure 5.12 **a)**.

n	**Thermionic emission onset / cm^{-1}**	**Onset error / cm^{-1}**
5	907.7	54.6
6	887.2	65.1
7	731.4	27.6
8	779.3	60.5
9	881.0	39.3
10	824.7	51.4
11	821.4	27.1
12	777.3	26.9
13	717.6	18.7
14	777.9	22.4

from the two linear fits. Figure 5.12 **b)** compares the calculated thermionic onsets using the intersection points of the linear fits (black marks, with their associated errors) with known ionisation potentials for the Ta_n clusters (red marks).[328] There appears to be some similarity in the general trends of the two plots, as their shapes generally match, except for extreme deviations at $n = 7, 8$, and to a lesser extent for $n = 10$. As can be seen again, the reduction in the thermionic emission onset frequency with increasing cluster size is reflective of the equivalent trend in the ionisation potentials and the decrease in the number of photons required to ionise the larger Ta neutral clusters. It would appear that for $n = 7, 8$ and to a lesser degree $n = 10$, there are additional physical factors that affect the onset of the thermionic emission beyond the change in the ionisation potential.

5.5 Investigating Neutral Tantalum Oxide Clusters, Ta_nO_x (x=1,2)

5.5.1 Background of Ta_nO_x Clusters

Although refractory metals such as tantalum may be suitable for catalytic purposes, the increased reactivity means that they can easily form surface nitrides and oxides at high temperatures. This in turn can increase the work function of the bulk material and subsequently reduce the thermionic emission capabilities required for electron emitting devices, such as filaments and electron guns.[363] Tantalum electron sources are typically operated at high temperature and under high vacuum to prevent oxide formation, but these conditions may be impractical if they were used within an industrial catalytic system. Characterisation of the oxides that Ta forms may allow improvements in the designs of catalytic and cathode materials that can use their properties.

Experiments have already been performed to determine the ionisation potentials for tantalum oxide species of the form $(TaO_2)_{x=0-2}(Ta_2O_5)_yO_{z=0-3}$.[364] Additionally, Fielicke *et al.* investigated the structure of oxygen-containing Ta clusters, $[Ta_nO_{m=0-2}\text{-Ar}]^+$ by performing IR-MPD studies which monitored the loss of Ar tags following IR irradiation from the FHI free-electron laser.[346] As has been shown in previous mass spectra, cationic Ta clusters were able to break apart NO to form $Ta_n(N/O)^+$ complexes. Additionally, when trace amounts of oxygen gas were added *via* the reactant gas valve, Ta_nO clusters were clearly present, both for the cationic and neutral species. Therefore, it was determined that the photoionisation spectra of the neutral Ta_nO_x clusters would also be measured.

5.5.2 Experimental Results with Ta_nO Neutral Clusters

Figure 5.13 shows the photoionisation spectra for the neutral tantalum monoxide clusters, Ta_nO ($n = 4 - 13$). Similarly to bare Ta clusters, the signal is measured in the emergence of cationic tantalum oxide peaks, $[Ta_nO]^+$ following IR irradiation from FELICE. Comparisons must be made immediately between the Ta_n and Ta_nO clusters, such as the relative ion signal varying with the size of the cluster. There is a broad non-resonant band

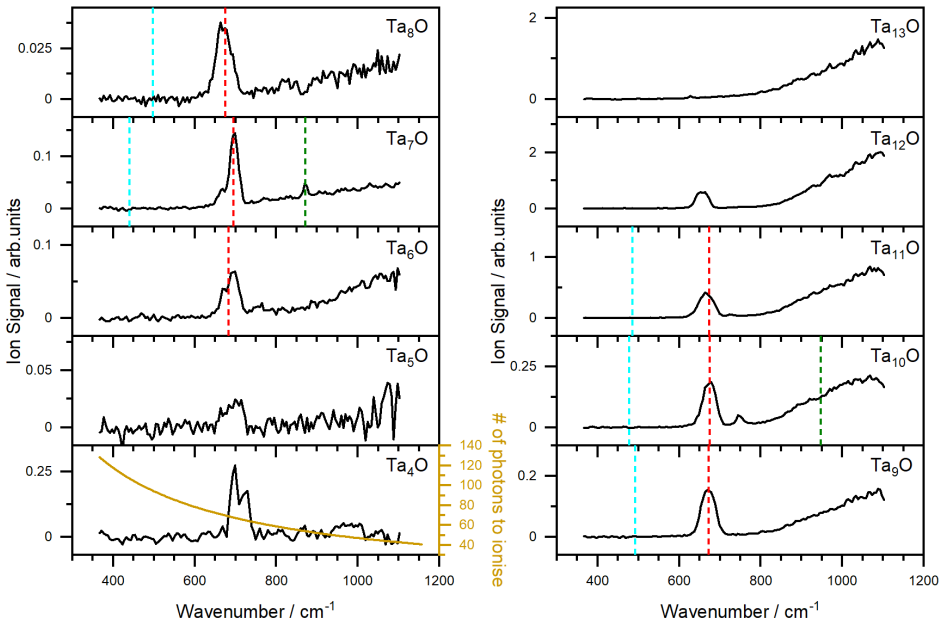

Figure 5.13: Photoionisation spectra of Ta_nO ($n = 4-13$) measured in the appearance channel of $[Ta_nO]^+$. The bottom left panel also includes a plot showing the minimum number of IR photons required for non-resonant photoionisation of Ta_4O. Frequencies of literature vibrations of the bridged oxide asymmetric stretches, symmetric stretches and overtones of the asymmetric stretches are marked in blue, red and green respectively where available

---

which appears around 800 cm^{-1} for the larger clusters, which again is associated with the reduction in the ionisation potential of the cluster. However, with the Ta_nO spectra, new bands appear between 650 cm^{-1} and 750 cm^{-1}, which correspond to the Ta-O stretching mode. Some of these peaks contain shoulders, for example in $n = 4, 6, 7$. Additionally, a new peak arises to the blue of the main Ta-O stretching frequency for $n = 10, 11$. The panel for Ta_4O in Figure 5.13 illustrates the number of IR photons required to ionise this specific cluster, which varies from 40 to 120 as the photon frequency decreases.

Assuming that after photoionisation the geometry of the cluster does not change, literature values can be used to assign the peaks in Figure 5.13 as bridged oxide asymmetric stretches (blue), symmetric stretches (red), or overtones of asymmetric stretches (green).[346] For Ta_7O, the overtone of the asymmetric oxide stretch at around 870 cm^{-1} is consistent with the small feature that arises to the blue of the Ta-O stretching fre-

quency. However, this cationic feature is not repeated for $n = 10$, although this may be because it is enveloped by the thermionic emission. The shoulders seen for $n = 4 - 7$ may be present in the larger clusters but are merged with the main spectral feature. These features may result from vibrations of multiple low-lying minima or fragmentation of larger clusters. This later point may be relevant for explaining the small redshift in this peak position for $n > 8$. For fragmentation to occur, a neutral cluster has to be ionised at a specific wavenumber. Regardless of whether fragmentation is induced post-ionisation, a peak will only appear at a wavenumber that matches a resonant frequency in a neutral species; this could however be from a larger neutral species. The spectra recorded therefore can contain only features present in the equivalent neutral spectra. The intensity of the signal, as well as the signal-to-noise ratio (S/N) between the different panels in Figure 5.13 can also be compared. The absolute ion signal for $n = 4 - 10$ is low, with the S/N ratio for $n = 5$ being especially poor. For $n = 4$, there is the strong resonant feature associated with the Ta-O stretch. However, the background for this cluster size does not show a significant increase in ion signal at higher photon energies (> 800 cm^{-1}), as is the case for larger clusters. For example, for $n = 13$, the resonant vibrational feature is almost negligible compared to the non-resonant absorption which begins from around 800 cm^{-1}. This may be in part due to the highly symmetric icosahedral structure for Ta_{13} causing the transition dipole moment for the Ta-O stretch to dramatically decrease, but it also suggests that reducing the ionisation potential does not automatically correlate with an increase in the ion signal. This implies that Ta_4O^+ production arises in part from photofragmentation.

To assist in the assignment of the spectral features and the structures that produce them, DFT calculations were performed at the B3P86/def2TZVP level of theory for the neutral Ta_nO clusters. To start with, the lowest energy structures for the bare neutral Ta_n clusters were calculated before they were reoptimised following the addition of an oxygen atom. The initial guesses for the structures of the neutral clusters ($n = 2 - 14$) were generated using structures from the literature.[365] Figure 5.14 provides the experimental ionisation spectra and the simulated vibrational spectra for Ta_nO ($n = 6, 9$ and 10) generated from unscaled DFT harmonic frequencies. These structures were chosen because of their good agreement between the experimental results and the computational

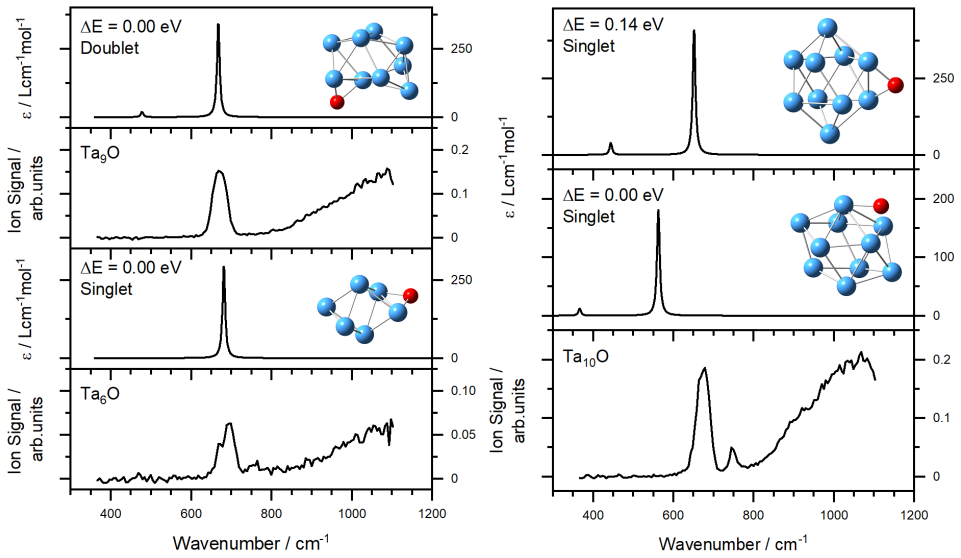

Figure 5.14: Comparison of experimental and simulated photoionisation spectra of $Ta_{6,9,10}O$. Simulated spectra are generated from B3P86/def2TZVP unscaled harmonic frequency calculations and convoluted with a Lorentz function (FWHM = 8 cm^{-1}).

spectra. These clusters possess low spin multiplicities, and all contain oxygen atoms that are bound in bridging positions, in most cases along the edges of the Ta clusters.

For $n = 10$ (right panels in Figure 5.14), the oxygen atom in the lowest energy calculated structure ($\Delta E = 0.00$ eV, $2S+1 = 1$) is attached to one of the faces of the Ta cluster that has been formed by three Ta atoms. The frequency of Ta-O stretching is reduced due to the increased reduced mass as the oxygen atom is bound to three Ta atoms rather than two, as is the case for the next lowest-energy structure ($\Delta E = 0.14$ eV, $2S+1 = 1$). The spectra for both of these conformers, which are separated by a relatively small energy difference, can be used to explain the experimental spectral features observed. For $n = 9$, the lowest energy facially-bound cluster is 0.43 eV higher in energy than the putative global minimum (top spectrum in the left panels). No facially bound cluster lies within 2 eV of the putative global minimum for $n = 6$. Instead, a cluster with an oxygen bound to the edge and triplet spin multiplicity ($\Delta E = 0.49$ eV) is the second-lowest-energy structure.

Within the computational spectra for $n = 9, 10$ is a weaker feature to the red of the

main peak. This is the asymmetric stretching mode of the bridged oxygen and lies in a region comparable to the vibrational peaks observed in the cationic IRMPD spectra.[346] This mode is also present in the two lowest calculated structures for $n = 6$ (ΔE = 0.00 eV: 2S+1 = 1, Ta-O stretch peak positions: 512 and 681 cm^{-1}, ΔE = 0.49 eV: 2S+1 = 3, Ta-O stretch peak positions: 497 and 678 cm^{-1}). However, the intensity of the spectral feature for the asymmetric stretch is much weaker for both of these structures than that for the symmetric stretch. For example, for the lowest-energy structure (ΔE = 0.00 eV), the relative intensities of asymmetric and symmetric Ta-O vibrations are 0.04 and 85.12 km/mol, respectively. This is largely due to the higher degree of symmetry present in the bare Ta_6 cluster, which is a near-perfect octahedral, compared to the structures for $n = 9$ and $n = 10$. With the base Ta_6, the oscillation of oxygen parallel to the edge of the octahedral cluster induces little change in the dipole moment. In the larger clusters, where the overall bare cluster is lower in symmetry, the change in local charge density from this motion induces an overall change in dipole moment and hence a stronger spectral feature.

5.5.3 Experimental Results with Ta_nO_2 Neutral Clusters

Mass spectra were recorded by irradiating the neutral clusters with FELICE at frequencies close to the Ta-O stretching frequency to monitor whether additional infrared absorption occurred. Figure 5.15 provides a mass spectrum produced when neutral clusters were irradiated with FELICE at 675 cm^{-1} (top panel), compared to the reference ArF spectrum (bottom panel). There is an inset (highlighted by the green dashed box) in the top panel that shows the formation of the $Ta_{8,9}O_n$ signal, with up to three oxygen atoms attached to the neutral Ta clusters. The IP for TaO_2 and TaO_3 is predicted to be higher than for Ta and TaO (TaO_2: 8.5-9.0 $\pm$ 0.5 eV, TaO_3: 10.65 $\pm$ 0.05 eV).[366]

The ionisation of Ta clusters with multiple oxides has been investigated using 193, 118, and 46.9 nm light by Bernstein *et al.*. Here, when the shortest wavelength laser was used, a standard Ta cluster distribution was observed when the Ta was ablated in a pure He gas expansion, which also contained some more complex peak shapes that arose from the production of oxides and carbides as well as some delayed fragmentation.[364] When a gas mixture containing 5% O_2 was used, only TaO^+_{0-2} was observed when the 193 nm laser was used to ionise the clusters, whereas much larger clusters with many more oxy-

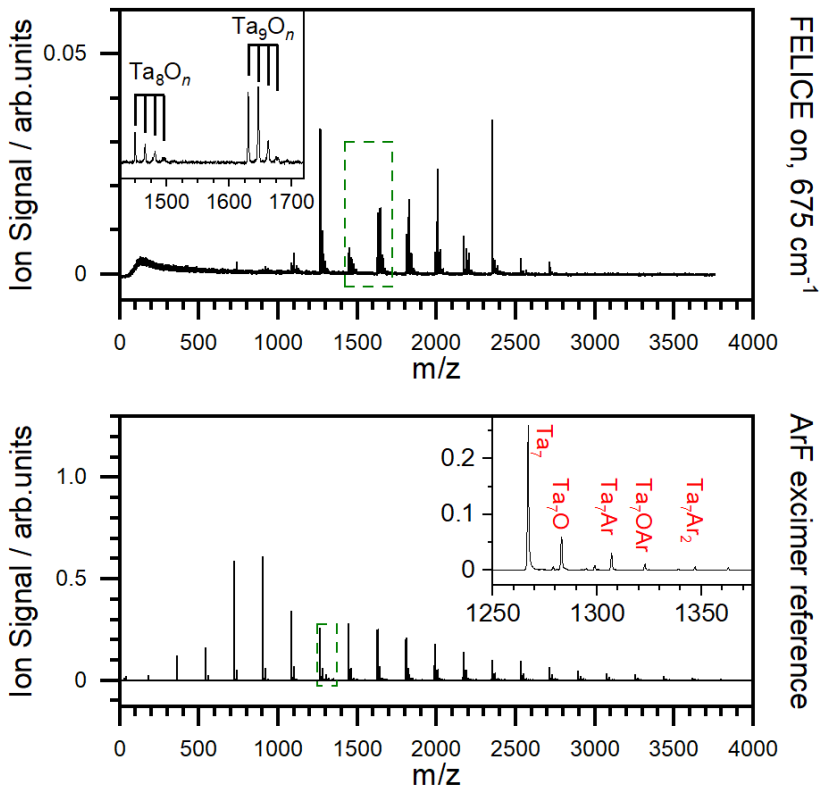

Figure 5.15: Top panel: Mass spectra of the Ta_nO_x clusters from irradiation by FELICE at 675 cm^{-1} (near the resonant absorption of oxide stretches). **Bottom panel**: Mass spectra recorded using the ArF excimer laser. The inset in the top panel shows the appearance of $[Ta_{8,9}O_{0-3}]^+$ with relatively larger ion cross-sections for oxide species compared to pure Ta_n clusters.

gen atoms attached to them (up to 22 oxygen atoms for Ta_9) were ionised when the 46.9 nm laser was used. This lack of larger oxide clusters was explained by Bernstein *et al.* by stating that after irradiation from the ArF excimer, fragmentation occurred following the absorption of multiple photons. However, it is not clear whether the underlying neutral cluster distribution is different. In the mass spectrum presented in Figure 5.15, the larger Ta_nO_x clusters are observed. This may be because the clusters possessed a greater amount of internal energy because they were hotter and therefore could be irradiated under single-photon ionisation conditions. Alternatively, the clusters that are being surveyed in our mass spectrum possess different geometric structures.

The photoionisation spectra of the Ta_nO_2 clusters are then presented in Figure 5.16.

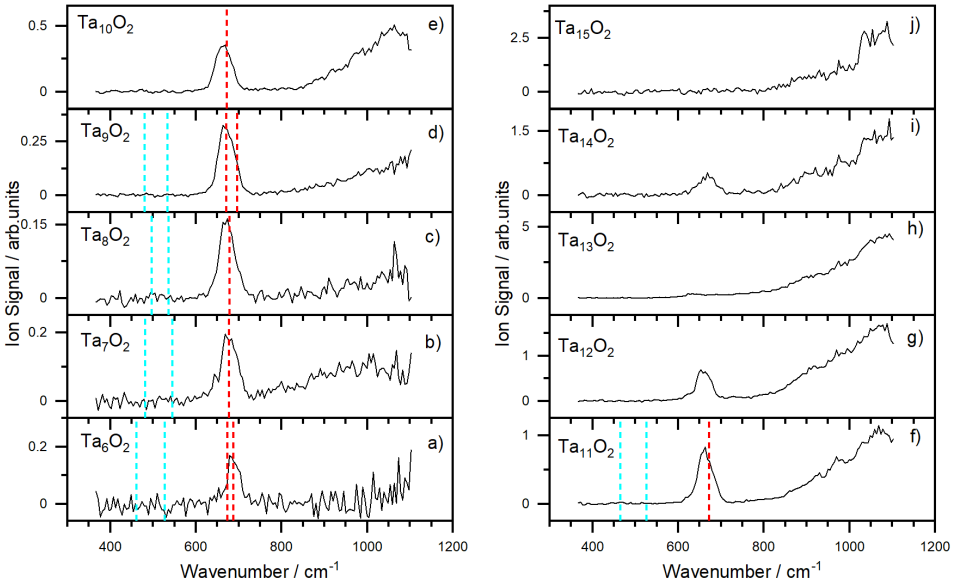

Figure 5.16: Photoionisation spectra of Ta_nO_2 ($n = 6-15$) measured in the appearance channel of $[Ta_nO_2]^+$. Frequencies of literature vibrations of the bridged oxide asymmetric stretches and symmetric stretches are marked in blue and red respectively where available.[346]

There are similarities with the corresponding Ta_nO photoionisation spectra in Figure 5.13, such as the vibrational modes associated with in- and out-of-phase asymmetric oxide stretches, as well as the non-resonant feature to the blue that is present in all of the Ta cluster IR spectra. The literature vibrational frequencies for both the asymmetric (blue) and symmetric (red) stretches are added to the panels in Figure 5.16 as dotted lines. As in the case of the monoxide clusters, the Ta-O stretching peaks in the equivalent cationic clusters are extremely similar to those found in our experiment. Additionally, the oxide peak is anomalously weak for $Ta_{13}O_2$. This can be partially explained by the fact that the thermionic emission is stronger than those of the other sizes.

The unscaled harmonic frequencies for Ta_nO_2 were determined using DFT calculations and compared with the experimental spectra. Figure 5.17 shows the comparison of the DFT calculations for $n = 7, 9$. In both cases, two calculated structures are shown: one with the form of a dioxide and one with the O_2 molecule being bound which is much higher in energy compared to the dioxide. In the Ta_9O_2 cluster, the calculated cluster structure

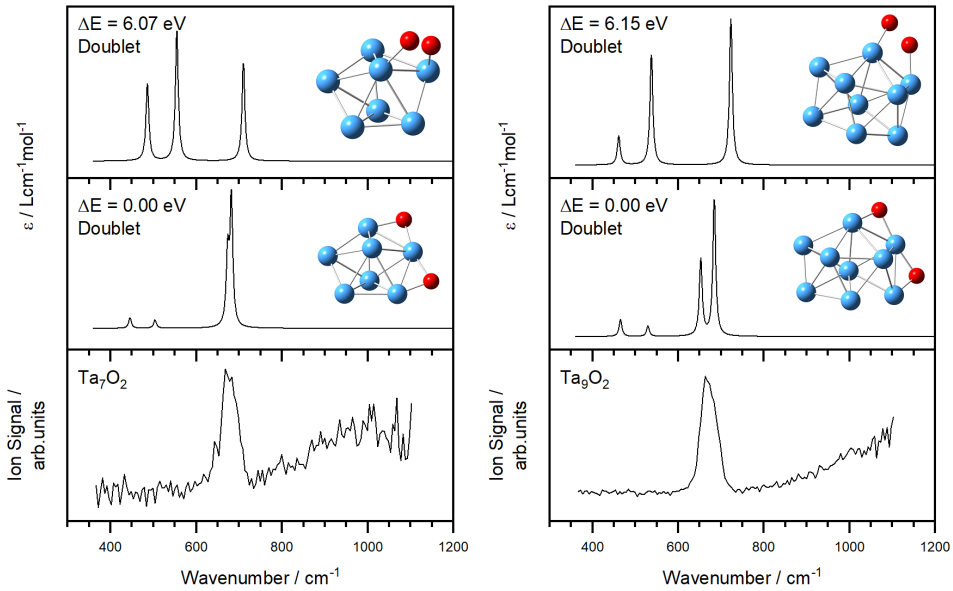

Figure 5.17: Comparison of experimental and simulated photoionisation spectra of $Ta_{7,9}O_2$, with both dioxide (Ta_nO_2) and oxygen bound ($Ta_n(O_2)$) clusters shown. Simulated spectra are generated from B3P86/def2TZVP unscaled harmonic frequency calculations and convoluted with a Lorentz function (FWHM = 8 cm^{-1}).

---

is best described as a pentagonal bipyramid with two additional Ta atoms adjoining the two upper faces. Two oxygen atoms are bound equatorially with respect to the centre of the bipyramid along sequential edges of the cluster. One of the oxygen atoms sits directly opposite the two bound Ta atoms and therefore induces a larger change in the dipole moment in its symmetric stretch compared to the oxygen attached along the other edge. This results in Ta-O stretch frequencies appearing at 653 and 684 cm^{-1}. Although separated, these modes appear as a single absorption in the photoionisation spectrum (panel **d)** in Figure 5.16). As was the case for the Ta_nO spectra, the asymmetric stretches are weaker and are therefore not observed in our spectra. For both $n = 7$ and $n = 9$, the higher energy isomers with the O_2 molecule attached along one of the edges do produce simulated spectral peaks that match well with the experimental features at $\sim$ 680 cm^{-1}, but they also have much more intense bands to the red that are not replicated in the experimental spectrum. Given this and the energy difference between these isomers and the putative ground state, it is unlikely that these isomers contribute substantially to the experimental spectrum unless they are kinetically trapped in an entrance channel.

5.5.4 Tantalum Oxide Stretch Excitation

The effect of specifically pumping the oxide resonance can be investigated by considering the mass spectrum taken with FELICE set at 675 cm^{-1}, shown in the top panel of Figure 5.15. 675 cm^{-1} was chosen as the reference value for the Ta-O stretching frequency, but there will be some variation of the true frequency as the size of the cluster changes. In a system where only photoionisation occurs, it is expected that the only peaks that will be observed in the mass spectrum will be those corresponding to the $Ta_nO_{x=1,2}$ species. The value of 675 cm^{-1} was chosen as an approximate value for the Ta-O stretching vibration, even if it does not provide the fairest representation of the distribution. In Figure 5.15, the 675 cm^{-1} mass spectrum contains significant amounts of signal for the larger cluster sizes relative to the smaller clusters compared to what is seen in the excimer spectrum, or the spectra taken at higher wavenumbers (Top panel of Figure 5.10, for example). However, the overall ion signal of the peaks is lower in the 675 cm^{-1} spectrum. This is perhaps unsurprising given the greater number of lower energy photons required to induce ionisation for a given IP. The relative intensity of the oxide peaks is significantly higher in the 675 cm^{-1} spectrum than in the ArF mass spectrum.

The observation of Ta_n^+ peaks in the mass spectrum is difficult to rationalise when the oxide transition is being driven. It is possible that other species, which do have a resonance around 675 cm^{-1} photofragment, give Ta_n^+ species as a product, as described by the following equation:

$$Ta_nO_x + n\ h\nu \rightarrow Ta_{n-m}^+ + Ta_mO_x + e^-, \tag{5.4}$$

where it is likely that $m = 1$.

The extent of fragmentation can be judged by comparing the ion signal of the Ta_n^+ peak in the 675 cm^{-1} mass spectrum. The right panel of Figure 5.18 shows the fraction of the overall ion signal for a cluster of a given size, made up of the bare Ta cluster ions, as well as the monoxide and dioxide cluster ions. The difference in these proportions for the ArF and FELICE mass spectra reflects the fact that irradiating the cluster with the FELICE beam pumps energy directly into the oxide stretch, favouring ionisation of oxide and dioxide species rather than the bare clusters. The proportion of the overall

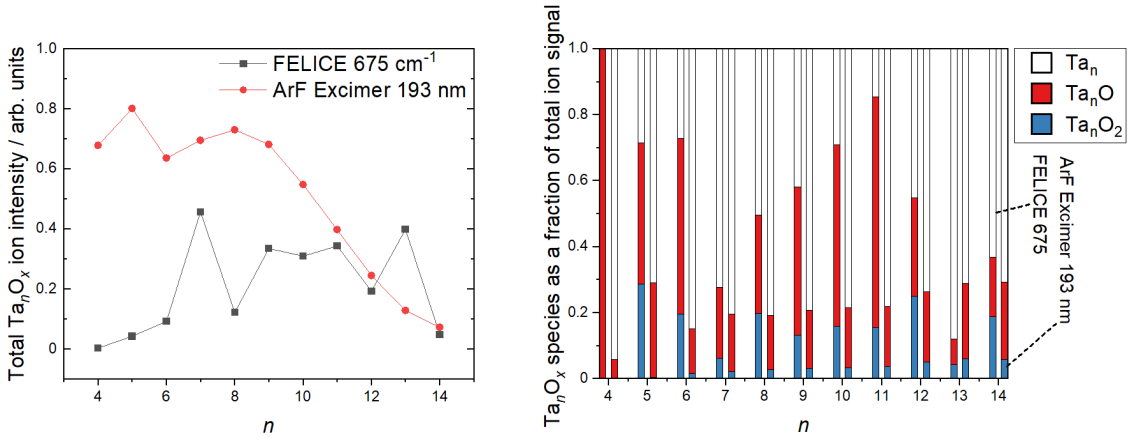

Figure 5.18: Left panel: Relative total ion intensities for $[Ta_nO_x]^+$ clusters ($n = 4-14$), upon irradiation of the neutral Ta_nO_x clusters by FELICE at 675 cm^{-1} (black) and an ArF excimer pulse (red). Right panel: Proportion of ions produced (Ta_n, Ta_nO and Ta_nO_2) for each $n = 4 - 14$ upon irradiation by FELICE at 675 cm^{-1} (left histogram bar) and an ArF excimer pulse (right histogram bar).

signal in the 675 cm^{-1} mass spectrum that is due to Ta_n species is particularly large for $n = 7, 13, 14$. For $n = 13$, the proportion of the overall signal contributed by the bare cluster is greater in the 675 cm^{-1} spectrum than in the excimer reference spectrum. This is not a surprising result for $n = 7, 13$, as fragmentation is more energetically favourable when a stable product is formed, and these cluster sizes are considered 'magic number' sizes that possess greater stability.

The left panel of Figure 5.18 shows how the overall ion signal varies with the size of the cluster in both mass spectra. In the ArF spectra, from $n = 5$ onwards, a Poisson distribution is observed with the ion signal peaking at $n = 8$ before reducing in intensity with increasing cluster size, as the likelihood of the correct number of tantalum atoms coming together decreases. The trend in the 675 cm^{-1} spectrum is markedly different, with maxima at $n = 7, 13$ and minima at $n = 4, 8, 12, 14$. Additionally, there is a small increase in the signal with increasing cluster size due to both the ionisation potentials of the clusters and their stabilities as fragmentation products. The Ta_n peaks appearing in the mass spectrum taken with FELICE mean that fragmentation, at least of the kind described in Equation 5.4 must occur upon irradiation, meaning that more complex post-ionisation processes must be considered.

5.6 Conclusions

This chapter has presented the results of a multiple photon-induced ionisation study of neutral $Ta_nO_{x=0-2}$ clusters using the free-electron laser, FELICE. Preliminary computational work on cationic Ta clusters reacting with nitrogen oxides was completed to predict possible structures that would be investigated using IR-(M)PD. Anomalous enhancements in the mass spectral features when FELICE was turned on led to the investigation of the neutral species instead. IR enhancement spectra were generated in the range 360-1200 cm^{-1} by monitoring changes in the intensity of mass spectral features compared to a reference spectrum generated using an ionisation laser (ArF, 193 nm). The low-energy isomers of the neutral gas-phase clusters were determined by DFT calculations, with their corresponding simulated IR spectra being used to identify experimental features.

The broad features observed in the photoionisation spectra of the majority of $Ta_nO_{x=0-2}$ clusters have been assigned as thermionic emission induced by multiple photons. The trend in the emission's onset has been shown to reflect the ionisation potential of the neutral clusters. The observation of thermionic emission, a process requiring ∼40-120 photons for Ta_4O in the range of frequencies studied, shows that the clusters can absorb multiple photons on the timescale of the experiment after irradiation from FELICE.

Spectral features observed in the photoionisation spectra in the range of 650-750 cm^{-1} for the neutral tantalum oxides, $Ta_nO_{1,2}$, are assigned to the symmetric oxide stretches. The spectra agree well with the simulated spectra from the lowest-energy isomers for most cluster sizes studied, with the oxygen atoms binding *via* a bridged motif along the edges of the Ta clusters. The observed redshift in peak position with increasing cluster size is replicated in the simulated spectra, and this can be explained by the Ta-O bond weakening as the properties of the clusters tend towards those of the bulk metal.

The experimental and simulated spectra for the Ta_nO_2 clusters showed that the lowest-energy structures, which have dissociatively bound O_2, were produced within the experiment. The Ta clusters that contained molecularly bound O_2 were calculated to be much higher in energy, and their simulated spectra did not replicate the experimental spec-

tra well. Evidence of IR-induced fragmentation of clusters has also been discussed, with $Ta_{n=7,13}$ being common fragmentation products; this is consistent with previous literature that showed that these sizes correspond to 'magic number' cluster sizes with increased stability. The presence of fragmentation is assumed to be responsible for additional oxide peaks in the Ta_nO mass spectra.

Part C: In-House Development Work

Chapter 6

Development of a New Bimetallic Cluster Source

This chapter outlines the work done to design, develop, and test a new cluster source to produce gas-phase bimetallic clusters. Completed as part of the EPSRC New Directions in Molecular Scattering programme grant, the development of a new source was done to allow the Mackenzie group to perform new experiments, such as colliding clusters with reactant gases and examining the role of cluster size and composition on reactivity and structure.

Here, the design principles involved and the components that were made to detect the clusters generated by the source are presented. Simulation work has been completed to deduce the optimum experimental conditions to form and detect clusters. Ionisation studies using nitric oxide were completed to understand the behaviour of the gas pulse passing through the source block and toward the time-of-flight mass spectrometer. Following the initial studies with NO, work was performed that led to the generation of neutral and cationic Au clusters, $Au_n^{0/+}$.

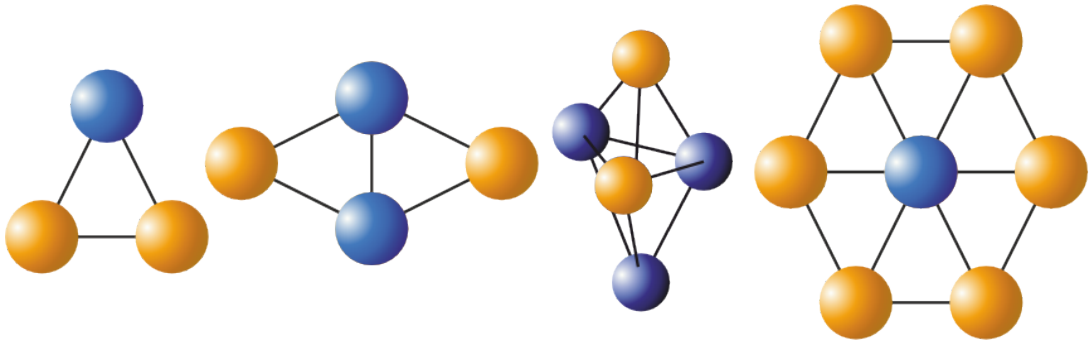

Figure 6.1: Cartoons of the structures of example bimetallic clusters. The different colours are used to represent different elements within the cluster.

The design work, simulations, experiments, and analysis were led by myself, with assistance provided by Prof. Stuart Mackenzie, Dr. Peter Watson, Dr. Christian Haakansson, Dr. Edward Brewer, and Dr. Alice Green.

6.1 Introduction to Bimetallic Clusters

As has been outlined in previous chapters, gas phase metal clusters can be used as tractable models to replicate active sites on the surfaces of catalytic materials. Cluster sources that can produce clusters that contain many metal atoms, such as those used in the HFML-FELIX facility or the Fritz-Haber Institute[119, 232] allow the users there to investigate the structural and reactive properties of clusters of a specific metal. This can include observing odd-even alternations in the chemical properties of these clusters because they have open-shell or closed-shell electronic configurations.[367–370] In addition to changing the size of the cluster, variations in the structure and physical properties of these clusters can be achieved by changing their chemical compositions by adding atoms of different elements.[48, 51, 54, 66, 276, 371] Figure 6.1 provides a cartoon of different bimetallic clusters and the structures they could adopt. Many catalytic materials contain multiple elements to fine-tune their chemical properties in order to go beyond what is achievable using single elements; therefore, the investigation of these bimetallic clusters is of interest because it will aid in the understanding of these types of materials.

Much work has been done to investigate clusters that contain more than just one element; an obvious example being the investigation of metal clusters that contain main

group elements (metal carbides, oxides, sulphides, *etc.*). Given that many heterogeneous catalysts will have the atoms of main group elements on the surface or embedded in the material, there have been a number of studies on these types of clusters,[281, 354, 355, 372–375] including in this thesis with the Ta_nO neutral clusters in Chapter 5. Gas-phase metal oxide clusters were used as analogues of the catalytic metal centres in photosynthetic proteins,[315] as well as in oxidation reactions of simple molecules, such as carbon monoxide.[270, 287] Given the extensive use of fullerenes in electronics and nanotechnology,[103] the physical and chemical properties of metal carbide clusters have been investigated to see how the addition of metals into the structure will affect the structure.[376] Metal sulphide clusters have also been studied[374, 377] given the prevalence of these clusters in biological systems, with iron sulphide clusters (Fe_xS_y) being shown to activate C-H bonds for example.[378] The physical properties of metal-boron clusters have also studied extensively by Wang and co-workers, with metal-boron complexes adopting a range of structures, including metal-centred borometallic rings ($M@B_n^-$), half-sandwich complexes, and metal-centred tubular structures.[379–381] Bimetallic clusters (*i.e.* clusters that contain two different metals) have also been studied extensively both experimentally and computationally. This includes studying their structures, magnetic properties, and reactivity with simple molecules. For example, $IrRh_n^+$ clusters cause NO to dissociate when it binds to it, whereas pure Ir_n^+ binds NO molecularly.[276] Clearly, the ability to control how molecules bind and react on gas-phase clusters by varying their composition will provide useful information for the development of new catalytic materials.

In order to produce gas-phase clusters that contain multiple elements, a number of approaches can be used. In a cluster source, when metal atoms and ions have been liberated, a reactant gas can be added into the carrier gas or in a reaction cell to produce the clusters. This approach was used in Chapter 5, where molecular oxygen, as well as nitric oxide, were added *via* the reactant gas valve to form the Ta_nO species. Other gases such as methane, ammonia, and hydrogen sulphide could be added to produce metal carbides, nitrides, and sulphides, respectively.[375] Other cluster sources are able to produce bimetallic clusters by making a target disc or rod that contains the two elements; often by mixing together powders of the two materials under investigation, before the target

is ablated using a laser or vaporised using a sputtering source.[54, 382–384] As discussed in Chapter 1, bimetallic sources such as CORDIS use Xe cations (Xe^+) to sputter metal atoms from multiple metal targets before they are cooled in a He-filled ion guide to form clusters.[71, 261] One approach that is widely used is to have two separate metal targets that are ablated by two different laser beams. This approach has been used by a number of groups, including Lievens and co-workers who have two metal plates situated next to each other in a clustering channel,[98, 100] before two lasers ablate the surface by passing through pinhole channels in the block. Nonose and co-workers,[51, 385] as well as Fielicke and co-workers[119] have adopted a similar approach, with two metal rods being placed on the edge of the clustering channels, before two laser beams are directed into the block in order to ablate the metal surfaces. Additional reaction channels and cells that can be temperature controlled have also been added onto these sources in order to coat the surface of the clusters with the reactant gas of interest in the study they are performing.

Within the Mackenzie Group at The University of Oxford, we wanted to develop a bimetallic cluster source that allowed us to perform in-house IRPD and collision experiments on these systems. Within the group, the cluster sources that existed in the experiments were mainly tailored to produce metal ion-molecule complexes, such as the ones detailed in Chapters 3 and 4. Experiments on metal clusters have recently been performed at HFML-FELIX or at the Fritz-Haber Institute because they had existing sources tailored to produce clusters, in addition to the benefits provided by the free-electron lasers at these facilities; namely the powers and frequency ranges that were unachievable within the laboratory in Oxford. Experiments were completed, but the group was limited by the wavelength range that the IR free-electron laser at the facility could span, meaning that if a source was built in Oxford, the clusters could be investigated using the OPO/OPA laser system the group possesses. Additionally, the ability to produce bimetallic clusters would allow the group to expand the number of systems that could be studied and to compare the reactivity of these clusters with their corresponding bulk alloys.

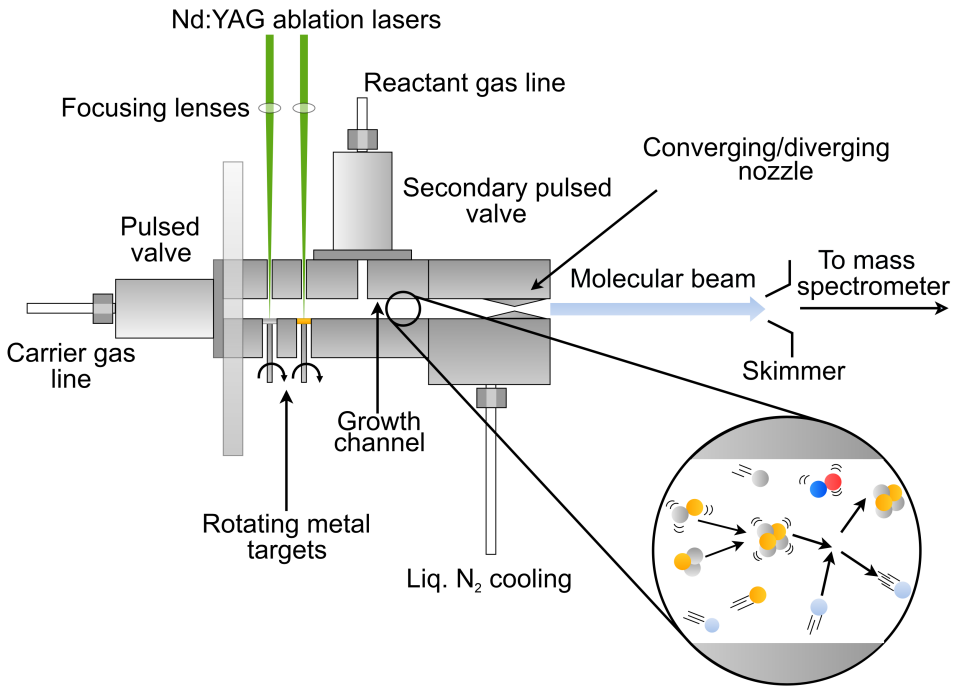

Figure 6.2: Illustration of the bimetallic cluster source. There are two sets of pinholes of light from Nd:YAG lasers to pass through in order to ablate two rotating metal targets. There are two pulsed gas valves on the source; one to add the carrier gas, and another to add in reactant gas to coat the clusters. A nozzle, which can be cryogenically cooled, is attached at the end before the clusters are transported in a molecular beam towards the mass spectrometer. The circular inset shows the clustering process occurring inside of the main channel.

6.2 Designing the Cluster Source

The design for the bimetallic cluster source was based around a number of principles, namely:

- Transportability, so it can be moved between experimental setups.
- Creating an ablation source for consistency with the other sources.
- Incorporate some form of temperature control (*i.e.* cryogenic cooling).
- Having a secondary gas valve to allow the reactant molecules to attach to the generated clusters.

Figure 6.2 provides an illustration of the type of source design that was decided upon. It has similar properties to the cluster sources described in Chapter 1, with focused light from a Nd:YAG laser ablating two different rotating disc targets on the very edge of the clustering channel. A pulsed valve (Parker General Valve Series 9) adds the carrier gas to the channel to cause clustering *via* three-body collisions. Later, a second pulse valve attached to the main block would fire, adding in the reactant gas of choice. The cluster block would have to be relatively long to accommodate the metal targets, as well as the second valve. At the end of the main block, a nozzle would be attached. This would have a converging-diverging restriction in it to maximise the number of collisions between the metal clusters and the carrier gas before it forms the molecular beam travelling towards the detection region. The nozzle block would be cooled using a liquid nitrogen (Liq.N_2) inlet with the cryogenic liquid being provided from a dewar connected to the experiment.

As a guide to make the new source transferable and consistent with the existing source, the dimensions of the other cluster blocks and the disc target mounting used within the group were examined. The dimensions of the existing blocks were measured; the clustering channel had a diameter of 3 mm and the ablation channel diameter was 1 mm. Figure 6.3 provides a layout of the clustering channel block and nozzle that would be incorporated into the new source. The new block would also have a clustering channel with a diameter of 3 mm and would have a length of l_1 (this would be achieved by making different prototype blocks). There would be four ablation pinholes, each with a diameter of 1 mm. The new blocks were designed to have the same clustering channel diameter, given that this is the same diameter used on the cluster source at HFML-FELIX and has been shown to effectively generate clusters.[232] The ablation channel diameters were also set to be 1 mm, to minimise the size of the hole the gas could escape out of, whilst being large enough to allow the focused laser to pass through. On one side (bottom of the block in Figure 6.3), there would be a recess to place the metal targets within to ensure that they are as close to the clustering channel as possible. At the end of the clustering block, a nozzle block would be attached. This would have a length of l_2, and the main channel within this nozzle before the restriction would also have a diameter of 3 mm. The diameter of the nozzle restriction, d_{nr}, could be varied to examine how this affects the flow of gas through the block. The end of the nozzle block would then be positioned

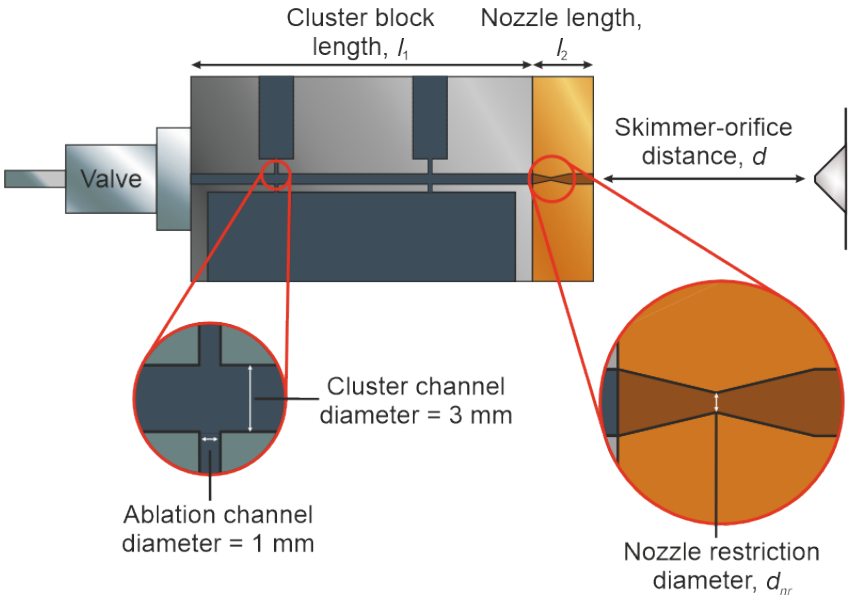

Figure 6.3: Layout of the source block and nozzle used within the bimetallic source. In each of the cluster blocks that have been made, they have a cluster channel diameter of 3 mm, and the pinhole diameter is 1 mm. The source blocks vary in their length, l_1. The nozzle blocks also vary in their length, l_2, and have different restriction diameters, d_{nr}. The front face of the cluster source is then positioned a distance d away from the skimmer.

---

a distance d from the skimmer that would lead to the time-of-flight extraction optics chamber; the value of d can be adjusted to ensure that the molecular beam generated from the source is skimmed effectively.

Figure 6.4 provides the CAD diagram of one of the new clustering channel blocks. The block is 10 cm long and has the two pinholes drilled into the side to allow the ablation lasers to pass through. The block was made to be 10 cm long in order to accommodate the larger target mounting block that would be required to attach the motor mounting plate onto. Additionally, the block was longer to accommodate the reactant gas valve; the idea was to maximise the amount of time that the metal atoms would have to collisionally cool and aggregate, before the reactant gas was added to coat the surface of the cluster. As can be seen in panel **a)**, on the side of the block, there are two circular recesses on the side through which the ablation laser pulses come through. In the middle of these recesses are the 1 mm diameter pinholes. In addition to that, there is a circular recess on

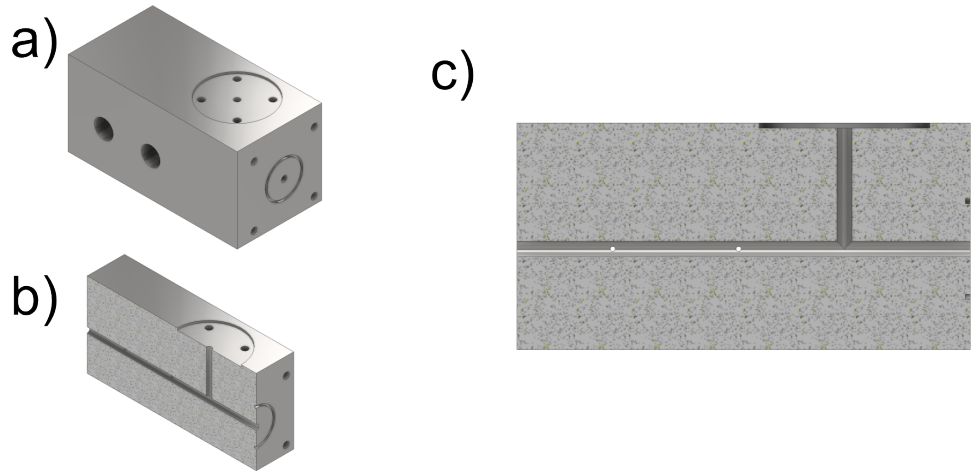

Figure 6.4: CAD diagrams of the large cluster block. **a)**: the entire cluster block, showing the recesses on the laser light entrance side (left hand side), the exit side of the main clustering channel (front face), and the recess for the valve used to add reactant gas (top face). **b)**: half view of the cluster block, showing the internal channels. **c)** side view of the large cluster block, showing the larger internal channels, as well as the two small pins holes in the clustering channel used for the laser ablation.

---

the top surface, which is where the secondary gas valve is attached. Panel **b)** shows the half-cut view of this block, with the clustering channel passing through the length of the block. There is also a channel passing from the top surface to the main channel, where the reactant gas will travel through towards the clustering channel. In panel **c)**, the two small holes that pass through the main clustering can be seen.

A second, shorter source block was built with the intention of making the entire source configuration more compact. Figure 6.5 provides the CAD diagram of this new block, which is 6 cm long. The length of the block was shortened to provide a comparison with the larger block described above, and it was thought that metal atoms and clusters could be lost within the cluster source by colliding with the channel walls if the length of the block was too long. The diameter of the clustering and ablation channels was kept the same between the two blocks, so the length of the block l was the only critical dimension to change. As shown in panel **a)**, the block has been milled more extensively to reduce the weight of the block and to reduce the distance between the edges of the block and the internal clustering channel. On the upper surface, there are four tapped holes that

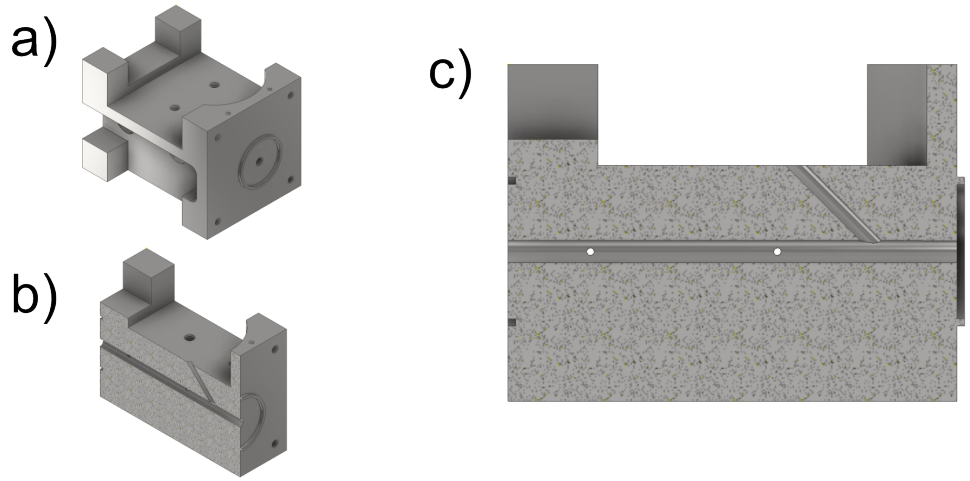

Figure 6.5: CAD diagrams of the small cluster block. **a)**: the entire cluster block, showing the exit of the clustering channel (front face), as well as the holes used to mount the reactant gas valve (top face) and the side the ablation laser light enters (left hand side). **b)**: half view of the cluster block, showing the internal channels. The gas inlet channel is angled at 45° to the main channel. **c)** side view of the large cluster block, showing the two small pins holes in the clustering channel used for the laser ablation.

---

are used to secure the secondary valve.

In panel **b**, the internal channels can be seen. In this smaller block, the channel for the reactant gas is slanted at 45° to reduce the length of the block and ensure that the gas is directed in the same direction the molecular beam travels. There is a circular recess on the top surface, which is where the secondary gas valve is attached. As in Figure 6.4, panel **c)** shows the half-cut view from the side to illustrate the two small holes in the clustering channel.

The nozzle blocks that are attached to the end of the clustering blocks are shown in Figure 6.6. Panels **a)** to **c)** show the brass nozzle block used with the larger diameter of the nozzle restriction ($d_{nr} = 2$ mm). This block was the first prototype, so it was initially decided that the cross sectional area of the exit orifice should be reduced to be equal with the total cross sectional area of all of the ablation channel pinholes. The block is secured with four screws, with the recessed holes for those in the corners of the front face, as seen in panel **a)**. Panel **b)** shows the channel in the middle of the block, and panel

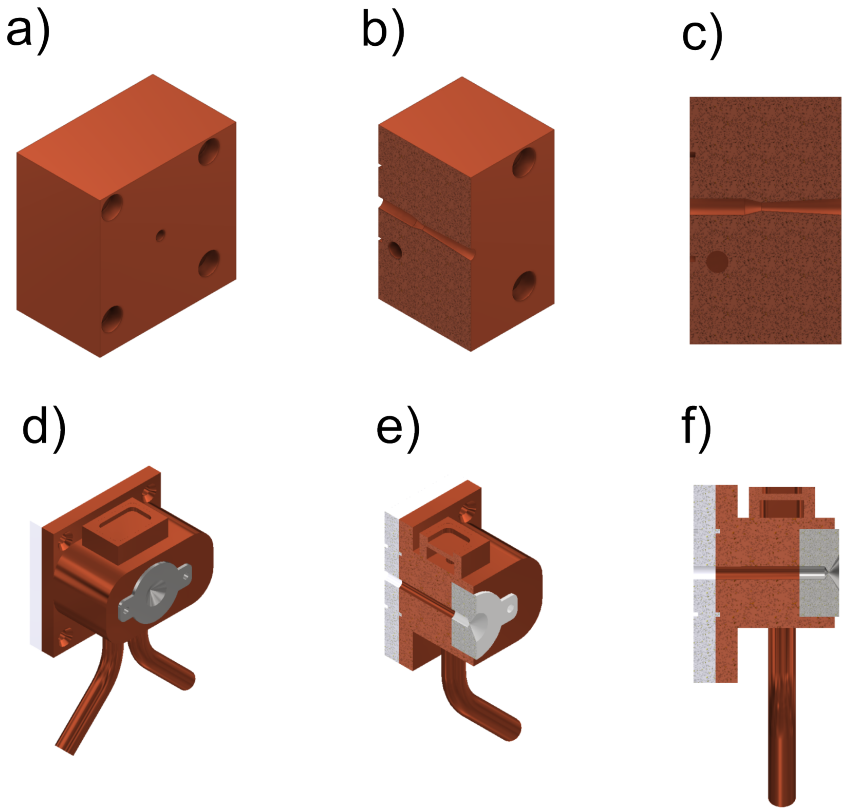

Figure 6.6: CAD diagrams of the nozzle blocks used on the source. Panels **a)** to **c)** are for the nozzle with the large restriction diameter (d_{nr} = 2 mm), and panels **d)** to **f)** are for the block with the smaller diameter (d_{nr} = 0.4 mm). Panels **b)**, **c)**, **e)**, and **f)** show the internal channel in these block, with the restrictions being shown. The smaller diameter nozzle also has tubes which are used for cryogenic cooling.

---

c) shows the restriction within this channel. The location of the restriction was partially determined by the manufacturing process, and the block itself was made relatively large so additional channels could be drilled in to add cryogenic cooling at a later date. The problem with this nozzle block is that the size of the orifice is fixed because it is drilled directly into the metal.

Panels **d)** to **f)** show the alternative nozzle that was built. The benefit of this design is that the diameter of the nozzle compression can be adjusted by changing the steel insert that is attached to the brass casing, as shown in the panel **d)**; an idea taken from the cluster source design at HFML-FELIX. This design also has tubes on the underside that can be used for cryogenic cooling, with liquid nitrogen flowing in and out of a reservoir that is contained within the brass frame. This reservoir at the top of the nozzle block can

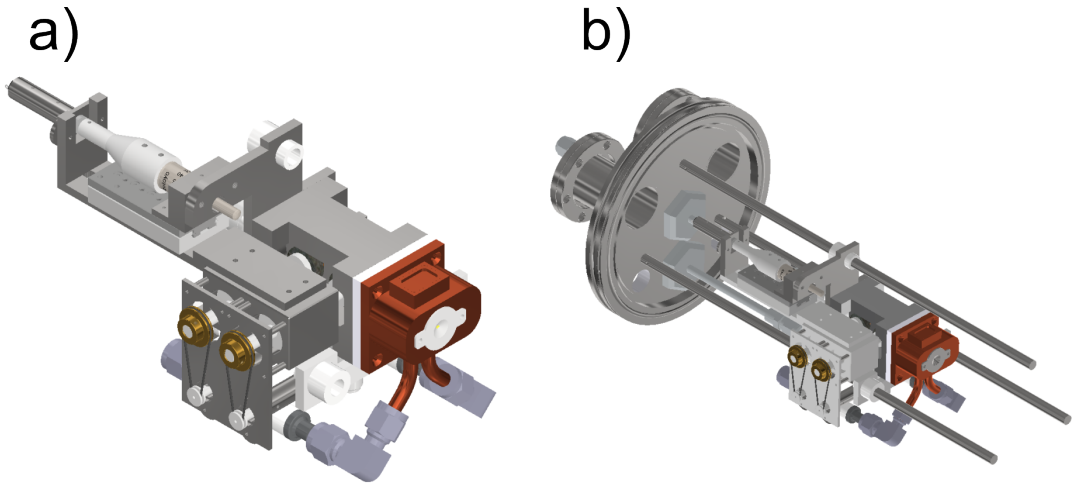

Figure 6.7: CAD diagram of entire cluster source assembly. **a)**: The cluster source incorporates a number of components: a Faulhaber and micrometer (left hand side) are used to translate the target mounting block (centre left). The targets are mounted inside of this block and pushed up to the laser ablation pinhole on the cluster block (centre right). The nozzle (left) is attached to the front face of the cluster block. **b)**: The cluster source mounted on the ISO flange using the locating rods. The flange also has holes which are used to different feedthroughs to the source block.

---

be seen in the cut in panel **e)**. Panel **f)** shows the steel inset inside the block with the restriction in the inset being very close to the front face. In this work, the steel inset had a constriction diameter of 0.4 mm, 5 times smaller than the diameter in the other nozzle block. Between the brass nozzle block and the main clustering block is a ceramic spacer (shown as a white block in Figure 6.6 **e)** to **f)**). This is used to thermally isolate the nozzle from the rest of the block. The dimensions of the blocks and nozzles are provided in Table 6.1.

The chosen source block and nozzle are assembled with the other components to form the entire cluster source, as shown in Figure 6.7. Panel **a)** shows the other components used to make the entire source work. On the left hand side is a micrometer attached to a Faulhaber motor. This is used to translate the target mounting block forward and backward, moving where the ablation laser hits the metal target. This is done to provide a fresh surface once the target has been ablated away. The entire assembly is mounted on a plate; within the plate, there are three holes for PEEK spacers, which are used to

Table 6.1: Geometrical properties of source components.

Source block properties				
Block	**Channel length / m**	**Channel radius / m**	**Channel cross sectional area / m^2**	**Channel volume / m^3**
Large block	1.0×10^{-1}	1.5×10^{-3}	7.07×10^{-6}	7.07×10^{-7}
Small block	6.0×10^{-2}	1.5×10^{-3}	7.07×10^{-6}	4.24×10^{-7}

Nozzle properties						
Nozzle	**Channel length / m**	**Channel radius / m**	**Channel cross sectional area / m^2**	**Channel volume / m^3**	**Constriction radius / m**	**Constriction cross sectional area / m^2**
Large nozzle	1.5×10^{-2}	1.5×10^{-3}	7.07×10^{-6}	1.06×10^{-7}	1.0×10^{-3}	3.14×10^{-6}
Small nozzle	2.97×10^{-2}	1.50×10^{-3}	7.07×10^{-6}	2.10×10^{-7}	2.0×10^{-4}	1.26×10^{-7}

Ablation laser pinhole			
Pin hole radius / m	**Pin hole cross sectional area / m^2**	**2 pin holes cross sectional area / m^2**	**4 pin holes cross sectional area / m^2**
5.0×10^{-4}	7.85×10^{-7}	1.57×10^{-6}	3.14×10^{-6}

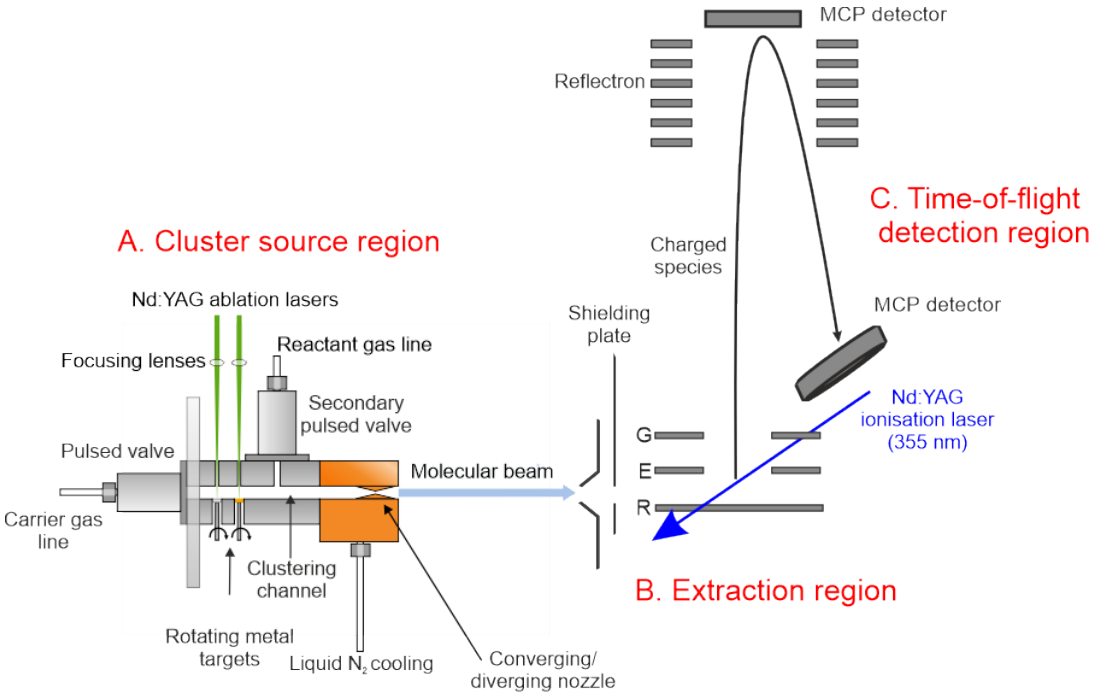

Figure 6.8: Illustration of the experimental setup used to study the gas phase metal clusters produced by the bimetallic cluster source. The clusters are generated in the cluster source (region A), forming a molecular beam and travelling into the extraction region. The charged species are then extracted into the time-of-flight region (region C) before being detected using an MCP. Neutral species can be extracted *via* non-resonant ionisation in the WM lens using a 355 nm Nd:YAG laser (100 mJ/pulse, 10 Hz).

---

mount the metal plate onto the locating rods. Panel **b)** shows the cluster source assembly resting on the locating rods, which themselves are attached to an ISO flange; the same type of flange used for the other sources within the group, and the rods fit into locating pins that screw into the vacuum chamber. The flange has gas, cryogenic, and electrical feedthroughs which are used to operate the source, such as applying voltages to the valves and rotation motors.

6.3 Experimental Setup

In order to study the clusters that are produced by the source, a custom reflectron time-of-flight (ToF) mass spectrometer was built. This produces a setup similar to that of the existing IRPD experiment, except for the quadrupole mass filter and quadrupole bender. Figure 6.8 shows the experimental setup used to investigate the species produced. The

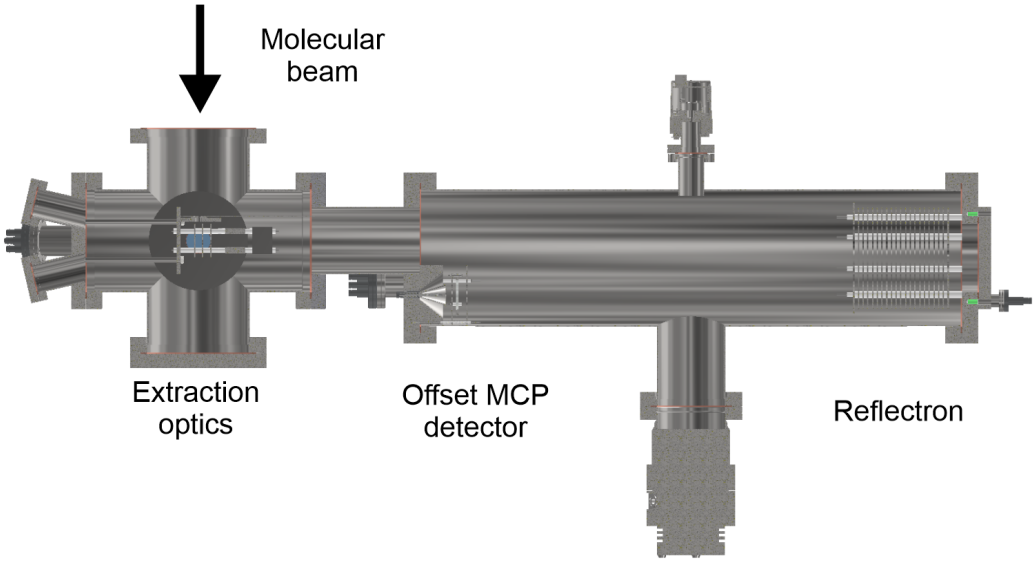

Figure 6.9: Cut-through CAD diagram of the custom made time-of-flight mass spectrometer. The direction of the molecular beam is shown, with the position of the extraction optics, offset MCP detector, and reflectron highlighted.

species entrained within the molecular beam produced by the source passes through a skimmer (2 mm diameter) before entering the ToF extraction optics which is made up of a simple Wiley-McLaren lens setup. An ultraviolet laser pulse (Continuum Surelite, 355 nm, 10 ns pulse width, 10 Hz rep. rate, up to 100 mJ/pulse) can enter the extraction optics chamber, after being focused by a lens outside of the experiment, and can be used to ionise the clusters within the extraction optics, in a similar way to what was done in the HFML-FELIX setup in Chapter 5. A custom built reflectron was also made to improve the resolving power of the mass spectrometer before the charged species were detected on an offset MCP.

Figure 6.9 shows the CAD diagram of the a cut-through of the custom-made time-of-flight mass spectrometer. The mass spectrometer is built using two chambers, the extraction optics chamber and the time-of-flight chamber, connected using a custom DN160 to DN200 CF adapter offset flange, with the offset MCP being mounted on this flange. This is pumped using a Leybold Turbovac 850iX mounted on a T-chamber, as well as a smaller Turbovac 151 molecular pump mounted on the ToF chamber. The pressure that can be achieved within the experiment can be as low as 2×10^{-7} mbar. The molecular beam

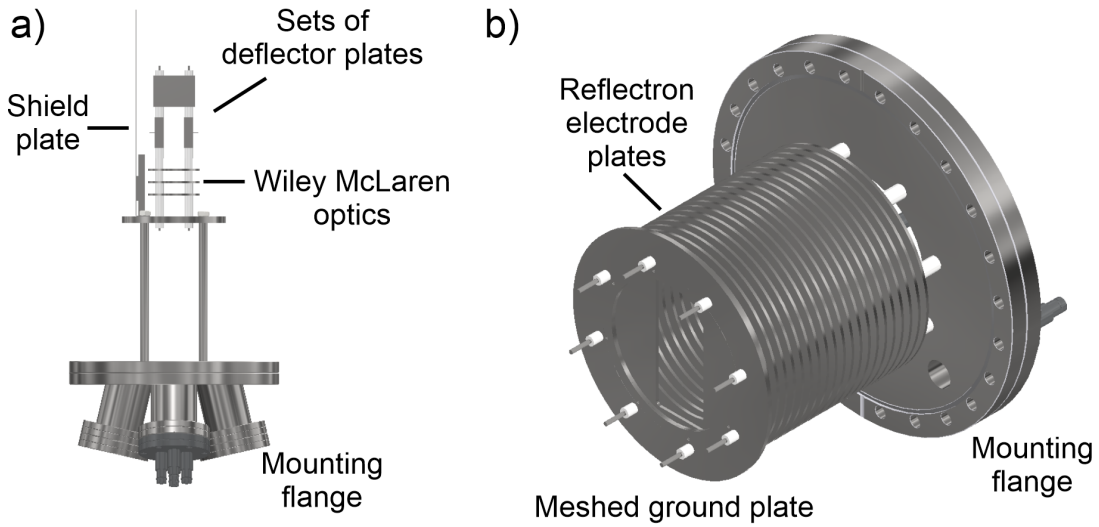

Figure 6.10: CAD diagrams of the extraction optics (panel **a)**), and the reflectron (panel **b)**) within the custom built time-of-flight mass spectrometer. The components of the ion optics are labelled; namely the Wiley-McLaren optics, deflector plates, and shield plate in the extraction optics, and the electrode stack in the reflectron.

---

produced within the source chamber is directed towards the vacuum chamber containing the extraction optics. The arrangement of the extraction optics has been set so that the midpoint between the repeller and extractor plates is in the same plane as the skimmer orifice between the source and extraction optics chambers. At the top of the time-of-flight chamber is the reflectron, which also has a mounting point for an MCP to operate the mass spectrometer in a linear mode (*i.e.*, when no voltages are applied to the reflectron).

The CAD diagrams of the custom ion optics and flanges are provided in Figure 6.10. Panel **a)** shows the setup of the extraction optics; they are mounted on a plate that itself was mounted *via* four rods onto a multi-feedthrough flange. This was done to make alterations easier and to apply the voltages to each of the optics. The PEEK spacers between the optics were arranged to ensure that the midpoint between the repeller and extractor plates in the WM setup was in the same plane as the midpoint of the skimmer. The plates (2 mm thick, 50 mm diameter, 10 mm hole in the middle of the extractor and ground plates, 10 mm separation between them) also had an electroformed mesh attached to them in order to reduce the electric field from the different regions permeating through. Deflector blocks (40 mm × 30 mm × 9 mm) were placed above the WM lens

to allow a fixed potential to be applied that could steer the ions to the MCP detector. A shield plate was mounted in front of the optics to reduce the number of stray fields that affect the flight path of the ions once they enter the extraction optics chamber.

Panel **b)** shows the CAD diagram of the custom built reflectron. At the front of the reflectron is a grounded plate with an electroformed mesh going across it. Subsequently, there are 20 circular plates (outer diameter: 150 mm, inner diameter: 100 mm) that are connected in series by a chain of resistors, all with the same resistance (200 MΩ). A voltage is applied to the front and back plates in the reflectron using the feedthroughs on the DN200 CF flange, and the voltages on each plate are evenly spaced. The reflectron flange also has a smaller adapter on it to allow an MCP to be mounted there.

6.3.1 SIMION Simulations

Before the ion optics were built, simulations were conducted using the SIMION software package to examine how the ion optics setup that has been designed would operate. For example, simulations were performed to examine which WM voltage ratio would be required to achieve the sharpest peaks in the ToF spectrum, based on the conditions set out in Equation 1.13 in Chapter 1. In addition, the lines of equipotential in the extraction optics were visualised to examine whether shielding would be required.

Figure 6.11 shows the lines of equipotential within the extraction optics assembly (WM lens and the first set of deflector plates) with (panel **a)**) and without (panel **b)**) the ground shield plate. The voltages were set as such:

- Repeller plate: 4000 V
- Extractor plate: 3000 V
- Ground plate: 0 V
- Top deflector plate: 200 V
- Bottom deflector plate: 0 V
- Shield: 0 V

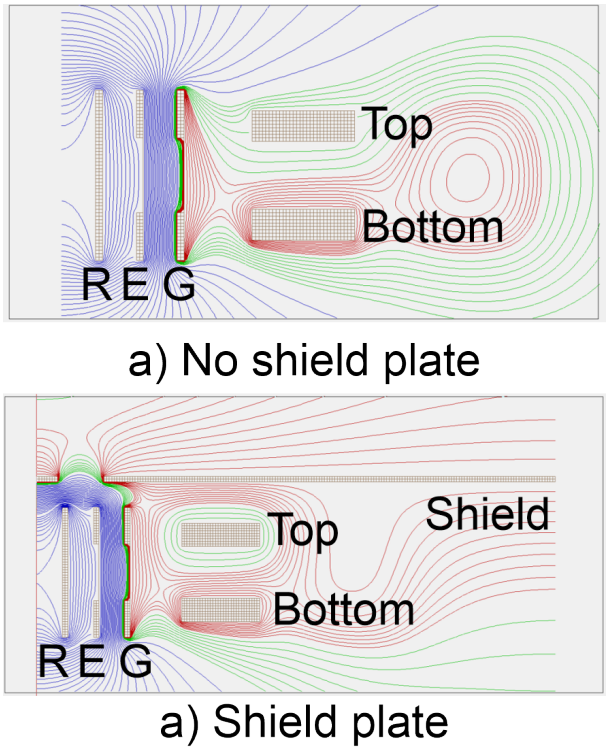

Figure 6.11: SIMION simulation of the lines of equipotential within the extraction optics with (panel **a)**) and without (panel **b)**) the shielding plate in front of the optics. The voltages applied to the plates are as follow: R = 4000 V, E = 3000 V, G = 0 V, Top deflector = 200 V, Bottom deflector = 0 V, Shield = 0 V. The red lines represent potentials between 0-100 V (10 V steps), green for 125-300 V (25 V steps), and blue for 400-4000 V (100 V steps).

The lines of equipotential are colour coded: red for 0-100 V (10 V steps), green for 125-300 V (25 V steps), and blue for 400-4000 V (100 V steps). As can be clearly seen, without the shield in place, the equipotential lines from the WM plates can extend out to the sides, as do the equipotential lines from the deflector plates. This is especially a problem with the deflector plates as they have a fixed DC voltage, meaning that these lines will always be present as long as the voltage is applied. The WM optics are pulsed, and the time at which they are pulsed can be altered to ensure that they only fire when ions are between the plates. However, the field strength between these plates is large and could significantly deflect any charged species. Additionally, if multiple species are produced, a significant portion could be reflected away depending on their mass as they will be travelling at different speeds. From looking at the simulated lines of equipotential, the shield plate was made and installed in front of the ions to minimise the effect of the

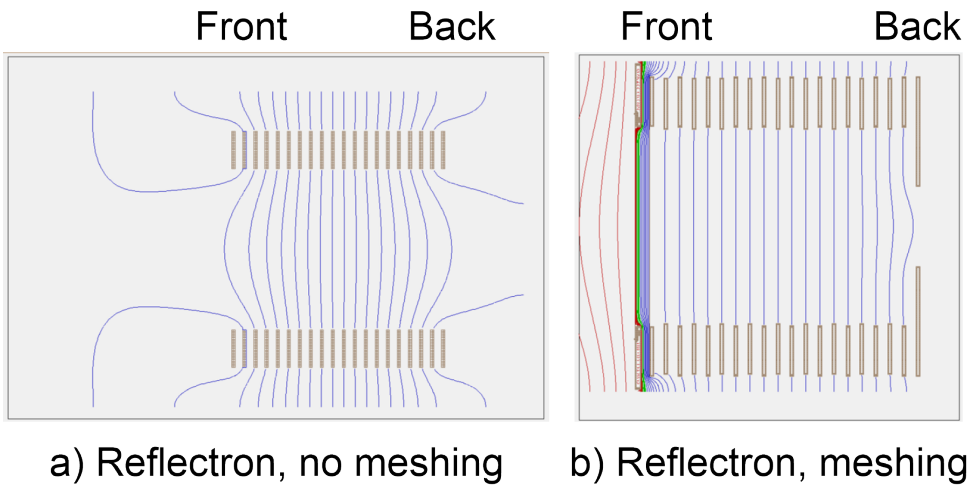

Figure 6.12: SIMION simulation of the lines of equipotential within the reflectron optics with (panel **a)**) and without (panel **b)**) meshing the front ground plate of the electrode stack. The voltages applied to the plates are as follow: Front = 1100 V, Back = 3000 V, Ground plate = 0 V. The red lines represent potentials between 0-100 V (10 V steps), green for 125-300 V (25 V steps), and blue for 400-4000 V (100 V steps).

electric fields permeating and deflecting the incoming charged species.

Simulations were also conducted to examine the effect of adding a meshed and grounded front plate to the reflectron, as well as adding a plate at the back with a smaller internal diameter (40 mm) at the back. The plate at the back was made to allow the ions to pass through the MCP at the top of the ToF chamber. This was done instead of using a solid plate, or by meshing one of the electrodes with the larger inner diameter. Figure 6.12 shows the lines of equipotential within the reflectron without (panel **a)**) and with (panel **b)**) electroformed mesh across the front. The front electrode of the reflectron (left side in both panels) is set at 1100 V, and the back electrode is set at 3000 V. As shown, the lines of equipotential are much flatter when the electroformed mesh was applied to the grounded front plate, and the high-voltage equipotential lines do not permeate out. In panel **b)**, there is some curvature of the equipotential lines at the very back by the hole in the plate, but the voltages in the reflectron can be adjusted to control how far into it the charged species travel; therefore reducing the likelihood of them being deflected. Looking at the two reflectron simulations, the configuration with the meshed ground plate was adopted to make the equipotential lines as flat as possible and therefore to maximise the

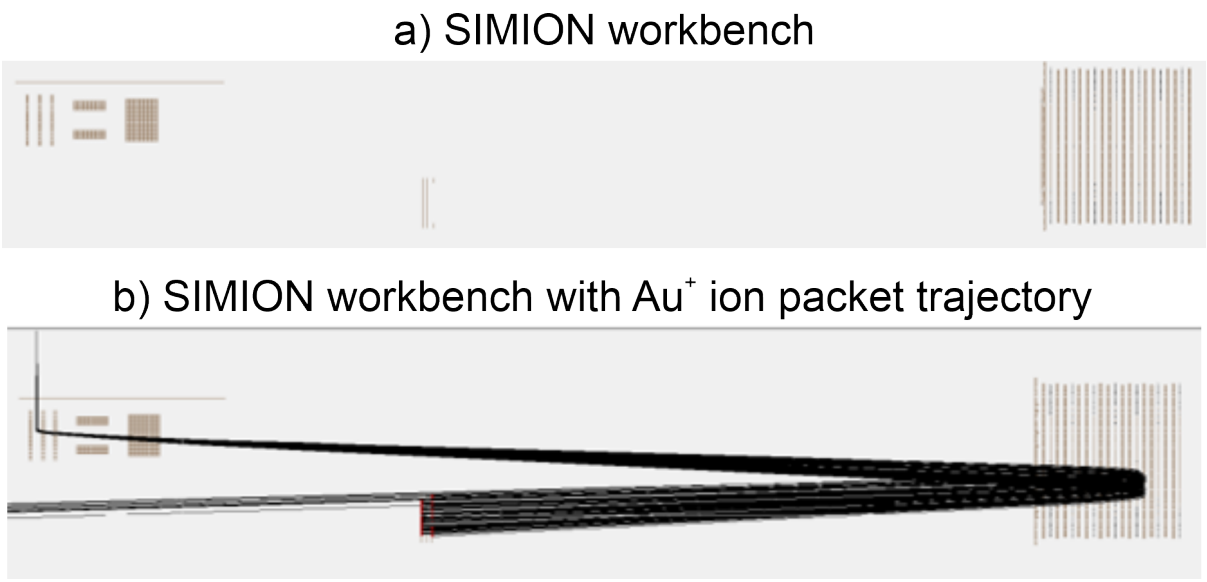

Figure 6.13: SIMION workbenches used to simulate the ion optics arrangement within the ToF mass spectrometer. **a)**: The extraction optics, reflectron and MCP potential arrays (PAs) arranged in the same way as the components in panel **d)** of Figure 6.9. **b)** Au^+ ion packet containing 100 ions, with kinetic energies equally spaced in the range 29.5-30.49 eV, passing through the PAs, and landing on the offset MCP.

---

number of charged species being directed onto the offset detector.

The optimised ion optics configurations were then added to a SIMION work bench, positioned where they would be within the experiment. This is shown in Figure 6.13 **a)**. Following the setup of the workbench, a simulated packet of monoatomic Au cations, Au^+, was flown into the extraction optics, as shown in Figure 6.13 **b)**. The ion beam consists of 100 ions, with an arithmetic range of kinetic energies ranging from 29.5 to 30.49 eV. The beam has a conical distribution, with a half angle of 0.5° relative to the axis vector, and is centred on the midpoint between the repeller and extractor plates. The simulation voltages used to produce Figure 6.13 and the pulse widths are as follows:

- Repeller voltage: 4000 V, pulse width: 20 µs
- Extractor voltage: 3300 V, pulse width: 20 µs
- Ground voltage: 0 V
- Bottom deflector plate: 25 V

- Reflectron bottom: 1000 V
- Reflectron top: 4000 V

Using this configuration, it was shown that most of the ions could be directed onto the offset MCP. The collection effeciency could be improved by adding an einzel lens to minimise how much the ions fan out. optimisation. However, it was decided that an einzel lens would not be included initially in order to reduce the complexity of the system and the number of conditions that would have to be optimised.

The optimum WM conditions required were also examined, with simulations being performed for different WM repeller-extractor ratios. Using Equation 1.13 and the distances established in the experiment (D = 126 cm, s_0 = 0.5 cm, s = d = 1 cm), the optimum ratio of the electric fields in the extraction and acceleration regions $\frac{E_d}{E_s}$ was calculated to be 12.63, which corresponded to the ratio of the repeller and extractor voltages, $\frac{R}{E}$, being 1.079 on the specific experimental layout. Using a $\frac{R}{E}$ ratio of 4000 V / 37000 V (equal to 1.08) generated simulated ToF spectra with the narrowest peaks, showing that the custom WM lens could temporally focus the Au^+ ions generated by the cluster source.

6.4 Gas Flow Properties Within the Source Blocks

It was decided that simulations should also be performed to predict the pressures within the cluster channel and to determine the shape of the gas pulse exiting the source block; this was done by applying a simple kinetic model. To study this experimentally, a nitric oxide gas mixture was used to generate a molecular beam, before being ionised using the 355 nm laser across a range of timings relative to when the gas valve was fired. He and Becker were able to ionise NO (ionisation potential = 9.26 eV) using four 532 nm photons (photon energy = 2.33 eV).[386] It was determined that the 355 nm laser (photon energy = 3.49 eV) could also non-resonantly ionise the gas with one fewer photon. By monitoring the NO^+ signal as a function of the valve trigger-laser fire delay, the gas pulse's shape could be determined, thus allowing the voltages and timings to be optimised in order to maximise the amount of species entrained within the gas pulse being extracted and directed onto the MCP detectors.

6.4.1 Applying Kinetic Model

In order to calculate the rate of gas flow in and out of the source blocks, a simple kinetic model of effusion was applied. The effusion rate $\frac{dN}{dt}$ is the rate at which gas molecules pass through a narrow orifice in a container in a vacuum, without collisions between the molecules and without bulk flow of the gas.[134] The rate at which gas molecules pass from the gas valve into the block is defined as:

$$\frac{dN}{dt} = \frac{p_0 A_0}{\sqrt{2\pi m k_B T}}, \tag{6.1}$$

where p_0 is the backing pressure in the gas valve reservoir, A_0 is the cross-sectional area of the valve orifice (calculated to be 7.85×10^{-9} m^2), m is the atomic mass of the gas (here, the gas is assumed to be He), k_B is Boltzmann's constant, and T is temperature (assumed to be 300 K).[134] It is assumed that there are no gas molecules in the block before the gas valve opens. When the valve is closed, the gas within the source block will escape at a rate defined by the equation:

$$\frac{dN}{dt} = -\frac{AN}{V}\sqrt{\frac{k_B T}{2\pi m}}, \tag{6.2}$$

where A is the total cross sectional area of the holes in the source, N is the number of molecules within the block, and V is the total volume of the clustering channel.[134] A steady-state pressure within the channel is achieved when the rate of gas entering the channel equals the rate of it exiting. Following an algebraic rearrangement and the application of the ideal gas law, the value of the steady-state pressure is defined as:

$$p_{ss} = \frac{p_0 A_0}{A} \tag{6.3}$$

The predicted shape for the gas pulse would include a rising edge, where gas effuses across the valve orifice, followed by a plateau when there are equal rates of effusion in and out of the clustering channel, before an exponential decaying edge when the valve is closed again.

Figure 6.14 shows the pressure in the source blocks as a function of the time since the gas valve was opened. The x-axes in both panels extends to 5000 µs in order to show steady-state conditions have been reached. In panel **a)**, the simulated effect of the backing pressure was examined from 1 bar to 9 bar, using He and a configuration made of the large source block and the large nozzle described previously. As shown by Equation

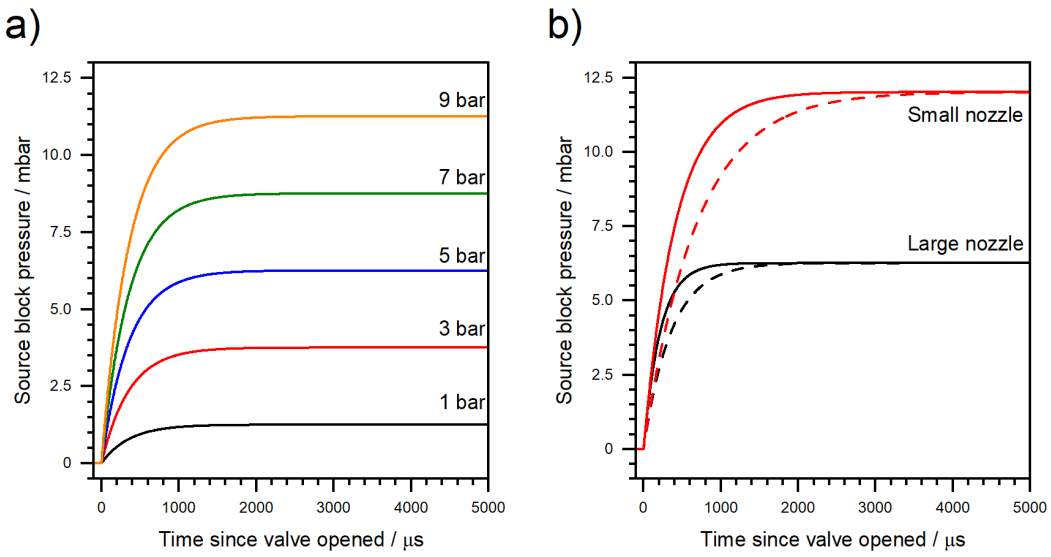

Figure 6.14: Simulated source block pressures as a function of time since valve opened. **a)**: multiple simulated pressure curve showing the effect of backing pressure, p_0, on the shape of the curve and the final steady state pressure being achieved. **b)**: The effect of different nozzles on the maximum pressure achieved inside of the source, with black lines being for the 2 mm diameter nozzle, and red for the 0.4 mm diameter nozzle. The solid lines are for the 6 mm long cluster block, and the dashed lines are for the 10 mm long cluster block.

6.3, the steady-state pressure increases with increasing backing pressure. In addition, the gradient of the initial pressure rise appears to increase with the backing pressure. In panel **b)**, the pressure change is shown using different source block and nozzles, with a backing pressure of 5 bar. The black lines represent the source configurations using the larger nozzle (d_{nr} = 2 mm), while the red lines represent the smaller nozzle (d_{nr} = 0.4 mm). The reduction in the source cross-sectional area causes an increase in steady-state pressure. In addition, line styles are used to represent different volumes of the clustering channel, with the solid line used for the smaller source block (l_1 = 6 cm), while the dashed line is for the longer source block (l_1 = 10 cm); as the volume decreases, the rate at which the steady state is reached increases.

Figure 6.15 shows how the pressure inside the source block decreases once the valve is closed. In panel **a)**, the simulated valve is turned off at 250, 500, 1000 and 2500 µs (shown in red, blue, green and orange, respectively). The simulated configuration used

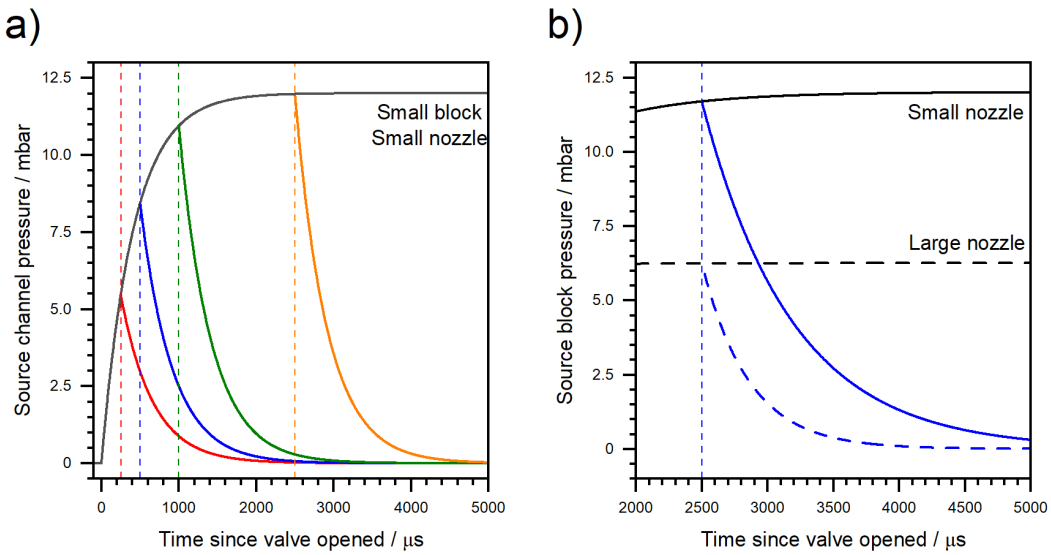

Figure 6.15: Source block pressure curves when the valve is closed after time t. **a)**: using the small cluster block and small nozzle configuration, the pressure curves are simulated for different valve closing times ($t = 250, 500, 1000, 2500$ µs). **b)**: The decay curves are shown for the large block using the small (solid lines) and large (dashed lines) nozzles after the valve closes at $t = 2500$ µs. The rate at which they decay is different, with the large nozzle configuration decaying more quickly.

---

the small source block and small nozzle, with a backing pressure of 5 bar. As shown, for short gas pulse widths (*i.e.* the valve is closed earlier), the pressure inside the channel has not reached an equilibrium, resulting in a sharp peak before the exponential decay. For longer pulse widths ($t = 2500$ µs), a plateau is reached before exponential decay; thus matching the predicted structure. In panel **b)**, the large cluster block is simulated using the two different nozzles, with the solid lines representing the small nozzle and the dashed lines representing the large nozzle. At $t = 1000$ µs, the valve is closed. The exponential decay of pressure is slower for the smaller nozzle. This can be explained by Equation 6.2 as the effusion rate decreases when the cross-sectional area decreases. If the same nozzle were used on two different blocks with different volumes, the effusion rate would be greater in the block with the smaller volume.

In order to examine the effect of the different source configurations, it was useful to define each of them depending on which source and nozzle blocks they used. Additionally, when the targets were positioned near the ablation laser pinholes, it was assumed that the cross

Table 6.2: Summary of configurations, components, and A/V ratios.

Configuration	Components	Targets in?	A/V ratio
1	Valve only	No	-
2	Large source block	No	14.44
3	Large source block, large nozzle	No	7.73
4	Small source block	No	24.08
5	Small source block, large nozzle	No	11.85
6	Small source block, small nozzle	No	5.16
7	Large source block, small nozzle	No	3.56
8	Large source block, small nozzle	Yes	1.85

section was reduced because it would prevent the gas from exiting. In the simulations, in order to replicate the effect of the targets being inserted in the source, it is assumed that two of the ablation channel pinholes are fully blocked; even if in reality there may be some gas escaping from the pinholes next to the targets. Table 6.2 provides the different configurations tested in the experimental setup and their corresponding cross-sectional area to volume ratio $\frac{A}{V}$. As shown in Equation 6.2, the rate of effusion out of the block is proportional to this ratio.

6.4.2 NO Ionisation Studies

Before the NO ionisation study began, the experimental setup was further simplified by removing the ToF chamber from the experiment and placing an MCP detector directly above the extraction optics, in order to maximise the amount of NO^+ reaching the detector. Additionally, only the gas valve was attached to the source chamber (configuration 1), in order to examine the effect of adding the cluster blocks on the shape of the gas pulse. The valve was positioned 2.5 cm away from the skimmer orifice and pure NO was initially used at 2.5 bar backing pressure. Figure 6.16 shows the 1000 shot average ToF spectra recorded at two different valve trigger - laser fire delays (*i.e.* how long after the valve opening does the ionisation laser fire). Panel **a)** was recorded at 250 µs, with the ionisation laser firing before the gas pulse arrived. There are weak features in the spectrum that correspond to H^+, H_2O^+, and NO^+. In panel **b)**, the ToF spectrum is

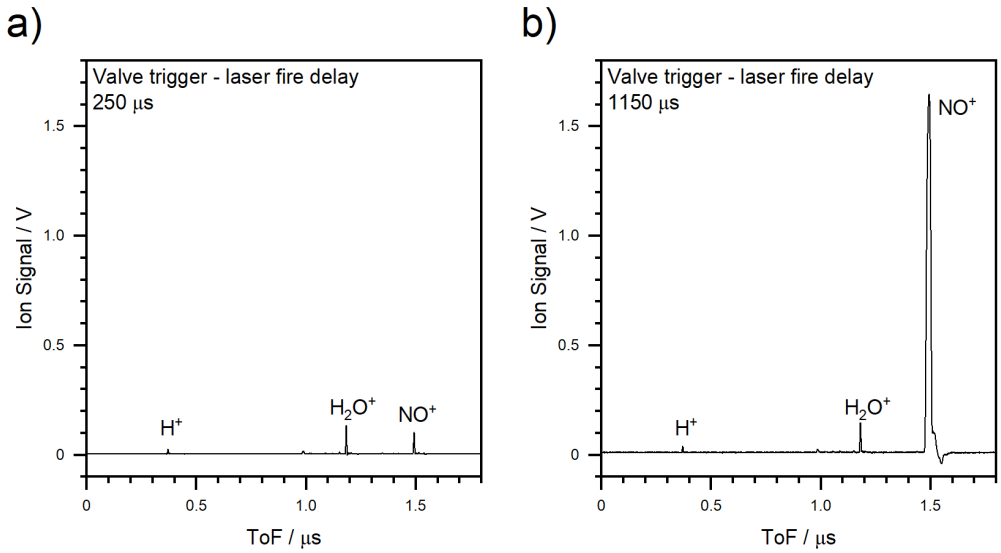

Figure 6.16: Initial ToF spectra produced by ionising NO with 355 nm light. **a)**: The ToF spectrum produced when the ionisation laser is fired before the NO gas pulse enters the WM lens (valve trigger-laser fire delay = 250 µs). **b)**: The ToF spectrum produced when the ionisation laser is fired when the NO gas pulse is within the WM lens (valve trigger - laser fire delay = 1150 µs).

---

recorded at a greater delay (1150 µs). Here, the signal for NO^+ is much more intense, which means that the laser is ionising the target gas within the gas pulse.

In order to visualise the gas pulse shape, the area under the NO^+ curve was plotted as a function of valve trigger - laser fire delay. The absolute area was extracted by integrating the curve, with an associated error in the area, σ_A, calculated as:

$$\sigma_A = \sigma \times \sqrt{N} \times \Delta t, \tag{6.4}$$

where σ is the standard deviation of the noise, $\sqrt{N}$ is the square root of the number of points used in the integral and Δt is the time step size.

To illustrate this idea, Figure 6.17 shows normalised NO^+ as a function of the valve trigger - laser fire delay using two different gas valve driver boxes in a range of input pulse widths. In this case, the gas mixture used was 2% NO in He, at a backing pressure of 5 bar. Panel **a)** shows the results when a Parker Iota One driver was used, whereas panel **b)** is for a driver built in-house, which has an additional ability to control the

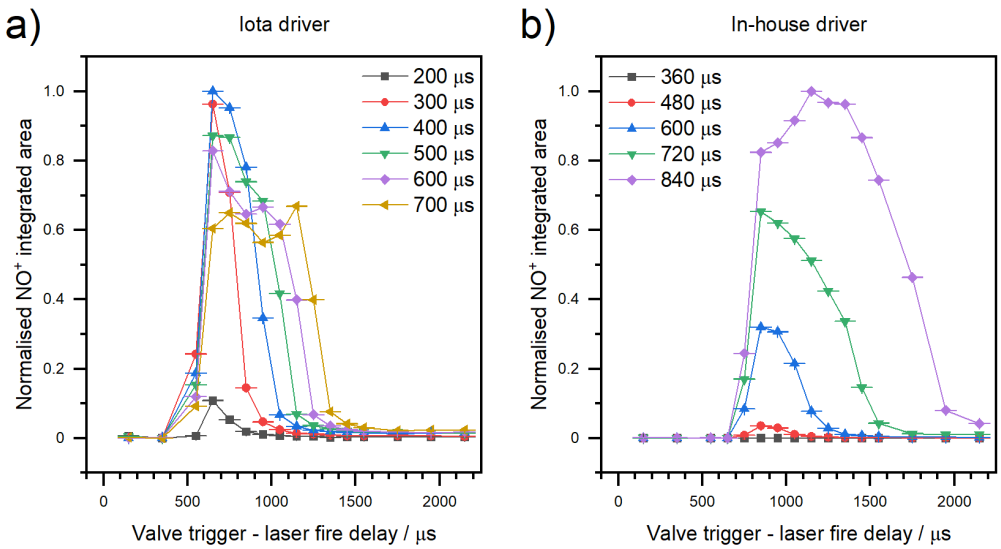

Figure 6.17: Gas pulse width study using two different gas valve driver boxes. The curves were produced by integrating the NO^+ ion signal in multiple mass spectra generated at different valve trigger - laser fire delays. **a)**: Spectra produced using a Parker Iota One driver, with gas pulse widths between 200 and 700 µs. **b)**: Spectra produced using an custom built in-house valve driver, with gas pulse widths between 360 and 840 µs.

---

trigger pulse voltage; something the Iota driver cannot do. As the input gas pulse width was increased, the width of the curve produced from the ionisation study also increased. Additionally, each curve is largely symmetric about their centre point, with the rising and decaying edges having similar gradients.

Examining the gas pulse shape following the addition of the clustering block was the next step. The larger cluster block was attached to the mounting plate, with no nozzle block attached on the front (configuration 2), before the exit orifice was positioned 2.5 cm away from the skimmer. Figure 6.18 shows the normalised NO^+ peak integral as a function of the valve trigger - laser fire delay for configurations 1 and 2. There are a number of differences between the two curves; for example, the rising edge of the curve for the large cluster block begins later than for the valve-only curve. This is because in order to make the orifice-to-skimmer distance the same between the two systems, the valve moves back by the length of the large cluster block, so the gas has to travel further and the ionisation laser has to fire later. Additionally, the red curve has a different shape

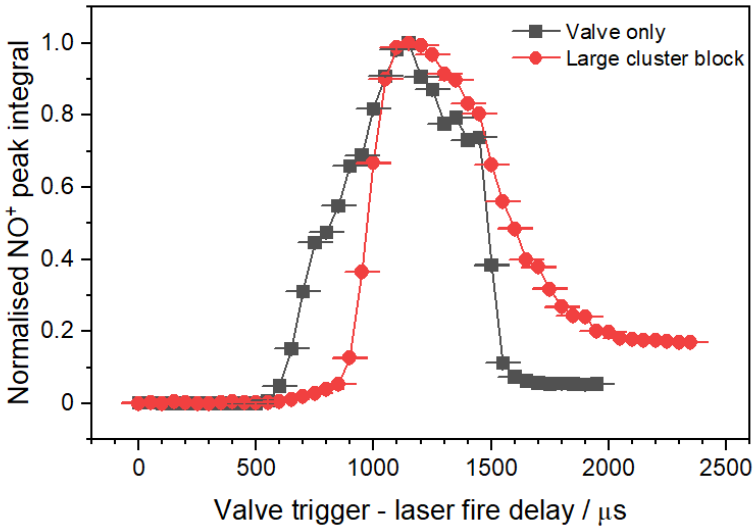

Figure 6.18: Normalised NO^+ peak integrals as a function of valve trigger - ionisation laser fire delay for two different source configurations: valve only (configuration 1, black squares) and large cluster block (configuration 2, red circles). The black curve is more symmetric, with the rising and falling edges appearing to have the same gradient. The red curve has a fast rising edge, and slower decaying edge, matching what was seen in Figure 6.15

---

than the black curve, namely the red curve has a sharp rising edge, a short plateau, and then a decaying edge that takes a longer time to fall away. This is similar to what was observed in the simulated curves, suggesting that in a first approximation the simple kinetic model is replicating what is seen experimentally. The red curve also does not fall all the way back to zero, suggesting that there is still gas within the source block over 2 ms after the valve opens.

The same type of valve trigger - ionisation laser fire delay study was replicated for each of the configurations discussed in Table 6.2. Figure 6.19 shows the normalised NO^+ peak integral as a function of valve trigger - laser fire delay for configurations 2,3,4, and 5. Panel **a)** is for the large block without (black curve) and with (red curve) the large nozzle block, while panel **b)** is for the small block without (blue curve) and with (green curve) the large nozzle block. Each of these curves has a similar structure; that is, a sharp rise in NO^+ signal, a small plateau, before an exponential decay. The peak centre is shifted

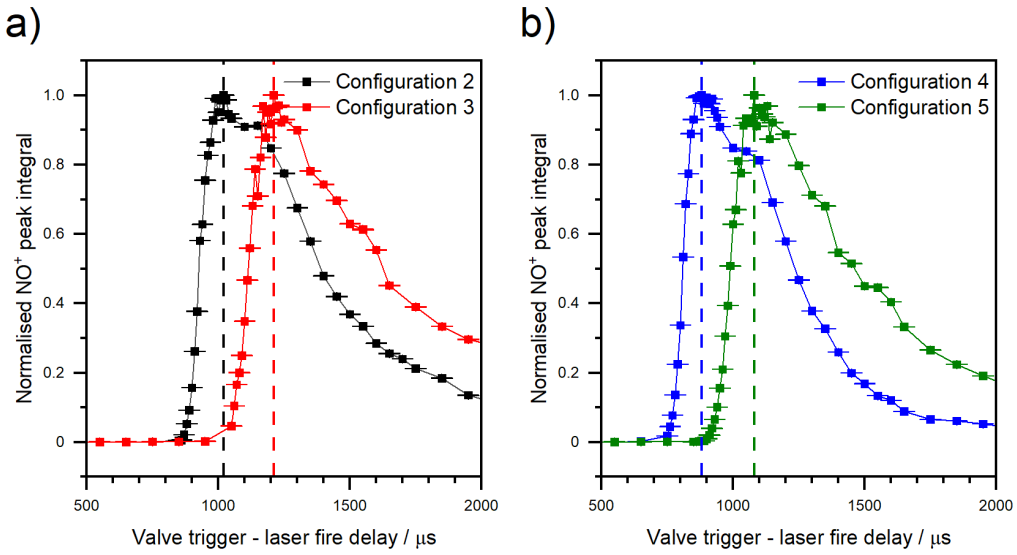

Figure 6.19: Normalised NO^+ peak integrals as a function of valve trigger - ionisation laser fire delay for configurations 2-5. **a)**: the two curves represent the gas flow through the large cluster block, without (black) and with (red) the 2 mm diameter nozzle. **b)**: the two curves represent the gas flow through the large cluster block, without (blue) and with (green) the 2 mm diameter nozzle.

---

between each configuration, for the same reason that was used to explain the offset seen in Figure 6.18. In panel **b)**, it appears that the signal drops away faster on the decaying edge for configuration 4 than it does for configuration 5. This would be consistent with the $\frac{A}{V}$ value for configuration 4 being approximately double that of configuration 5, and as shown in Equation 6.2, the effusion rate out of the block depends on this ratio.

To obtain a numerical value of the rate of decay of these experimental curves, an exponential fit was applied to each of the decaying edges. The exponential fit was defined as:

$$y = y_0 + A_1 \exp\left(-\frac{t}{\tau}\right), \tag{6.5}$$

where y is the intensity of the integrated NO^+ signal at time t, y_0 is the intensity of the integrated NO^+ signal intensity at time $t = 0$, A_1 is a scaling factor and τ is the decay time constant. The time constant τ is equal to $\frac{V}{A}\sqrt{\frac{2\pi m}{k_B T}}$. Table 6.3 presents the decay constants, both simulated and experimental, for each configuration. There is relatively good agreement between the experiment and the theory, implying that the model cap-

Table 6.3: Summary of experimental and theoretical exponential decay time constants, τ, for the different cluster source configurations. The theoretical values are for He gas, which is assumed to be at 300 K.

Configuration	**A/V**	**Experimental τ/µs**	**Simulated τ/µs**
2	14.44	320.7 ± 15.0	219.8
3	7.73	424.6 ± 52.8	410.7
4	24.07	234.3 ± 6.9	234.3
5	11.85	323.2 ± 15	267.8
6	5.15	542.1 ± 46.6	616.0
7	3.56	836.9 ± 60.1	890.7
8	1.85	1201 ± 86.7	1715.4

tures the qualitative form of the signal produced.

Additional studies were also performed to examine the effect of increasing the backing pressure and gas pulse width. Figure 6.20 **a)** shows the integrated NO^+ peak area as a function of the valve trigger - laser fire delay across a range of backing pressures; this study was carried out using configuration 5. As the backing pressure increases, the gradient of the rising edge also increases, which appears to be in line with what was shown with Equation 6.1 as the effusion rate scales linearly with the backing pressure. The rising edge of each curve was fitted with a linear fit to determine its gradient, and the gradients are plotted as a function of pressure in Figure 6.20 **b)**. The red lines that are imposed on the data are for two different linear fits; one for the lower pressures (1-3 bar) and one for the higher pressures (3-5 bar). The gradient is greater for the linear fit for the larger backing pressures; it is unclear why this is the case.

In addition to conducting backing pressure studies, the effect of increasing the gas pulse width was investigated using the in-house valve driver box. Figure 6.21 **a)** shows the integrated NO^+ peak area as a function of the valve trigger - laser fire delay for three different pulse widths of the gas. As the pulse width of the gas increases from 240 to 360 µs, the widths of the curves in panel **a)** also increase. This is comparable to what was

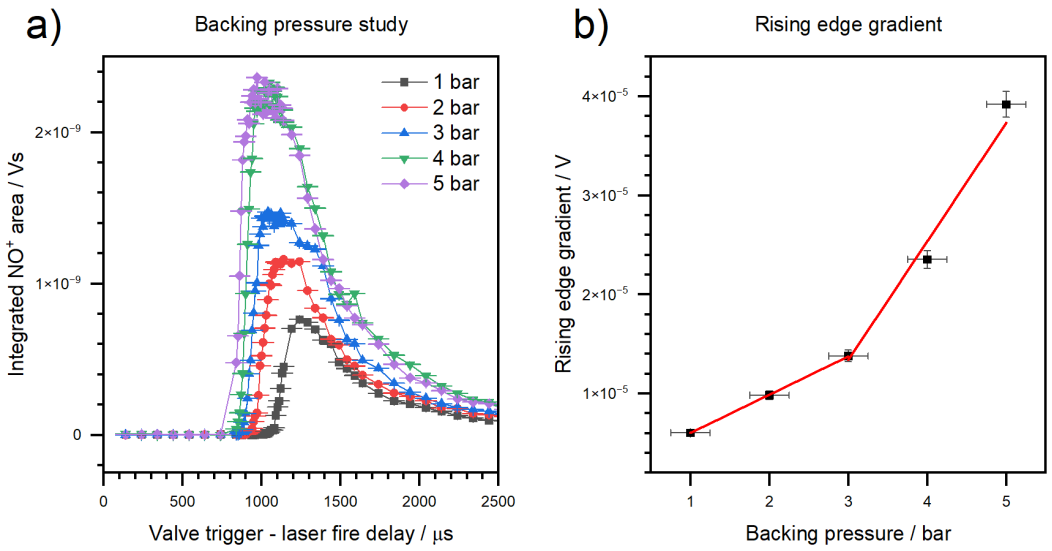

Figure 6.20: Backing pressure study on the shape of the NO^+ gas pulse. **a)**: NO^+ peak integral as a function of valve trigger - laser fire delay for different backing pressures (p_0 = 1-5 bar). **b)**: Gradient of the rising edge of the curves in panel **a)** against backing pressure. The red lines are produced from linear fits for the data points between 1-3 bar, and also between 3-5 bar.

---

shown in Figures 6.15 and 6.17. For the 240 µs curve, once the signal reaches its maximum, it begins to decay away. For the 300 µs and 360 µs curves, the NO^+ signal appears to plateau for approximately 300 µs and 500 µs, respectively. On first inspection, each of these curves appears to have rising and decaying edges that have the same gradient. Panel **b)** shows the natural log of the ion signal of the decaying edge for the three pulse widths (the colours between the two panels represent the same gas pulse width). This is done to show that the gradient of the decaying edge for each of these curves should be the same, given that the pulse width does not affect the rate of effusion. Each of the curves are, to a first approximation, parallel to each other, with their intercepts being defined by the backing pressure. Furthermore, the rising edge for each of these curves appears to be similar. By applying the same fitting techniques defined above, the gradient of the rising edge and the decay time constants for the decaying edge were extracted, as shown in Table 6.4. The experimental decay constants for each curve are within the errors of each other, which supports the idea that the decay constants should not vary with input gas-pulse width.

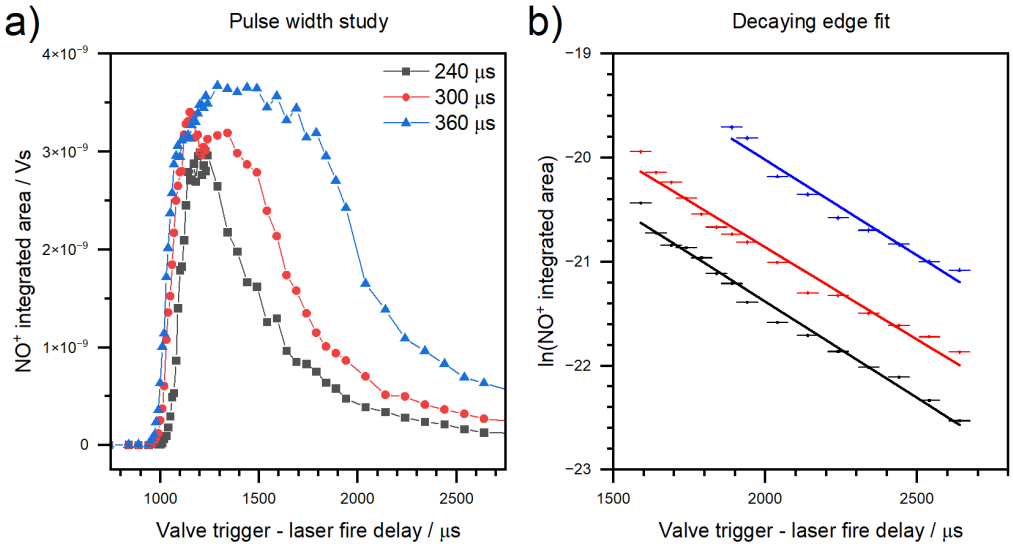

Figure 6.21: Gas pulse width study on the shape of the NO^+ gas pulse. **a)**: NO^+ peak integral as a function of valve trigger - laser fire delay for different gas pulse widths (240-360 µs) using the in-house valve driver box. **b)**: natural log of the NO^+ integrated area on the decaying edge of the curves in panel **a)** against valve trigger - laser fire delay. The three lines, colours corresponding the colours of the curves in panel **a)**, are parallel with each other, showing the gas pulse width has no effect of the rate of effusion out of the block.

To conclude this section, the NO ionisation studies provided useful information about how changing the source conditions would affect the gas pulse shape. The simulation work was able to show that the configuration of the source block played a major role; with the length of the block affecting the maximum pressure that could be achieved within the source and the size of the nozzle restriction affecting the rate at which the steady-state pressure was reached. The source configuration also affected the rate the gas flowed out of the source block and towards the extraction optics. The experimental studies performed by ionising NO^+ across a range of valve trigger - laser fire delays were able to replicate the general behaviour observed from the simulations; namely, the fast rising edge as the gas enters the block, the plateau when the steady-state conditions are achieved, and an exponential decay in ion signal once the valve is closed. Additionally, with the tail of the gas pulse extending for a longer time as the $\frac{A}{V}$ ratio decreases.

The role of the input gas pulse from the carrier gas valve was also investigated, with

Table 6.4: Summary of the rising edge gradient and the exponential decay time constants, τ, for the different input gas pulse widths, using configuration 5 (small source block, large nozzle).

Gas pulse width / µs	**Rising edge gradient / V**	**Experimental τ/µs**
240	$(2.73 \pm 0.14) \times 10^{-5}$	347.2 ± 28.1
300	$(2.45 \pm 0.14) \times 10^{-5}$	323.2 ± 15.0
360	$(3.00 \pm 0.11) \times 10^{-5}$	340.7 ± 21.8

the increase in the input gas pulse width causing the molecular beam's width to also increase, and a plateau also emerges. In general, there is good qualitative agreement between theory and experiment, which provides confidence in the predicted pressure profiles within the clustering channel. The conditions and timings determined from these studies were then used to optimise the experimental setup before the search for metal clusters began.

6.5 Production of Metal Clusters

6.5.1 First Evidence of Metal Atom Signal

The next step was to see whether any neutral metal atoms or clusters would be produced within the source when the ablation laser was turned on. Before doing this, the offset flange and ToF chamber were reattached to the experiment, and an MCP detector was added at the top of the chamber. A tantalum target was added onto the mounting rod, and the 355 nm laser was used to ionise any neutral metal species that were produced. Figure 6.22 shows the mass spectra recorded on the vertical MCP when the 532 nm ablation laser was turned off (panel **a)**) and on (panel **b)**). The gas mixture used was 2% NO in He, hence the appearance of the NO^+ peak in the ablation laser-off mass spectrum. In panel **b)**, there are several new peaks, including Ta^+, TaO^+, as well as a peak at 90.57 amu which corresponds to the doubly charged cation, Ta^{2+}. The second ionisation energy of Ta is 16.17 eV,[387] which means between 4-5 355 nm photons (3.56 eV) are required to remove an electron from a Ta^+ ion. The NO^+ peak is the sharpest in each of these spectra, as the voltages for the extraction optics had been optimised for it, meaning the other peaks are much broader. The oxide peak could have been produced from a surface

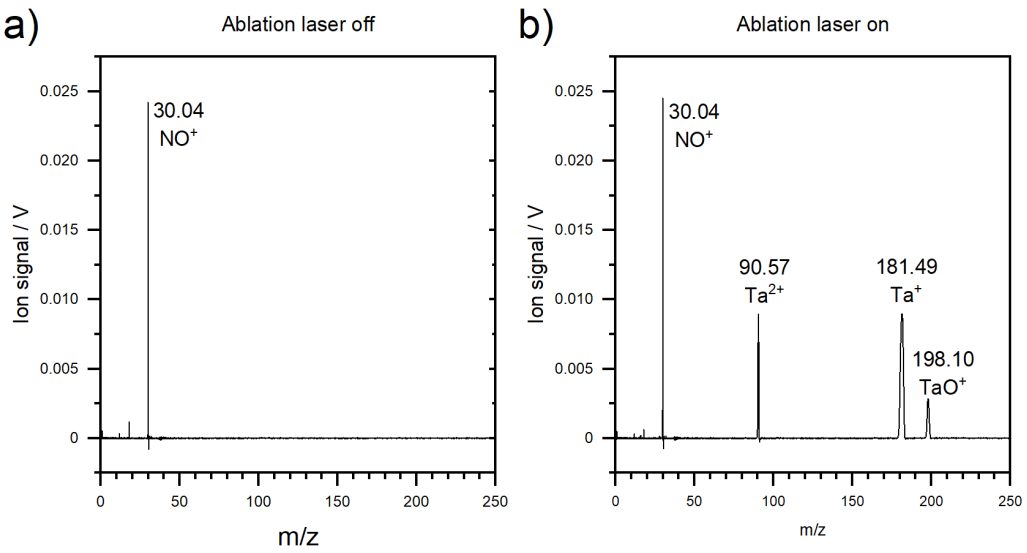

Figure 6.22: Mass spectra recorded with the source ablation laser turned off (panel **a)**) and on (panel **b)**), with the 355 nm laser on. The target in the source was tantalum, and the gas mixture was 2% NO in He at 5 bar backing pressure. In panel **b)**, new peaks for Ta^+ and TaO^+ emerge, along with a peak for the doubly charge Ta cation, Ta^{2+}.

oxide layer on the metal target, or it could have been produced by Ta^+ reacting with nitric oxide in the molecular beam.

6.5.2 Production of Neutral Au Clusters

Given that one of the systems of interest for the Mackenzie Group is Au_{10}^+, it was decided that the Ta metal target should be replaced with Au. Following the change, and the experimental conditions being optimised, a mass spectrum was recorded following the Au neutrals being ionised by the 355 nm laser. Figure 6.23 shows the mass spectrum recorded for m/z between 10 and 2500 amu using a He gas mixture at 5 bar backing pressure. Here, the mass spectrum contains multiple peaks that correspond to Au_n^+ clusters that have been generated by the ionisation laser. The most intense features are the peak for Au^+, with the intensity of the signal decreasing for Au_2^+ and Au_3^+. The inset of Figure 6.23 shows the zoomed-in mass spectrum between 600 and 2500. This shows Au clusters ranging from Au_4^+ to Au_{12}^+, with the intensity of the ion signal showing an odd-even alternation. This is because the odd numbered clusters have open shell electronic configurations, meaning they will have lower IPs than the Au clusters with even

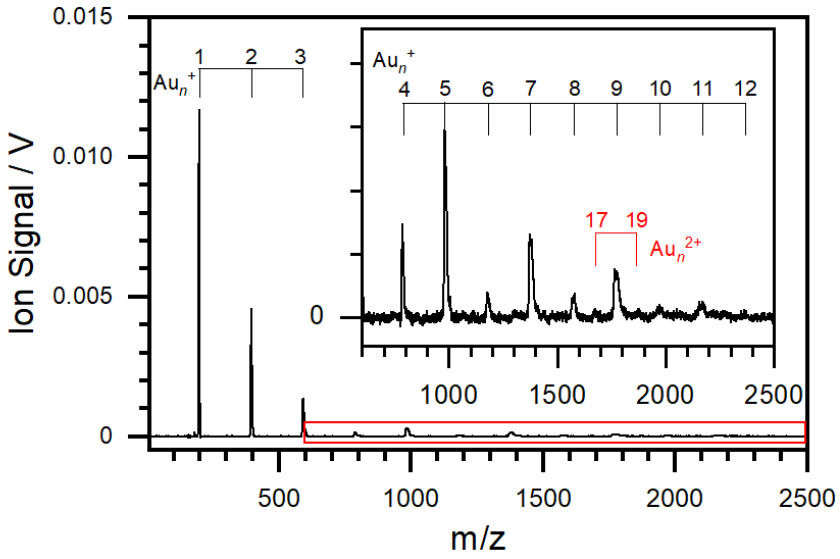

Figure 6.23: Mass spectrum of neutral Au clusters, Au_n, following multiple photon ionisation using the 355 nm laser. The most intense features are for the smallest clusters, $n = 1 - 3$, with larger clusters being shown in the inset (corresponding to the red box). An even-odd alternation is observed in the ion signal intensity from $n = 4$ onwards. Small features for doubly charged Au_n^{2+} cluster as shown for $n = 17$ and $n = 19$.

---

numbers of atoms. In addition to mass spectral peaks that correspond to clusters with integer numbers of atoms, there appear to be some very weak features midway between the peaks for Au_8^+ and Au_9^+, as well as for Au_9^+ and Au_{10}^+ (highlighted by the red labels). These appear to be larger doubly charged clusters, Au_{17}^{2+} and Au_{19}^{2+}, respectively.[388, 389] Only doubly charged clusters are seen for odd numbered clusters, since even numbered clusters would be obscured by the signal of singly charged clusters.

Studies were performed to investigate the conditions required to optimise signal intensity for the larger neutral clusters. To start with, changes were made to the gas mixture to see whether the addition of a gas with heavier molecules would promote clustering, and the heavier molecules would be able to promote more efficient collisional cooling. Figure 6.24 shows the mass spectra recorded using different gas mixtures (black:pure He, red: 5% N_2 in He) at a backing pressure of 5 bar. As can be seen, the signal strength increases when N_2 is used in the He mixture, with all the peaks increasing in intensity. The weaker doubly charged species also grow in intensity, but they are still very weak compared to

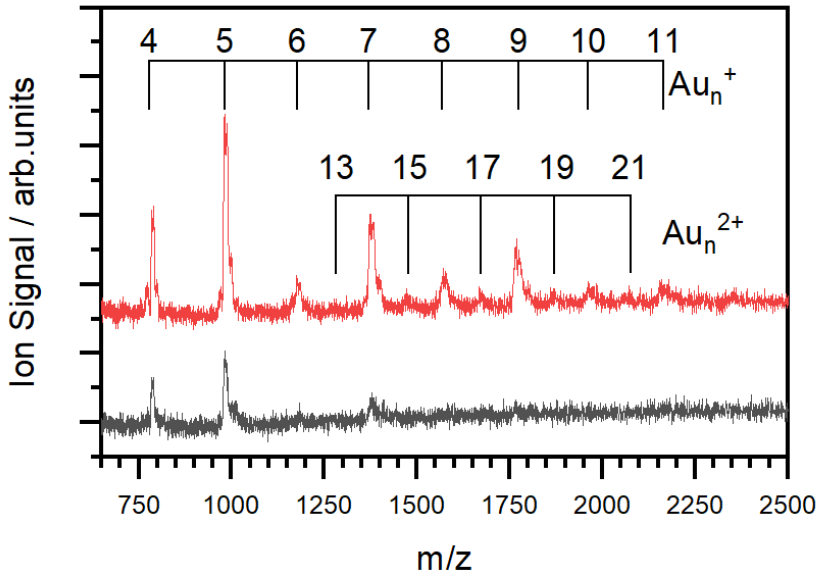

Figure 6.24: Mass spectrum of neutral Au clusters, Au_n ($n = 4 - 11$) after they have been ionised using the 355 nm laser using two different carrier gas mixture (black: pure He, red: 5% N_2 in He). The cluster sizes are labelled, along with small features for the doubly charged clusters, Au_n^{2+}.

---

the singly charged species. From this study, it appears that the use of a heavier gas can assist in the clustering of the clusters.

Following the study with the different gas mixtures, a backing pressure study was completed, this time using the pure He backing gas. This was done because the maximum pressure that could be achieved using the gas mixture was lower than that for pure He. Multiple 1000 shot averaged mass spectra were recorded across a range of backing pressures (1-9 bar, step size of 2 bar). The integrated area was recorded for the peaks of each of the clusters generated in the ToF spectrum, before it was plotted as a function of backing pressure.

Figure 6.25 shows the integrated ion signal as a function of the backing pressure for Au_n ($n = 1 - 7$). For 3 bar and below, the amount of signal generated for each of the clusters was close to zero. The ion signal increases as the backing pressure is increased, with a significant jump in the ion signal when the pressure was increased from 7 bar to 9 bar. The inset shows the trend line for the largest clusters, Au_{4-7}. The same trend is repeated,

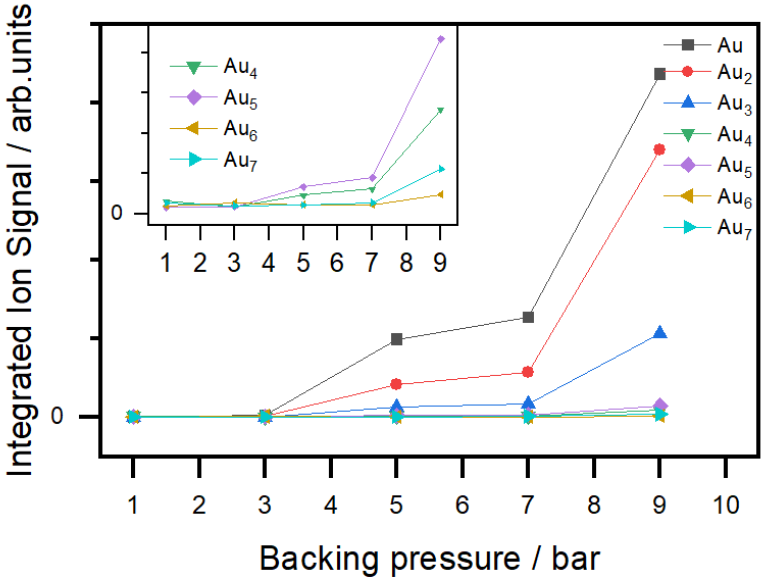

Figure 6.25: Integrated ion signal for different Au cluster sizes ($n = 1-7$) as a function of backing pressure. From 3 bar onwards, the ion signal for all sizes increases as a function of backing pressure. The most intense ion signals are for the smallest cluster sizes, with the clusters with odd numbers of atoms being more intense from $n = 4$ onwards.

with the signal increasing with increasing backing pressure. As shown in Figures 6.23 and 6.24, the ion signal for the clusters with an odd number of atoms is greater than for the clusters with an even number of atoms. Furthermore, the largest clusters could only be observed when the backing pressure was set at 9 bar; close to the maximum that the regulator on the gas manifold used to control the backing pressure could achieve (10 bar).

The intense signal of the smallest clusters, Au_{1-3}, compared to the larger clusters raised questions of whether fragmentation of the larger clusters was happening. The Au-Au BDE in the Au_2^+ dimer has been measured to be 2.2 eV,[390] while the ionisation potential for Au and Au_2 has been measured as 9.22 eV[391] and 9.16 eV,[392] respectively. That means fragmentation will require less energy (*i.e.* fewer photons from the 355 nm laser than ionisation. One way of testing this was to measure the integrated ion signal of the Au monomer and see how it varied as a function of the ionisation laser pulse energy. For an n-photon process, the ionisation signal, S, scales with the laser intensity approximately as:[360]

$$S \propto I^n. \tag{6.6}$$

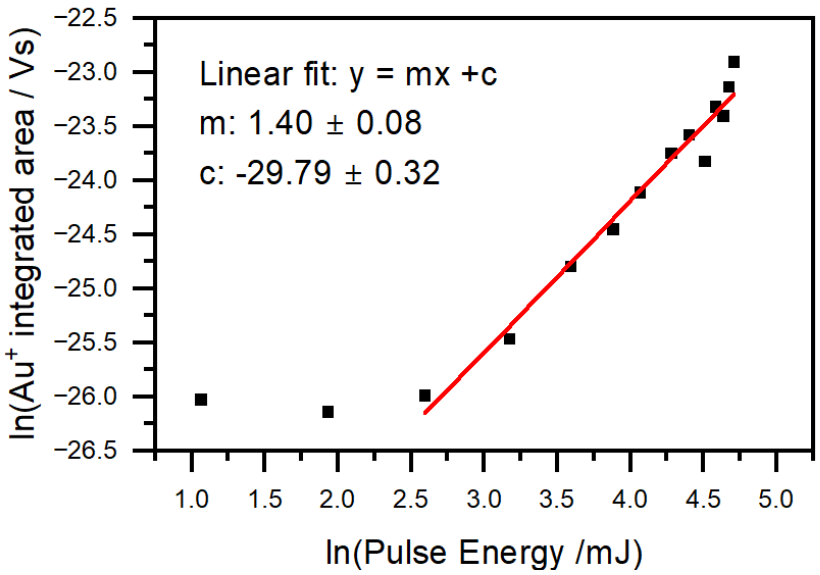

Figure 6.26: Ionisation laser pulse energy study. The natural log of the integrated Au^+ signal is plotted against the natural log of the pulse energy. A linear fit is added in order to determine the number of photons involved in the ionisation, with a gradient of 1.40 ± 0.08.

By taking the natural log of the two sides, we have the following equation:

$$\ln S = n \ln I + \text{constant}. \tag{6.7}$$

By plotting the natural log of the integrated ion signal against the natural log of the pulse energy, we can apply a linear fit to the data to estimate the number of photons involved in the ionisation process by measuring the gradient. Figure 6.26 shows the natural log of the Au^+ integrated area as a function of the natural log of the pulse energy. The Au^+ signal was very weak for the lower pulse energies, with an insufficient photon flux to ionise the neutral atom. The linear fit is therefore applied in the region where the ion signal increases. The linear fit gradient is equal to 1.40 ± 0.08, implying that the number of photons involved in the process was between one and two. This would suggest that fragmentation could be taking place, as at least three photons are required to ionise the cluster, and the gradient is lower than that.

The neutral ion signal so far was measured on the MCP directly above the reflectron. The next step was to direct the ionise onto the offset MCP to test that the reflectron

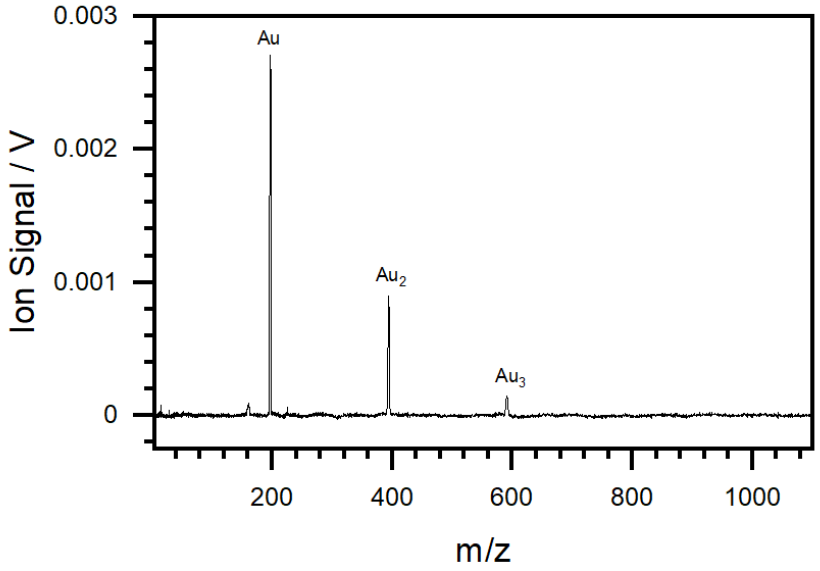

Figure 6.27: Mass spectrum recorded for the neutral Au_n clusters ionised with the 355 nm laser, measured on the offset MCP. The spectrum was recorded using a pure He gas mixture with 9 bar backing pressure.

works. Figure 6.27 shows the mass spectrum recorded for the three smallest Au clusters, Au_{1-3}, on the offset MCP. The spectrum was recorded using a pure He gas mixture with a backing pressure of 9 bar. The peaks within this spectrum are well resolved, but the ion signal is weaker than it was on the vertical MCP. It also appears that there are no peaks for clusters larger than $n = 3$. The ion optics do not appear to be doing well in reflecting a large portion of the ion optics onto the offset MCP. However, it does seem to temporally focus those that do reach the detector relatively well. More work is required to improve this transmission efficiency, and to ensure that more of the larger clusters are also detected. This may require a component such as an einzel lens positioned after the WM lens to better focus the ions onto the MCP detectors.

6.5.3 Production of Cationic Au Clusters

Once an issue with the Kapton wiring not delivering the pulsed voltage to the WM electrodes was resolved by insulating the wires using PEEK spacers, mass spectra were recorded of the cationic clusters produced directly from the source. Figure 6.28 shows a mass spectrum recorded on the vertical MCP directly above the reflectron using pure He at a backing pressure of 9 bar. Within the mass spectrum, there is strong feature

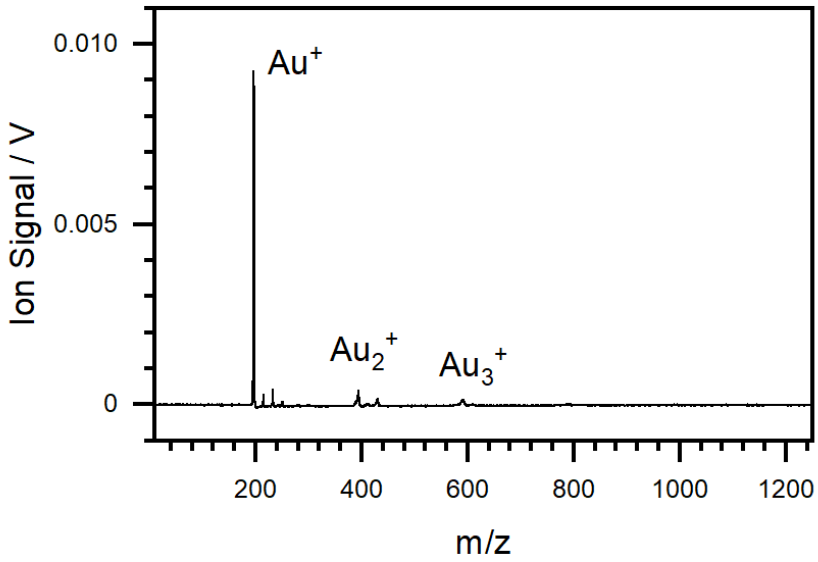

Figure 6.28: Mass spectrum of the cationic Au clusters, recorded on the MCP at the top of the ToF chamber. The clusters were generated in a pure He gas mixture with a backing pressure of 9 bar. Additional peaks arise from H_2O contamination.

for the Au cation, with smaller peaks for the cationic Au dimer and trimer. There are also small features appearing that are due to water contamination within the experiment (possibly atmospheric water that was introduced when the extraction optics chamber was opened to allow the PEEK spacers to be installed). Finally, the cationic species that were produced from the source could be directly detected on the MCP at the top of the ToF chamber. Following that, work was done to try and produce larger clusters, such as by increasing the ablation laser pulse energy (∼7 mJ/pulse) to ablate more metal from the target, as well as by keeping the backing pressure high. Additionally, a preamplifier was added to enhance the ion signal and a 5000 shot average was applied to improve the signal-to-noise ratio.

Figure 6.29 shows the mass spectrum produced when conditions were optimised to produce and detect larger cationic Au clusters. Clusters ranging from Au_2^+ to Au_{18}^+ can be seen in this spectrum, but the signal-to-noise ratio is poorer than for the other spectrum for the cationic species. The width of the peaks in the ToF spectrum also appears to increase as the cluster size increases, suggesting that the voltages applied to the ion optics setup have not been optimised for these larger species. Furthermore, the clusters could

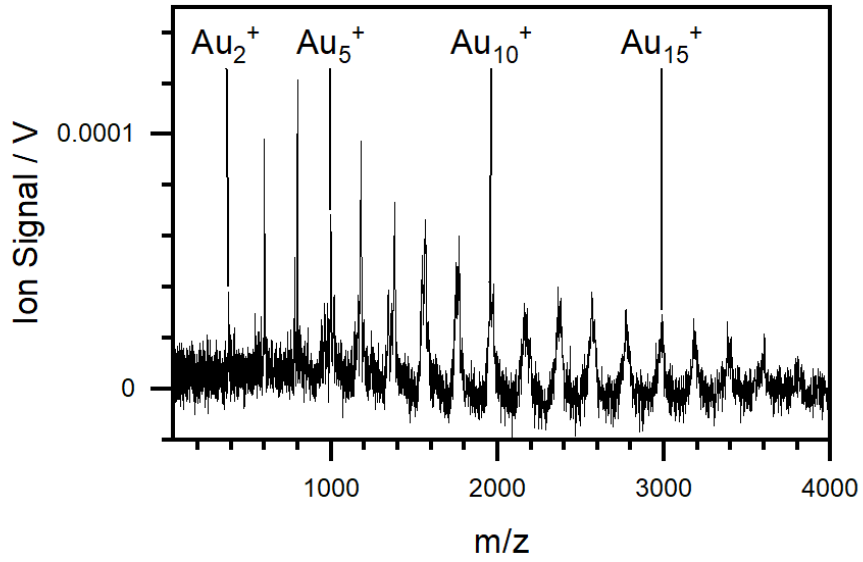

Figure 6.29: Mass spectrum of the cationic Au clusters, Au_n^+ $(n = 2 - 18)$, recorded on the MCP at the top of the ToF chamber. The clusters were generated in a pure He gas mixture with a backing pressure of 9 bar.

---

only be generated under harsh conditions, with the pressure in the source chamber being approximately 10^{-3} mbar; four orders of magnitude higher than it would be without the gas valve being turned on. However, this does provide evidence that cationic clusters can be generated and extracted using the ion optics onto the vertical MCP.

6.6 Conclusions and Future Work for Metal Cluster / Bimetallic Cluster Source

This chapter presents work that has been completed to design, build, and test a new bimetallic cluster source. An experimental setup has been built, which comprises the new cluster source and a custom built time-of-flight mass spectrometer. The components within the ToF mass spectrometer have been simulated using a simple SIMION workbench to examine how well they can direct the ions produced by the source. The extraction optics and reflectron do appear to direct the ions onto the MCP detectors; both at the top of the ToF chamber and also on the offset flange. The source configuration experiments, conducted by ionising NO within the WM lens, have been able to examine the shape of the gas pulse. This, in conjunction with the simulations of the

kinetic model, has allowed predictions to be made about how quickly the pressure at the cluster source increases and decays when the pulsed valve opens and closes. This in turn provided useful information about the timings, pressures, and voltages required to produce and extract the clusters. Neutral and cationic Au clusters have been produced up to Au_{18}, with a clear even-odd alternation in the ion signal being observed in neutral species following their ionisation by the 355 nm laser. These clusters have been produced using high backing pressures and have been directed onto the MCP detectors at the top of the ToF chamber, as well as onto the offset MCP in the case of the neutral species.

Due to time restraints and other difficulties that arose within the experimental setup, such as electronic and vacuum equipment failures, this thesis does not contain work that investigates the role of cryogenically cooling the cluster source nozzle. Additionally, no bimetallic clusters were generated, apart from some species that arose when the edge of the ablation laser pinhole channel were ablated, causing the elements within the stainless steel (C, H, Cr, Fe) to be released and aggregate in the source. In addition, the reactant gas valve was not used, so the clusters shown here have not been coated with atoms or molecules of interest. There are still a number of studies that need to be completed before this source can be transferred across the different experimental setups.

Several changes could be made to the source block to promote more clustering. For example, because the laser ablation requires multiple pinholes through the clustering channel, it means that gas can flow out of them. As the diameter of the nozzle decreases, the cross section of these holes contributes a greater part of the total cross section, which means that the carrier gas and the clusters entrained within it will likely exit through these holes. As a result, the metal clusters may not be directed towards the extraction optics. Additionally, the pressure within the cluster channel could be higher if the number of exit holes were reduced. This could be fixed by adding small glass windows to the laser inlet on the block in order to prevent gas leaking out. Alternatively, the targets could be placed in the channel, as long as there is some way to seal the gap that the target will have to enter through. Other valves could be used, which would produce a shorter, more intense gas pulse to maximise the number of collisions within the cluster source. For extraction optics, a larger, circular shielding plate could be introduced to minimise

the likelihood of stray fields deflecting clusters away from the optics. Einzel lenses could also be installed to focus the ions entering and exiting the WM lens in order to capture as many of the charged clusters as possible and direct them onto the MCP detectors.

Chapter 7

Conclusions and Future Work

Gas-phase metal clusters can possess interesting size- and composition dependent properties and can be used as tractable model systems for understanding catalytic processes. The work presented in this thesis has studied cluster systems that vary in size and composition; from generating and studying ion-ligand complexes that contain a single metal atom (Chapters 3 and 4), to examining larger metal clusters; both by using existing instrumentation at the HFML-FELIX facility (Chapter 5) and by developing a new experiment to generate them within the laboratory in Oxford (Chapter 6). The conclusions here describe the key findings from each part and the additional studies that could be completed to build on the work presented in this thesis.

7.1 Part A: Infrared Studies on Metal Ion–Ligand Complexes

Gas-phase Group 9 (Co, Rh, Ir) cationic nitrosyl complexes, $[M(NO)_n]^+$, have been investigated using IRPD spectroscopy. The experimental spectra of the Co and Ir complexes ($n = 3 - 5$) are similar, and the energetically low-lying calculated isomers for these met-

als exhibit similar structures. The Rh spectra are qualitatively different from those of the other two metals; with a clear redshift being observed as the size of the complex increased. By comparison of the experimental results with simulated spectra from the calculated structures, it was determined that the NO ligands bind to the metal centres both linearly and non-linearly; with the Rh complexes having a greater propensity to bind the ligands non-linearly. As was observed in previous studies on gas-phase nitrosyl complexes,[301–303], there is clear evidence of NO dimer once the first coordination shell has been filled; and dimer formation occurs for $n \geq 5$. This is displayed through the emergence of satellite bands in the IR action spectrum, including a strongly red-shifted band (≤ 1700 cm^{-1}). The mode assignment is assisted by the differences in the action spectra for different fragmentation channels.

In addition to the Group 9 nitrosyl complexes, complementary studies were performed on gas-phase cationic platinum and platinum oxide complexes, $[PtO_x(NO)_n]^+$. For the $[Pt(NO)_n]^+$ species, the spectral features red-shifted as the number of ligands binding to the metal centre increased from $n = 3$ to $n = 6$; similar to what was observed for the $[Rh(NO)_n]^+$ complexes in Chapter 3. There is evidence that the inner shell can accommodate up to six NO ligands in an octahedral structure before NO dimer formation begins, with new satellite features appearing to illustrate the formation of NO dimer moieties that only appear from $n = 7$ onwards. This is a greater number of ligands binding in the first coordination shell than other gas-phase metal nitrosyl complexes that have been investigated in comparable IRPD studies. The $[PtO(NO)_n]^+$ spectra possess an intense feature to the blue of the free NO stretching frequency, which is indicative of the formation of an N_2O_3 moiety. The DFT calculations for the oxygen-rich species support this assignment, with good agreement between the experimental spectrum and the calculated energetically low-lying structures that included an N_2O_3 moiety. The formation of these $[Pt(NO_2)(NO)_{n-3}]^+$ complexes from $[Pt(NO)_n]^+$ with an N_2O molecule being lost was shown to be energetically viable, although the kinetics of this reaction have not been investigated. The structures of the $[Pt(NO_2)(NO)_n]^+$ complexes also follow the same pattern as seen for $[Pt(NO)_n]^+$, with up to six ligands binding in the first coordination shell.

One of the most notable differences across these studies was the spectral red-shift observed for the Rh and Pt species, but not in the Co and Ir. Further studies could focus on gas-phase ion-molecule complexes using other Group 10 elements (Ni, Pd) to determine whether the red-shift is dependent on the electronic configuration of the metal centre and whether this has an effect on the propensity of NO ligands to bind either linearly or non-linearly. Studies are now being conducted to investigate the role of adding an additional gas to form mixed ligand complexes,[205, 306] for example studies are ongoing to investigate the role of cooperative and competitive binding in $[Pt(CO)_m(NO)_n]^+$ complexes. The spectra and computed structures for these mixed ligand complexes will be compared with those for the species with one type of ligand (*i.e.* $[Pt(CO)_n]^+$, $[Pt(NO)_n]^+$) to examine which structural arrangements are preferred.[293] Furthermore, kinetic studies could be conducted on the $[Pt(NO)_n]^+$ species to investigate whether $[PtO(NO)_n]^+$ is produced *via* the loss of an N_2O molecule.

7.2 Part B: Infrared Free-Electron Laser Studies on Metal Clusters

Multiple photon-induced ionisation studies have been completed on neutral $Ta_nO_{x=0-2}$ clusters using the free-electron laser, FELICE. Multiple photon-induced thermionic emission was observed in the IR enhancement spectra, with the intensity and onset frequencies of the emission reflecting the ionisation potential of the neutral clusters.[328] For the tantalum oxide clusters, spectral features in the range 650-750 cm^{-1} are assigned to the symmetric oxide stretches.[346] There is good agreement between the energetically low-lying structures calculated using DFT, with the oxygen atom being shown to bind in an μ_2 bridging motif along the edges of the Ta clusters. Evidence of IR-induced fragmentation of clusters has also been discussed when the Ta-O stretching vibration was excited using FELICE, with $Ta_{n=7,13}$ being common fragmentation products; which is in agreement with previous literature that showed that these sizes correspond to 'magic number' cluster sizes with increased stability.[336, 362]

Future studies could be conducted to thoroughly investigate the fragmentation dynamics of these clusters when they are irradiated with IR light. The calculations for the cationic

Ta clusters with nitrogen oxides have been completed, but because of the experimental setup at the HFML-FELIX facility, it was not possible to separate the neutral and cationic clusters. If an experiment used a quadrupole bender to separate the cationic clusters from the molecular beam and direct them towards the time-of-flight mass spectrometer, it would be possible to perform the IR-(M)PD study on them, and then see whether they dissociatively bind NO and N_2O. If nitrogen oxides were shown to dissociatively bind to cationic clusters, it would also be interesting to perform collision experiments with small molecules, such as CH_4 or CO, to see whether these molecules are oxidised.

7.3 Part C: In-House Development Work

A new laser ablation source designed to produce bimetallic clusters has been built and tested. Following simulations to predict the optimum conditions required to direct the ions onto the detectors in the custom built time-of-flight mass spectrometer, and calculations to determine the shape of the gas pulse generated by the source, ionisation studies were conducted to experimentally verify this. By non-resonantly ionising nitric oxide, the gas pulse shape could be mapped out for different source configurations and conditions in order to determine the optimum conditions required to extract the clusters produced from the source. Mass spectra for neutral and cationic gold clusters, $Au_n^{0/+}$ have been recorded, with evidence that clusters with sizes up to $n = 18$ are generated.

Further work needs to be completed to optimise the cluster ion signal, such as by adding additional ion optics to better focus the ions produced by the source and extracted using the Wiley-McLaren extraction optics. The next steps to characterise this source will include using cryogenic cooling to see how well it promotes clustering. Additionally, a second laser pulse needs to be directed onto the other target to examine how well it generates bimetallic clusters, and whether changing the order of them will affect the composition. Additional gases should also be added *via* the secondary valve to examine how well it is able to coat the clusters and whether new cluster compositions can be produced. Once the characterisation studies are completed, the bimetallic cluster source will be used to perform IRPD and collisional studies with small molecules. The metal clusters and cluster-ligand complexes will be model systems to replicate catalytic surfaces

and will allow comparisons to be made with the bulk material.

In summary, infrared spectroscopic studies have been completed across a range of metal cluster and metal ion-ligand complexes with the assistance of quantum chemical calculations. Specific structural motifs have been identified in the metal nitrosyl complexes, such as the $(NO)_2$ dimer and N_2O_3 moiety, and the bridging oxide motif in the neutral tantalum oxide clusters. A new experimental setup has been built to study the properties of the new bimetallic source, which in time will open new avenues for experimental exploration; with the ability to study the effect of size and composition being more readily accessible within the group.

Bibliography

[1] S. M. Lang and T. M. Bernhardt, *Phys. Chem. Chem. Phys.*, 2012, **14**, 9255–9269.

[2] K. J. Laidler, *Chemical Kinetics*, HarperCollins, New York, 3rd edn., 1987.

[3] G. Ertl, *Angew. Chem., Int. Ed.*, 2008, **47**, 3524–3535.

[4] P. G. Levi and J. M. Cullen, *Environ. Sci. Technol.*, 2018, **52**, 1725–1734.

[5] T. Degnan, *Focus Catal.*, 2019, **2019**, 1–2.

[6] X. Hu and A. C. K. Yip, *Front. Catal.*, 2021, **1**, 1–3.

[7] R. A. Van Santen, *Modern Heterogeneous Catalysis: An Introduction*, John Wiley & Sons, 2017.

[8] J. Nørskov, F. Studt, F. Abild-Pedersen and T. Bligaard, in *Fundamental Concepts in Heterogeneous Catalysis*, John Wiley & Sons, Ltd, 2014, ch. 9, pp. 138–149.

[9] P. Sánchez-López, Y. Kotolevich, R. I. Yocupicio-Gaxiola, J. Antúnez-García, R. K. Chowdari, V. Petranovskii and S. Fuentes-Moyado, *Front. Chem.*, 2021, **9**, 716745.

[10] M. D. Marcinkowski, M. T. Darby, J. Liu, J. M. Wimble, F. R. Lucci, S. Lee, A. Michaelides, M. Flytzani-Stephanopoulos, M. Stamatakis and E. C. H. Sykes, *Nat. Chem.*, 2018, **10**, 325–332.

[11] C. K. Narula, L. F. Allard, G. M. Stocks and M. Moses-DeBusk, *Sci. Rep.*, 2014, **4**, 7238.

[12] J. Humphreys and S. Tao, *Johnson Matthey Technol. Rev.*, 2024, **68**, 280–292.

[13] H. Liu, *Chin. J. Catal.*, 2014, **35**, 1619–1640.

[14] M. E. Dry, *Catal. Today*, 2002, **71**, 227–241.

[15] B. H. Davis, *Top. Catal.*, 2005, **32**, 143–168.

[16] R. A. Copeland, *Enzymes: A Practical Introduction to Structure, Mechanism, and Data Analysis*, 2000, 146–150.

[17] G. W. Parshall, *Science*, 1980, **208**, 1221–1224.

[18] U. Wietelmann and J. Klett, *Z. Anorg. Allg. Chem.*, 2018, **644**, 194–204.

[19] J. A. Osborn, F. H. Jardine, J. F. Young and G. Wilkinson, *J. Chem. Soc. A*, 1966, 1711–1732.

[20] A. Haynes, in *Advances in Catalysis*, Academic Press, 2010, vol. 53, ch. 1, pp. 1–45.

[21] M. C. Román-Martínez and C. Salinas-Martínez de Lecea, in *New and Future Developments in Catalysis*, Elsevier, Amsterdam, 2013, ch. 3, p. 55–78.

[22] Z. Luo, J. Castleman and S. N. Khanna, *Chem. Rev.*, 2016, **116**, 14456–14492.

[23] Y. Luo and Y. Wu, *Nanomaterials (Basel)*, 2023, **13**, 1116.

[24] F. Jensen, *Introduction to Computational Chemistry*, John Wiley & Sons, 2017.

[25] H. Schwarz, *Isr. J. Chem.*, 2014, **54**, 1413–1431.

[26] P. Armentrout, *Annu. Rev. Phys. Chem.*, 2001, **52**, 423–461.

[27] A. W. Castleman and R. G. Keesee, *Science*, 1988, **241**, 36–42.

[28] R. Pal, A. Poddar and P. K. Chattaraj, *Front. Chem*, 2021, **9**, 730548.

[29] V. Hermann, B. D. Kay and A. W. Castleman, *Chem. Phys.*, 1982, **72**, 185–200.

[30] D. K. Böhme and H. Schwarz, *Angew. Chem., Int. Ed.*, 2005, **44**, 2336–2354.

[31] H. Gholipour-Ranjbar, Deepika, P. Jena and J. Laskin, *Commun. Chem.*, 2022, **5**, 130.

[32] C. Comby-Zerbino, X. Dagany, F. Chirot, P. Dugourd and R. Antoine, *Mater. Adv.*, 2021, **2**, 4896–4913.

[33] R. A. J. O'Hair, *Int. J. Mass Spectrom.*, 2015, **377**, 121–129.

[34] K. Koyasu and T. Tsukuda, *J. Chem. Phys.*, 2021, **154**, e202408335.

[35] P. Weis, *Int. J. Mass Spectrom.*, 2005, **245**, 1–13.

[36] R. A. J. O'Hair and G. N. Khairallah, *J. Cluster Sci.*, 2004, **15**, 331–363.

[37] J. M. Bakker, C. J. Owen, S. W. Nooteboom, O. V. Lushchikova and P. B. Armentrout, *J. Mol. Spectrosc.*, 2021, **378**, 111472.

[38] O. W. Wheeler, M. Salem, A. Gao, J. M. Bakker and P. B. Armentrout, *J. Phys. Chem. A*, 2016, **120**, 6216–6227.

[39] G. E. Johnson, E. C. Tyo and A. W. Castleman, *Proc. Natl. Acad. Sci. U. S. A.*, 2008, **105**, 18108–18113.

[40] I. S. Parry, A. Kartouzian, S. M. Hamilton, O. P. Balaj, M. K. Beyer and S. R. Mackenzie, *Angew. Chem., Int. Ed.*, 2015, **54**, 1357–1360.

[41] A. Amrein, R. Simpson and P. Hackett, *J. Chem. Phys.*, 1991, **95**, 1781–1800.

[42] A. Fielicke, J. T. Lyon, M. Haertelt, G. Meijer, P. Claes, J. de Haeck and P. Lievens, *J. Chem. Phys.*, 2009, **131**, 171105.

[43] M. B. Knickelbein, S. Yang and S. J. Riley, *J. Chem. Phys.*, 1990, **93**, 94–104.

[44] E. J. Robbins, R. E. Leckenby and P. Willis, *Adv. Phys.*, 1967, **16**, 739–744.

[45] D. E. Powers, S. G. Hansen, M. Geusic, A. Puiu, J. Hopkins, T. Dietz, M. Duncan, P. Langridge-Smith and R. Smalley, *J. Phys. Chem.*, 1982, **86**, 2556–2560.

[46] S. Yang and M. B. Knickelbein, *J. Chem. Phys.*, 1990, **93**, 1533–1539.

[47] P. Ferrari, J. Vanbuel, E. Janssens and P. Lievens, *Acc. Chem. Res.*, 2018, **51**, 3174–3182.

[48] L. E. Gálvez-González, A. Posada-Amarillas and L. O. Paz-Borbón, *J. Phys. Chem. A*, 2021, **125**, 4294–4305.

[49] A. Nakajima, T. Kishi, T. Sugioka, Y. Sone and K. Kaya, *J. Phys. Chem.*, 1991, **95**, 6833–6835.

[50] A. Alvarez-Garcia, E. Flórez, A. Moreno and C. Jimenez-Orozco, *Mol. Catal.*, 2020, **484**, 110733.

[51] S. Nonose, Y. Sone and K. Kaya, *Z. Phys. D:At., Mol. Clusters*, 1991, **19**, 357–359.

[52] P. L. Rodríguez-Kessler, A. Muñoz-Castro, P. A. Alonso-Dávila, F. Aguilera-Granja and A. R. Rodríguez-Domínguez, *J. Alloys Compd.*, 2020, **845**, 155897.

[53] E. Janssens, G. Santambrogio, M. Brümmer, L. Wöste, P. Lievens, J. Sauer, G. Meijer and K. R. Asmis, *Phys. Rev. Lett.*, 2006, **96**, 233401.

[54] N. S. Khetrapal, T. Jian, G. V. Lopez, S. Pande, L.-S. Wang and X. C. Zeng, *J. Phys. Chem. C*, 2017, **121**, 18234–18243.

[55] Y. Sone, K. Hoshino, T. Naganuma, A. Nakajima and K. Kaya, *J. Phys. Chem.*, 1991, **95**, 6830–6832.

[56] W. A. de Heer, *Rev. Mod. Phys.*, 1993, **65**, 611–676.

[57] I. R. Dunkin, *Matrix-Isolation Techniques: A Practical Approach*, Oxford University Press, 1998.

[58] R. A. Larsen, S. K. Neoh and D. R. Herschbach, *Rev. Sci. Instrum.*, 1974, **45**, 1511–1516.

[59] D. Preuss, S. Pace and J. Gole, *J. Chem. Phys.*, 1979, **71**, 3553–3560.

[60] K. Sattler, J. Mühlbach and E. Recknagel, *Phys. Rev. Lett.*, 1980, **45**, 821–824.

[61] S. J. Riley, E. K. Parks, C. R. Mao, L. G. Pobo and S. Wexler, *J. Phys. Chem..*, 1982, **86**, 3911–3913.

[62] W. Knight, K. Clemenger, W. A. De Heer, W. A. Saunders, M. Chou and M. L. Cohen, *Phys. Rev. Lett.*, 1984, **52**, 2141.

[63] T. Martin, T. Bergmann, H. Göhlich and T. Lange, *J. Phys. Chem.*, 1991, **95**, 6421–6429.

[64] I. Goldby, B. Von Issendorff, L. Kuipers and R. Palmer, *Rev. Sci. Instrum.*, 1997, **68**, 3327–3334.

[65] J. Ho, K. M. Ervin and W. C. Lineberger, *J. Chem. Phys.*, 1990, **93**, 6987–7002.

[66] G. Ganteför, H. R. Siekmann, H. O. Lutz and K. H. Meiwes-Broer, *Chem. Phys. Lett.*, 1990, **165**, 293–296.

[67] C. Cha, G. Ganteför and W. Eberhardt, *Rev. Sci. Instrum.*, 1992, **63**, 5661–5666.

[68] S. Marc-Hermann, J. Jean-François, P. François and S. Wolf-Dieter, *J. Phys. D:Appl. Phys.*, 1998, **31**, 3177.

[69] S. Hirabayashi and M. Ichihashi, *J. Phys. Chem. A*, 2014, **118**, 1761–1768.

[70] T. Hanmura, M. Ichihashi, Y. Watanabe, N. Isomura and T. Kondow, *J. Phys. Chem. A*, 2007, **111**, 422–428.

[71] R. Keller, F. Nöhmayer, P. Spädtke and M. H. Schönenberg, *Vacuum*, 1984, **34**, 31–35.

[72] D. Ratschko, B. G. Zhou, D. Knolle and M. Gläser, *Nucl. Instrum. Methods Phys. Res., Sect. B*, 1996, **119**, 549–554.

[73] G. Bräuer, B. Szyszka, M. Vergöhl and R. Bandorf, *Vacuum*, 2010, **84**, 1354–1359.

[74] A. D. T. de Sá, V. T. Abrao Oiko, G. di Domenicantonio and V. Rodrigues, *J. Vac. Sci. Technol. B*, **32**, 061804.

[75] P. J. Kelly and R. D. Arnell, *Vacuum*, 2000, **56**, 159–172.

[76] Z. Luo, W. H. Woodward, J. C. Smith and A. W. Castleman, *Int. J. Mass Spectrom.*, 2012, **309**, 176–181.

[77] M. W. Thompson, J. S. Colligon, R. Smith, C. Xirouchaki and R. E. Palmer, *Philos. Trans. R. Soc., A*, 2004, **362**, 117–124.

[78] M. Yamashita and J. B. Fenn, *J. Phys. Chem.*, 1984, **88**, 4451–4459.

[79] P. Kebarle and U. H. Verkerk, *Mass Spectrom. Rev.*, 2009, **28**, 898–917.

[80] A. T. Blades, P. Jayaweera, M. G. Ikonomou and P. Kebarle, *Int. J. Mass Spectrom. Ion Processes*, 1990, **102**, 251–267.

[81] M. F. Bush, R. J. Saykally and E. R. Williams, *ChemPhysChem*, 2007, **8**, 2245–2253.

[82] J. T. O'Brien and E. R. Williams, *J. Phys. Chem. A*, 2008, **112**, 5893–5901.

[83] G. Hulthe, G. Stenhagen, O. Wennerström and C.-H. Ottosson, *J. Chromatogr. A*, 1997, **777**, 155–165.

[84] K. McQuinn, F. Hof and J. S. McIndoe, *Int. J. Mass Spectrom.*, 2009, **279**, 32–36.

[85] C. Hao, R. E. March, T. R. Croley, J. C. Smith and S. P. Rafferty, *J. Mass Spectrom.*, 2001, **36**, 79–96.

[86] T. G. Dietz, M. A. Duncan, D. E. Powers and R. E. Smalley, *J. Chem. Phys.*, 1981, **74**, 6511–6512.

[87] D. Powers, S. Hansen, M. Geusic, D. Michalopoulos and R. Smalley, *J. Chem. Phys.*, 1983, **78**, 2866–2881.

[88] L. Zheng, P. Brucat, C. Pettiette, S. Yang and R. Smalley, *J. Chem. Phys.*, 1985, **83**, 4273–4274.

[89] P. J. Brucat, L. Zheng, C. L. Pettiette, S. Yang and R. E. Smalley, *J. Chem. Phys.*, 1986, **84**, 3078–3088.

[90] V. Bondybey and J. English, *J. Chem. Phys.*, 1981, **74**, 6978–6979.

[91] S. Maruyama, L. R. Anderson and R. E. Smalley, *Rev. Sci. Instrum.*, 1990, **61**, 3686–3693.

[92] M. A. Duncan, *Rev. Sci. Instrum.*, 2012, **83**, 41101.

[93] J. Ready, *Effects of High-Power Laser Radiation*, Elsevier, 2012.

[94] J. C. Miller and R. F. Haglund, *Laser Ablation and Desorption*, Academic Press San Diego, 1998, vol. 30.

[95] A. Fridman, *Plasma Chemistry*, Cambridge University Press, 2008.

[96] J. Pilgrim and M. Duncan, *J. Am. Chem. Soc.*, 1993, **115**, 4395–4396.

[97] M. A. Duncan, *Annu. Rev. Phys. Chem.*, 1997, **48**, 69–93.

[98] W. Bouwen, P. Thoen, F. Vanhoutte, S. Bouckaert, F. Despa, H. Weidele, R. E. Silverans and P. Lievens, *Rev. Sci. Instrum.*, 2000, **71**, 54–58.

[99] P. Ferrari, J. Vanbuel, Y. Li, T.-W. Liao, E. Janssens and P. Lievens, in *The Double-Laser Ablation Source Approach*, 2017, p. 59–78.

[100] Y. Huttel, *Gas-phase Synthesis of Nanoparticles*, Wiley-VCH, Weinheim, Germany, 1st edn., 2017.

[101] K. S. Molek, T. D. Jaeger and M. A. Duncan, *J. Chem. Phys.*, 2005, **123**, year.

[102] O. F. Hagena, *Surf. Sci.*, 1981, **106**, 101–116.

[103] K. D. Sattler, *Handbook of Nanophysics: Clusters and Fullerenes*, CRC press, 2010.

[104] J. van der Tol and E. Janssens, *Phys. Rev. A*, 2020, **102**, 022806.

[105] I. N. Levine, *Quantum chemistry*, Allyn and Bacon, Boston, 1970.

[106] A. Kantrowitz and J. Grey, *Rev. Sci. Instrum.*, 1951, **22**, 328–332.

[107] D. H. Levy, *Annu. Rev. Phys. Chem.*, 1980, **31**, 197–225.

[108] J. M. Hayes, *Chem. Rev.*, 1987, **87**, 745–760.

[109] R. E. Smalley, L. Wharton and D. H. Levy, *Acc. Chem. Res.*, 1977, **10**, 139–145.

[110] J. A. Faust and J. E. House, *Physical Chemistry of Gas-Liquid Interfaces*, Elsevier, Amsterdam, Netherlands, 2018.

[111] J. Koperski and E. S. Fry, *J. Phys. B:At., Mol. Opt. Phys.*, 2006, **39**, S1125–S1150.

[112] S. Rampino, A. Gauzzi, M. Baldini, M. Bindi, E. Gilioli, S. Ginocchio, M. Rocca and S. Zannella, *IEEE Trans. Appl. Supercond.*, 2007, **17**, 3286–3289.

[113] O. F. Hagena, *Z. Phys. D:At., Mol. Clusters*, 1987, **4**, 291–299.

[114] G. Scoles, *Atomic and Molecular Beam Methods*, Oxford University Press, 1988.

[115] J. B. Anderson and J. B. Fenn, *The Physics of Fluids*, 1965, **8**, 780–787.

[116] R. T. Laaksonen, D. A. Goetsch, D. W. Owens, D. M. Poirier, F. Stepniak and J. H. Weaver, *Rev. Sci. Instrum.*, 1994, **65**, 2267–2275.

[117] M. Sun, D. T. Halfen, J. Min, B. Harris, D. J. Clouthier and L. M. Ziurys, *J. Chem. Phys.*, 2010, **133**, 174301.

[118] M. F. Jarrold, J. E. Bower and J. S. Kraus, *J. Chem. Phys.*, 1987, **86**, 3876–3885.

[119] N. X. Truong, M. Haertelt, B. K. A. Jaeger, S. Gewinner, W. Schöllkopf, A. Fielicke and O. Dopfer, *Int. J. Mass Spectrom.*, 2016, **395**, 1–6.

[120] P. Price, *J. Am. Soc. Mass Spectrom.*, 1991, **2**, 336–348.

[121] M. Guilhaus, *J. Mass Spectrom.*, 1995, **30**, 1519–1532.

[122] W. C. Wiley and I. H. McLaren, *Rev. Sci. Instrum.*, 1955, **26**, 1150–1157.

[123] M. Guilhaus, V. Mlynski and D. Selby, *Rapid Commun. Mass Spectrom.*, 1997, **11**, 951–962.

[124] J. M. Thompson, *Infrared Spectroscopy*, Pan Stanford Publishing, Singapore, 1st edn., 2018.

[125] D. Halliday, J. Walker and R. Resnick, *Principles of Physics*, John Wiley & Sons, 2023.

[126] P. W. Atkins, J. De Paula and J. Keeler, *Atkins' Physical Chemistry*, Oxford University Press, Oxford, 12th edn., 2023.

[127] C. Cramer, *Essentials of Computational Chemistry: Theories and Models*, Wiley, 2013.

[128] P. K. Mallick, *Fundamentals of Molecular Spectroscopy*, Springer Nature Singapore, Singapore, 1st edn., 2023.

[129] M. Abramowitz and I. A. Stegun, *Handbook of Mathematical Functions: with Formulas, Graphs, and Mathematical Tables*, Courier Corporation, 1965, vol. 55.

[130] E. I. Brewer, Ph.D. Thesis, University of Oxford, 2023.

[131] E. B. Wilson, J. C. Decius and P. C. Cross, *Molecular Vibrations: The Theory of Infrared and Raman Vibrational Spectra*, Courier Corporation, 1980.

[132] D. J. Willock, *Molecular Symmetry*, John Wiley & Sons, 2009.

[133] C. N. Banwell and E. M. McCash, *Fundamentals of Molecular Spectroscopy*, Indian Edition, 2017.

[134] D. A. McQuarrie and J. D. Simon, *Physical Chemistry: A Molecular Approach*, Viva Books, New Delhi, 2011.

[135] J. L. McHale, *Molecular Spectroscopy*, CRC Press, 2017.

[136] P. Rayer, *Pressure Broadening of Spectral Lines: The Theory of Line Shape in Atmospheric Physics*, Cambridge University Press, Cambridge, 2020.

[137] J. Levine, *Spectrochim. Acta, Part B*, 2012, **69**, 61–66.

[138] C. S. Goldenstein, R. M. Spearrin, J. B. Jeffries and R. K. Hanson, *Prog. Energy Combust. Sci.*, 2017, **60**, 132–176.

[139] J. M. Hollas, *Modern Spectroscopy*, Wiley, Chichester, West Sussex, 4th edn., 2004.

[140] D. A. Wild, P. S. Weiser, Z. M. Loh and E. J. Bieske, *J. Phys. Chem. A*, 2002, **106**, 906–910.

[141] D. F. Swinehart, *J. Chem. Educ.*, 1962, **39**, 333.

[142] M. D. Wheeler, S. M. Newman, A. J. Orr-Ewing and M. N. Ashfold, *J. Chem. Soc., Faraday Trans.*, 1998, **94**, 337–351.

[143] R. Casaes, R. Provençal, J. Paul and R. J. Saykally, *J. Chem. Phys.*, 2002, **116**, 6640–6647.

[144] N. Heine, Ph.D. Thesis, Freie Universität Berlin, 2014.

[145] G. Gagliardi and H.-P. Loock, *Cavity-Enhanced Spectroscopy and Sensing*, Springer, Berlin, Germany, 2014, vol. 179.

[146] J. Scherer, D. Voelkel, D. Rakestraw, J. Paul, C. Collier, R. Saykally and A. O'Keefe, *Chem. Phys. Lett.*, 1995, **245**, 273–280.

[147] K. R. Asmis and J. Sauer, *Mass Spectrom. Rev.*, 2007, **26**, 542–562.

[148] M. A. Duncan, *Int. J. Mass Spectrom.*, 2000, **200**, 545–569.

[149] N. C. Polfer, *Chem. Soc. Rev.*, 2011, **40**, 2211–2221.

[150] G. von Helden, I. Holleman, G. M. H. Knippels, A. F. G. van der Meer and G. Meijer, *Phys. Rev. Lett.*, 1997, **79**, 5234–5237.

[151] M. J. Carlo and A. L. Patrick, *J. Mass Spectrom. Adv. Clin. Lab*, 2022, **23**, 14–25.

[152] N. R. Walker, R. S. Walters and M. A. Duncan, *New J. Chem.*, 2005, **29**, 1495–1503.

[153] K. K. Lehmann, G. Scoles and B. H. Pate, *Annu. Rev. Phys. Chem.*, 1994, **45**, 241–274.

[154] T. H. Maiman, *Nature*, 1960, **187**, 493–494.

[155] S. Hooker and C. E. Webb, *Laser Physics*, Oxford University Press, Oxford, United Kingdom, 2010.

[156] J. E. Geusic, H. M. Marcos and L. G. Van Uitert, *Appl. Phys. Lett.*, 1964, **4**, 182–184.

[157] A. E. Siegman, *Lasers*, University Science Books, Mill Valley, Calif, 1986.

[158] F. J. McClung and R. W. Hellwarth, *J. Appl. Phys.*, 1962, **33**, 828–829.

[159] J.-Y. Zhang, *Optical Parametric Generation and Amplification*, Routledge, 2019.

[160] C. Chen, *Nonlinear Optical Borate Crystals: Principles and Applications*, Wiley-VCH, Weinheim, 1st edn., 2012.

[161] R. Boyd, *Contemporary Nonlinear Optics*, Academic Press, 2012.

[162] J. D. Jackson, *Classical Electrodynamics*, John Wiley & Sons, 2021.

[163] G. New, *Introduction to Nonlinear Optics*, Cambridge University Press, 2011.

[164] R. Shankar, *Principles of Quantum Mechanics*, Springer Science & Business Media, 2012.

[165] A. Szabo and N. S. Ostlund, *Modern Quantum Chemistry: Introduction to Advanced Electronic Structure Theory*, Dover Publications, Garden City, New York, 1996.

[166] D. R. Hartree, *Math. Proc. Cambridge Philos. Soc.*, 1928, **24**, 89–110.

[167] D. R. Hartree, *Math. Proc. Cambridge Philos. Soc.*, 1928, **24**, 111–132.

[168] D. R. Hartree and W. Hartree, *Proc. R. Soc. London, Ser. A*, 1935, **150**, 9–33.

[169] P. Echenique and J. L. Alonso, *Mol. Phys.*, 2007, **105**, 3057–3098.

[170] J. C. Slater, *Phys. Rev.*, 1928, **32**, 339–348.

[171] J. C. Slater, *Phys. Rev.*, 1951, **81**, 385–390.

[172] V. Gupta, *Principles and Applications of Quantum Chemistry*, Academic Press, 2015.

[173] J. G. Hill, *Int. J. Quantum Chem.*, 2013, **113**, 21–34.

[174] B. Nagy and F. Jensen, in *Basis Sets in Quantum Chemistry*, 2017, p. 93–149.

[175] M. Bursch, J.-M. Mewes, A. Hansen and S. Grimme, *Angew. Chem., Int. Ed.*, 2022, **61**, e202205735.

[176] H. Zhou, B. Kincaid, G. Wang, A. Annaberdiyev, P. Ganesh and L. Mitas, *J. Chem. Phys.*, 2024, **160**, 084302.

[177] K. Fægri and K. G. Dyall, in *Theoretical and Computational Chemistry*, Elsevier, 2002, vol. 11, ch. 5, pp. 259–290.

[178] C. Møller and M. S. Plesset, *Phys. Rev.*, 1934, **46**, 618–622.

[179] J. R. Sabin and E. J. Brändas, *Advances in Quantum Chemistry*, Academic Press, 2011, vol. 62.

[180] P. E. M. Siegbahn, J. Almlöf, A. Heiberg and B. O. Roos, *J. Chem. Phys.*, 1981, **74**, 2384–2396.

[181] K. Burke and L. O. Wagner, *Int. J. Quantum Chem.*, 2013, **113**, 96–101.

[182] K. Burke, *J. Chem. Phys.*, 2012, **136**, 150901.

[183] E. Fermi, *Rend. Accad. Naz. Lincei*, 1927, **6**, 5.

[184] L. H. Thomas, *Math. Proc. Cambridge Philos. Soc.*, 1927, **23**, 542–548.

[185] P. Hohenberg and W. Kohn, *Phys. Rev.*, 1964, **136**, B864–B871.

[186] W. Kohn and L. J. Sham, *Phys. Rev.*, 1965, **140**, A1133–A1138.

[187] R. G. Parr, Horizons of Quantum Chemistry, p. 5–15.

[188] A. D. Becke, *J. Chem. Phys.*, 1993, **98**, 5648–5652.

[189] J. P. Perdew and K. Schmidt, *AIP Conf. Proc.*, 2001, **577**, 1–20.

[190] T. J. Giese and D. M. York, *J. Chem. Phys.*, 2010, **133**, 244107.

[191] L. Goerigk and S. Grimme, *Wiley Interdiscip. Rev.:Comput. Mol. Sci.*, 2014, **4**, 576–600.

[192] P. W. Atkins and R. S. Friedman, *Molecular Quantum Mechanics*, Oxford University Press, Oxford, 2011.

[193] D. Sheppard, R. Terrell and G. Henkelman, *J. Chem. Phys.*, 2008, **128**, 134106.

[194] M. J. Frisch, G. W. Trucks, H. B. Schlegel, G. E. Scuseria, M. A. Robb, J. R. Cheeseman, G. Scalmani, V. Barone, G. A. Petersson, H. Nakatsuji, X. Li, M. Caricato, A. V. Marenich, J. Bloino, B. G. Janesko, R. Gomperts, B. Mennucci, H. P. Hratchian, J. V. Ortiz, A. F. Izmaylov, J. L. Sonnenberg, Williams, F. Ding, F. Lipparini, F. Egidi, J. Goings, B. Peng, A. Petrone, T. Henderson, D. Ranasinghe, V. G. Zakrzewski, J. Gao, N. Rega, G. Zheng, W. Liang, M. Hada, M. Ehara, K. Toyota, R. Fukuda, J. Hasegawa, M. Ishida, T. Nakajima, Y. Honda, O. Kitao, H. Nakai, T. Vreven, K. Throssell, J. A. Montgomery Jr., J. E. Peralta, F. Ogliaro, M. J. Bearpark, J. J. Heyd, E. N. Brothers, K. N. Kudin, V. N. Staroverov, T. A. Keith, R. Kobayashi, J. Normand, K. Raghavachari, A. P. Rendell, J. C. Burant, S. S. Iyengar, J. Tomasi, M. Cossi, J. M. Millam, M. Klene, C. Adamo, R. Cammi,

J. W. Ochterski, R. L. Martin, K. Morokuma, O. Farkas, J. B. Foresman and D. J. Fox, *Gaussian 16 Rev. C.01*, 2016.

[195] R. Dennington, T. A. Keith and J. M. Millam, *Semichem Inc.: Shawnee Mission, KS, USA*, 2016, 143–150.

[196] H. B. Schlegel, *J. Comput. Chem.*, 1982, **3**, 214–218.

[197] X. Li and M. J. Frisch, *J. Chem. Theory Comput.*, 2006, **2**, 835–839.

[198] M. A. Addicoat and G. F. Metha, *J. Comput. Chem.*, 2009, **30**, 57–64.

[199] M. A. Addicoat, S. Fukuoka, A. J. Page and S. Irle, *J. Comput. Chem.*, 2013, **34**, 2591–2600.

[200] R. S. Mulliken, *J. Chem. Phys.*, 1955, **23**, 1833–1840.

[201] S. Huzinaga and S. Narita, *Isr. J. Chem.*, 1980, **19**, 242–254.

[202] F. L. Hirshfeld, *Theor. Chim. Acta*, 1977, **44**, 129–138.

[203] E. I. Brewer, A. E. Green, A. S. Gentleman, P. W. Beardsmore, P. A. J. Pearcy, G. Meizyte, J. Pickering and S. R. Mackenzie, *Phys. Chem. Chem. Phys.*, 2022, **24**, 22716–22723.

[204] P. D. Watson, G. Meizyte, P. A. J. Pearcy, E. I. Brewer, A. E. Green, A. J. Stace and S. R. Mackenzie, *J. Phys. Chem. A*, 2025, **129**, 3867–3875.

[205] P. D. Watson, G. Meizyte, P. A. J. Pearcy, E. I. Brewer, A. E. Green, C. Robertson, M. J. Paterson and S. R. Mackenzie, *Phys. Chem. Chem. Phys.*, 2024, **26**, 16589–16596.

[206] S. O'brien, Y. Liu, Q. Zhang, J. Heath, F. Tittel, R. Curl and R. Smalley, *J. Chem. Phys.*, 1986, **84**, 4074–4079.

[207] D. R. Denison, *J. Vac. Sci. Technol.*, 1971, **8**, 266–269.

[208] R. E. March and J. F. Todd, *Quadrupole Ion Trap Mass Spectrometry*, John Wiley & Sons, 2005.

[209] M. Henchman and C. Steel, *J. Chem. Educ.*, 1998, **75**, 1049.

[210] D. Douglas, *Mass Spectrom. Rev.*, 2009, **28**, 937–960.

[211] L. Ding and S. Kumashiro, *Rapid Commun. Mass Spectrom.*, 2006, **20**, 3–8.

[212] R. Loss, *Pure Appl. Chem.*, 2003, **75**, 1107–1122.

[213] A. S. Gentleman, A. E. Green, D. R. Price, E. M. Cunningham, A. Iskra and S. R. Mackenzie, *Top. Catal.*, 2018, **61**, 81–91.

[214] U. Boesl, R. Weinkauf and E. W. Schlag, *Int. J. Mass Spectrom. Ion Processes*, 1992, **112**, 121–166.

[215] W. R. Bosenberg and D. R. Guyer, *J. Opt. Soc. Am. B*, 1993, **10**, 1716–1722.

[216] R. Danielius, A. Piskarskas, P. Di Trapani, A. Andreoni, C. Solcia and P. Foggi, *Opt. Lett.*, 1996, **21**, 973–975.

[217] D. Armstrong, W. Alford, T. Raymond, A. Smith and M. Bowers, *J. Opt. Soc. Am. B*, 1997, **14**, 460–474.

[218] A. Smith, D. Armstrong and W. Alford, *J. Opt. Soc. Am. B*, 1998, **15**, 122–141.

[219] R. J. Gehr, M. W. Kimmel and A. V. Smith, *Opt. Lett.*, 1998, **23**, 1298–1300.

[220] G. C. Catella and D. Burlage, *MRS Bull.*, 1998, **23**, 28–36.

[221] U. Willer, T. Blanke and W. Schade, *Appl. Opt.*, 2001, **40**, 5439–5445.

[222] J. Raffy, T. Debuisschert, J. P. Pocholle and M. Papuchon, *Appl. Opt.*, 1994, **33**, 985–7.

[223] B. Ziegler and K. Schepler, *Appl. Opt.*, 1991, **30**, 5077–5080.

[224] I. O. Kinyaevskiy, P. Danilov, S. Kudryashov, P. Pakholchuk, S. Ostrikov, N. N. Yudin, M. Zinovev, S. N. Podzyvalov and Y. M. Andreev, *Appl. Opt.*, 2022, **62**, 16–20.

[225] A. Iskra, Ph.D. Thesis, University of Oxford, 2017.

[226] G. A. West, J. J. Barrett, D. R. Siebert and K. V. Reddy, *Rev. Sci. Instrum.*, 1983, **54**, 797–817.

[227] G. Herzberg, *Molecular Spectra and Molecular Structure, Vol. I. Spectra of Diatomic Molecules,*, Krieger Publishing, Malabar, Florida, Reprint with corr. edn., 1991.

[228] G. Herzberg, *Molecular Spectra and Molecular Structure, Vol. II. Infrared and Raman Spectra of Polyatomic Molecules*, Krieger Publishing, Malabar, Florida, 1991, vol. 2.

[229] D. Oepts, A. F. G. van der Meer and P. W. van Amersfoort, *Infrared Phys. Technol.*, 1995, **36**, 297–308.

[230] B. L. Militsyn, G. von Helden, G. J. M. Meijer and A. F. G. van der Meer, *Nucl. Instrum. Methods Phys. Res., Sect. A*, 2003, **507**, 494–497.

[231] O. V. Lushchikova, S. Reijmer, P. B. Armentrout and J. M. Bakker, *J. Am. Soc. Mass Spectrom.*, 2022, **33**, 1393–1400.

[232] O. V. Lushchikova, Ph.D. Thesis, Radboud University, 2021.

[233] P. Schmüser, M. Dohlus, J. Rossbach and C. Behrens, *Free-Electron Lasers in the Ultraviolet and X-Ray Regime : Physical Principles, Experimental Results, Technical Realization*, Springer International Publishing, Cham, 2nd edn., 2014.

[234] E. J. Jaeschke, S. Khan, J. R. Schneider and J. B. Hastings, *Synchrotron Light Sources and Free-Electron Lasers: Accelerator Physics, Instrumentation and Science Applications*, Springer International Publishing, Cham, 2nd edn., 2020.

[235] J. M. J. Madey, *J. Appl. Phys.*, 1971, **42**, 1906–1913.

[236] L. R. Elias, W. M. Fairbank, J. M. J. Madey, H. A. Schwettman and T. I. Smith, *Phys. Rev. Lett.*, 1976, **36**, 717–720.

[237] W. Schöllkopf, S. Gewinner, H. Junkes, A. Paarmann, G. von Helden, H. Bluem and A. M. Todd, *The new IR and THz FEL facility at the Fritz Haber Institute in Berlin*, SPIE, 2015, vol. 9512.

[238] J. P. Perdew, *Phys. Rev. B*, 1986, **33**, 8822–8824.

[239] F. Weigend, *Phys. Chem. Chem. Phys.*, 2006, **8**, 1057–1065.

[240] F. Weigend and R. Ahlrichs, *Phys. Chem. Chem. Phys.*, 2005, **7**, 3297–3305.

[241] T. Boningari and P. G. Smirniotis, *Curr. Opin. Chem. Eng.*, 2016, **13**, 133–141.

[242] J. A. McCleverty, *Chem. Rev.*, 2004, **104**, 403–418.

[243] R. M. Palmer, A. G. Ferrige and S. Moncada, *Nature*, 1987, **327**, 524–526.

[244] C. A. Barth, K. D. Mankoff, S. M. Bailey and S. C. Solomon, *J. Geophys. Res.:Space Phys.*, 2003, **108**, 1027.

[245] E. E. van Faassen, S. Bahrami, M. Feelisch, N. Hogg, M. Kelm, D. B. Kim-Shapiro, A. V. Kozlov, H. Li, J. O. Lundberg, R. Mason, H. Nohl, T. Rassaf, A. Samouilov, A. Slama-Schwok, S. Shiva, A. F. Vanin, E. Weitzberg, J. Zweier and M. T. Gladwin, *Med. Res. Rev.*, 2009, **29**, 683–741.

[246] J. H. Seinfeld and S. N. Pandis, *Atmospheric Chemistry and Physics: from Air Pollution to Climate Change*, John Wiley & Sons, 2016.

[247] L. T. Murray, *Curr. Pollut. Rep.*, 2016, **2**, 115–133.

[248] C. T. Bowman, *Symp. (Int.) Combust., [Proc.]*, 1992, **24**, 859–878.

[249] J. Kašpar, P. Fornasiero and N. Hickey, *Catal. Today*, 2003, **77**, 419–449.

[250] B. Gao, N. Zhang, H. Zhang, R. Qiu, Z. Chen, Y. Li and Z. Yang, *J. Environ. Chem. Eng.*, 2022, **10**, 108669.

[251] K. Hauff, U. Tuttlies, G. Eigenberger and U. Nieken, *Appl. Catal., B*, 2012, **123-124**, 107–116.

[252] W. Hauptmann, M. Votsmeier, J. Gieshoff, A. Drochner and H. Vogel, *Appl. Catal., B*, 2009, **93**, 22–29.

[253] A. u. R. Salman, B. C. Enger, X. Auvray, R. Lødeng, M. Menon, D. Waller and M. Rønning, *Appl. Catal., A*, 2018, **564**, 142–146.

[254] B. M. Weiss and E. Iglesia, *J. Phys. Chem. C*, 2009, **113**, 13331–13340.

[255] A. C. A. de Vooys, M. T. M. Koper, R. A. van Santen and J. A. R. van Veen, *Electrochim. Acta*, 2001, **46**, 923–930.

[256] T. P. Kobylinski and B. W. Taylor, *J. Catal.*, 1974, **33**, 376–384.

[257] Z.-P. Liu, S. J. Jenkins and D. A. King, *J. Am. Chem. Soc.*, 2003, **125**, 14660–14661.

[258] K. Otto and H. C. Yao, *J. Catal.*, 1980, **66**, 229–236.

[259] Y. Bai and M. Mavrikakis, *J. Phys. Chem. B*, 2018, **122**, 432–443.

[260] S. S. Mulla, N. Chen, L. Cumaranatunge, G. E. Blau, D. Y. Zemlyanov, W. N. Delgass, W. S. Epling and F. H. Ribeiro, *J. Catal.*, 2006, **241**, 389–399.

[261] T. M. Bernhardt, *Int. J. Mass Spectrom.*, 2005, **243**, 1–29.

[262] M. Beyer, C. Berg, H. W. Görlitzer, T. Schindler, U. Achatz, G. Albert, G. Niedner-Schatteburg and V. E. Bondybey, *J. Am. Chem. Soc.*, 1996, **118**, 7386–7389.

[263] M. Beyer, U. Achatz, C. Berg, S. Joos, G. Niedner-Schatteburg and V. E. Bondybey, *J. Phys. Chem. A*, 1999, **103**, 671–678.

[264] G. Niedner-Schatteburg and V. E. Bondybey, *Chem. Rev.*, 2000, **100**, 4059–4086.

[265] M. L. Anderson, A. Lacz, T. Drewello, P. J. Derrick, D. P. Woodruff and S. R. MacKenzie, *J. Chem. Phys.*, 2009, **130**, 064305.

[266] T. Hanmura, M. Ichihashi and T. Kondow, *Isr. J. Chem.*, 2007, **47**, 37–42.

[267] T. Hanmura, M. Ichihashi, R. Okawa and T. Kondow, *Int. J. Mass Spectrom.*, 2009, **280**, 184–189.

[268] J. J. Klaassen and D. B. Jacobson, *J. Am. Chem. Soc.*, 1988, **110**, 974–976.

[269] K. Koyama, S. Kudoh, K. Miyajima and F. Mafuné, *J. Phys. Chem. A*, 2015, **119**, 9573–9580.

[270] Y. Xie, F. Dong, S. Heinbuch, J. J. Rocca and E. R. Bernstein, *Phys. Chem. Chem. Phys.*, 2010, **12**, 947–959.

[271] W. D. Vann, R. C. Bell and A. W. Castleman, *J. Phys. Chem. A*, 1999, **103**, 10846–10850.

[272] W. D. Vann, R. L. Wagner and A. W. Castleman, *J. Phys. Chem. A*, 1998, **102**, 8804–8811.

[273] W. D. Vann, R. L. Wagner and A. W. Castleman, *J. Phys. Chem. A*, 1998, **102**, 1708–1718.

[274] M. S. Ford, M. L. Anderson, M. P. Barrow, D. P. Woodruff, T. Drewello, P. J. Derrick and S. R. Mackenzie, *Phys. Chem. Chem. Phys.*, 2005, **7**, 975–980.

[275] D. Harding, S. R. Mackenzie and T. R. Walsh, *J. Phys. Chem. B*, 2006, **110**, 18272–18277.

[276] Y. Zhang, M. Yamaguchi, K. Kawada, S. Kudoh, O. V. Lushchikova, J. M. Bakker and F. Mafuné, *J. Phys. Chem. A*, 2022, **126**, 36–43.

[277] M. L. Anderson, M. S. Ford, P. J. Derrick, T. Drewello, D. Phil Woodruff and S. R. Mackenzie, *J. Phys. Chem. A*, 2006, **110**, 10992–11000.

[278] J. Hagen, L. D. Socaciu-Siebert, J. Le Roux, D. Popolan, S. Vajda, T. M. Bernhardt and L. Wöste, *Int. J. Mass Spectrom.*, 2007, **261**, 152–158.

[279] M. Yamaguchi, Y. Zhang, O. V. Lushchikova, J. M. Bakker and F. Mafuné, *J. Phys. Chem. A*, 2022, **126**, 6668–6677.

[280] A. Fielicke, G. Von Helden, G. Meijer, B. Simard and D. M. Rayner, *Phys. Chem. Chem. Phys.*, 2005, **7**, 3906–3909.

[281] C. Kerpal, D. J. Harding, A. C. Hermes, G. Meijer, S. R. Mackenzie and A. Fielicke, *J. Phys. Chem. A*, 2013, **117**, 1233–1239.

[282] D. J. Harding and A. Fielicke, *Chemistry*, 2014, **20**, 3258–3267.

[283] U. Achatz, C. Berg, S. Joos, B. S. Fox, M. K. Beyer, G. Niedner-Schatteburg and V. E. Bondybey, *Chem. Phys. Lett.*, 2000, **320**, 53–58.

[284] I. Balteanu, O. Petru Balaj, M. K. Beyer and V. E. Bondybey, *Phys. Chem. Chem. Phys.*, 2004, **6**, 2910–2913.

[285] M. Brönstrup, D. Schröder, I. Kretzschmar, H. Schwarz and J. N. Harvey, *J. Am. Chem. Soc.*, 2001, **123**, 142–147.

[286] A. E. Green, J. Justen, W. Schöllkopf, A. S. Gentleman, A. Fielicke and S. R. Mackenzie, *Angew. Chem., Int. Ed.*, 2018, **57**, 14822–14826.

[287] A. C. Hermes, S. M. Hamilton, G. A. Cooper, C. Kerpal, D. J. Harding, G. Meijer, A. Fielicke and S. R. Mackenzie, *Faraday Discuss.*, 2012, **157**, 213–225.

[288] E. Hernández, V. Bertin, J. Soto, A. Miralrio and M. Castro, *J. Phys. Chem. A*, 2018, **122**, 2209–2220.

[289] C. Kerpal, D. J. Harding, D. M. Rayner and A. Fielicke, *J. Phys. Chem. A*, 2013, **117**, 8230–8237.

[290] Y. Shi and K. M. Ervin, *J. Chem. Phys.*, 1998, **108**, 1757–1760.

[291] D. Trevor, D. Cox and A. Kaldor, *J. Am. Chem. Soc.*, 1990, **112**, 3742–3749.

[292] D. Trevor, R. Whetten, D. Cox and A. Kaldor, *J. Am. Chem. Soc.*, 1985, **107**, 518–519.

[293] J. Velasquez and M. A. Duncan, *Chem. Phys. Lett.*, 2008, **461**, 28–32.

[294] H. Yamamoto, K. Miyajima, T. Yasuike and F. Mafuné, *J. Phys. Chem. A*, 2013, **117**, 12175–12183.

[295] K. Koszinowski, D. Schröder and H. Schwarz, *J. Phys. Chem. A*, 2003, **107**, 4999–5006.

[296] J. Yamagishi, K. Miyajima, S. Kudoh and F. Mafuné, *J. Phys. Chem. Lett.*, 2017, **8**, 2143–2147.

[297] V. Blagojevic, E. Flaim, M. J. Y. Jarvis, G. K. Koyanagi and D. K. Bohme, *J. Phys. Chem. A*, 2005, **109**, 11224–11235.

[298] J. H. Enemark and R. D. Feltham, *Coord. Chem. Rev.*, 1974, **13**, 339–406.

[299] T. W. Hayton, P. Legzdins and W. B. Sharp, *Chem. Rev.*, 2002, **102**, 935–992.

[300] J. Gräfenstein and D. Cremer, *Phys. Chem. Chem. Phys.*, 2000, **2**, 2091–2103.

[301] L. Wang, G. Wang, H. Qu, C. Wang and M. Zhou, *J. Phys. Chem. A*, 2014, **118**, 1841–1849.

[302] L. Wang, G. Wang, H. Qu, H. Li and M. Zhou, *Phys. Chem. Chem. Phys.*, 2014, **16**, 10788–10798.

[303] Y. Li, L. Wang, H. Qu, G. Wang and M. Zhou, *J. Phys. Chem. A*, 2015, **119**, 3577–3586.

[304] G. Meizyte, P. A. J. Pearcy, P. D. Watson, E. I. Brewer, A. E. Green, M. Doll, O. A. Duda and S. R. Mackenzie, *J. Phys. Chem. A*, 2022, **126**, 9414–9422.

[305] A. Iskra, A. S. Gentleman, A. Kartouzian, M. J. Kent, A. P. Sharp and S. R. Mackenzie, *J. Phys. Chem. A*, 2017, **121**, 133–140.

[306] A. E. Green, R. H. Brown, G. Meizyte and S. R. Mackenzie, *J. Phys. Chem. A*, 2021, **125**, 7266–7277.

[307] C. Walther, S. Becker, G. Dietrich, H. J. Kluge, M. Lindinger, K. Lützenkirchen, L. Schweikhard and J. Ziegler, *Z. Phys. D:At., Mol. Clusters*, 1996, **38**, 51–58.

[308] G. Meizyte, R. H. Brown, E. I. Brewer, P. D. Watson and S. R. Mackenzie, *J. Phys. Chem. A*, 2023, **127**, 9220–9228.

[309] X.-G. Zhang and P. Armentrout, *Eur. J. Mass Spectrom.*, 2004, **10**, 963–975.

[310] M. Z. Martin, S. R. Desai, C. S. Feigerle and J. C. Miller, *J. Phys. Chem.*, 1996, **100**, 8170–8174.

[311] J. A. McCleverty, *Chem. Rev.*, 1979, **79**, 53–76.

[312] S. C. Rasmussen, *ChemTexts*, 2015, **1**, 10.

[313] R. J. Farrauto and R. M. Heck, *Catal. Today*, 1999, **51**, 351–360.

[314] S. Lang, D. Popolan and T. Bernhardt, in *The Chemical Physics of Solid Surfaces*, Elsevier, 2007, vol. 12, ch. 2, pp. 53–90.

[315] S. M. Lang, T. M. Bernhardt, J. M. Bakker, R. N. Barnett and U. Landman, *Phys. Chem. Chem. Phys.*, 2023, **25**, 32166–32172.

[316] P. T. Rubli, C. T. Haakansson, P. A. J. Pearcy, R. G. Spratt, J. M. Bakker, P. D. Watson and S. R. Mackenzie, *J. Phys. Chem. A*, 2025, **129**, 5810–5819.

[317] F. Mafuné, Y. Tawaraya and S. Kudoh, *J. Phys. Chem. A*, 2016, **120**, 4089–4095.

[318] S. M. Hamilton, W. S. Hopkins, D. J. Harding, T. R. Walsh, M. Haertelt, C. Kerpal, P. Gruene, G. Meijer, A. Fielicke and S. R. Mackenzie, *J. Phys. Chem. A*, 2011, **115**, 2489–2497.

[319] E. M. Fernández and L. C. Balbás, *J. Chem. Phys.*, 2022, **157**, 074310.

[320] G. Meizyte, A. E. Green, A. S. Gentleman, S. Schaller, W. Schöllkopf, A. Fielicke and S. R. Mackenzie, *Phys. Chem. Chem. Phys.*, 2020, **22**, 18606–18613.

[321] E. M. Cunningham, A. E. Green, G. Meizyte, A. S. Gentleman, P. W. Beardsmore, S. Schaller, K. M. Pollow, K. Saroukh, M. Förstel, O. Dopfer, W. Schöllkopf, A. Fielicke and S. R. Mackenzie, *Phys. Chem. Chem. Phys.*, 2021, **23**, 329–338.

[322] J. M. Bakker and F. Mafuné, *Phys. Chem. Chem. Phys.*, 2022, **24**, 7595–7610.

[323] T. Nagata, K. Koyama, S. Kudoh, K. Miyajima, J. M. Bakker and F. Mafuné, *J. Phys. Chem. C*, 2017, **121**, 27417–27426.

[324] M. Yamaguchi, S. Kudoh, K. Miyajima, O. V. Lushchikova, J. M. Bakker and F. Mafuné, *J. Phys. Chem. C*, 2019, **123**, 3476–3481.

[325] G. K. Koyanagi and D. K. Bohme, *J. Phys. Chem. A*, 2006, **110**, 1232–1241.

[326] L. Holmgren and A. Rosén, *J. Chem. Phys.*, 1999, **110**, 2629–2636.

[327] M. Kraft, J. R. Flores, W. Klopper, M. M. Kappes and D. Schooss, *J. Phys. Chem. A*, 2021, **125**, 3135–3145.

[328] B. Collings, D. Rayner and P. Hackett, *Int. J. Mass Spectrom. Ion Processes*, 1993, **125**, 207–214.

[329] Q. Wu and S. Yang, *Int. J. Mass Spectrom.*, 1999, **184**, 57–65.

[330] A. Fielicke, C. Ratsch, G. von Helden and G. Meijer, *J. Chem. Phys.*, 2007, **127**, 234306.

[331] S. Heinbuch, F. Dong, J. J. Rocca and E. R. Bernstein, *J. Chem. Phys.*, 2010, **133**, 174314.

[332] W.-g. Wang, Z.-c. Wang, S. Yin, S.-g. He and M.-f. Ge, *Chin. J. Chem. Phys.*, 2007, **20**, 412–418.

[333] C. L. Briant and M. K. Banerjee, in *Refractory Metals and Alloys*, Elsevier, 2016.

[334] H. Shelton, *Phys. Rev.*, 1957, **107**, 1553–1557.

[335] A. Jiang, T. A. Tyson and L. Axe, *J. Phys.:Condens. Matter*, 2005, **17**, 6111.

[336] X. Li, Y. Chen, P. Basnet, J. Luo and H. Wang, *RSC Adv.*, 2019, **9**, 1015–1028.

[337] F. Siegele, M. Tschurl, D. Schooss and U. Heiz, *ChemPhysChem*, 2025, **26**, e202400513.

[338] J. Lengyel, N. Levin, F. J. Wensink, O. V. Lushchikova, R. N. Barnett, U. Landman, U. Heiz, J. M. Bakker and M. Tschurl, *Angew. Chem., Int. Ed.*, 2020, **59**, 23631–23635.

[339] J. F. Eckhard, D. Neuwirth, C. Panosetti, H. Oberhofer, K. Reuter, M. Tschurl and U. Heiz, *Phys. Chem. Chem. Phys.*, 2017, **19**, 5985–5993.

[340] J. F. Eckhard, D. Neuwirth, M. Tschurl and U. Heiz, *Phys. Chem. Chem. Phys.*, 2017, **19**, 10863–10869.

[341] K. Lange, B. Visser, D. Neuwirth, J. F. Eckhard, U. Boesl, M. Tschurl, K. H. Bowen and U. Heiz, *Int. J. Mass Spectrom.*, 2015, **375**, 9–13.

[342] J. F. Eckhard, T. Masubuchi, M. Tschurl, R. N. Barnett, U. Landman and U. Heiz, *J. Phys. Chem. C*, 2018, **122**, 25628–25637.

[343] D. V. Fries, M. P. Klein, A. Steiner, M. H. Prosenc and G. Niedner-Schatteburg, *Phys. Chem. Chem. Phys.*, 2021, **23**, 11345–11354.

[344] X. Li, Y. Tang, S. Li and Y. Gui, *Spectrochim. Acta, Part A*, 2019, **216**, 335–341.

[345] M. Meta, M. E. Huber, T. Michaelsen, A. Ayasli, M. Ončák, R. Wester and J. Meyer, *J. Phys. Chem. Lett.*, 2023, **14**, 5524–5530.

[346] A. Fielicke, P. Gruene, M. Haertelt, D. J. Harding and G. Meijer, *J. Phys. Chem. A*, 2010, **114**, 9755–9761.

[347] Z. J. Wu, Y. Kawazoe and J. Meng, *JJ. Mol. Struct.:THEOCHEM*, 2006, **764**, 123–132.

[348] X. Sun and X. Huang, *ACS Omega*, 2022, **7**, 22682–22688.

[349] P. Wang, S. Gong, Y. Li and Y. Mo, *J. Chem. Phys.*, 2024, **160**, 014304.

[350] K. A. Moltved and K. P. Kepp, *J. Phys. Chem. C*, 2019, **123**, 18432–18444.

[351] F. Huffman, in *Thermionic Energy Conversion*, Academic Press, New York, 2003, p. 627–638.

[352] K. Athanassenas, T. Leisner, U. Frenzel, D. Kreisle and E. Recknagel, *Z. Phys. D:At., Mol. Clusters*, 1993, **26**, 153–155.

[353] B. Baguenard, J. Pinaré, C. Bordas and M. Broyer, *Phys. Rev. A*, 2001, **63**, 023204.

[354] D. van Heijnsbergen, A. Fielicke, G. Meijer and G. von Helden, *Phys. Rev. Lett.*, 2002, **89**, 013401.

[355] D. van Heijnsbergen, G. von Helden, M. A. Duncan, A. J. van Roij and G. Meijer, *Phys. Rev. Lett.*, 1999, **83**, 4983.

[356] E. E. B. Campbell and R. D. Levine, *Annu. Rev. Phys. Chem.*, 2000, **51**, 65–98.

[357] G. von Helden, D. van Heijnsbergen and G. Meijer, *J. Phys. Chem. A*, 2003, **107**, 1671–1688.

[358] V. J. Lapoutre, M. Haertelt, G. Meijer, A. Fielicke and J. M. Bakker, *J. Chem. Phys.*, 2013, **139**, 121101.

[359] M. Koskinen and M. Manninen, *Phys. Rev. B*, 1996, **54**, 14796–14806.

[360] Y. Fujimura and S. H. LinR. A. Meyers, Academic Press, New York, 2003, p. 199–229.

[361] M. B. Knickelbein and S. Yang, *J. Chem. Phys.*, 1990, **93**, 5760–5767.

[362] P. Gruene, A. Fielicke and G. Meijer, *J. Chem. Phys.*, 2007, **127**, 234307.

[363] R. O. Jenkins, *Vacuum*, 1969, **19**, 353–359.

[364] F. Dong, S. Heinbuch, S. G. He, Y. Xie, J. J. Rocca and E. R. Bernstein, *J. Chem. Phys.*, 2006, **125**, 164318.

[365] A. S. Chaves, M. J. Piotrowski and J. L. Da Silva, *Phys. Chem. Chem. Phys.*, 2017, **19**, 15484–15502.

[366] M. Perera, K. Roenitz, R. Metz, O. Kostko and M. Ahmed, *J. Spectrosc. Dyn.*, 2014, **4**, 21.

[367] A. E. Green, S. Schaller, G. Meizyte, B. J. Rhodes, S. P. Kealy, A. S. Gentleman, W. Schöllkopf, A. Fielicke and S. R. MacKenzie, *J. Phys. Chem. A*, 2020, **124**, 5389–5401.

[368] M. Manninen, J. Mansikka-aho, H. Nishioka and Y. Takahashi, *Z. Phys. D:At., Mol. Clusters*, 1994, **31**, 259–267.

[369] H. Grönbeck and A. Rosén, *Z. Phys. D:At., Mol. Clusters*, 1996, **36**, 153–157.

[370] M. Kabir, A. Mookerjee and A. K. Bhattacharya, *Eur. Phys. J. D*, 2004, **31**, 477–485.

[371] K. Koyasu, M. Mitsui, A. Nakajima and K. Kaya, *Chem. Phys. Lett.*, 2002, **358**, 224–230.

[372] L.-H. Mou, Q.-Y. Liu, T. Zhang, Z.-Y. Li and S.-G. He, *J. Phys. Chem. A*, 2018, **122**, 3489–3495.

[373] M. Sierka, J. Dobler, J. Sauer, G. Santambrogio, M. Brummer, L. Woste, E. Janssens, G. Meijer and K. R. Asmis, *Angew. Chem., Int. Ed. Engl.*, 2007, **46**, 3372.

[374] G.-D. Jiang, L.-H. Mou, J.-J. Chen, Z.-Y. Li and S.-G. He, *J. Phys. Chem. A*, 2020, **124**, 7749–7755.

[375] J. M. Lightstone, H. A. Mann, M. Wu, P. M. Johnson and M. G. White, *J. Phys. Chem. B*, 2003, **107**, 10359–10366.

[376] M. A. Duncan, *J. Cluster Sci.*, 1997, **8**, 239–266.

[377] K. Fisher, I. Dance, G. Willett and M. Yi, *J. Chem. Soc., Dalton Trans.*, 1996, 709–718.

[378] W. R. Buratto, R. B. Ferreira, V. J. Catalano, R. García-Serres and L. J. Murray, *Dalton Trans.*, 2021, **50**, 816–821.

[379] T. Jian, X. Chen, S.-D. Li, A. I. Boldyrev, J. Li and L.-S. Wang, *Chem. Soc. Rev.*, 2019, **48**, 3550–3591.

[380] T. Jian, W.-L. Li, I. A. Popov, G. V. Lopez, X. Chen, A. I. Boldyrev, J. Li and L.-S. Wang, *J. Chem. Phys.*, 2016, **144**, 154310.

[381] C. Romanescu, T. R. Galeev, W.-L. Li, A. I. Boldyrev and L.-S. Wang, *Acc. Chem. Res.*, 2013, **46**, 350–358.

[382] S. Pande, T. Jian, N. S. Khetrapal, L.-S. Wang and X. C. Zeng, *J. Phys. Chem. C*, 2018, **122**, 6947–6954.

[383] S. Du, X. Liu, Z. Liu, G. Li, H. Fan, H. Xie and L. Jiang, *JACS Au*, 2023, **3**, 1723–1727.

[384] N. S. Khetrapal, T. Jian, R. Pal, G. V. Lopez, S. Pande, L.-S. Wang and X. C. Zeng, *Nanoscale*, 2016, **8**, 9805–9814.

[385] S. Nonose, Y. Sone, K. Onodera, S. Sudo and K. Kaya, *J. Phys. Chem.*, 1990, **94**, 2744–2746.

[386] C. He and C. H. Becker, *Phys. Rev. A*, 1997, **55**, 1300–1306.

[387] W. Finkelnburg and W. Humbach, *Naturwissenschaften*, 1955, **42**, 35–37.

[388] J. Ziegler, G. Dietrich, S. Krückeberg, K. Lützenkirchen, L. Schweikhard and C. Walther, *Hyperfine Interact.*, **115**, 171–179.

[389] W. Schulze, B. Winter and I. Goldenfeld, *Phys. Rev. B*, 1988, **38**, 12937–12941.

[390] C. J. Owen, N. R. Keyes, C. Xie, H. Guo and P. B. Armentrout, *J. Chem. Phys.*, 2019, **150**, 174305.

[391] S. Dyubko, V. Efremov, V. Gerasimov and K. MacAdam, *J. Phys. B:At., Mol. Opt. Phys.*, 2005, **38**, 1107.

[392] G. A. Bishea and M. D. Morse, *J. Chem. Phys.*, 1991, **95**, 5646–5659.